

# **Electrolytic Reduction of Metal Oxides in Molten $\text{Li}_2\text{O}/\text{LiCl}$**

A Dissertation

Presented in Partial Fulfillment of the Requirements for the

Degree of Doctor of Philosophy

with a

Major in Chemical Engineering

in the

College of Graduate Studies

University of Idaho

by

Meng Shi

Major Professor: Haiyan Zhao, Ph.D.

Committee Members: Vivek Utgikar, Ph.D.; Soumya Srivastava, Ph.D.; Shelly Li, Ph.D.

Department Administrator: Ching-An Peng, Ph.D.

August 2020

### Authorization to Submit Dissertation

This dissertation of Meng Shi, submitted for the degree of Doctor of Philosophy with a Major in Chemical Engineering and titled "Electrolytic Reduction of Metal Oxides in Molten  $\text{Li}_2\text{O}/\text{LiCl}$ ," has been reviewed in final form. Permission, as indicated by the signatures and dates below, is now granted to submit final copies to the College of Graduate Studies for approval.

Major Professor: \_\_\_\_\_ Date: \_\_\_\_\_  
Haiyan Zhao, Ph.D.

Committee Members: \_\_\_\_\_ Date: \_\_\_\_\_  
Vivek Utgikar, Ph.D.

\_\_\_\_\_ Date: \_\_\_\_\_  
Soumya Srivastava, Ph.D.

\_\_\_\_\_ Date: \_\_\_\_\_  
Shelly Li, Ph.D.

Department

Administrator: \_\_\_\_\_ Date: \_\_\_\_\_  
Ching-An Peng, Ph.D.

## Abstract

Electrolytic reduction of metal oxides is a promising approach to produce high purity metals. However, the commercialization of the process is challenged by low current efficiency. The low current efficiency is due to the slow oxygen ion diffusion through the oxide particles. In order to improve the current efficiency, it is important to understand the reduction mechanism and find solutions to the key factors.

This project focuses on fundamental electrolytic studies and the sonication operating mechanisms in molten salts. Metal oxides (NiO, and TiO<sub>2</sub>) were reduced in a small scale through electrolytic approaches in molten Li<sub>2</sub>O/LiCl at 650 °C. The reductions were carried out by controlling the total applied charges, and the cathodic potential at overpotentials and underpotentials. To accurately control the cathodic potential, a three-terminal electrolytic cell was used, including an oxide basket cathode, a glassy carbon crucible anode and a Ni/NiO reference electrode (RE). The reduced products were characterized for compositions and oxygen levels using X-ray diffraction (XRD) and Thermogravimetric Analysis (TGA). The XRD results were analyzed with the Rietveld refinement to get the quantitative analysis of the components. Salts after reductions were analyzed for metal element contents using Inductively Coupled Plasma Mass Spectrometry (ICP-MS). The reduction extent, current efficiency were calculated as the key parameters in evaluating the process.

Ni/NiO reference electrode was used in the reduction, for the advantage of its stable performance in electrolyte with varying O<sup>2-</sup> concentrations, compared with glassy carbon (GC), tungsten (W), and molybdenum (Mo) reference electrode. The correlation of the electrode potentials among the GC, W, Mo and Ni/NiO reference electrode was defined in both molten LiCl and 1 w.t.% Li<sub>2</sub>O/LiCl. The lithium deposition potential measured with Ni/NiO reference electrode was -1.75 V or -1.90 V vs. Ni/NiO, based on the fabrication method of the Ni/NiO reference electrode.

In the overpotential reductions of NiO, Ni metal was produced at a high current efficiency of 96.1%. The reduction followed a simple one-step reduction mechanism in a fast kinetics. The NiO was reduced directly to nickel metal by the lithium metal and electrons without any intermediate involved. Samples were analyzed with XRD and TGA. The success in the NiO reduction verified the feasibility of the experiment setup and the methodology.

Electroreduction of TiO<sub>2</sub> at overpotentials generated lithium titanates Li<sub>2</sub>TiO<sub>3</sub> and LiTiO<sub>2</sub>. The reduction followed multiple steps and generate multiple interfaces. Li<sub>2</sub>TiO<sub>3</sub> was formed on the outer shell of the particle through a spontaneous chemical combination reaction of TiO<sub>2</sub> and Li<sub>2</sub>O. When the lithium metal was generated on the cathode, it reduced the TiO<sub>2</sub> core to LiTiO<sub>2</sub>. Finally, the Li<sub>2</sub>TiO<sub>3</sub>

shell was reduced with Li metal to  $\text{LiTiO}_2$ .  $\text{LiTiO}_2$  was the final product of the reduction at  $-0.3$  V vs.  $\text{Li/Li}^+$  with 150% of the theoretical charge, resulting in a 25% of reduction extent and 16.7% reduction extent. The oxygen ion diffusion through the solid phase was found to be the rate-limiting factor in the reduction.

The sonication was coupled with the  $\text{TiO}_2$  electroreduction process in both overpotential and underpotential controls. By using the ultrasound agitation, the current efficiency was improved. For overpotential reductions, the current efficiency was increased from 26.7% to 27.4%; and for the underpotential reductions, the increment was more significant, from 36.7% to 44.5%. So, the introduction of sonication in the reductions could enhance the internal oxygen ion diffusion inside the metal oxides, and as the result, improve the current efficiency.

The results and conclusion in this work could promote the commercialization of the metal production through electrolytic reductions and ultrasound technique in molten salts, and impact the pyroprocessing technology for the treatment of spent nuclear fuels.

## Acknowledgements

I would like to express my deepest gratitude towards my advisor Dr. Haiyan Zhao for her guidance and confidence in me. She was very patient in my growth, and helped me get through the hard time throughout my Ph.D.

I sincerely appreciate Dr. Shelly Li from the INL for her technical guidance and support. She is the principle investigator of this LDRD project. Her technical guidance and financial support guarantee the progress of this project. As an expert in the field, Dr. Li was always willing to help me in all kinds of technical questions and difficulties. She had high tolerance of my incessant questions.

I am particularly indebted to Dr. Vivek Utgikar and Dr. Soumya Srivastava for their time and consideration. Their suggestion and questions were pertinent and kept me in the right path in thinking and addressing problems.

I acknowledge Dr. Bin Liu from the Kansas State University (Manhattan, KS). He spent his precious time doing the complicated DFT calculations which played an essential role in clarifying the mechanism of oxide reductions.

I also thank staff and support technicians from the Center of Advanced Energy Studies (CAES, Idaho Falls, ID). Their assistance was important in carrying out the project safely and smoothly. They contributed their time sitting in meetings about the safety concerns and progress report of the study.

My appreciation is extending to staff from the University of Idaho. They were very helpful in answering questions related to my graduation studies. They also responded quickly and efficiently in administrative problems of the project.

A special mention goes to the past and present group members contributed to this project, especially Eugene Engmann, William Armour, Amey Shigrekar, Jieun Lee, Dustin Jeremiah, Seungje Oh, Ruixue Wang, and Eric Song.

This work is supported through the INL Laboratory Directed Research & Development (LDRD) Program under DOE Idaho Operations Office Contract DE-AC07-05ID14517.

## Table of Contents

Authorization to Submit Dissertation .....	ii
Abstract .....	iii
Acknowledgements .....	v
Table of Contents .....	vi
List of Tables .....	x
List of Figures .....	xii
Nomenclature .....	xvi
Statement of Contribution .....	xix
Chapter 1: Introduction .....	1
1.1 Research Motivation .....	3
1.2 Dissertation Scope .....	4
Chapter 2: Literature Review .....	6
2.1 Metal Oxide Electroreductions .....	6
2.1.1 FFC and OS Processes in Molten CaCl <sub>2</sub> Salts .....	6
2.1.1.1 TiO <sub>2</sub> .....	6
2.1.1.2 NiO .....	14
2.1.1.3 Tb <sub>4</sub> O <sub>7</sub> .....	16
2.1.1.4 WO <sub>3</sub> .....	17
2.1.1.5 Nb <sub>2</sub> O <sub>5</sub> .....	17
2.1.1.6 Ta <sub>2</sub> O <sub>5</sub> .....	18
2.1.1.7 Cr <sub>2</sub> O <sub>3</sub> .....	19
2.1.2 Electrolytic Reduction in Molten LiCl Salts .....	21
2.1.2.1 Pyroprocessing .....	21
2.1.2.2 TiO <sub>2</sub> .....	26
2.1.2.3 Ta <sub>2</sub> O <sub>5</sub> .....	28
2.1.2.4 Nb <sub>2</sub> O <sub>5</sub> .....	29

2.1.3 Electrolytic Reduction System .....	30
2.1.3.1 Electrolyte.....	30
2.1.3.2 Electrode.....	32
2.2 Research Challenges and Gaps.....	37
2.3 Research Objectives .....	38
Chapter 3: Methodology.....	40
3.1 Electrolytic Techniques.....	40
3.3.1 Cyclic Voltammetry .....	40
3.3.2 Constant Potential Chronoamperometry .....	42
3.3.2.1 Chronoamperometry for Electrode Surface Cleansing.....	42
3.3.2.2 Chronoamperometry for Electrolytic Reductions.....	43
3.2 Application of Sonication.....	44
3.3 Experimental Setup .....	46
3.3.1 A Three-electrode Electrolytic Cell.....	46
3.3.1.1 Metal Oxide Precursors .....	46
3.3.1.2 Anode / Crucible.....	47
3.3.1.3 Cathodes and Oxide Baskets .....	49
3.3.1.4 Reference Electrode.....	51
3.3.1.5 Electrolyte Selection.....	52
3.3.1.6 Reduction Atmosphere Control.....	53
3.3.2 Sonication Apparatus.....	55
3.4 Characterization of Reduced Products and Used Salts.....	57
3.4.1 Reduced Sample Treatment and Used Salt Sampling .....	57
3.4.2 XRD Analysis of Reduced Products .....	58
3.4.3 TGA Analysis of Reduced Products.....	59
3.4.4 ICP-MS Analysis of Used Salts .....	60
Chapter 4: Investigation on Reference Electrodes in Molten $\text{Li}_2\text{O}/\text{LiCl}$ .....	61

4.1 Abstract .....	61
4.2 Introduction .....	61
4.3 Experimental .....	63
4.4 Results and Discussion .....	65
4.4.1 Correlation among Different Reference Electrodes .....	65
4.4.2 Effects of O <sup>2-</sup> Concentrations on Electrode Performances .....	70
4.4.3 Effects of Ni/NiO Fabrication Methods .....	75
4.5 Conclusion .....	77
Chapter 5: High Current Efficiency of NiO Electro-Reduction in Molten Salt .....	78
5.1 Abstract .....	78
5.2 Introduction .....	78
5.3 Experimental .....	79
5.3.1 Chemicals and Materials .....	79
5.3.2 Experimental Setup .....	79
5.3.3 Methodology .....	80
5.3.3.1 CV Measurements .....	80
5.3.3.2 Electrolytic Reduction of NiO Particles .....	81
5.3.3.3 Post-reduction Analyses .....	81
5.3.3.4 Theory and Calculations .....	81
5.4 Results and Discussion .....	82
5.4.1 CVs in 1 w.t.% Li <sub>2</sub> O/LiCl Salts .....	82
5.4.2 NiO Electroreduction .....	84
5.4.3 Post-reduction XRD and TGA Analysis .....	85
5.4.4 NiO Reduction Mechanism .....	87
5.5 Conclusion .....	88
Chapter 6: Electroreduction of Titanium Dioxide in Molten Li <sub>2</sub> O/LiCl .....	90
6.1 Abstract .....	90



6.2 Introduction .....	90
6.3 Experimental .....	92
6.4 Results and Discussion .....	94
6.4.1 Soaking Test of TiO <sub>2</sub> .....	94
6.4.2 Effect of Reduction Potential on TiO <sub>2</sub> Electrolytic Reductions .....	97
6.4.3 The Effect of Applied Charges on TiO <sub>2</sub> Reductions at -0.3 V vs. Li/Li <sup>+</sup> .....	103
6.4.4 Reusability of Lithium Salts for TiO <sub>2</sub> Electroreductions .....	107
6.4.5 DFT for TiO <sub>2</sub> Reduction Mechanism.....	107
6.5 Conclusion.....	114
Chapter 7: Sonication Assisted Electroreduction of TiO <sub>2</sub> in Li <sub>2</sub> O/LiCl.....	115
7.1 Abstract .....	115
7.2 Introduction .....	115
7.3 Experimental .....	119
7.4 Results and Discussion.....	120
7.4.1 Sonication Parameters Optimization .....	120
7.4.1.1 Effect of the Basket Depth .....	120
7.4.1.2 Effect of the Sonication Pulse Modes.....	125
7.4.1.3 Effect of the Sonication Power with 20 s Pulsed Mode .....	127
7.4.2 Effects of Sonication on Temperatures .....	128
7.4.3 Effects of Sonication on TiO <sub>2</sub> Reductions.....	129
7.4.4 Corrosion of Sonicator Probes under Different Operation Conditions .....	135
7.5 Conclusion.....	136
Chapter 8: Conclusion and Future Work.....	137
References .....	140

## List of Tables

Table 2.1 Current efficiency and oxygen content in product for FFC TiO <sub>2</sub> reductions .....	10
Table 2.2 Product compositions and oxygen concentrations, and current efficiency of TiO <sub>2</sub> reductions at 2.6~2.9 V under different reaction conditions [24,29] .....	13
Table 2.3 Products of Ta <sub>2</sub> O <sub>5</sub> reduction in NaCl/CaCl <sub>2</sub> and CaO/NaCl/CaCl <sub>2</sub> at 850 °C.....	19
Table 2.4 Results of electroreductions of Cr <sub>2</sub> O <sub>3</sub> prepared at different sintering temperature. ....	20
Table 2.5 Constituent concentrations in spent oxide fuel [49] .....	23
Table 2.6 Fuel baskets design on current efficiency [50].....	26
Table 2.7 Methods in increasing current efficiency in literatures .....	37
Table 3.1 Table of Li <sub>2</sub> O/LiCl salt compositions.....	53
Table 3.2 Standard electrode potentials in aqueous solution at 25 °C.....	54
Table 3.3 XRD setting parameters .....	58
Table 4.1 Summary of ELiLi + using various reference electrodes in molten Li <sub>2</sub> O/LiCl salts.....	63
Table 6.1 Rietveld refinement results for the soaked products .....	95
Table 6.2 Rietveld refinement results for the reduced products using 80% of the theoretical charge .	99
Table 6.3 Rietveld refinement results for reduced products at -0.3 V vs. Li/Li <sup>+</sup> .....	104
Table 6.4 Optimized bulk lattice parameters.....	109
Table 6.5 Equation of state, equilibrium volumes (V <sub>0</sub> ) determined from corresponding BM4 EOS, bulk moduli, and electronic potentials for the materials modeled from DFT. ....	111
Table 6.6 Gibbs free energy change and reaction potentials for reactions at 650 °C by DFT calculations.....	112
Table 7.1 Mass transfer coefficients with RDE and sonication at 25 °C and 50 °C .....	117
Table 7.2 Rietveld refinement results for the products reduced at +0.05 V vs. Li/Li <sup>+</sup> with different basket depth. Sonication interval: 20 s, ultrasound power: 30% of 1500 W.....	123
Table 7.3 Summary of products in reductions at +0.05 V vs. Li/Li <sup>+</sup> at different basket positions ....	124
Table 7.4 Rietveld refinement results for the products reduced at -0.3 V vs. Li/Li <sup>+</sup> with and without sonication. Sonication interval: 20 s, ultrasound power: 30% of 1500 W. ....	132

Table 7.5 Rietveld refinement results for the products reduced at +0.05 V vs. Li/Li <sup>+</sup> with and without sonication. Sonication interval: 20 s, ultrasound power: 30% of 1500 W. ....	133
Table 7.6 Summary of products in reductions at -0.3 V and +0.05 V vs. Li/Li <sup>+</sup> with and without sonication.....	134

## List of Figures

Figure 1.1 Industrial titanium demand in 2012~2021[3].....	2
Figure 2.1 Sketch of an experiment setup of the FFC process .....	7
Figure 2.2 Steps of TiO <sub>2</sub> reduction through the FFC process. TEM results are from literatures.[12,13] .....	8
Figure 2.3 Illustration of (a) experimental setup and (b) conceptual design of future setup.....	11
Figure 2.4 Plot of current efficiency achieved at different cell voltages [31] .....	15
Figure 2.5 Reaction pathway of Tb <sub>4</sub> O <sub>7</sub> electroreduction in molten CaCl <sub>2</sub> .....	16
Figure 2.6 Sketches of the setup for (a) electrorefining process, and (b) electroreduction process .....	21
Figure 2.7 Reaction pathways of TiO <sub>2</sub> reduction in 1 w.t.% Li <sub>2</sub> O/LiCl.....	27
Figure 2.8 Carbon cycle in the electrolyte between the cathode and carbon anode .....	34
Figure 2.9 Sketch of (a) Ag/AgCl and (b) Ni/NiO reference electrode.....	36
Figure 3.1 Typical potential-time profiles in an exemplary (a) single and (b) multiple cycles of cyclic voltammetry measurement. ....	41
Figure 3.2 Potential setting for the overpotential electroreductions.....	43
Figure 3.3 Front panel of the ultrasound control box .....	45
Figure 3.4 (a) NiO powder, and (b) NiO particles sizing between 0.25~0.85 mm .....	47
Figure 3.5 Sectional views of a glassy carbon crucible (a) at a new condition, and (b) after used for several times. The dashed lines represent the solidified salt bulk. ....	49
Figure 3.6 (a) configuration, and (b) a picture of the cathode oxide basket.....	50
Figure 3.7 Sketch of the assembly of the reference electrodes.....	52
Figure 3.8 Sketch of the cell including the electrolytic reduction and sonication.....	55
Figure 3.9 Temperature setting for the TGA analysis .....	59
Figure 4.1 Experimental setup for CV measurements. 1: Ni spiral counter electrode. 2: S.S. working electrode for cathodic CVs. 3: Pt wire working electrode for anodic CVs. 4: GC rod reference electrode. 5: W wire reference electrode. 6: Mo wire reference electrode. 7: Ni/NiO (1) reference electrode. 8: Ni/NiO (2) reference electrode .....	64
Figure 4.2 Cathodic CVs with Ni/NiO (1) reference electrode in Li <sub>2</sub> O/LiCl at 650 °C. W.E.: Stainless steel. C.E.: Nickle spiral. Scan rate = 20 mV s <sup>-1</sup> . ....	66

Figure 4.3 Cathodic CVs with glassy carbon reference electrode in Li <sub>2</sub> O/LiCl at 650 °C. W.E.: Stainless steel. C.E.: Nickle spiral. Scan rate = 20 mV s <sup>-1</sup> .	67
Figure 4.4 Cathodic CVs with tungsten reference electrode in Li <sub>2</sub> O/LiCl at 650 °C. W.E.: Stainless steel. C.E.: Nickle spiral. Scan rate = 20 mV s <sup>-1</sup> .	68
Figure 4.5 Cathodic CVs with molybdenum reference electrode in Li <sub>2</sub> O/LiCl at 650 °C. W.E.: Stainless steel. C.E.: Nickle spiral. Scan rate = 20 mV s <sup>-1</sup> .	69
Figure 4.6 Comparisons among reference electrodes at 650 °C in (a) LiCl and (b) 1 w.t.% Li <sub>2</sub> O/LiCl	70
Figure 4.7 Anodic CVs in Li <sub>2</sub> O/LiCl with Ni/NiO (1) reference electrode at 650 °C. Scan rate = 20 mV s <sup>-1</sup> .	72
Figure 4.8 Plots of Li <sub>2</sub> PtO <sub>3</sub> formation potential with Ni/NiO (1) RE as a function of ln(1/[O <sup>2-</sup> ]). The oxygen ion concentrations were in mol%.	72
Figure 4.9 Plots of surface reaction potential of glassy carbon electrode, molybdenum electrode, tungsten electrode as a function of ln(1/[O <sup>2-</sup> ]). The oxygen ion concentrations were in mol%.	73
Figure 4.10 Cathodic CVs (a) and anodic CVs (b) in Li <sub>2</sub> O/LiCl with Ni/NiO (2) reference electrode at 650 °C. Scan rate = 20 mV s <sup>-1</sup> .	75
Figure 4.11 Structural changes in Ni/NiO (2) reference electrode during CV measurements	76
Figure 5.1 (a) Electrochemical Cell setup for NiO reduction, and (b) the fuel basket electrode assembly	80
Figure 5.2 (a) CVs in 1.0 w.t. % Li <sub>2</sub> O/LiCl at 20 mV s <sup>-1</sup> using 0.025” stainless steel working electrode before and after NiO reductions, and (b) enlargement of the anodic branches of the CVs in (a).	83
Figure 5.3 Procedures in identification of half-cell potentials (vs. Ni/NiO).	84
Figure 5.4 (a) Current-time profiles for NiO reductions in fresh (red) and used (blue) 1.0 w.t. % Li <sub>2</sub> O/LiCl salt at - 0.3 V vs. Li/Li <sup>+</sup> using 100% of the theoretical charge, and cathodic potential-time profile (green) for reductions. (b).	85
Figure 5.5 (a) NiO pellet samples before reduction; (b) NiO powder samples after reduction; (c) Ni metal disc in 1/16” thickness (compressed powders from Fig 5.4b)	85
Figure 5.6 XRD profiles for reduced NiO samples in fresh and used salt 1 w.t.% Li <sub>2</sub> O/LiCl at 650 °C.	86

Figure 5.7 TGA analysis profile for the reduced Ni sample (10.314 mg) at a temperature programming with dry air flow rate at 20 ml min <sup>-1</sup> .....	87
Figure 5.8 Schematic diagram of a shrinking core model for NiO electroreduction.[14].....	88
Figure 6.1 XRD results (blue solid lines) and Rietveld refinement fittings (red dash lines, with TiO <sub>2</sub> , Li <sub>2</sub> TiO <sub>3</sub> and Li <sub>0.54</sub> Ti <sub>2.86</sub> O <sub>6</sub> ) of fresh TiO <sub>2</sub> and product soaked in molten 1 w.t.% Li <sub>2</sub> O/LiCl for 5 hours at 650 °C.....	95
Figure 6.2 CVs in fresh 1 w.t.% Li <sub>2</sub> O/LiCl and the used salt right after TiO <sub>2</sub> reduction at -0.3 V vs. Li/Li <sup>+</sup> with 80% of the theoretical charge at 650 °C (Scan rate = 20 mV s <sup>-1</sup> ).....	97
Figure 6.3 XRD results (blue solid lines) and Rietveld refinement analysis (red dash lines) of reduced TiO <sub>2</sub> samples at -0.2 V, -0.3 V and -0.4 V vs. Li/Li <sup>+</sup> with 80% of the theoretical charge; b) Reduced sample compositions, current efficiencies, and reduction extents for TiO <sub>2</sub> reduction at -0.2 V, -0.3 V and -0.4 V vs. Li/Li <sup>+</sup> .....	98
Figure 6.4 XRD for salt sample on the external surface of the cathode basket used for TiO <sub>2</sub> reduction at -0.3 V vs. Li/Li <sup>+</sup> using 80% of the theoretical charge.....	101
Figure 6.5 Current-time profiles for 2 g TiO <sub>2</sub> reductions at cathodic reduction potentials at -0.2 V, -0.3 V and -0.4 V (vs. Li/Li <sup>+</sup> ) with intervals using 80% of the theoretical charge.....	102
Figure 6.6 a) XRD results (blue solid lines) and Rietveld refinement fittings (red dash lines, with TiO <sub>2</sub> , Li <sub>2</sub> TiO <sub>3</sub> and LiTiO <sub>2</sub> ) of TiO <sub>2</sub> reduction products at -0.3 V (vs. Li/Li <sup>+</sup> ) using 80%, 130% and 150% of the theoretical charge; b) Product distribution, current efficiencies and reduction extents for TiO <sub>2</sub> reductions at -0.3 V vs. Li/Li <sup>+</sup> using 80%, 130% and 150% of the theoretical charge.....	103
Figure 6.7 Current-time profiles for TiO <sub>2</sub> reductions at -0.3 V (vs. Li/Li <sup>+</sup> ) using 80%, 130% and 150% of the theoretical charge for 2 g TiO <sub>2</sub> .....	106
Figure 6.8 CVs for lithium salt before and after TiO <sub>2</sub> reductions at -0.3 V vs. Li/Li <sup>+</sup> with 150% of the theoretical charge (Scan rate = 20 mV s <sup>-1</sup> ).....	107
Figure 6.9 Optimized bulk crystal structures for the Li system, TiO <sub>2</sub> , TiO, and Ti. Ti, Li, and O are in grey, green, and red, respectively. Black lines indicate the boundaries of the unit cell. Axis labels along the a, b, c directions are also shown.....	108
Figure 6.10 Unit cell volumes for the related chemicals during the TiO <sub>2</sub> electrolytic reduction in molten 1 w.t.% Li <sub>2</sub> O/LiCl at 650 °C.....	112
Figure 6.11 Shrinking core model for (a) the TiO <sub>2</sub> soaking process, and (b) for the electrolytic reduction of TiO <sub>2</sub> process with passivation layers.....	113

Figure 7.1 I-t curves of TiO <sub>2</sub> reductions at +0.05 V vs. Li/Li <sup>+</sup> with sonication at three different depths. Inset: the geometries of the relative positions of the sonication probe and cathode baskets. Inset: sketch of the probe and cathode basket. ....	121
Figure 7.2 Schematic drawing of a typical flow pattern around a sonication probe[142].....	122
Figure 7.3 XRD analysis of samples in reduction processes with different basket positions .....	122
Figure 7.4 (a) Schematic drawing of setup when the sonication is on. (b) Flow analysis at the basket when the basket is close to the molten salt surface. ....	125
Figure 7.5 (a) Current-time profiles and (b) XRD results for TiO <sub>2</sub> reductions at -0.3V vs. Li/Li <sup>+</sup> with sonication in 20 s and 40 s interval pulse modes.....	126
Figure 7.6 Current-time profiles in TiO <sub>2</sub> reductions at -0.3 V vs. Li/Li <sup>+</sup> with 30% and 50% of maximum power output 1500 W at (a) whole range, (b) current decrease section and (c) current plateau section .....	127
Figure 7.7 A portion of temperature profile with pulsed sonication (20 s interval) when (a) electrolysis is ON and (b) electrolysis is OFF .....	128
Figure 7.8 CVs in molten 1 w.t. % Li <sub>2</sub> O/LiCl at 20 mV s <sup>-1</sup> before and after TiO <sub>2</sub> reductions at -0.3 V vs. Ni/NiO. W.E.: Stainless steel wire. C.E.: glassy carbon.....	129
Figure 7.9 I-t curves of sonication-assisted TiO <sub>2</sub> reductions at (a) overpotential at -0.3 V vs. Li/Li <sup>+</sup> and (b) underpotential at +0.05 V vs. Li/Li <sup>+</sup> .....	130
Figure 7.10 XRD analysis of reduction products at (a) -0.3 V and (b) +0.05 V vs. Li/Li <sup>+</sup> .....	131
Figure 7.11 Sonicator probes when it is (a) new, (b) tested in air without electrolysis, and (c) tested in argon without electrolysis. (d) is the probe (c) used in argon after reduction. ....	135

## Nomenclature

### List of Abbreviations

3PI	Three phase interlines
ANL	Argonne National Laboratory
CE	Counter electrode
CV	Cyclic voltammetry
DFT	Density Functional Theory
DI	Diameter
EBR-II	Experimental Breeder Reactor II
FFC	Fray-Farthing-Chen
GC	Glassy carbon
ICP-MS	Inductively couple plasma – mass spectrometry
INL	Idaho National Laboratory
Li	Lithium
LWR	Light Water Reactor
Ni	Nickel
Mo	Molybdenum
OCP	Open circuit potential
OS	Ono Suzuki
RE	Reference electrode
SEM	Scanning electron microscopy
S.S.	Stainless steel
Ti	Titanium
W	Tungsten
WE	Working electrode



WPPF	Whole Powder Pattern Fitting
XRD	X-ray diffraction
TGA	Thermogravimetric analysis

## List of Symbols

$\beta$	Line broadening at half the maximum intensity	rad
$\gamma$	Activity coefficient	
$\theta$	Bragg angle	rad
$\lambda$	X-ray wavelength	Å
$\nu$	Scan rate	mV s <sup>-1</sup>
$\rho_T$	Density at temperature T	g cm <sup>-3</sup>
$\rho_m$	Density at melting point	g cm <sup>-3</sup>
$a$	Activity	mol%
$d$	Particle diameter	m
$E$	Potential	V
$E^0$	Standard reaction potential	V
$F$	Faraday constant (96485 C mol <sup>-1</sup> )	C mol <sup>-1</sup>
$G$	Gibbs free energy	J mol <sup>-1</sup>
$I$	Current	A
$K$	Shape factor (0.9)	
$k$	Temperature difference related coefficient	g cm <sup>-3</sup> °C <sup>-1</sup>
$M$	Molar weight	g mol <sup>-1</sup>
$m$	Mass	g
$n$	Number of moles	mol
$P$	Partial pressure	Pa

$R$	Universal gas constant (8.314 J K <sup>-1</sup> mol <sup>-1</sup> )	J K <sup>-1</sup> mol <sup>-1</sup>
$T$	Temperature	°C or K
$T_m$	Melting point	°C
$z$	Number of electrons transferred	

### **Statement of Contribution**

In Chapter 6, the DFT modeling was done by Dr. Bin Liu. It helped the derivation of Gibbs free energy change of reactions and unit volumes of all species. Descriptions of the modeling procedures in Session 6.3 were also provided by Dr. Bin Liu.

The rest of the work, including experimental design, conduction of experiments, product characterizations and data analyses were done by Meng Shi.

## Chapter 1: Introduction

Metal generation from electrolysis in molten salts has a long history dating back to the early nineteenth century. The first industrial electrolytic cell for metallurgy was an electrorefining plant for copper production in Pembrey, Wales in 1869.[1,2] In US, the first commercial copper electrorefining plant was the Balbach Smelting & Refining Co., constructed in 1883. The electrorefining takes place in a  $\text{CuSO}_4/\text{H}_2\text{SO}_4$  aqueous bath. Copper releases from the anode in an ionic status and reduced to copper metal at the cathode. Copper production rate was 2~3 tons per day in 1883 (Newark, NJ), and it has been improved to 450~500 tons per day so far (ASARCO, AZ). In 1886, an aluminum production process through electrolysis was patented as the Hall-Héroult process.[2] It was commercialized when the Pittsburgh Reduction Company (now Alcoa Inc.) was established by Hall in 1888. As Hall improved the process, the price of aluminum dropped from \$4.86 /pound in 1888 to \$0.78 /pound in 1893, which is further reduced to \$0.16 /pound in 2020. In the Hall-Héroult process, the bauxite ore is mixed with lime and caustic soda at high temperature and pressure, and it results in white alumina powders. Then the alumina is dissolved in a cryolite ( $\text{Na}_3\text{AlF}_6$ ) bath and electrolyzed to aluminum metal.

As discussed above, the classic electrolytic copper metallurgy is carried out in aqueous solution, but the Hall-Héroult process takes place in molten cryolite salts. It is for the reason that the electrolysis of aluminum ion requires a higher reduction potential than water electrolysis. It can be found that the electrolysis in molten salts allows a much wider potential window for electrolytic reactions than that in aqueous environment. For this reason, molten salt electrolysis finds its wide applications in metal generations, through both electrorefining and electroreduction processes.

Pyroprocessing is a step in the spent fuel recycling, which is an electrolysis process in high temperature chloride salt. It recovers metals from the wastes and the process includes both electrorefining and electroreduction. The electrorefining in pyroprocess achieves purified uranium metal from the waste fuel in the Experimental Breeder Reactor II (EBR-II). It utilizes molten  $\text{UCl}_3$  (10 w.t.%)/ $\text{LiCl}/\text{KCl}$  at 500 °C as the electrolysis mediate. The spent metal fuel is loaded in a basket anode, and uranium metal is collected at the cathode. In the electroreduction process, the feed was spent oxide fuels from the Light Water Reactor (LWR) containing uranium oxides. The electroreduction occurs in a molten 1 w.t.%  $\text{Li}_2\text{O}/\text{LiCl}$  bath at 650 °C. The waste fuel is loaded in the cathode basket and the product metallic uranium is collected at the same location after the electrolysis.

In the extraction of metal from non-radioactive metal oxides, electrolysis in high temperature molten salts is also a widely studied area. The electroreduction of metal oxides in molten salt has been studied in recent decades, for the advantages of a wide range of metal productions, low hazard emission,

low equipment requirement compared with conventional methods. It is an effective way in achieving metals which require a higher potential than water electrolysis. Research efforts are drawn in this area for the purpose of achieving metal at a lower cost and a higher yield. Some widely used structural metals, such as titanium, finds increasing demands in extensive applications, including the aerospace industry, marine, medical, armor, sporting goods, etc. Fig. 1.1 displays the industrial demand for titanium from 2012 to 2021.[3] The distributions among different aspects were different, but the total demand for the titanium metal was generally in on the rise. So, the market for the titanium metal keeps increasing and it stimulates the growth of R&D in generating more high quality titanium metal products. However, the traditional method, such as the Kroll process[4] for the titanium generation, requires high temperatures, complicated manufacturing equipment, large hazards emissions and low product impurity. The cost of titanium metal is high, but the market is still huge due to its excellent properties, such as the strength to density ratio, and the corrosion resistance. In order to reduce the cost of the titanium, research efforts have been put on finding alternative producing approaches. Among many other metal generation process, the electroreduction of metal oxides in molten salts started to attract research interests due to several advantages.

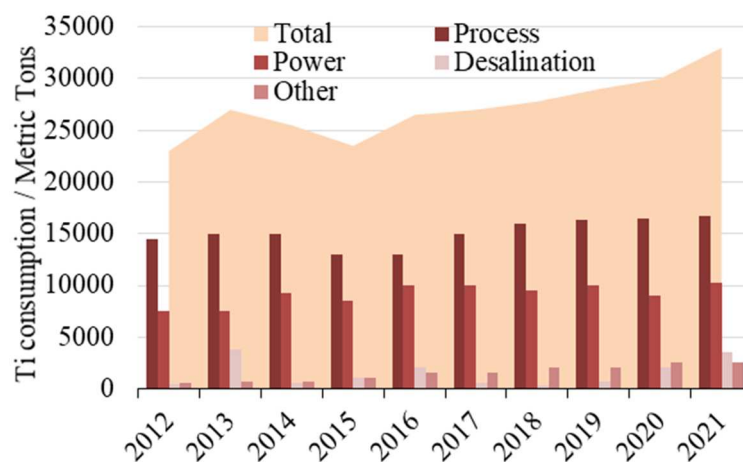


Figure 1.1 Industrial titanium demand in 2012~2021[3]

As discussed above, electroreduction of metal oxides is a practical approach to produce high purity metals at a low cost, and it is also an integral step of pyroprocessing in spent nuclear oxide fuels recycling. However, the promotion and commercialization of this promising method is limited by the low current efficiency which is a critical evaluation criterion. The slow oxygen ion diffusion through the particulates inside the cathode basket is the limiting factor, which leads to not only the low current efficiencies, but also long operating hours, and re-oxidation of reduced metals. Researchers have tried different methods in increasing the current efficiency, including using more porous precursors, adding

stirring methods, changing electrolyte compositions, and pretreating metal oxides. Nevertheless, the improvement is still unsatisfactory.

In this project, the technique of sonication will be introduced in the electroreduction of metal oxides. The sonication is a mature technology which has been employed in a variety of chemical and physical processes to improve the mass transfer and increase the yields in moderate operation environment. In terms of experiments, metal oxides reductions will be carried out through electrochemical methods coupled with ultrasound in 1 w.t.%  $\text{Li}_2\text{O}/\text{LiCl}$  at 650 °C. Electroreductions of  $\text{TiO}_2$  and  $\text{NiO}$  are under study in this project. It will lead fundamental studies of electroreductions and the sonication working mechanism. The mass transfer is expected to be improved with the ultrasound, and it will lead an increment in the current efficiency. By proving that the sonication is an effective method in increasing the current efficiency, it would promote the commercialization of the metal production through electroreductions in molten salts, and also accelerate the treatment of spent nuclear fuels through pyroprocessing.

### **1.1 Research Motivation**

The electrolytic reduction is an outstanding method in reducing metal oxides for the advantages of lower operation condition requirements, easier parameter control and lower oxygen concentration in product. It should be taken in commercial productions at an industrial scale. However, the electrolytic metal oxides reduction has not been put into the market, and the reason is its low current efficiency due to the difficulty in oxygen ion transfer in the solid phase. Extensive research and development actions have been conducted in the past decade to improve the oxygen diffusion process associated with the electrolytic reduction of metal oxides in high temperature molten salts. Methods have been tested to increase the current efficiency, such as using precursors at different particle sizes and porosity, and varying the reactor setup design. However, the improvement was not significant. The gap of the process lies in the low oxygen diffusion inside the solid phase.

Sonication is a technology which improves a variety of processes including chemical reactions and mass transports. And so far, it has not been explored for the purpose of improving oxygen diffusion in high temperature molten salts. In this research project, the ultrasound agitation is expected to accelerate oxygen ion diffusion through the fuel particulate packed in the cathode basket. Furthermore, application of sonication will improve the contact between the fuel particulate and the cathode, and will drive the concentrated oxygen diffusing out of the packed oxide bed in the adhesive molten salt.

## 1.2 Dissertation Scope

The purpose of this dissertation is to obtain fundamental understanding in electroreductions of metal oxides and sonication, and transferable knowledge to pyroprocessing of nuclear spent oxide fuel.

Chapter 1 summarized the entire project, including the state of art and challenges in the electroreduction field, the function and expectation of the application of the sonication, and the significance of this study.

Chapter 2 expands detailed discussions about the background of the electroreduction processes in high temperature molten salts. It covers the pyroprocessing of the spent fuel treatment, and two typical methods for the electrolytic reductions non-radioactive materials. In the review of pyroprocessing, it emphasizes on the electroreduction of the waste metal oxide fuel from the light water reactor.  $\text{TiO}_2$  is taken as the example of the non-radioactive metal oxides, and the reductions are proceeded in two ways, the Fray-Farthing-Chen (FFC) Cambridge process and the Ono-Suzuki (OS) process. These processes are initially used in molten calcium salts, but the operations are also applied in molten lithium salts. Electroreduction of other metal oxides, including  $\text{NiO}$ ,  $\text{Tb}_4\text{O}_7$ ,  $\text{WO}_3$ ,  $\text{Nb}_2\text{O}_5$ ,  $\text{Ta}_2\text{O}_5$  and  $\text{Cr}_2\text{O}_3$ , are also reviewed and compared in this session. The reductions are discussed in details in terms of the reactor setups, operation parameters, reduction mechanisms, limitations and improvements. A short summary of the experimental details covers the electrolytes and electrodes used in the literatures. It also provide the foundations for selecting experiment elements based on specific requirements.

Chapter 3 describes the electrolytic methods, ultrasound techniques and controllable parameters employed in this study. Based on the experimental plan, an experimental setup is designed and assembled. It includes the selections of oxide precursors, anode, cathode, reference electrode, electrolyte, and the experiment environment. The sonication apparatus is also discussed in this session. The coupling of sonication with the electroreduction is challenging, so the solutions to the problems are discussed here. The operational parameters for both electrolytic reduction and sonication are included in each subtopic.

Chapter 4 presents a study of the comparisons among the performances of different reference electrodes, including the glassy carbon, tungsten, molybdenum, and  $\text{Ni/NiO}$  electrodes. Cyclic voltammetry is performed in molten  $\text{LiCl}$  with various  $\text{Li}_2\text{O}$  concentrations. The purpose is to determine the stability of the reference electrodes in an environment with changing  $\text{Li}_2\text{O}$  concentrations. This study is significant in guarantee the reliability and repeatability of the electrolytic measurements in this study. It is because, based on the literature reviews in Chapter 2, it is found that  $\text{Li}_2\text{O}$  concentration is

not identical during the reduction procedure and in different positions in the cell. At the success of this study, a proper reference electrode will be selected and involved in the following electrolytic studies based on the stability at varying  $\text{Li}_2\text{O}$  concentrations.

Chapter 5 focuses on the electroreduction of NiO in molten  $\text{Li}_2\text{O}/\text{LiCl}$  salt. The experimental procedures are described in details, including the reduction setup, parameter control and sample analysis. Data collected in the electrolytic measurements and product characterization are shown. The reduction results, including the reduction extent and current efficiency, are calculated and the reduction mechanism is derived. The success in the NiO electroreduction proves that the reaction setup and the reduction method are feasible and can be introduced in the reduction of more complication metal oxides.

Chapter 6 continues the electroreduction studies with  $\text{TiO}_2$  as the feed in the same reaction system as that used in the NiO reduction in Chapter 5. The reduction of  $\text{TiO}_2$  is more complicated than that of NiO. So, more reduction tests are carried out, and theoretical calculations are introduced to assist the understanding of the mechanism. After the study, the mechanism of the  $\text{TiO}_2$  reduction is proposed and the limiting step of the  $\text{TiO}_2$  reduction is defined.

Chapter 7 shows the effects of the coupled sonication on the  $\text{TiO}_2$  reduction. The reduction results of  $\text{TiO}_2$  reductions under the silent conditions (following steps in Chapter 6) are taken as the reference. By conducting the reduction assisted with sonication, the reduction phenomenon and the reduced products are analyzed and compared. Changes in the reduction extent and current efficiency are caused by the ultrasound power. Effect of sonication on the temperature is also measured. It is found that the current efficiency can be improved by the sonication.

Chapter 8 is the conclusion of the whole project. The performed work is summarized and the significance is defined. This chapter also suggests the future work based on the achievements and challenges from this study.



## Chapter 2: Literature Review

In this chapter, the electroreduction of metal oxides in high temperature molten salts was reviewed. The metal oxides reduction session covered the electroreduction of radiological metal oxides in the spent nuclear fuel through the pyroprocessing, and the electrolytic reduction of non-radioactive metal oxides through the Fray-Farthing-Chen Cambridge process and the Ono-Suzuki processes.

### 2.1 Metal Oxide Electroreductions

Reductions of metal oxides through electrochemical methods in molten salts attract research attentions in producing pure metal as an engineering material or a complex as a battery component. High temperature molten salt electrolysis provides paths to achieve reductions which are not practicable in aqueous solutions. Electrolytes involved in metal oxide electroreductions includes molten calcium chloride and molten lithium chloride. In molten calcium chloride salts, electrolytic reductions mostly follows the typical Fray-Farthing-Chen Cambridge process for underpotential reductions and the Ono-Suzuki process for overpotential reductions. Electroreductions in molten lithium chloride salts includes the pyroprocessing of spent nuclear fuel and other non-radioactive oxides reductions.

#### 2.1.1 FFC and OS Processes in Molten $\text{CaCl}_2$ Salts

The Fray - Farthing - Chen (FFC) Cambridge process and the Ono – Suzuki (OS) calciothermic reduction process are the two main methods in metal oxides reductions in molten calcium salts. These two approaches are discussed in details in the  $\text{TiO}_2$  electroreduction.

##### 2.1.1.1 $\text{TiO}_2$

Titanium metal is an excellent structural metal with low density, high strength, and corrosion resistance. It has found extensive applications in many areas, including the aerospace industry, marine, medical, armor, sporting goods, etc. However, it is quite costly to extraction titanium metal from titanium dioxide through the Kroll process.[4] So, the electroreduction of  $\text{TiO}_2$  in molten salts is promising for Ti metal production for a lower cost and easier operations. The reduction of  $\text{TiO}_2$  in molten  $\text{CaCl}_2$  salts can be carried out in different methods, FFC and OS processes.

### 2.1.1.1.1 The Fray-Farthing-Chen (FFC) Cambridge Process

#### 2.1.1.1.1.1 Introduction

Calcium chloride molten salts started to draw attentions when the Fray - Farthing - Chen (FFC) Cambridge process was discovered for the electrochemical reduction of  $TiO_2$ . [5] The FFC process utilized molten  $CaCl_2$  salt at 850-950 °C. [5] It was a competitive method in producing Ti metal compared with the traditional Kroll process which required two separate reactors at a high temperature over 1100 °C and released toxic chloride gas. [4] The Kroll process is a two-step titanium generation at around 800~900 °C from the titanium ore. In the first step, the raw titanium ore is chlorinated and distilled to pure titanium tetrachloride ( $TiO_2 + C + 2Cl_2 \rightarrow TiCl_4 + CO/CO_2$ ) in a chlorinator. And then, the  $TiCl_4$  is transferred to a separation vessel and reduced with magnesium through  $2Mg(l) + TiCl_4(l) \rightarrow 2MgCl_2 + Ti(s)$ . The typical FFC process has been demonstrated for reductions of many other metal oxides in multiple molten salts at underpotentials. [6]

The FFC processes were carried out in a closed chamber with argon purging (Fig. 2.1). It utilized molten  $CaCl_2$  salt as the electrolyte. [7] The salts were contained in a crucible (made of titanium, graphite or stainless steel [8]) and heated to 850~950 °C. A water cooling system was installed around the connection of the chamber body and the lid. A graphite rod was used as the anode, and a metal lead (Ti or Mo [9]) worked as the cathode. In most of the studies, the  $TiO_2$  was prepared into a big disc and fixed to the cathode.

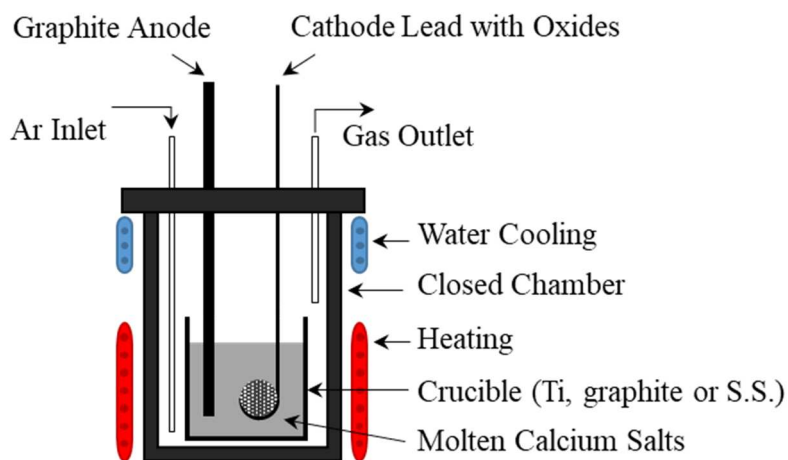


Figure 2.1 Sketch of an experiment setup of the FFC process

During a typical reduction of  $TiO_2$  in molten  $CaCl_2$ , a cell potential lower than the salt decomposition potential (3.18 V) was applied between the  $TiO_2$  pellet cathode and a thick graphite rod anode. [7,10,11] As the products, Ti metal was collected on the cathode and gases were detected on the

anode, including  $O_2$  (Eq. 2.1),  $CO$  (Eq. 2.2) and  $CO_2$  (Eq. 2.3).[8] The released gases were defined by analyzing the outlet gas from the closed reactor chamber.

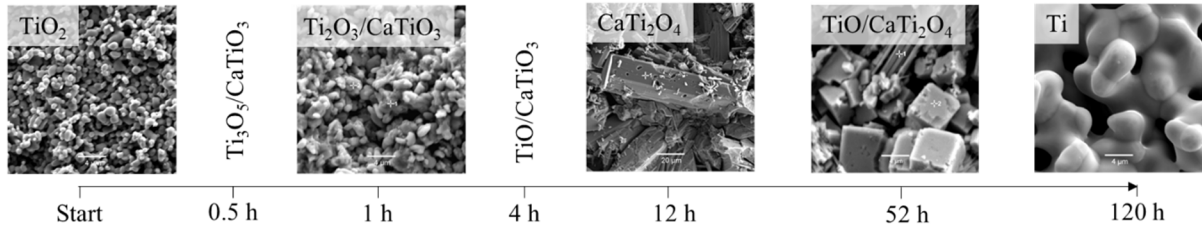
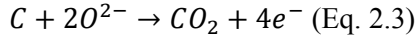
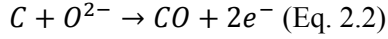
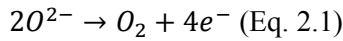
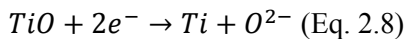
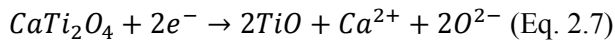
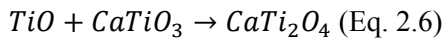
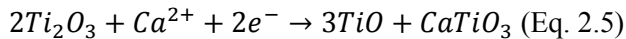
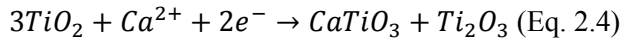


Figure 2.2 Steps of  $TiO_2$  reduction through the FFC process. TEM results are from literatures.[12,13]

The reduction mechanism was proposed including a series of reaction steps.[12,13] Fig. 2.2 presented the FFC products of 8 g  $TiO_2$  (porosity=25%~30%) along with time. The reduction followed a multiple-step process. In the first stage,  $TiO_2$  reacted with  $CaCl_2$  to form perovskite  $CaTiO_3$  and  $Ti_3O_5$  and  $Ti_2O_3$  (Eq. 2.4). Then,  $Ti_2O_3$  continued the reaction with  $CaO$  and generated  $TiO$  and more perovskite  $CaTiO_3$  (Eq. 2.5). In the third stage,  $TiO$  combined with  $CaTiO_3$  and produced  $CaTi_2O_4$  (Eq. 2.6). The generated  $CaTi_2O_4$  was reduced with electrons to  $TiO$  (Eq. 2.7); and the  $TiO$  was further reduced to titanium metal through direct electroreduction (Eq. 2.8).



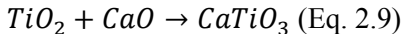
The process followed a multi-stage shrinking core model.[14] The model considered the Magnéli phases ( $TiO_{2n-1}$ ,  $n=4\sim 10$ ), exclusive of the perovskite and other calcium titanates. The oxide core shrank in an order starting from the feed  $TiO_2 \rightarrow Ti_3O_5 \rightarrow Ti_2O_3 \rightarrow TiO \rightarrow Ti$ . The reduction went through the propagation of the three-phase interlines (3PIs).[15,16] The 3PI in the  $TiO_2$  reduction in molten  $CaCl_2$  is different from the typical metal|oxide|electrolyte 3PI [17]; however, FFC reduction was a much complicated process involving multiple phases and interlines. The reduction could be

simplified to formation and movement of four 3PIs, including  $\text{TiO}_2|\text{CaTiO}_3|\text{electrolyte}$ ,  $\text{CaTiO}_3|\text{titanium suboxides}|\text{electrolyte}$ ,  $\text{titanium suboxides}|\text{TiO}|\text{electrolyte}$  and  $\text{TiO}|\text{Ti}|\text{electrolyte}$ . [16]

#### 2.1.1.1.1.2 State of Art of the FFC Process

Through the FFC process, the reduction of  $\text{TiO}_2$  (porosity = 25%~30%) in molten  $\text{CaCl}_2$  resulted in a current efficiency at 10%~20%. [12] However, the low current efficiency did not meet the criteria for the commercial production of Ti metal. Therefore, the recent research efforts focused on the opportunities to increase the current efficiency. Attempts were made in terms of utilizing different precursors, changing composition of the electrolyte, and varying operation parameters.

During the reduction, it was found that the formation of the perovskite  $\text{CaTiO}_3$  was inevitable and took quite long time in the reduction of  $\text{TiO}_2$ . So, to avoid the *in situ* formation of  $\text{CaTiO}_3$ , it was pre-synthesized through the chemical combination reaction (Eq. 2.9). [9] By using the  $\text{CaTiO}_3$  as the precursor, Ti (2800 ppm of oxygen) was produced via stable  $\text{Ti}^{3+}$  and  $\text{Ti}^{2+}$  intermediates. By directly reducing  $\text{CaTiO}_3$ , it took less than half of the time to reduce the same amount of  $\text{TiO}_2$ , and the current efficiency was increased to 28%, compared with 15% in  $\text{TiO}_2$  reduction under the same conditions.



In order to initiate the  $\text{O}^{2-}$  flow, decrease the oxygen level in the metal product, and increase the  $\text{O}^{2-}$  activity,  $\text{CaO}$  was added to  $\text{CaCl}_2$  in preparation of a 2 mol%  $\text{CaO}/\text{CaCl}_2$  mixture (Table 2.1). By applying -1.5 V vs. graphite reference electrode, 2 g of  $\text{TiO}_2$  (porosity 15%~16%) was reduced to Ti metal with oxygen content at 12000~36000 ppm after 16 h, following a mechanism similar with that in  $\text{CaCl}_2$ . [18] In the reduction of the dense  $\text{TiO}_2$ , it was found that there was no sufficient free volume in the particles to allow the contact with the calcium. So, the mechanism for porous  $\text{TiO}_2$  reduction was different from that for reduction of dense  $\text{TiO}_2$ . The reduction proceeded from the shell to the core layer by layer; after the outer layer was fully converted to Ti, the reaction interline started to migrate inwards. The  $\text{TiO}_2$  was firstly converted to  $\text{Ti}_8\text{O}_{15}$  and perovskite  $\text{CaTiO}_3$  (Eq. 2.10). The titanium oxide  $\text{Ti}_8\text{O}_{15}$  was reduced to  $\text{Ti}_2\text{O}_3$  (Eq. 2.11) which was reduced to  $\text{TiO}$  (Eq. 2.12). For the perovskite  $\text{CaTiO}_3$ , it was also reduced to  $\text{TiO}$  (Eq. 2.13). Finally, Ti metal was produced through the electrolytic reduction of  $\text{TiO}$  (Eq. 2.8). Formation of  $\text{CaTiO}_3$  was limited due to the insufficient contact with calcium in the dense structure. The current efficiency was improved to 32%, but the oxygen content in the product was high at 12000 ppm. Porous  $\text{TiO}_2$  (porosity 25%~30%) particles were also reduced in 2 mol%  $\text{CaO}/\text{CaCl}_2$ . In the first stage of the reduction, perovskite  $\text{CaTiO}_3$  and titanium suboxides such

as  $Ti_2O_3$  were generated (Eq. 2.4). However,  $Ti_2O_3$  was absent in the surface layer, owing to a direct reduction to  $TiO$  (Eq. 2.14). After  $CaTiO_3$  was generated, a significant amount of the material was dissolved in the electrolyte. The fate of the  $CaTiO_3$  lead to two results. It can be directly reduced to  $TiO$  (Eq. 2.13). At the same stage, a large amount of  $CaTi_2O_4$  was produced from the combination reaction of  $TiO$  and  $CaTiO_3$  (Eq. 2.6), but it was then broken down to  $TiO$  (Eq. 2.7). The last step was the deoxidation of  $TiO$  to  $Ti$  metal (Eq. 2.8). In this reduction process in 2 mol%  $CaO/CaCl_2$  with porous  $TiO_2$ , the current efficiency reached to 40% and the oxygen content in  $Ti$  metal was decreased to 2000 ppm. Oxide pellets were modified for the purpose of increasing the surface area to allow faster oxygen ion transfer.[19] A thin layer of high porosity (>75%)  $TiO_2$  pellet was tested and proved to be effective in shorten the reduction time and lower down the oxygen residual in the products. Reduction of a thin layer (300~400  $\mu m$ ) after 6 h contained less than half of oxygen in the product than reduction of a thick pellet (3 mm). So, compared with reductions in calcium melt without  $CaO$ , the addition of  $CaO$  increased the current efficiency and shortened the processing time.[20] A model was established for the  $TiO_2$  reduction in calcium molten salt based on a core-shell structure of the metal oxide particles.[14,21]

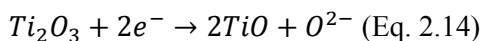
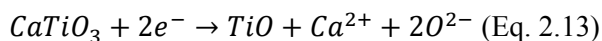
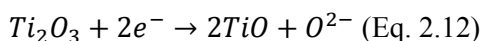
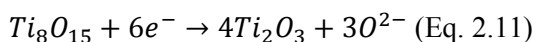
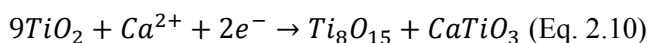


Table 2.1 Current efficiency and oxygen content in product for FFC  $TiO_2$  reductions

Electrolyte	$TiO_2$ porosity	Calcium titanates	Current efficiency	Oxygen content	Reference
$CaCl_2$	25% ~ 30%	$CaTiO_3$ , $CaTi_2O_4$	~ 20%	3,000 ppm	[12]
2 mol% $CaO/CaCl_2$	15% ~ 16%	$CaTiO_3$	~ 32%	12,000 ppm	[18]
2 mol% $CaO/CaCl_2$	25% ~ 30%	$CaTiO_3$ , $CaTi_2O_4$	~ 40%	2,000 ppm	[20]

Experimental parameters were also varied aiming at a higher current efficiency. The study on the effect of applied charge showed that more charge were required to decrease the oxygen content in the products. However, the current efficiency was also reduced at the same time.[22] By applying 100% of theoretical charge, oxygen in the solid was 10.5 w.t.% and the current efficiency was 41.1%. When 200% of theoretical of charge was applied the oxygen level decreased to 6.3 w.t.%, and the current efficiency was also reduced to 33.3%. With 300% of theoretical of charge, the oxygen content and the current efficiency were 2.7 w.t.% and 27.4%, respectively.

In the FFC reductions, researchers concluded that the removal of oxygen from the solid phase is a slow process, especially the removal of the last amount of oxygen from the metal.

#### 2.1.1.1.2 The Calciothermal Reduction (Ono-Suzuki (OS) Process)

##### 2.1.1.1.2.1 Introduction

The Ono – Suzuki calciothermic process is a type of  $\text{TiO}_2$  reduction in the molten  $\text{CaCl}_2$  mediates by introducing the *in situ* generated calcium metal as the reductive agent.[23]

In the  $\text{CaO}/\text{CaCl}_2$  molten salt systems, cell potentials were applied between the cathode lead and the graphite anode. The applied potential was high enough to decompose  $\text{CaO}$ , but below the decomposition potential of  $\text{CaCl}_2$ . [24] The  $\text{TiO}_2$  was either loaded in a titanium net cathode, or could be added to the system by dropping from the top of the S.S. cathode vessel (Fig. 2.3a). The final metallic Ti was collected either on the cathode tray, or at the bottom of the reaction vessel.

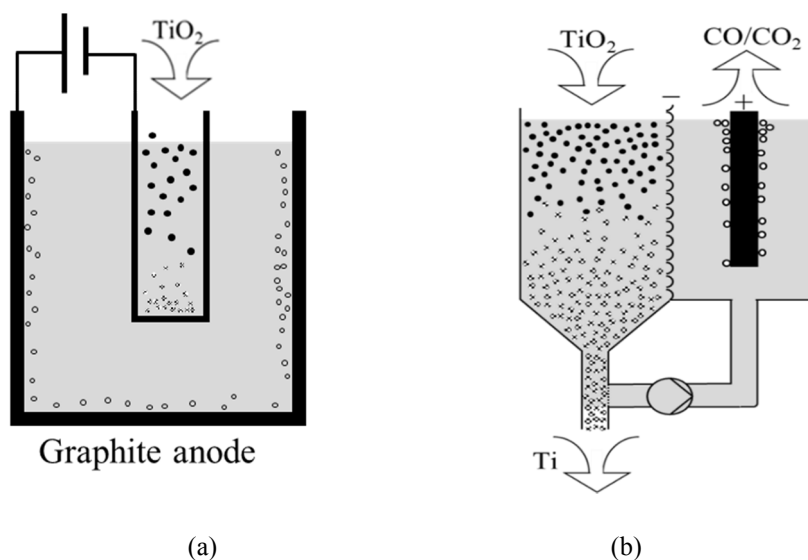
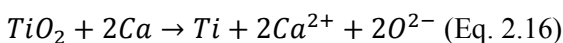
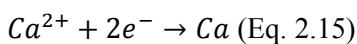


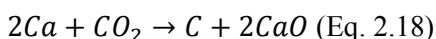
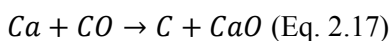
Figure 2.3 Illustration of (a) experimental setup and (b) conceptual design of future setup

In the OS process,  $\text{Ca}^{2+}$  was reduced to Ca metal on the cathode (Eq. 2.15) which directly reduced  $\text{TiO}_2$  to Ti metal sponge (Eq. 2.16).[23–28] In some studies, it was found that the titanium metal was produced through Megnelli phases, such as  $\text{Ti}_2\text{O}$ , and calcium titanates  $\text{CaTiO}_3$  as the intermediate products.[26] On the anode, due to the component of carbon, CO (Eq. 2.2) and  $\text{CO}_2$  (Eq. 2.3) were generated and dissolved in the melt. The current efficiency of the OS process was 12.9%, which was the highest value can be achieved and it was in the molten 0.5 mol%  $\text{CaO}/\text{CaCl}_2$ .[24]



#### 2.1.1.1.2.2 State of Art of the OS Process

Ti metal with a low oxygen level was successfully produced via the OS process. In an OS process, it took 3 hours to fully reduce 1 g  $\text{TiO}_2$  in 0.5 mol%  $\text{CaO}/\text{CaCl}_2$ . The oxygen level in the product was 2000 ppm in the product and current efficiency was around 12.9%.[24] The low current efficiency was partially due to the energy consumption to generate extra Ca metal; meanwhile, part of the Ca metal took part in side reactions with the dissolved CO (Eq. 2.17) and  $\text{CO}_2$  (Eq. 2.18) gases generated on the graphite anode.



Attempts were made to increase the current efficiency, including utilizing  $\text{TiO}_2$  at different sizes, changing the molten salt compositions, and modifying the reactor design.

Different sizes of particles were investigated for the reductions, including micro- ( $D=2.0 \mu\text{m}$ ), submicro- ( $D=90 \text{ nm}$ ) and nano- ( $D=13 \text{ nm}$ ) particles.[26] Ti metal was achieved by reducing nano-particles, and a mixture of Ti and  $\text{Ti}_2\text{O}$  was generated in the reduction of submicro particles. In the reduction of micro  $\text{TiO}_2$  particles, Ti metal, as well as intermediates  $\text{CaTiO}_3$  and  $\text{Ti}_2\text{O}$  were observed. Lower titanium oxide  $\text{Ti}_2\text{O}$  was an intermediate product which could be further reduced to Ti metal. The formation of  $\text{CaTiO}_3$  was due to the slow diffusion of CaO away from the particle and it reacted with the residual unreacted  $\text{TiO}_2$  particles. It was found that the  $\text{TiO}_2$  reduction rate increased with the decreasing particle size, due to the increasing surface area of the particles.

Effect of electrolyte composition on the reduction product was also studied, in terms of CaO concentrations (Table 2.2). When  $\text{TiO}_2$  powder was reduced in  $\text{CaCl}_2$  using 100% of theoretical charge,

the product was  $\text{TiO}_{0.325}$ , and with 500% of theoretical charge, the product was still  $\text{TiO}_{0.325}$ . [24,29] There was no increase in the current efficiency even with much more charge, probably due to the low current response in electrolysis of  $\text{CaCl}_2$ .  $\text{CaO}$  was added to  $\text{CaCl}_2$  to form  $\text{Ca}$  metal. In 0.5 mol%  $\text{CaO}/\text{CaCl}_2$  electrolyte,  $\text{Ti}$  metal containing 2000 ppm of oxygen was achieved. With the  $\text{CaO}$  addition, the current on the cathode was increased that  $\text{Ca}$  metal was generated efficiently. So, higher  $\text{CaO}$  concentrations were tested to find an optimized composition for a better reduction result. By increasing the  $\text{CaO}$  to 1 mol%, oxygen level in the generated  $\text{Ti}$  metal was increased to 6200 ppm. At even higher  $\text{CaO}$  concentration in  $\text{CaCl}_2$  at 15 mol%, the products were mixtures of  $\text{Ti}$  metal and titanium oxides including  $\text{TiO}_{0.325}$ ,  $\text{Ti}_6\text{O}$  and  $\text{TiO}$ . It was because when the concentration of  $\text{CaO}$  was high in the electrolyte, the diffusion of  $\text{CaO}$  released from the  $\text{TiO}_2$  reduction was delayed. The highest current efficiency that could achieved was 12.9% from reductions in 0.5 mol%  $\text{CaO}/\text{CaCl}_2$ . The low current efficiency was due to generation of extra  $\text{Ca}$  metal; meanwhile, part of the  $\text{Ca}$  was consumed in side reactions including the dissolution of  $\text{Ca}$  in the bulk, and the reaction with  $\text{CO}_2$  released on anode.

Table 2.2 Product compositions and oxygen concentrations, and current efficiency of  $\text{TiO}_2$  reductions at 2.6~2.9 V under different reaction conditions [24,29]

Molten Salt	Charge of theoretical /%	Phases by XRD	Oxygen concentration / ppm	Current efficiency / %
$\text{CaCl}_2$	113	$\text{TiO}_{0.325}$	Not measured	Not measured
$\text{CaCl}_2$	525	$\text{TiO}_{0.325}$	Not measured	Not measured
0.5 mol% $\text{CaO}/\text{CaCl}_2$	767	$\text{Ti}$	2000	12.9
1 mol% $\text{CaO}/\text{CaCl}_2$	833	$\text{Ti}$	6200	11.8
15 mol% $\text{CaO}/\text{CaCl}_2$	478	$\text{Ti}_6\text{O}$ , $\text{TiO}$	Not measured	Not measured
15 mol% $\text{CaO}/\text{CaCl}_2$	11220	$\text{Ti}$ , $\text{TiO}_{0.325}$	Not measured	Not measured

In order to overcome the shortages of generating extra calcium and side reactions consuming the necessary  $\text{Ca}$  metal, a conceptual design was proposed (Fig. 2.3b). In the conceptual model,  $\text{TiO}_2$  was added by dropping to the cell and was reduced by  $\text{Ca}$  as it went down to the bottom.  $\text{CO}$  and  $\text{CO}_2$  were released from graphite anode in a separated chamber. As a result, the calcium metal was expected to be fully used in  $\text{TiO}_2$  calciothermic reductions. A rotating cathodic basket was tested, but the product contained a quite high oxygen level at 11 w.t.%. The stirring increased the transfer of  $\text{Ca}$  to the salt bulk, leaving less time for the contact of  $\text{Ca}$  and  $\text{TiO}_2$ . [24] For the purpose of increasing the  $\text{Ca}$  spreading on the  $\text{TiO}_2$  particles, a rotating cathodic basket was tested, but the product contained a high

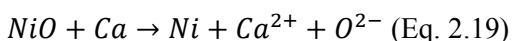


oxygen level at 11 w.t.%.[24] The stirring accelerated the diffusion of Ca to the salt bulk, leaving less time for the contact of Ca and TiO<sub>2</sub>.

#### 2.1.1.2 NiO

Nickel is a widely used structural material and magnetic material for a high melting point and good corrosion resistance. So, research effort were also placed on the reduction of NiO to Ni.

NiO could be reduced in CaO/CaCl<sub>2</sub> through the OS process at 900 °C. NiO was reduced by the calcium to the nickel metal (Eq. 2.19). The current efficiency was 16.8%~79.2% based on the distance of the NiO to the cathode.[30] A higher current efficiency could be achieved from the oxides closer to the cathode. The reduction followed a modified core-shell model that the surface of the oxide was reduced first, then the interface went into the particle to reduce the core. Other parameters were also tested in the reductions, such as various CaO concentrations in CaCl<sub>2</sub> molten salts. By conducting the experiment for 30 min, different amounts of charges could be applied in salt of 0~5 mol% CaO in CaCl<sub>2</sub>. In pure CaCl<sub>2</sub> melt, 126.3% of the theoretical charge was applied and only the outer layer of the oxides was reduced to Ni metal, leaving a mixture of Ni and NiO inside. As the CaO concentration increased from 0.5 mol% to 3 mol%, more charges were applied, from 129.5% to 197.3% of the theoretical charge. It was found that with more CaO in the electrolyte, the reduction was more thorough inside the oxide, and for the reduction in 3 mol% CaO/CaCl<sub>2</sub>, the NiO was fully reduced to Ni metal. In an electrolyte with 5 mol% CaO concentration in CaCl<sub>2</sub>, the total applied charge decreased to 182.3% of the theoretical charge and the reduction extent was dramatically decrease, observing NiO even on the surface of the feed. The study on the CaO concentration concluded that the oxide ion transfer was enhanced and the reaction rate was improved at a higher CaO concentration. However, with a much high CaO concentration, the generated Ca liquid metal droplet formed a ‘metal fog’ and deposit on the external surface of the oxide basket. As the result, the Ca precipitate on the outside of the basket accumulated and would not transfer inside for effective NiO reduction.



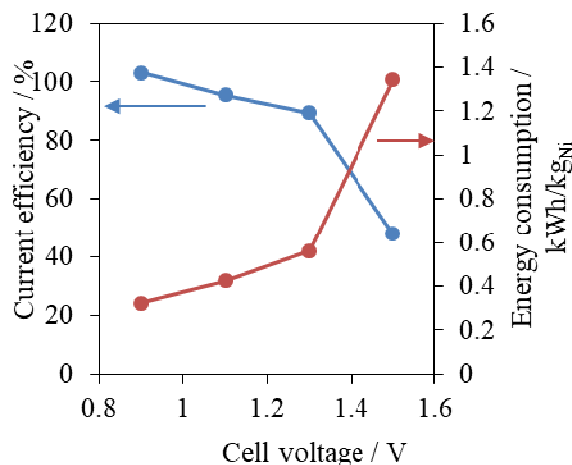
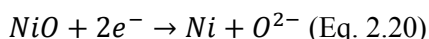


Figure 2.4 Plot of current efficiency achieved at different cell voltages [31]

NiO electroreductions were also performed in a molten salt mixture  $\text{Na}_2\text{CO}_3/\text{K}_2\text{CO}_3$  at  $750\text{ }^\circ\text{C}$ . In underpotential reduction at  $1.1\text{ V}$ , NiO was fully reduced with the electrons (Eq. 2.20). The current efficiency reached a high value of  $95.4\%$ , however, the operation time was very long. It took  $11\text{ h}$  to reduced  $0.6\text{ g NiO}$ . [31] The applied cell potential was studied as a controllable parameter in the reduction. The retention time of the current plateau in the I-t curve became shorter under a higher cell voltage, which was the result of higher reduction driving force. When comparing the current efficiency at different applied cell voltages (Fig. 2.4), it was found that the current efficiency and energy efficiency decreased with the increasing cell voltage. It was because at a higher cell voltage, the background current became greater and more portion of the energy was consumed by the side reaction. The high current efficiency and affordable process made the molten carbonate electrolysis a green process for the metal extraction from its oxides.



NiO was also reduced in NaOH molten salt at  $550\text{ }^\circ\text{C}$  at underpotential. [32] When reducing in pure NaOH, the current efficiency was  $25.9\%$ . The low current efficiency was due to the side reaction of electrolysis of the  $\text{OH}^-$  ( $2\text{NaOH} \rightarrow \text{Na}_2\text{O} + \text{H}_2\text{O}$ ). So in order to prohibit the electrolysis of  $\text{OH}^-$  and decrease the activity of water,  $\text{Na}_2\text{O}$  was added to the NaOH as a second component of the electrolyte. By adding  $1\text{ w.t.}\%$  of  $\text{Na}_2\text{O}$ , the potential window of the electrolyte was much broadened. The increase of oxygen ion concentration accelerated the reduction of NiO, and distinctly increase the current efficiency to  $87.2\%$ .

In the XRD analysis of the products, all the studies detected just Ni and NiO. It indicated that the reduction of NiO was a one-step mechanism (Eq. 2.19 and Eq. 2.20) and there was no intermediate

involved in the process. The reduction mechanism was simple and the reduction was relative easy. But the larger scale production of Ni metal was limited by the high operation temperature, long operation hours or low current efficiency.

### 2.1.1.3 $Tb_4O_7$

The electrolytic reduction of  $Tb_4O_7$  was carried out in molten  $CaCl_2$  at 850 °C to 900 °C.[33] An overpotential was applied to the cell between  $Tb_4O_7$  and the graphite rod anode. The phase analysis showed the presences of  $Tb_2O_3$ ,  $TbOCl$ , and  $Tb$  (Fig. 2.5).  $Tb_2O_3$  was the generated through both thermal decomposition and  $Tb_4O_7$  underpotential reduction. Side product  $TbOCl$  was produced from the reaction of  $Tb_2O_3$  and  $CaCl_2$ . Both  $Tb_4O_7$  and  $Tb_2O_3$  were reduced by either metallic calcium or electrons to terbium metal.

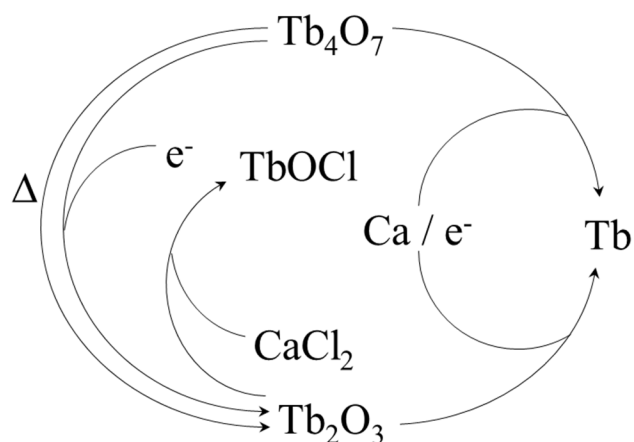


Figure 2.5 Reaction pathway of  $Tb_4O_7$  electroreduction in molten  $CaCl_2$

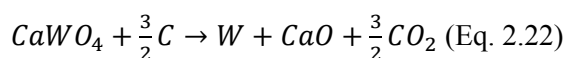
The study concluded that  $Tb_4O_7$  could be reduced to  $Tb$  metal with the  $Ca$  deposition. With and increasing cell potential, the generation rate of  $Ca$  metal and the calciothermic reduction remained at the same rate, but the direct electrolytic reduction became faster. So, in the section view of the product pellet, it could be seen that the reduction depth increased with higher cell potentials. However, with the cell potential higher than 3.5 V, the reduction depth was not changed. Also, a liquid  $Ca$  layer could be detected, leaving the interior oxide partially reduced. The overdeposited liquid  $Ca$  metal covered the reactant and impeded the ion transfer within the oxides. It blocked the ion change between the oxides and the mediate, and prohibited the release of oxygen after electroreductions, resulting a retard of the electroreduction process. It was concluded that the mass transfer of  $O^{2-}$  or  $CaO$  in the non-linear pores of the pellet in the rate-control step.

#### 2.1.1.4 WO<sub>3</sub>

Attempts were made to reduce WO<sub>3</sub> in molten calcium chloride molten salts at 900 °C.[34] Under the experimental conditions, WO<sub>3</sub> chemically reacted with CaCl<sub>2</sub> and generated CaWO<sub>4</sub> and WO<sub>2</sub>Cl<sub>2</sub> (Eq. 2.21). And then the CaWO<sub>4</sub> was reduced to tungsten by electrolysis. There was a great mass loss during the process. 50 w.t.% of WO<sub>3</sub> was lost on the cathode in the form of WO<sub>2</sub>Cl<sub>2</sub> vapor due to high volatility of WO<sub>2</sub>Cl<sub>2</sub>, and around 15 mol% of intermediate CaWO<sub>4</sub> dissolved in the CaCl<sub>2</sub>. So, there was almost no product after reductions, and it made the process quite low in efficiency.



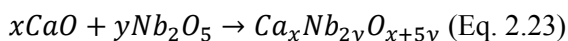
In order to increase the efficiency, two improvements were made to the reduction process. CaWO<sub>4</sub> was used as the feed to avoid the formation of WO<sub>2</sub>Cl<sub>2</sub> through the reaction of WO<sub>3</sub> and CaCl<sub>2</sub>. It was pre-synthesized by mixing equimolar CaO and WO<sub>3</sub> at 1200 °C for 6 h ( $2WO_3 + CaO \rightarrow CaWO_4$ ). Also, NaCl was added to CaCl<sub>2</sub> electrolyte to create a NaCl/CaCl<sub>2</sub> (48 mol% NaCl) eutectic salt system for the purpose of decreasing the solubility of CaWO<sub>4</sub> to 1 mol%. The advantage of using NaCl/CaCl<sub>2</sub> as the melt also lied in a relative lower melting point. At a lower operation temperature 600 °C, the nano-size (100 nm) tungsten powder was generated from CaWO<sub>4</sub> reduction on the cathode and CO<sub>2</sub> was released on the anode (Eq. 2.22). However, the product was contaminated by calcium compounds and needed to be leached with dilute HCl. Impurities in the product included CaCO<sub>3</sub> and Ca(OH)<sub>2</sub>, which were the products of the CaO with side products. The CaO was not initially added, but generated due to the accumulated O<sup>2-</sup> ion. So, the diffusion of O<sup>2-</sup> away from the cathode played an important role in the getting high quality tungsten product and improving the producing rate. Sintered and nonsintered CaWO<sub>4</sub> pellets were used in reductions. It was found that the current response on the non-sintered pellets was higher than that on the sintered pellets, and the researchers expected a shorter reduction time for smaller pellet sizes. It was the effect of a higher mass diffusion in more porous and bigger surface area materials. So, the mass diffusion in the solids was an important factor in the reduction process.



#### 2.1.1.5 Nb<sub>2</sub>O<sub>5</sub>

Nb<sub>2</sub>O<sub>5</sub> was reduced in a NaCl/CaCl<sub>2</sub> electrolyte systems at a cell potential of 3.1 V at 900 °C.[35] This applied potential was high enough for oxygen ionization on the cathode, but was lower than the decomposition potential of the salt. Based on the thermodynamic calculations, it was proposed

that the preferred reaction on the cathode was the oxygen ionization of the cathode to release oxygen ions. So the reduction should follow a pathway only with niobium suboxides involved, and the oxygen ions released from the cathode supposed to transfer to the graphite anode and form oxygen gas. However, during the reduction process, the products phase identification showed that the cathode  $\text{Nb}_2\text{O}_5$  was converted into a series of intermediates, including calcium niobate phases ( $\text{Ca}_4\text{Nb}_2\text{O}_9$ ,  $\text{Ca}_3\text{Nb}_2\text{O}_8$ ,  $\text{Ca}(\text{NbO}_3)_2$ , and  $\text{CaNbO}_3$ ) and niobium suboxides ( $\text{Nb}_4\text{O}_5$ ,  $\text{NbO}_2$ ,  $\text{NbO}$ , etc). It was because, in reality, the oxygen ion diffusivity among the oxides was low and also depended on the type of niobium oxides. The accumulation of released oxygen ions increased the local activity of  $\text{CaO}$  which reacted with the nearby niobium oxides to form calcium niobate intermediates (Eq. 2.23), and the niobates were difficult to reduce. 90.78% of oxygen was removed from the cathode in 4.2 h through oxygen ionization of niobium oxides, but it took up to 48 h to fully reduce the calcium niobate intermediates to niobium (oxygen level 2311 ppm). So, due to the low oxygen diffusion in the cathode, the calcium niobates were formed and it dramatically reduced the reduction efficiency. The addition of  $\text{NaCl}$  in the salt mixture was to decrease the  $\text{CaO}$  activity and prevent the dissolution of  $\text{Nb}_2\text{O}_5$  in the  $\text{CaO}/\text{CaCl}_2$  melt. But the effect of  $\text{NaCl}$  was limited where the local  $\text{CaO}$  concentrations were very high. In conclusion, the reduction of  $\text{Nb}_2\text{O}_5$  was limited by the diffusion of the interstitial oxygen in the niobium oxides towards the cathode surface.



#### 2.1.1.6 $\text{Ta}_2\text{O}_5$

The electrolytic reduction of  $\text{Ta}_2\text{O}_5$  in  $\text{NaCl}/\text{CaCl}_2$  at 850 °C followed a one-step electroreduction mechanism (Eq. 2.24), meaning that the  $\text{Ta}_2\text{O}_5$  could be directly reduced to Ta metal without any tantalum oxides at other valences.[36] However, the oxygen ions extracted from the cathode were accumulated to form  $\text{CaO}$ , and the  $\text{CaO}$  could chemically combine with the unreduced  $\text{Ta}_2\text{O}_5$ , leaving a mixture of  $\text{Ta}_2\text{O}_5 \cdot n\text{CaO}$  ( $n=0, 0.5, 1, 2, 4$ ). The combination products would have a larger  $n$  value at longer contacting time and increasing  $\text{CaO}$  concentrations in the melt. As a comparison (Table. 2.3), a batch of  $\text{CaO}$  (1 mol%)/  $\text{NaCl}/\text{CaCl}_2$  salt was also used in the reduction.  $\text{CaO}$  was added to mimic the high  $\text{CaO}$  concentration environment during the reduction.

For reductions in  $\text{NaCl}/\text{CaCl}_2$ , Ta metal was generated at 0.5 h, accompanied with a second phase of  $\text{Ta}_2\text{O}_5 \cdot 0.5\text{CaO}$ . However, when  $\text{CaO}$  existed in the surroundings, phases identified at 0.5 h were  $\text{Ta}_2\text{O}_5$  and  $\text{Ta}_2\text{O}_5 \cdot 0.5\text{CaO}$ . In a high  $\text{CaO}$  concentration environment, Ta metal was detected after 1 h as well as  $\text{Ta}_2\text{O}_5 \cdot 0.5\text{CaO}$  and  $\text{Ta}_2\text{O}_5 \cdot 2\text{CaO}$ . In the electrolyte without added  $\text{CaO}$ , the oxide was

reduction to Ta metal after 12 h reduction. However, in electrolyte with high CaO concentration, the full conversion was 1 h delayed. In conclusion, due to the slow diffusion of oxygen ion to the outside of the cathode, the CaO formed by the residual oxygen ions delayed the tantalum metal production and prolonged the reduction time.

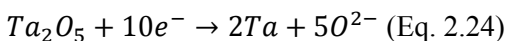


Table 2.3 Products of Ta<sub>2</sub>O<sub>5</sub> reduction in NaCl/CaCl<sub>2</sub> and CaO/NaCl/CaCl<sub>2</sub> at 850 °C

Reduction period	Products in NaCl/CaCl <sub>2</sub>	CaO/NaCl/CaCl <sub>2</sub>
0.5 h	Ta; Ta <sub>2</sub> O <sub>5</sub> ·0.5 CaO	Ta <sub>2</sub> O <sub>5</sub> ; Ta <sub>2</sub> O <sub>5</sub> ·0.5 CaO
1 h	Ta; Ta <sub>2</sub> O <sub>5</sub> ·0.5 CaO; Ta <sub>2</sub> O <sub>5</sub> ·2 CaO	Ta; Ta <sub>2</sub> O <sub>5</sub> ·0.5 CaO; Ta <sub>2</sub> O <sub>5</sub> ·2 CaO
2 h	Ta; Ta <sub>2</sub> O <sub>5</sub> ·2 CaO; Ta <sub>2</sub> O <sub>5</sub> ·4 CaO	Ta; Ta <sub>2</sub> O <sub>5</sub> ·2 CaO; Ta <sub>2</sub> O <sub>5</sub> ·4 CaO
4 h	---	Ta; Ta <sub>2</sub> O <sub>5</sub> ·2 CaO; Ta <sub>2</sub> O <sub>5</sub> ·4 CaO
5 h	Ta; Ta <sub>2</sub> O <sub>5</sub> ·4 CaO	Ta; Ta <sub>2</sub> O <sub>5</sub> ·4 CaO
12 h	Ta	---
13 h	---	Ta

#### 2.1.1.7 Cr<sub>2</sub>O<sub>3</sub>

In molten CaCl<sub>2</sub>, electrolytic reductions of Cr<sub>2</sub>O<sub>3</sub> were carried out at underpotential in a two-electrode cell with a graphite anode at 2.8 V.[17,37] The reduction followed the three-phase interlines (3PIs) model. The change in the 3PI could be identified in the I-t curves recorded during the controlled potential reductions. Initial current increase corresponds to the metallization on the surface of the oxide pellet. At this stage, the reduction occurs at the Cr|Cr<sub>2</sub>O<sub>3</sub>|electrolyte 3PI at the surface of the pellet. This phenomenon was different from that in the TiO<sub>2</sub> reductions. It was because that Cr<sub>2</sub>O<sub>3</sub> itself was semi-conductive and there were no other stable phase between Cr<sub>2</sub>O<sub>3</sub> and Cr. So the current increase in Cr<sub>2</sub>O<sub>3</sub> reduction was not because of the formation of intermediates. Before the current started to increase, a current decrease occurred in the first several seconds which it was a very short double layer charging period. After the current peak, current decreased to a plateau. The current was related to the length of the 3PI. The 3PI propagation continued layer by layer into the pellet, but the speed became slower. It was because the diffusion and migration of oxygen ion needed to pass a long distance to the bulk

electrolyte. The current plateau was a combined effect of (1) the inward-propagating 3PI from the outer surface decreases in length, and (2) outward propagating 3PI from the central hole increases in length. So it resulted in a constant 3PI until the full metallization of the pellet. Two different sizes of chromium cubic particles were observed in the products, and the larger particles of a few tens of micrometer diameter was the dominant morphology. The current efficiency reached 75% and the oxygen content was controlled below 0.2 w.t.%. A process of sintering was in the preparation of the oxide cathode, and the sintering temperature was a key parameter (Table 2.4). It showed that reductions of  $\text{Cr}_2\text{O}_3$  sintered at 1150 °C to 1450 °C achieved the Cr metal containing oxygen content of 0.8 w.t.% to 4.3 w.t.% with current efficiencies from 78.2% to 23.9%, respectively. So, reductions of precursors prepared at higher temperatures resulted in a low current efficiency and higher oxygen level. It was because the sintering at a high temperature would result in a large particle size, leading to a long distance for oxygen transfer from the oxides to the bulk salt, and hence a long reduction time.

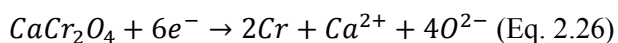
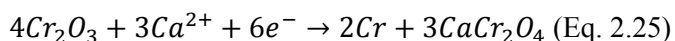
Table 2.4 Results of electroreductions of  $\text{Cr}_2\text{O}_3$  prepared at different sintering temperature.

Sintering Temperature	Weight loss	Current efficiency	Oxygen content
1150 °C	30.9 %	78.2%	0.8w.t.%
1300 °C	24.1%	68.1%	1.5w.t.%
1450 °C	7.7%	23.9%	4.3w.t.%

Reductions were in molten  $\text{CaCl}_2$  at 2.8 V for 4 hours

Reductions of  $\text{Cr}_2\text{O}_3$  were also carried out in  $\text{CaO}/\text{CaCl}_2$ , in 1 mol%  $\text{CaO}/\text{CaCl}_2$  using a two-terminal cell at 3.0 V [38], and in 2 mol%  $\text{CaO}/\text{CaCl}_2$  with a three-terminal cell at a cathodic potential -1 V vs. graphite [39]. By applying -1 V (below the  $\text{Ca}^{2+}$  reduction potential) on the oxide, calcium ion inserted in the  $\text{Cr}_2\text{O}_3$  and with the assist of the electron, the  $\text{Cr}_2\text{O}_3$  was partially reduced to Cr metal and left unreduced  $\text{CaCr}_2\text{O}_4$  (Eq. 2.25). Then the  $\text{CaCr}_2\text{O}_4$  underwent a direct electron reduction to Cr metal and released  $\text{Ca}^{2+}$  and  $\text{O}^{2-}$  (Eq. 2.26). A layer of calcium chromite  $\text{CaCr}_2\text{O}_4$  was always in between the outer Cr metal and center  $\text{Cr}_2\text{O}_3$  core. On the anode, it showed an overpotential coordinating with the cathodic potential, and  $\text{CO}_2$  was formed on the carbon anode. Kilby pointed out that the generated  $\text{CO}_2$  dissolved in the melt and combined with  $\text{O}^{2-}$  to form  $\text{CO}_3^{2-}$  ( $\text{CO}_2 + \text{O}^{2-} \rightarrow \text{CO}_3^{2-}$ ). After transferring to the cathode, the  $\text{CO}_3^{2-}$  was reduced to solid carbon by electron consumptions ( $\text{CO}_3^{2-} + 4e^- \rightarrow \text{C} + 3\text{O}^{2-}$ ). So, the application of a carbon anode would not only lower the current efficiency, but also introduce impurities due to the anode reactions.[38] As a modification of the setup, a  $\text{SnO}_2$ -based anode was introduced in the  $\text{Cr}_2\text{O}_3$  electrolytic reduction. By using a graphite anode (5.5  $\text{cm}^2$  surface area),

the current efficiency was 30 %; with a SnO<sub>2</sub>-based anode at the same surface area, the current efficiency was increase to 55%. Other than the improvement in the current efficiency, the chromium product was free from the carbon or carbide and the electrolyte salt was uncontaminated with carbon.



## 2.1.2 Electrolytic Reduction in Molten LiCl Salts

### 2.1.2.1 Pyroprocessing

The pyroprocessing technology has been developed since the 1980's at the Argonne National Laboratory (ANL).[40] It is a technology of high temperature electrochemical spent fuel recycling, as a part of the Integral Fast Reactor (IFR) system. The pyroprocessing was put into operation in 1996 at the Idaho National Laboratory (INL, formerly ANL West), for the purpose of dealing with the remaining spent nuclear fuels after the EBR-II was ceased.[41] In recent years, the pyroprocessing has been performed to close the LWR oxide fuel recycle.[42] In the INL, the researches have developed engineering scales for electrolytic reduction with over 700 g of molten salt and 50 g feeds in each reduction batch.

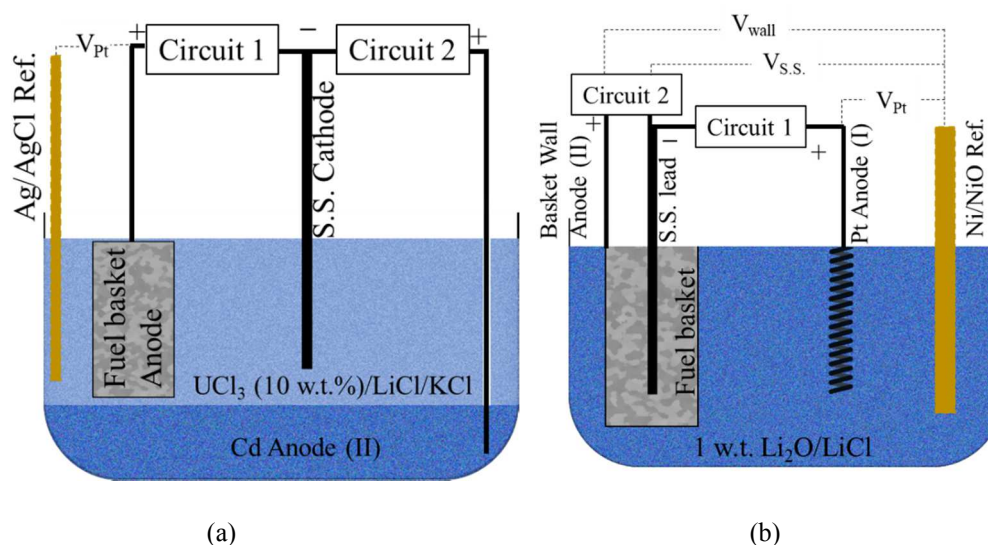


Figure 2.6 Sketches of the setup for (a) electrorefining process, and (b) electroreduction process

The initial goal for the electrorefining was to process the remaining EBR-II spent fuels. The spent fuels contain majorly uranium and zirconium as the originally driver fuel, and also sodium, neodymium, cesium, molybdenum, etc.[43] The purpose of the electrorefining was to separate the



uranium from other elements in the spent fuels, through metal dissolution on the spent fuel anode and then reduction on the cathode.[44,45] In some cases, the electrorefining was also introduced as the post-treatment of metals generated from the oxide reductions [46] and from waste salts in the electrochemical processing [42]. Fig. 2.6a shows the sketch of the Mark-IV electrorefining reactor setup. A stainless steel (2.25 Cr – 1 Mo) reaction cell had an inner diameter of 1.0 m and depth of 1.0 m. In an electrorefining salt batch, there were a bottom layer of around 10 cm depth of molten cadmium, and a top layer of 32 cm depth of  $\text{UCl}_3$  (10 w.t.%) /  $\text{LiCl/KCl}$ . The addition of  $\text{UCl}_3$  was to restrain the generation of Pu in the U products. The cathode was a mild steel mandrel, and the spent fuels were loaded in the anode fuel basket. A  $\text{Ag/AgCl}$  reference electrode was used in measuring the cathodic and anodic potentials. In the electrorefining process, the typical operation temperature was 500 °C and the electrolysis was in a controlled current mode. When the current was held at 30 A, a gradual increase in the anodic potential was observed, which indicated the electrochemical dissolution of uranium from the anode basket. In order to avoid the dissolution of other metal components in the basket, such as zirconium and other noble metal fission products, the current was gradually reduced to zero after the anodic potential reached 0.4 V vs.  $\text{Ag/AgCl}$ . A co-dissolution phenomenon was observed, meaning the dissolution of zirconium with uranium even though the anodic potential was not high enough to ionize the zirconium metal. The co-dissolution was a challenge to the electrorefining, due to the presence of  $\text{UZr}_2$ , leading to a low 73% zirconium retention rate with a 94 w.t.% uranium dissolution. It was found that with a high anodic potential, more zirconium was dissolved and also less noble metal fission products was retained. A periodic interrupting current was applied in the anodic process for the purpose of increase the retention rate zirconium and noble metals. A secondary circuit was built using the original mild steel mandrel working electrode, and the anode was the cadmium pool at the bottom. In operations, the current was applied on the steel – basket circuit for 6 s and then on the steel – cadmium circuit for 2 s. So, in terms of the anode fuel basket, the electrolysis was in an interrupted mode with 6 s on and 2 s off. The pulsed mode was proved to improve the retention rate of the zirconium and noble metals to 100% with an averaged uranium dissolution of 93.7 w.t.%. On the cathode, the uranium ions were reduced to uranium metal, forming a dendrite shape. A rotating anode basket was tested and the results showed that the efficiency was improved to 70%, compared with 50% by using a stationary basket.[47] When the feed was the metal fuels generated from the electroreduction process, the electrorefinement could achieve an efficiency of 78%.[46] Though efforts were made to increase the current efficiency, it was still low due to the difficulty in internal diffusion which referred to the mass transfer of reactants inside the fuel segments.[44,48] The electrorefinement has played an important and irreplaceable role in the spent fuel treatment. Around 830 kgHM of spent driver fuels have been electrorefined by the Mark-IV Electrorefiner since 2012.[48]

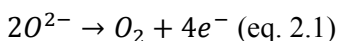
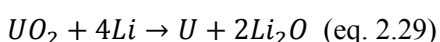
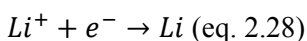
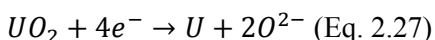
In recent years, the pyroprocessing has found its extended applications to close the LWR oxide fuels recycle, by reducing LWR oxide spent fuels to metals.[42,46,49–51] After the spent oxide fuels were transferred out from the nuclear reactors, they were chopped into operational sizes, and pyro-processed to reusable metal fuels. The reductions were carried out at 650 °C in a mixture of molten Li<sub>2</sub>O and LiCl (Li<sub>2</sub>O at 1 w.t.%). The feed oxide fuels (Table 2.5), dominantly UO<sub>2</sub>, were loaded in a stainless steel (S.S.) fuel basket. Other than uranium, elements in the LWR spent fuels included rare earths (Nd, Ce, La, Pr, etc), transuranic (Pu, Np, and Am), noble metals (Zr, Mo, Ru, etc) and salt soluble (Cs, Ba, etc). Two electrolysis circuits were built in the cell (Fig. 2.6b). In the primary electrolysis control for oxides reduction, the charge was applied between the S.S. lead – basket cathode and a platinum anode. A Ni/NiO reference electrode was placed in the cell for the monitoring purpose. The current of the primary circuit was controlled in order to maintain the anodic potential just below the Pt anode dissolution ( $Pt \rightarrow Pt^{2+} + 2e^{-}$ ) potential at +1.5 V (vs. Ni/NiO). The metal oxides were reduced at both overpotential (potential higher than the electrolyte decomposition potential) and underpotential (potential lower than the electrolyte decomposition potential) conditions. At overpotentials, the Li<sup>+</sup> was reduced to Li metal which would cover the basket and corroded the basket wall. So, in order to eliminate the impact of the lithium metal on the experimental setup, a secondary circuit was installed. The secondary circuit connected the S.S. lead as the cathode and the basket wall as the anode. A secondary power supply started to energize the basket wall at a potential more positive than the lithium formation potential (-1.75 V vs. Ni/NiO). Li metal generated on the basket wall dissolved at the lithium oxidation potential. This process mitigated the diffusion of lithium metal outside the fuel basket and prevented the fuel basket from the attack by metallic lithium on the wall.

Table 2.5 Constituent concentrations in spent oxide fuel [49]

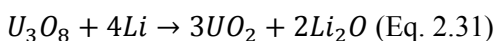
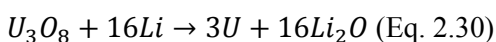
Rare earths	ppm	U/TRU	ppm	Noble metals	ppm	Salt soluble	ppm
Nd	4,200	U	838,000	Zr	3,300	Cs	2,500
Ce	2,600	Pu	6,060	Mo	2,600	Ba	2,200
La	1,300	Np	421	Ru	1,200	Sr	790
Pr	1,200	Am	230	Tc	540	Rb	530

Studies on the electroreductions of spent oxide fuels have been carried out by researchers in the INL.

The spent oxide fuel was reduced in the cathode fuel basket by controlling the current between the cathode and anode. Inside the fuel basket, the  $UO_2$  was reduced in two approaches, direct reduction by electrons at underpotential, and lithiothermic reduction by Li metal at overpotential.[46,49] In the direct reductions,  $UO_2$  was reduced with electron to uranium metal and released  $O^{2-}$  (Eq. 2.27). In the lithiothermic reductions (reductions with lithium metal as the reductive agent), lithium metal was reduced on the cathode (Eq. 2.28), then the Li attacked and reduced  $UO_2$  to U metal through a chemical reaction (Eq. 2.29). In both pathways,  $O^{2-}$  was oxidized to gaseous oxygen on the anode (Eq. 2.1). Nearly full conversions were achieved for metal oxides which were less electrochemically stable than  $Li_2O$ , such as 99.7% for uranium oxides and almost all the neptunium and noble metal oxides. For the metal oxides that were more stable than  $Li_2O$ , part of the feeds were reduced (98% for plutonium, 90% for americium and 28% ~ 80% for rare earths).[52]



Reductions of  $UO_2$  and  $U_3O_8$  were widely studied as a part of the spent nuclear fuel treatment, without the consideration of problem caused by other elements in the fuels.[53–56] Similar as the pyroprocessing treatment, electrolytic reductions of uranium oxides generally took place in 1 w.t.%  $Li_2O/LiCl$ . In the  $U_3O_8$  reduction, the process was under a pulsed cell potential control at 3 V. The applied cell potential was lower than the salt decomposition in value, but the potential on the cathode (-0.90 V vs. Li-Pb) was higher than the  $Li/Li^+$  reduction potential (-0.54 V vs. Li-Pb).[53] More than 98.1% of uranium was recovered with 140% of the theoretical charge. The XRD analysis of products at different positions of the basket were conducted. Uranium metal was generated at the lower part of the basket (Eq. 2.30); however, in the upper basket, lithium metal was detected, as well as the partially reduced  $UO_2$  (Eq. 2.31). It was because that the lithium metal could accumulated and cover the oxides particles and hinder the oxygen ion transfer out.[53]




In conclusion, the oxygen ion transfer from the metal oxides to the outside of the basket is the key challenge in the electroreduction of pyroprocessing.[52,57,58] There are three regions for the oxygen ion transfer, transfer inside the solid phases, transfer in the liquid phase among the oxides, and the diffusion to the bulk salt through the basket.

In order to increase the current efficiency, researchers tried different methods to improve the oxygen ion mass transfer. Different uranium oxides precursors,  $\text{UO}_2$  and  $\text{U}_3\text{O}_8$ , were used.  $\text{UO}_2$  is the composition in the spent fuel and the  $\text{U}_3\text{O}_8$  is the oxide fuels after the DEOX (Decladding by oxidation) process.[52] After the oxidation, the  $\text{UO}_2$  was turned to  $\text{U}_3\text{O}_8$  and there was a 30% volume expansion in the uranium compound. After the reductions, there was no significant difference in using  $\text{UO}_2$  and  $\text{U}_3\text{O}_8$ . The fuel basket design was another study interest in  $\text{O}^{2-}$  ion transfer. Studies on the effect of the fuel basket design on the reduction extent was carried out for the oxide fuel reductions, as shown in Table 2.6.[52,57,58] Two fuel baskets were involved in the comparison, a sintered S.S. basket and a S.S. wire mesh basket. Up to 150% of the theoretical charge was applied. After reductions,  $\text{Li}_2\text{O}$  concentrations in the basket were measured and the reduction extents were evaluated. The  $\text{Li}_2\text{O}$  concentrations in the sintered S.S. basket were 3.18~4.15w.t.% and the reduction extents were 8%~33%; and in the S.S. mesh basket, the  $\text{Li}_2\text{O}$  concentrations were 0.85~0.91 w.t.% and the reduction extents were increased to 43%~70%. The results showed that at a high  $\text{Li}_2\text{O}$  concentration, the reduction extents were low. So, the oxygen ion concentration is an important factor in the reductions, and the reduction extent is low at a high oxygen ion concentration. The key to increase the current efficiency is to improve the oxygen transfer from inside the metal oxides to the outside of the basket. To test the combined effect of the basket designs and oxide particle sizes on the oxygen ion transfer, a porous magnesia basket, a sintered S.S. basket and a S.S. mesh basket were used. The particles in the porous magnesia basket and sintered S.S. basket were smaller than 0.045 mm (diameter), while the particles in the mesh basket were larger to fit the bigger holes in the basket wall. It was found that the reduction current was around 1 A with the sintered metal basket, which was lower compared with higher than 2 A for reductions using a mesh basket. The low current was attributed to the high resistance of oxygen diffusion through the sintered metal basket, and it resulted in a low current efficiency. When up to 480% of the theoretical charge was applied, the current efficiencies varied from 21% (using small particles in the sintered metal basket) to 45% (using big particles in the mesh basket). The  $\text{Li}_2\text{O}$  dissolution rates were also measured in different baskets. The dissolution rate in the porous magnesia basket was  $6.9 \times 10^{-5}$  /s, but a great mass loss was observed with the porous magnesia basket. In the sintered S.S. basket, the dissolution rate was increased to  $1.0 \times 10^{-4}$  /s, and the rate was improved 8 times by using the S.S. mesh basket at  $8.6 \times 10^{-4}$  /s. When the S.S. mesh basket was rotated, the rate was further increased to  $6.9 \times 10^{-3}$  /s, which was 100 times higher than that with the porous magnesia basket.[57] So, by using a S.S. mesh basket in a rotational mode, the oxygen diffusion through the basket wall and diffusion among the oxides were improved, and a rotating S.S. mesh basket was used in electroreduction in pyroprocessing. Four different types of mesh cathode baskets were tested, with various opening size at 8~9  $\mu\text{m}$  up to 40~43  $\mu\text{m}$ . The reduction results were the same with different

baskets, indicating that the open area of these types of mesh was large enough that the transport of oxygen ion through the basket was not impeded.[55] However, with an in situ  $O^{2-}$  concentration measurement, the researchers found a slow  $O^{2-}$  diffusion rate from the metal oxide particles to the bulk salt.[56] In conclusion, the oxygen ion diffusion to the outside of the oxides determined the reduction efficiency.

Table 2.6 Fuel baskets design on current efficiency [50]

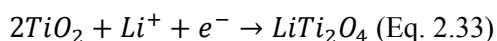
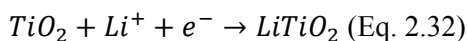
% of the theoretical charge	Li <sub>2</sub> O in basket /w.t.%		Reduction extent / %		Basket image	
	Sintered basket	Mesh basket	Sintered basket	Mesh basket	Sintered basket	Mesh basket
75	3.69	0.851	15	43		
100	4.15	0.878	11	70		
125	3.72	0.884	8	68		
150	3.18	0.912	33	67		

## 2.1.2.2 TiO<sub>2</sub>

### 2.1.2.2.1 Introduction

The lithium chloride salts used in pyroprocessing was also introduced in TiO<sub>2</sub> reductions at 650~700 °C. The advantage of the system mainly lied in the low operation temperature.

In pure LiCl, underpotential electrolysis of TiO<sub>2</sub> could not produce titanium metal. Instead, it generated partially reduced lithium titanates LiTiO<sub>2</sub> (Eq. 2.32) at a higher reduction cell potential 3.2 V and LiTi<sub>2</sub>O<sub>4</sub> (Eq. 2.33) at a lower reduction cell potential 1.8 V.[59] A CV study in the same system and it was concluded that the LiTi<sub>2</sub>O<sub>4</sub> could be further reduced to LiTiO<sub>2</sub>.



Li<sub>2</sub>O was added to LiCl, for the purpose of initializing the oxygen ion flow and increasing the oxygen transfer in the cell. The composition became 1 w.t.% Li<sub>2</sub>O/LiCl, which was the same electrolyte in the pyroprocessing. Ti metal produced through multiple steps and intermediates (Fig. 2.7). At overpotentials, Li<sup>+</sup> was reduced to Li metal *in situ* at the cathode. The lithium metal inserted to TiO<sub>2</sub> and produced both LiTi<sub>2</sub>O<sub>4</sub> (Eq. 2.34) and LiTiO<sub>2</sub> (Eq. 2.35). The higher oxide Li<sub>2</sub>TiO<sub>4</sub> could also be reduced by Li metal (Eq. 2.36). Then, assisted with Li metal, LiTiO<sub>2</sub> was reduced to Ti metal through

a series of titanium suboxides, such as TiO and Ti<sub>2</sub>O (Eq. 2.37 ~ 2.39). The current efficiency was at around 71.9% which was much higher than that of reductions in molten calcium mediates.[60,61]

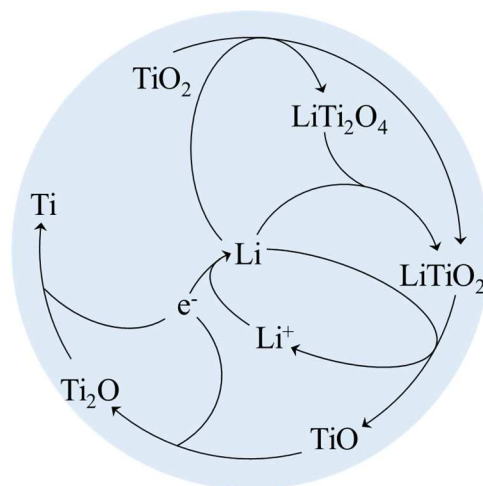
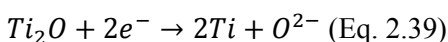
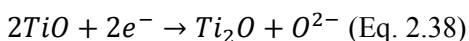
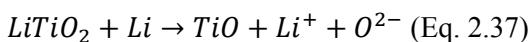
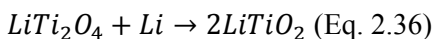
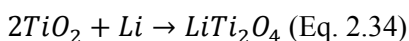


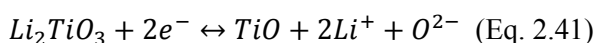
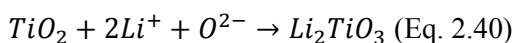
Figure 2.7 Reaction pathways of TiO<sub>2</sub> reduction in 1 wt.% Li<sub>2</sub>O/LiCl

#### 2.1.2.2.2 State of Art of TiO<sub>2</sub> Reduction in Molten Lithium Salts

Ti metal was generated from TiO<sub>2</sub> reduction in 1 wt.% Li<sub>2</sub>O/LiCl, through a series of lithium titanates (LiTi<sub>2</sub>O<sub>4</sub> and LiTiO<sub>2</sub>) and titanium suboxides (TiO and Ti<sub>2</sub>O). Due to the advantage of a relative low temperature, the process was conducted by many research groups and more reaction details were studied.

Other than the LiTi<sub>2</sub>O<sub>4</sub> and LiTiO<sub>2</sub>, generation of another lithium titanate Li<sub>2</sub>TiO<sub>3</sub> was predicted. In the cyclic voltammetry (CV) of TiO<sub>2</sub> in molten LiCl at 850 °C, it was found that there was a reduction peak which could not be assigned to the reduction of either TiO<sub>2</sub> or LiCl.[62] So, it was probably the reduction of a species whose formation did not associated with electron transfer, and the researchers

claimed the species to be  $\text{Li}_2\text{TiO}_3$ . This titanate was the result of a chemical combination reaction (Eq. 2.40). It was then reduced to  $\text{TiO}$  (Eq. 2.41). Instead of reducing single oxide  $\text{TiO}_2$ , a  $\text{TiO}_2$ - $\text{MoO}_2$  mixed oxide was also studied for reduction in molten  $\text{LiCl}$ . [62] The reduction was carried out at 3.2 V for 24 h, and produced a Ti-Mo alloy with residual oxygen at 1.8 w.t.%. By using the  $(\text{Ti}, \text{Mo})\text{O}_2$  as the feed, compared with reducing single  $\text{TiO}_2$  oxide, this oxide solid solution possessed a high oxygen mobility which improved the diffusion kinetics during the reduction. [62] As discussed above, in the calciothermic  $\text{TiO}_2$  reduction, the low current efficiency was the result of extra generation of Ca metal. For the overpotential reductions in molten lithium salts, in order to eliminate generation of excessive Li metal which was corrosive and lowered down the current efficiency, the cathodic potential was applied in a pulsed mode. The electrolysis was pulsed to measure the open circuit potential, and then the potential was resumed when the open circuit potential dropped to below the  $\text{Li}^+$  reduction potential. With a pulsed mode, the current efficiency in reduction of  $\text{TiO}_2$  was much higher than that in calciothermic  $\text{TiO}_2$  reductions. Increasing amount of charges were applied to get a higher reduction extent.  $\text{LiTiO}_2$  was generated with 25% of theoretical charge, and with 100% of theoretical charge, the product was single  $\text{Ti}_2\text{O}$ . Ti metal was collected with 150% of theoretical charge. Though the reduction extent was improve with more charge applied, the current efficiency was reduced. The current efficiency of  $\text{TiO}_2$  reduction to  $\text{LiTiO}_2$  was almost 100% but it decreased to 71.9% to produce Ti metal. So, the reduction of  $\text{LiTiO}_2$  may be the key factor in the reduction of  $\text{TiO}_2$  in molten  $\text{Li}_2\text{O}/\text{LiCl}$ .



Researchers derived the diffusion coefficient of  $\text{O}^{2-}$  transfer through the solid oxides in the order of  $10^{-8} \sim 10^{-6} \text{ cm}^2 \text{ s}^{-1}$  with the square root sweep method. This  $\text{O}^{2-}$  diffusion coefficient was very low, so the  $\text{O}^{2-}$  ion diffusion through the solid oxide was the rate-determining step in the reduction. [62]

### 2.1.2.3 Ta<sub>2</sub>O<sub>5</sub>

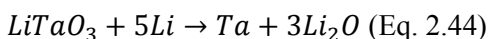
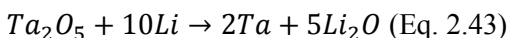
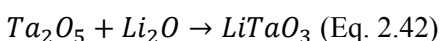
$\text{Ta}_2\text{O}_5$ , as well as  $\text{LiTaO}_3$  were reduced through chronopotentiometric measurements in 3 w.t.%  $\text{Li}_2\text{O}/\text{LiCl}$  at 650 °C. [63] Redactions were carried out in a customized sealed chamber with argon flow through. Oxide powders were added from a tube to the magnesia membrane basket.

Reactivity of  $\text{Ta}_2\text{O}_5$  in the molten salt was studied by maintained the  $\text{Ta}_2\text{O}_5$  powder in the molten salt. 30  $\text{Ta}_2\text{O}_5$  was gradually converted within 11 h.  $\text{LiTaO}_3$  (Eq. 2.42) was generated and became the only product after 24 h.  $\text{TaO}$  was observed between 5 h and 11 h. The  $\text{LiTaO}_3$  was formed

by reaction of Ta<sub>2</sub>O<sub>5</sub> and Li<sub>2</sub>O. So, the starting material of the reduction was considered as a mixture of the Ta<sub>2</sub>O<sub>5</sub> and LiTaO<sub>3</sub>.

A series of current was applied in the chronopotentiometric reductions of 30 g Ta<sub>2</sub>O<sub>5</sub>, including 0.8 A, 1.0 A, 1.2 A and 1.5 A. A potential decrease and plateau were observed in the potential-time profiles. The study compared the theoretical time and the actual experimental time for complete reductions. It was found that more time was spent than the theoretical calculation, and the difference between the theoretical and actual time tended to decrease at increasing current. It was because at a higher reduction current, the electrolysis rate of Li<sub>2</sub>O was increased. Reductions were also tested on 10 g LiTaO<sub>3</sub>, and the E-t curves were similar as that in Ta<sub>2</sub>O<sub>5</sub> reductions. With both reduction precursors Ta<sub>2</sub>O<sub>5</sub> and LiTaO<sub>3</sub>, Li metal worked as the reduction agent and reduced the feed through chemical reactions (Eq. 2.43 and Eq. 2.44). Under all reaction conditions, the potential was high enough to decompose Li<sub>2</sub>O, but not LiCl. So, O<sub>2</sub> was released on the anode. Also, an oxidation of Pt anode surface to Li<sub>2</sub>PtO<sub>3</sub> was also observed. With higher reduction current applied, the oxygen gas formed on the Pt anode was accelerated.

This study concluded that the O<sup>2-</sup> diffusion rate from the cathode to the salt bulk depended on two aspects, the thickness of the partial layer and the properties of the the magnesia member, such as the porosity and pore size.



#### 2.1.2.4 Nb<sub>2</sub>O<sub>5</sub>

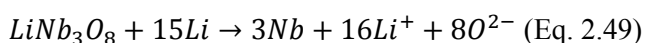
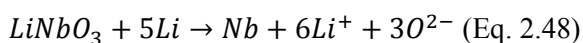
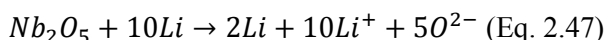
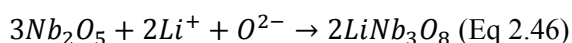
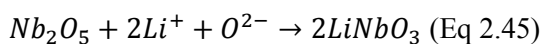
Nb<sub>2</sub>O<sub>5</sub> was reduced in 3 w.t.% Li<sub>2</sub>O/LiCl molten salt by controlling the current between cathode and anode at 0.8 A and 2.0 A.[64] The study took advantages of the setup used in Ta<sub>2</sub>O<sub>5</sub> reductions.[63]

A soaking test was conducted to study the chemical conversion of Nb<sub>2</sub>O<sub>5</sub> in the molten salt. XRD analysis was applied on the samples taken after soaking for 2 h, 5 h and 10 h. During 10 h of soaking, the amount of Nb<sub>2</sub>O<sub>5</sub> was gradually decreased, LiNbO<sub>3</sub> (Eq. 2.45) and LiNb<sub>3</sub>O<sub>8</sub> (Eq. 2.46) showed sharp intensity peaks in the XRD patterns. Another niobium species NbO<sub>2</sub> was also identified after 5 h.



In the potentiometric reductions, several stages were observed in the potential-time profiles. The Li metal was generated since the cathodic potential was higher than the  $\text{Li}_2\text{O}$  decomposition potential, resulting in a potential increase. Then, the lithium metal was consumed by reduction of the  $\text{Nb}_2\text{O}_5$  and lithium niobate species to the niobium metal (Eq. 2.47-2.49). As the process went on, lithium metal kept being generated. However, niobium compounds which could react with lithium became less. So, lithium metal started to accumulate in the magnesia membrane basket, and it caused a potential increase on the cathode. The amount of  $\text{Li}_2\text{O}$  in the electrolyte was found to be decreased gradually, with a faster decrease in reduction at 2.0 A. The decrease in  $\text{Li}_2\text{O}$  concentration indicated that the electrochemical reduction of  $\text{Nb}_2\text{O}_5$  was via the electrolysis of  $\text{Li}_2\text{O}$ , which was an indirect electrolytic reduction. By analyzing the reduction product at different charges, it was found that  $\text{LiNbO}_3$  appeared and disappeared during the process. It may be the product of reduction of  $\text{LiNbO}_3$  or  $\text{LiNb}_3\text{O}_8$ . On the anode, it was the evolution of oxygen gas.

In this study, it was concluded that the diffusion of  $\text{O}^{2-}$  was an important. By using a magnesia membrane basket to load the oxide, the oxygen ion diffusion from the inside to the outside of the basket helps to prevent  $\text{Li}_2\text{O}$  depletion in the electrolyte bulk. This process maintained a relative low  $\text{O}_2$ -concentration in the basket. It also allows a stable operation in a large scale electrolytic cell.



### 2.1.3 Electrolytic Reduction System

In this session, the electrolyte and electrodes involved in literatures were summarized and compared. It provided the clues in selecting proper experimental elements based on the research needs.

#### 2.1.3.1 Electrolyte

The choice of electrolyte is an essential factor in the electrolytic studies. It determines the operation temperatures, potentials, and changes the behaviors of reactant in the media. Mainly two

kinds of electrolytes were in use, the calcium electrolyte with  $\text{CaCl}_2$  as the main component and lithium electrolyte with  $\text{LiCl}$  as the dominating composition.

$\text{CaCl}_2$  molten salts started to get attentions when the Fray - Farthing - Chen (FFC) Cambridge process was discovered for the electrochemical reduction of  $\text{TiO}_2$ . The melting point of  $\text{CaCl}_2$  was  $772^\circ\text{C}$  and the general temperatures in the experiment were  $850^\circ\text{C} - 950^\circ\text{C}$ . The decomposition cell potential of  $\text{CaCl}_2$  was  $3.18\text{ V}$ . [37] Several extra components were added to the  $\text{CaCl}_2$  salt for different purposes.  $\text{CaO}$  was added to the system to introduce oxygen ions to start the oxygen ion flow. The melting point of  $\text{CaO}$  was  $2572^\circ\text{C}$ , but the melting points of the  $\text{CaO}/\text{CaCl}_2$  eutectic salts were reduced. And the decomposition cell potential of  $\text{CaO}$  was  $2.6\text{ V}$ . [37] In the reduction of  $\text{TiO}_2$ , it proved that it could increase the current efficiency and also decrease the oxygen content in the produced metal. [18,20] However, effect of  $\text{CaO}$  could be either improve or retrogress the metal oxide reductions. Calcium intermediates could be formed by the reactions with  $\text{CaO}$ . The intermediates were either hard to reduce, such as calcium niobates [35], or easily dissolved to the bulk salt, such as  $\text{CaWO}_4$  [34]. Also, in the reduction of  $\text{Ta}_2\text{O}_5$ ,  $\text{CaO}$  concentration was proved to have effects on the particle sizes of the final Ta metal, with larger particle sizes resulting from higher  $\text{CaO}$  concentrations. [36] The  $\text{CaO}$  concentration also had influence on the oxygen content in the product. By adding  $\text{CaO}$ , the product of calciothermic reduction of  $\text{TiO}_2$  could be alpha phase titanium metal. However, with increasing  $\text{CaO}$  concentration, the oxygen level increased from  $2000\text{ ppm}$  to  $6200\text{ ppm}$  when the concentration of  $\text{CaO}$  increased from  $0.5\text{ mol}\%$  to  $1\text{ mol}\%$ . And with more  $\text{CaO}$  at  $15\text{ mol}\%$  in  $\text{CaCl}_2$ , the reduced product was not only the alpha phase titanium metal, but also titanium suboxides, such as  $\text{TiO}_{0.325}$ ,  $\text{Ti}_6\text{O}$  and  $\text{TiO}$ . [24]  $\text{NaCl}$  was also a common additive to the molten  $\text{CaCl}_2$ . By adding  $\text{NaCl}$ , the operation temperature in the  $\text{NaCl}/\text{CaCl}_2$  could be reduced to  $600^\circ\text{C}$ . [34] Other than lowering down the required temperature, the  $\text{NaCl}$  in the salt could also restrain the dissolution of the oxides, such as  $\text{Nb}_2\text{O}_5$  [35], and calcium intermediates, such as  $\text{CaWO}_4$  [34]. The loss of materials caused by dissolution reduced the materials recovery and decrease the cell efficiency. In the reduction of  $\text{Nb}_2\text{O}_5$ , the existence of  $\text{NaCl}$  also reduced the activity of  $\text{CaO}$  and prevented the formation of intermediate which required much longer time to reduce. [35]

$\text{LiCl}$  salt was used in metal oxide reductions at a lower temperature compared with that in calcium salt. The melting point of  $\text{LiCl}$  was  $605^\circ\text{C}$  and the general operation temperature was  $650^\circ\text{C}$ . However, in pure  $\text{LiCl}$ , it was difficulty to start the oxygen flow in  $\text{TiO}_2$  reductions, and no metallic titanium was achieved. [59] The  $1\text{ w.t.}\%$   $\text{Li}_2\text{O}/\text{LiCl}$  was the electrolyte in pyroprocess for spent oxide fuels. [44,46] In the  $1\text{ w.t.}\%$   $\text{Li}_2\text{O}/\text{LiCl}$ , a lot of metal oxides can be reduced to metal, including uranium

oxides [53] and titanium oxides[60]. However, when applying overpotential during the reductions, lithium metal generated on the cathode was corrosive on the cathode basket.[46]

### 2.1.3.2 Electrode

#### 2.1.3.2.1 Cathode

The main cathode component was the materials of interest, including the metal oxides and the pre-synthesized complex precursor. The metal oxides could be fabricated in big pellets [17,37], small particles [60], or discs [9,39]. Other components of the cathode assembly included the current collectors and the holders of the materials for reductions.

The current collector was metal wires connecting the oxides with the potentiostat equipment. Various options of metal wires were used in the electrolysis. A stainless steel (S.S.) rod was inserted in a basket of  $\text{TiO}_2$  powder as the current collector.[60] The part of S.S. in the  $\text{TiO}_2$  bed was in a big size of 6 mm diameter for a large contact area with  $\text{TiO}_2$ . In some cases, the metal wires also wound the feed pellets to support the materials. A Kanthal wire was used in molten calcium salts electrolysis for its corrosion resistivity and low cost.[17,36] It was 1.5 mm in diameter and composited of 22-25 w.t.% Cr, 5-5.5 w.t.% Al, 1.5-3 w.t.% Co and the balanced with Fe. Ni wires was used to wind the  $\text{TiO}_2$  pellets for the reduction in  $\text{Li}_2\text{O}/\text{LiCl}$  [60]A molybdenum wire was also employed as the current collector to support the chromium oxide disk during the reductions in  $\text{CaO}/\text{CaCl}_2$  [39] and the  $\text{CaTiO}_3$  pellet in molten  $\text{CaCl}_2$  [9].

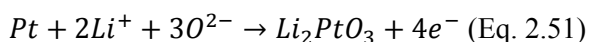
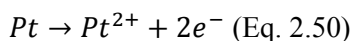
For the materials holders, several materials and configurations were used, and studies on the effect of holder designs were conducted. A Ti net current collector was also used to load the  $\text{TiO}_2$  in the calciothermic reduction.[27] As a conceptual cell design in the calciothermic reduction of  $\text{TiO}_2$ , a S.S. vessel would work as both a cathode and the container of the salt. Titanium products would be collected at the bottom of the vessel after the reactions.[23] A magnesia holder was employed in the  $\text{TiO}_2$  reductions.[61] The magnesia holder was porous to enable the diffusion of the molten salt to the cathode and  $\text{TiO}_2$  in the assembly. A S.S. spoon cathode was used to hold the  $\text{WO}_3$  pellets in molten  $\text{CaCl}_2$ . [34] After the reduction, the pellet was not left in the spoon, due to the generation of volatile  $\text{WO}_2\text{Cl}_2$  and soluble  $\text{CaWO}_4$ . A S.S. basket of 18 mm diameter was used to hold the  $\text{TiO}_2$  powder for reduction. [60] It was fabricated by surrounding a 325 mesh sheet. A detailed study of S.S. basket was conducted by using various mesh layers and sizes.[55] Basket walls were composed of inner and outer layers of big opening meshes, and four different types of meshes in between: three layers of 325 mesh (40-43  $\mu\text{m}$ ), five layers of 325 mesh, a layer of 1400 mesh (12-14  $\mu\text{m}$ ) or a layer of 2300 mesh (8-9

µm). Electrolytic reductions of UO<sub>2</sub> were carried out with these four basket. As the results, the openings of the mesh were sufficiently large that there was no oxygen ion transfer difficulty through the basket wall, evidenced by similar reduction results. A mesh S.S. basket and a sintered S.S. basket, as well as a magnesia porous basket, were tested in the reductions of spent nuclear oxide fuels in 1 w.t.% Li<sub>2</sub>O/LiCl.[57] After reductions, the Li<sub>2</sub>O concentrations in the basket were 26~46 w.t.% and 6.2~9.2 w.t.% in the sintered basket and mash basket, respectively. And the reduction extent in mesh basket was 43%~70% and that in the sintered basket was only 8%~33%. It was concluded that the oxygen ion diffusion through a mesh basket was 9 times higher than that in a sintered metal basket, and 10 times higher than that in a porous magnesia basket. Rotating and resting mesh baskets were tested for the lithium oxide dissolution rate, and it was found that the lithium oxide dissolution rate was improved 6 times by rotation.

#### 2.1.3.2.2 Anode

The reactions on the anodes were the half reaction paired with reactions on the cathodes. Problems on the anodes included the material dissolution, gas emissions, and contamination to the electrolyte.

Pt anodes were used in the reduction studies in spent nuclear fuel [46], uranium oxides [54,55], chromium oxides [38] and titanium oxides [60,61]. During the reduction of metal oxides, positive potentials were responded on the Pt anodes. Before the evolution of Cl<sub>2</sub>, the platinum was oxidized to Pt<sup>2+</sup> (Eq. 2.50) at +1.55 V vs. Ni/NiO [46] or +2.6 V vs. Li-Pb [54] in molten LiCl. And when Li<sub>2</sub>O was added to 0.5 w.t.% Li<sub>2</sub>O/LiCl, gas released on the anode was O<sub>2</sub> at a lower positive potential, +2.1 V vs. Li-Pb. Besides the generation of O<sub>2</sub>, a thin film was coated on the Pt electrode.[54] It was identified as the Li<sub>2</sub>PtO<sub>3</sub> (Eq. 2.51) with XRD. Researchers used different shapes of Pt anodes, including rods [38], spiral [46] and wide plates [55,60].



Graphite anode were widely used in LiCl [59], CaCl<sub>2</sub> [12,17,38], NaCl/CaCl<sub>2</sub> [35] and CaO/CaCl<sub>2</sub> molten salts [18,20]. By using a carbon anode, O<sub>2</sub>, as well as CO and CO<sub>2</sub>, emitted from the carbon electrode. The thick graphite rod had the problem of carbon release and high resistivity, but some features made it a relative competitive option as the anode. In molten calcium salts, platinum reacted with metal calcium, and molybdenum and nickel became brittle after several experiments.[65]

The graphite anode could be either a rod (1.5 cm diameter) [17] or a crucible [59]. With  $\text{CO}_2$  dissolved in the electrolyte,  $\text{CO}_3^{2-}$  was produced and diffused to the cathode. Reduction of  $\text{CO}_3^{2-}$  took place on the cathode and left solid carbon (Fig. 2.8). So, a mass loss was observed on the anode, and the reduced metals and electrolyte salts were contaminated by the carbon.[38] The reduction of  $\text{CO}_3^{2-}$  consumed electrons and this side reaction would decrease the current efficiency.[66]

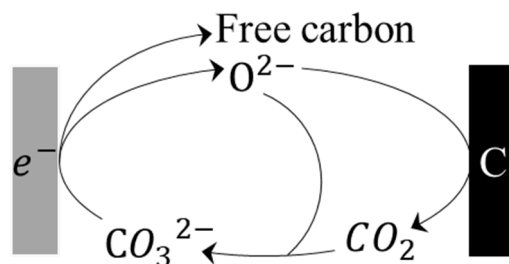


Figure 2.8 Carbon cycle in the electrolyte between the cathode and carbon anode

A  $\text{SnO}_2$  anode (1 cm diameter) was studied for the purpose of improving the current efficiency for  $\text{Cr}_2\text{O}_3$  reduction compared with the reduction with a graphite anode.[38] The  $\text{SnO}_2$  resulted in almost no weight loss, and  $\text{CO}$  and  $\text{CO}_2$  bubbles were larger. For a  $5.5 \text{ cm}^2$  anode surface area, the current efficiency was 55% with the  $\text{SnO}_2$  anode at 3.0 V; compared with 30% and 50% with graphite anode at 3.0 V and 2.0 V, respectively. The study concluded that by using the  $\text{SnO}_2$  anode, it achieved higher current efficiencies than that with a graphite anode. However, a  $\text{CaSnO}_3$  calcium stannate phase was detected on the  $\text{SnO}_2$  anode. It was the product of the reactions between  $\text{SnO}_2$  and Ca metal generated at the cathode, and it was an insulator. So, there would be a conductivity problem with the  $\text{SnO}_2$  anode in a longer term.

#### 2.1.3.2.3 Reference Electrode

In the three-electrode cell, the reference electrode is a necessary elements. The reference electrode was also applied in the two-electrode cell to measure the cathodic and anodic potentials. In this project, the electrolysis was conducted by controlling the cathodic potentials. However, so far, the electrolytic reductions were mostly carried out by controlling the cell potentials. So, the review on the reference electrodes was expanded, including the cyclic voltammetry studies, electroreduction and electrorefining.

A stainless steel reference electrode was used in CV measurements in  $0.30 \text{ CaCl}_2 - 0.17 \text{ CaCO}_3 - 0.43 \text{ LiCl} - 0.1 \text{ KCl}$  (molar ratio) in a potential range of -2 V to +0.5 V at 100 mV/s at 520 °C.[67] Three reduction peaks were observed at -0.8 V, -1.7 V and -2.0 V which were assigned to the deposition

of carbon, potassium and lithium, respectively. No reduction peak of  $\text{Ca}^{2+}$  was observed which means the decomposition potential for  $\text{Ca}/\text{Ca}^{2+}$  was higher than -2 V. However, the application of stainless steel as a reference electrode was limited by the localized corrosion which was very common in chloride molten system.[68] The corrosion would cause introduction of impurities to the system and potential drift due to the change in the reference electrode.

The electrochemistry of  $\text{LiCl}/\text{Li}_2\text{O}/\text{H}_2\text{O}$  molten salt system was studied with a molybdenum reference electrode.[69] CVs were measured in pure  $\text{LiCl}$  electrolyte and also in  $\text{LiCl}$  with 1 w.t.%  $\text{Li}_2\text{O}$  at 650 °C at 20 mV/s. The results showed that the cathodic decomposition potential was at around -1.9 V for pure  $\text{LiCl}$  and at -1.2 V for 1 w.t.%  $\text{Li}_2\text{O}/\text{LiCl}$ . The authors explained the positive potential shift of  $\text{Li}/\text{Li}^+$  after addition of  $\text{Li}_2\text{O}$  was due to an underpotential deposition (UPD).

A titanium crucible was used as both the molten salt container and the reference electrode.[65] CV measurements were taken to check the working conditions of the electrolysis cell. After pre-electrolysis of molten  $\text{CaCl}_2$  at 2.7 V (cell potential) for 2 hours, a first CV was measured in a region 0.2 V to -1.3 V at 50 mV/s. There was no current peak in cathodic CV until  $\text{Ca}/\text{Ca}^{2+}$  decomposed at -0.9 V, indicating a successful pre-electrolysis in removing the moisture in the melt. A second CV was measured in order to clarify the change on the glassy carbon working electrode. An oxidation peak at -1.0 V appeared when CV was repeated 6 times. After the glassy carbon working electrode was polished, this oxidation peak disappeared at the first CV cycle but showed again on the second measurement. The oxidation peak at -1.0 V was concluded as the decomposition of  $\text{CaC}_2$  which was the product of a chemical combination reaction of the deposited calcium and the glassy carbon working electrode.

A Li-Pb reference electrode was used to determine  $\text{TiO}_2$  reduction routine in 1 w.t.%  $\text{Li}_2\text{O}/\text{LiCl}$ .[60] CVs were carried out at a scan rate 100 mV/s using a Ni- $\text{TiO}_2$  working electrode, and a Pt plate counter electrode. The CVs were measured in multicycles from around -1.0 V ~ +1.0 V. A reduction peak in CV measurement at 0.3 V is assigned as the reduction of  $\text{TiO}_2$  to lithium titanate intermediate, and another reduction peak at -0.2 V was the reduction of titanates and titanium suboxides.

A Ca-Pb reference electrode was employed in deriving the decomposition potential of  $\text{Ca}/\text{Ca}^{2+}$  vs. at different  $\text{CaO}$  concentrations.[70] The decomposition potential from CV measurements was -0.51 V at 810 °C. After a series of measurements, it is found that the decomposition potential decreased with increasing  $\text{CaO}$  concentrations and temperatures.

$\text{Ag}/\text{AgCl}$  is a widely used reference electrode by establishing a redox couple (Eq. 2.52) which enhances the stability in electrolytes especially for electrolytes containing  $\text{Cl}^-$  ions. Ijije et al. identified

a carbon species loop by measuring CV cycles of molten  $\text{Li}_2\text{CO}_3/\text{K}_2\text{CO}_3$  with a  $\text{Ag}/\text{AgCl}$  reference electrode at  $540\text{ }^\circ\text{C}$ . [67] During cathodic CV scans,  $\text{CO}_3^{2-}$  was reduced to carbon with electrons at  $-1.65\text{ V}$ . And then in the anodic scans, carbon was oxidized at different potentials to different species. Carbon was oxidized with  $\text{O}^{2-}$  to  $\text{CO}_2$  at  $-1.28\text{ V}$ . And at  $-1.05\text{ V}$ , carbon was oxidized with  $\text{O}^{2-}$  to  $\text{CO}$  which was further oxidized to  $\text{CO}_3^{2-}$  at  $-0.6\text{ V}$ . At  $-0.2\text{ V}$ , carbon was oxidized with  $\text{CO}_3^{2-}$  to  $\text{CO}_2$ . And at  $+0.2\text{ V}$ ,  $\text{O}_2$  was evolved when  $\text{CO}_3^{2-}$  was converted to  $\text{CO}_2$ . The  $\text{Ag}/\text{AgCl}$  reference electrode is also employed in electrorefining in  $\text{KCl}/\text{LiCl}$  (44 w.t.%  $\text{LiCl}$ ) at  $500\text{ }^\circ\text{C}$ . [71,72] This  $\text{Ag}/\text{AgCl}$  reference electrode was fabricated by inserting a silver wire in a mixture of  $\text{AgCl}$  (5mol%)/  $\text{LiCl}/\text{KCl}$  in a Pyrex NMR tube (Fig. 2.9a). At the  $\text{LaCl}_3$  concentrations of 0.97 w.t.%, 2.68 w.t.% and 6.38 w.t.%, the cathodic decomposition potentials for  $\text{La}^{3+}$  were at  $-2.185\text{ V}$ ,  $-2.180\text{ V}$ , and  $-2.176\text{ V}$ , respectively.

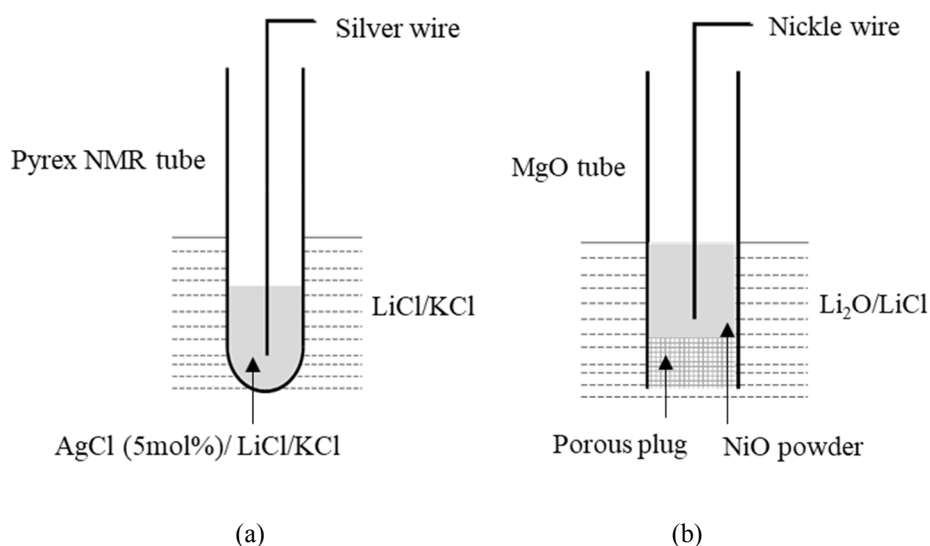
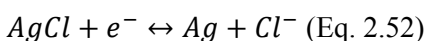
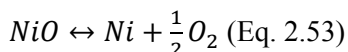


Figure 2.9 Sketch of (a)  $\text{Ag}/\text{AgCl}$  and (b)  $\text{Ni}/\text{NiO}$  reference electrode

$\text{Ni}/\text{NiO}$  (Fig. 2.9b) is also a commonly used reference electrode in system with free  $\text{O}^{2-}$  ions. An equilibrium (Eq. 2.53) is established within the electrode. Herrmann and Li used a  $\text{Ni}/\text{NiO}$  pseudo reference electrode in measuring CVs at  $20\text{ mV/s}$  in determination of cathodic and anodic decomposition potentials for  $\text{LiCl}$  with different  $\text{Li}_2\text{O}$  concentrations. [46,49]  $\text{LiCl}$  with 0, 0.25, 0.5 and 1 w.t.% of  $\text{Li}_2\text{O}/\text{LiCl}$  were stabilized at  $650\text{ }^\circ\text{C}$  and CVs were obtained in both cathodic side with stainless steel working electrode and anodic side with platinum working electrode. By using a  $\text{Ni}/\text{NiO}$  reference electrode, the cathodic decomposition potential of the lithium salt decreased with increasing  $\text{Li}_2\text{O}$  concentration and the  $\text{Li}/\text{Li}^+$  was at  $-1.75\text{ V}$  for 1 w.t.%  $\text{Li}_2\text{O}/\text{LiCl}$ . On the anodic CV side, after adding  $\text{Li}_2\text{O}$  in  $\text{LiCl}$ , gas evolved from anode was  $\text{O}_2$  instead of  $\text{Cl}_2$ , which lead to an obvious decrease

in anodic decomposition potential. Before O<sub>2</sub> evolution, an oxidation peak appeared was determined as the generation of Li<sub>2</sub>PtO<sub>3</sub> from Pt anode and Li<sub>2</sub>O. Ni/NiO reference electrode were also in CVs for spent nuclear fuel containing uranium oxides in 1 w.t.% Li<sub>2</sub>O/LiCl, in order to determine uranium oxides reduction potentials. CV peaks showed a series of reduction reactions, where U<sub>3</sub>O<sub>8</sub> was reduced to UO<sub>2</sub> at -1.45 V and UO<sub>2</sub> was reduced to U metal at -1.62 V.



## 2.2 Research Challenges and Gaps

The electrolytic reductions has been widely studied on various metal oxides with all kinds of operation setups, and the electrolysis control methods. However, the promotion of the electroreduction of metal oxides is hindered due to the low current efficiency. Based on the review of research discussed above, the low current efficiency is the result of the low oxygen ion diffusions inside the oxide solid particles to the bulk.

Table 2.7 Methods in increasing current efficiency in literatures

	Changes	Reductions	Current efficiency	Reference
Precursors	Dense → Porous TiO <sub>2</sub>	FFC of TiO <sub>2</sub>	32% → 40%	[18,20]
	TiO <sub>2</sub> → CaTiO <sub>3</sub>	FFC	15% → 28%	[9]
Electrolyte	CaCl <sub>2</sub> → 2 mol% CaO/CaCl <sub>2</sub>	FFC of TiO <sub>2</sub>	18% → 40%	[20]
	CaCl <sub>2</sub> → 0.5 mol% CaO/CaCl <sub>2</sub>	OS of TiO <sub>2</sub>	No Ti metal → 12.9%	[29]
Setup	NiO closer to the cathode	OS of NiO	16.8% → 79.2%	[30]
	Sintered → Mesh basket	Pyroprocessing	Faster O <sup>2-</sup> transfer	[50]
	Stationary → Rotating basket	Pyroprocessing	Faster O <sup>2-</sup> transfer	[57]

In order to increase the current efficiency, researchers have tried many methods. In terms of the precursors, different types are tested. By using the porous TiO<sub>2</sub> instead of dense TiO<sub>2</sub>, the current efficiency in FFC process increased from 32% to 40%.[18,20] To avoid the in situ formation of the CaTiO<sub>3</sub>, it was used directly as the precursor in the FFC process, and the current efficiency was increased from 15% with TiO<sub>2</sub> to 28% with CaTiO<sub>3</sub>.[9] In the aspect of electrolyte, by adding 2 mol% of CaO to CaCl<sub>2</sub>, the current efficiency in FFC process increased from 18% to 40%.[20] And for the OS reduction, titanium metal cannot be produced in pure CaCl<sub>2</sub>, but after adding 0.5 mol% of CaO, the



current efficiency in titanium generation is 12.9%.[29] The setup design also has impacts. In the OS reduction of NiO, it is found that by placing the NiO closer to the cathode, the current efficiency can be increased from 16.8% to 79.2%.[30] In the pyroprocessing, it was found that compared with a sintered basket, the mash basket has a higher O<sup>2-</sup> transfer rate.[50] And when the basket was rotating, the O<sup>2-</sup> transfer rate was further improved.[57]

The agitation through sonication is expected to achieve several goals. It will accelerate the diffusion of oxygen ion in the oxide bed to the outside of the solids. And the agitation should improve the contact between the oxide particulates with the electron from the cathode or the reductive metal on the cathode. Due to the adhesion property of the molten salt, the released oxygen molecules are trapped in the cathodic basket. So the sonication will also drive the trapped oxygen molecules diffusing out of the oxide particles. Should the proposed research proceed as expected, it will successfully resolve one of key needs associated with scale-up pyroprocessing, and promoting the commercialization of metal production through electroreductions.

Therefore, the sonication was introduced in this project mainly as an agitation method. It expected an improvement of the mass transfer in the electrolytic cell under a single or a combined mechanism.

### **2.3 Research Objectives**

This work combines the fundamental study in electrolytic reductions of metal oxides in high temperature molten salts, with the advanced technique of sonication. The combined technique has potentials being scaled-up and introduced in effective reductions of radiological metal oxides, which promotes the spent fuel recycling. This project is carried out in progressive procedures to accomplish the research goals as follows.

1. Understand the fundamental of electrolytic reductions of metal oxides

By varying the electrochemical parameters, such as the applied charge and reduction potentials, the electrolytic reductions of metal oxides can be controlled in a step-by-step way. The cathodic reduction potential is the main parameter in this study, and the reductions will be stopped after applying a desired amount of charge. This procedure will benefit a fundamental understanding of the reduction mechanism, in terms of reaction processes and the rate-determining step.

2. Couple electrolytic reduction with sonication

A sonication setup is first time introduced in electrolytic reduction of metal oxides in high temperature molten salts, which is a new and promising method in improving the oxygen diffusion and

current efficiency. A sonication setup is designed and built in the project. Challenges, such as high temperature heat working atmosphere, need to be overcome in the progress of the study. After the sonicator setup is completed, it will be coupled with the mature electrolytic reductions of metal oxides study. On the success of establishment of the sonication setup, the freedom in sonication combination can also be introduced in interdisciplines.

### 3. Improve process efficiency for metal oxides electrolytic reduction

The improvement of reduction due to application of sonication is identified by comparing the results of reductions in both silent and ultrasonic environment. When the combined technique is proved to be effective in increasing the current efficiency, it will be promoted in the area of electrolytic metal oxides reductions. Other than reduction of common metal oxides, it will also be applicable in recycling spent nuclear fuels. Currently, one of the most widely adopted methods in spent fuel management is disposal underground. However, the leakage of radiological materials raises the objections from the public. So the recycling of spent fuel will make the problem easier and reduce the worries from the society on nuclear energy.

## Chapter 3: Methodology

Research effort of this project focuses on the conduction of electroreduction experiments, derivation of the metal oxide reduction mechanism and improvement of the efficiency with ultrasound power. In this chapter, detailed experimental design is discussed including the choices of experimental elements, electrolytic techniques, and sample characterization methods.

### 3.1 Electrolytic Techniques

The electrolytic study is the principle throughout the whole project. It is a milestone of the project to establish the baseline for metal oxide reductions by performing electrochemical reductions on metal oxides in molten salts without sonication. Cyclic voltammetry and chronoamperometry were performed for the purpose of achieving the properties of the electrolyte, and carrying out electroreductions to derive the reduction mechanisms and create a baseline to define the change caused by the sonication.

The electrolytic control and data acquisition were realized with a VersaSTAT 4 Potentiostat (Princeton Applied Research) interfaced with the VersaStudio software.

#### 3.3.1 Cyclic Voltammetry

Cyclic Voltammetry is one of the most versatile electroanalytical techniques in the electroactive studies. It is widely used in organic and inorganic aqueous solutions [84] and molten salt mediates [60] thanks to its flexible application and quick responses at controllable scan rates and potential ranges. In this project, cyclic voltammograms were measured in both fresh and used salts to study the salt properties, including the thermodynamic uniformity, the salt decomposition potential, generation of impurities, and possible chemical reactions in the salts.

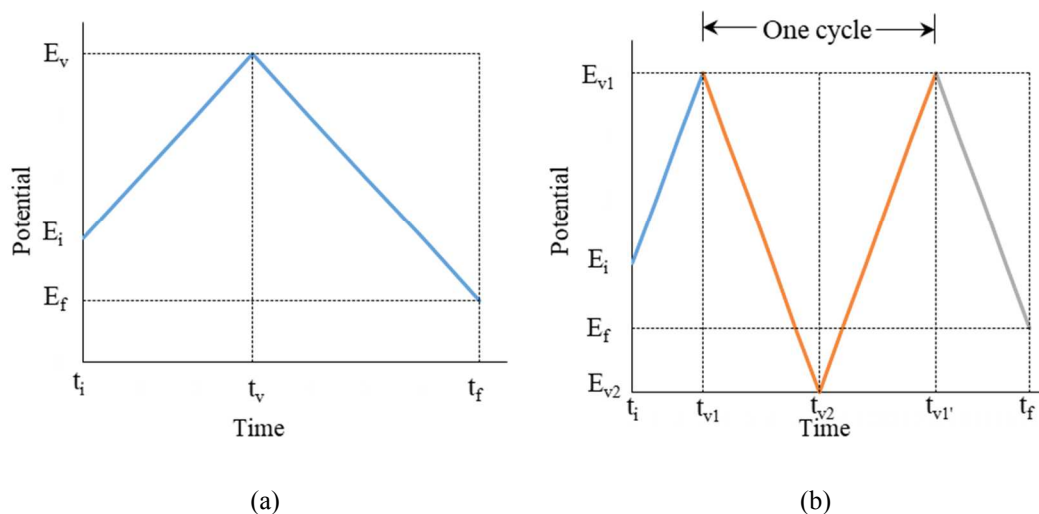


Figure 3.1 Typical potential-time profiles in an exemplary (a) single and (b) multiple cycles of cyclic voltammetry measurement.

There are several parameters in performing cyclic voltammetry. The initial potential, final potential, and the vertex potentials define the voltage range of the scans. The applied potentials should not be very high. It is because the current limit of 2 A according to the potentiostat, and big current peaks may cover some smaller peaks. The current responds vs. the applied potentials were the data collected as the CV results. Both single and multiple cycles were measured. The basic difference between the single CV and multiple cycle CV is straight forward. Fig. 3.1 shows typical potential-time profiles in CVs. In a single CV measurement (Fig. 3.1a), the scan is from the initial potential  $E_i$  to the vertex potential  $E_v$  and then reaches to the final potential  $E_f$ , and the derived whole potential-current is considered as a single cyclic voltammogram. For the multiple cycles CV measurement (Fig. 3.1b), the potential sweeps from the initial potential  $E_i$  to the first vertex potential  $E_{v1}$ , then it scan forward to the second vertex potential  $E_{v2}$  and back to  $E_{v1}$ , and finally stops at the final potential  $E_f$ . In a multiple cycle cyclic voltammogram, the scan between two vertex potentials is treated as a cycle in the data acquisition with software by default, which is the period between  $t_{v1}$  and  $t_{v1'}$ . In this project, both single CV and multiple cycles of CV were measured by setting  $E_i$  and  $E_f$  at the open circuit potential (OCP).  $E_v$  in single CV and  $E_{v1}$  in multiple cycle CV were potentials more negative than the salt decomposition potential.  $E_{v2}$  in the multiple cycle CV was a potential more positive than the OCP. For the multiple cycle CV measurement, only one entire cycle was measured and data was extracted for analysis. All the multiple cycle CV results reported in this dissertation are collected by running one entire CV cycle and the data are between  $t_{v1}$  and  $t_{v1'}$ . The scan rate is also an essential property in CV measurement, and all cyclic voltammograms achieved in this study were recorded at a scan rate of  $20 \text{ mV s}^{-1}$ . In order to achieve comparable and repeatable CV results, the working electrode surfaces were accurately

recorded, and either the potential ranges or the current responses of the CVs was controlled. The potential range was directly applied by inputting the values in the control interface. Desired current ranges were attained by varying applied potentials. CV measurement under each condition was repeated at least once to guarantee the reliability of the results.

Cyclic voltammetry measurements were taken in different salt compositions. CVs in fresh salt (the electrolyte free from metal oxides reductions) provided the information of the properties of the electrolyte, including the open circuit potentials, electrochemical reactions of components in the salt and the salt decomposition potentials. By varying the salt composition, the effect of species concentration on the salt properties was also defined by measuring CV in salts. For example, in Li<sub>2</sub>O/LiCl mixtures, the concentration of Li<sub>2</sub>O was the controllable factor. So, the influence of Li<sub>2</sub>O concentration on the OCP, Li deposition potential, O<sub>2</sub> emission potential, etc. were achieved from CV curves. CVs were measured each time before the electroreduction, for the purpose of checking the thermal uniformity of the system and determining the Li/Li<sup>+</sup> potential. Post-reduction CVs in used salts (salt melt after metal oxide reductions) were also measured to characterize changes in the electrolyte due to the metal oxide reductions. Attentions were paid on the shift and intensity change of original existing peaks, and the growth of new peaks.

### 3.3.2 Constant Potential Chronoamperometry

In a chronoamperometry measurement, a constant potential is applied on the working electrode and the current-time profile is usually recorded and reported. The duration time and the data collection time intervals are also variables in controlling the potential application. Limits such as current response and the charges applied, can be set as criteria to cease the electrolysis.

#### 3.3.2.1 Chronoamperometry for Electrode Surface Cleansing

After each CV measurement, the working electrode surface was cleaned with an anodic electrolysis method to remove the residual deposited metal. During the CV measurements, metal ions in the electrolytes are reduced to metal (eg.  $Li^+ + e^- \rightarrow Li$ ) which attaches on surface of the working electrode. Though in the backward CV scans, the metal is re-oxidized to ions ( $Li \rightarrow Li^+ + e^-$ ), there may be residual on the surface which will affect the next CV measurement. So, when a CV measurement is completed, a chronoamperometry run is followed at +0.1 V vs. OCP for 30 seconds. This process aims at dissolve any metal left on the electrode surface. If the surface is clean, the OCP

should be the same as the value before the CV measurement, or the CV curves are identical. The cleansing process can be repeated if these criteria are not satisfied.

### 3.3.2.2 Chronoamperometry for Electrolytic Reductions

Electroreductions are carried out by applying a constant cathodic potential on the working electrode. The current-time data are collected and filed. The primary parameter in chronoamperometry is the applied potential on the working electrode, and the criteria in stopping the electrolysis is either the experimental duration or the total charge applied.

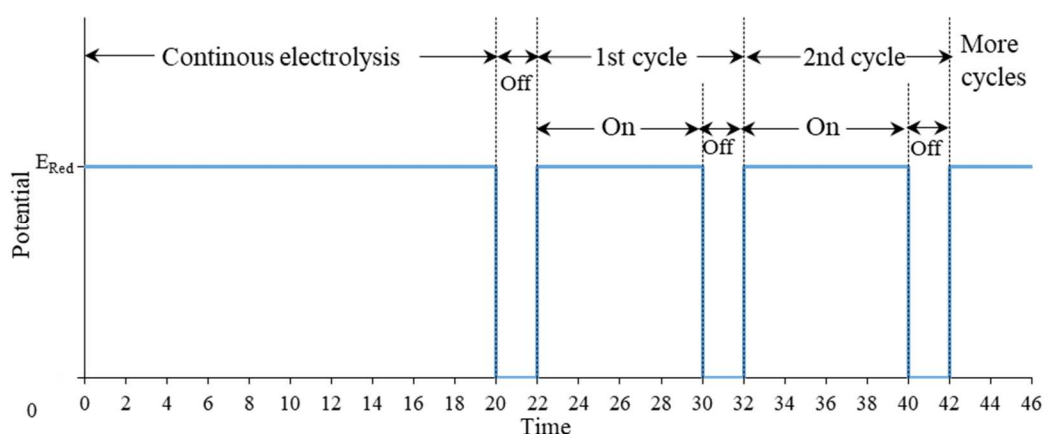


Figure 3.2 Potential setting for the overpotential electroreductions

To study the effect of reactive agent in the oxide reduction process, both overpotentials and underpotentials are applied in the chronoamperometry experiments. The overpotential is a potential more significant than the decomposition potential of the salt, so the reductive agent is the electrolyzed metal. For the underpotential reduction, the applied potential is lower than the salt's decomposition potential, so the electrons are the reductant. The decomposition potential of the salt is defined with the CV measurement before the chronoamperometry. In this study, the electrolyte system was  $\text{Li}_2\text{O}/\text{LiCl}$  (discussion in session 3.3.5), so the salt decomposition potential is the Li deposition potential ( $E_{\text{Li}/\text{Li}^+}$ ), and the potential values reported in this dissertation are versus the  $\text{Li}/\text{Li}^+$  unless otherwise specified. In overpotential reductions, the applied potentials were -0.2 V, -0.3 V and -0.4 V vs.  $\text{Li}/\text{Li}^+$ , and the potential in underpotential reductions was +0.05 V vs.  $\text{Li}/\text{Li}^+$ . In the overpotential reductions, as mentioned above, excess Li metal will slow down the metal oxide reduction, consume extra charge, and erode the elements in the electrolytic cell. Therefore, the overpotential will be applied in a pulsed mode. In the potential setting for the reductions (Fig. 3.2), a continuous potential is applied for 20 min,

followed by a 2 min rest. Then, cycles including 8 min of electrolysis and 2 min off time were repeated, until a desired amount of charge was applied.

The charge applied is also an essential parameter in the electroreduction. It is used in calculating and comparing the reduction efficiency (discussion in session 3.5). The amount of charge is expressed in terms of the theoretical charge to reduce the metal oxides to the metal. It is also an important standard in scaling up the experimental.

### **3.2 Application of Sonication**

Upon successfully demonstrating and measuring the baseline for metal oxide reduction, the sonication was added on to the electrochemical reduction of the metal oxides. The effect of the sonicator probe depth within the cell, the pulse frequency, and vibration amplitude on oxygen diffusion and reduction efficiency were investigated.

The ultrasound parameters under study include the operation mode (the continuous or pulsed mode), time interval of the pulsed mode, power load, and the position relative to the oxide basket. The operation mode is changed and adjusted by setting the timer built in the sonication control box (Fig. 3.3). The timer can be functioned in multiple ways, including a delayed operation, one-shot impulse and cyclic pulsed operating modes. In this study, a continuous mode (no timer setting) was used in testing the durability of the sonication probe, and the pulsed modes (with 20 s and 40 s interval) was used in the electroreduction processes. The maximum power of the equipment was 1500 W, and the ultrasound power supplied to the converter was adjusted from 30% to 80% of the power load by turning a knob at the control box. In this study, the power was applied starting from 30% of the maximum load. The depth of the probe in the salt was around 2~3 cm, and it was almost impossible to place the cathode basket right beneath the probe. So when placing the basket by the side of the probe, the depth of the basket relative to the probe tip was controllable and the effect of the depth on the reduction result were studied.

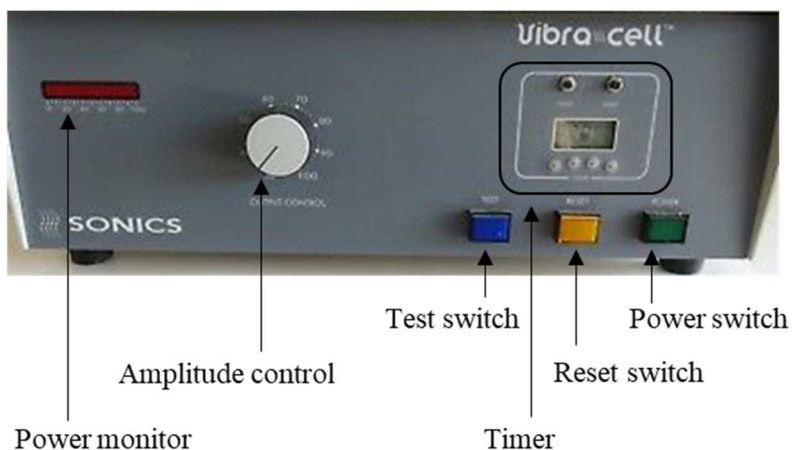


Figure 3.3 Front panel of the ultrasound control box

The sonication setup was tested in the fume hood first, before transferred into the glovebox. In the fume hood, air from the gas supply was directed to the sonication converter for the cooling purpose. A sonication probe of 0.5" in diameter was used in the 1 w.t.%  $\text{Li}_2\text{O}/\text{LiCl}$  molten salt in the continuous mode. After the successful test in the fume hood, the ultrasonic apparatus was transferred into the argon glovebox, excluded the sonication control box. In the glovebox, the test of the sonication was conducted again in the molten lithium salt, with the temperature monitored and time recorded.

When coupled with the electroreduction process, the sonication in a pulsed mode was started at the same time with the electrolysis. The applied ultrasound power was set at 30% of the maximum power load first, and the actual power supplied by the box was displayed on the power monitor (Fig. 3.3). When the power monitor bar showed the maximum load percentage, an overload problem occurred and the ultrasound power was stop automatically. So the sonication equipment was watched all the time during the electrolysis, to guarantee the simultaneous experiment. When the sonication was ceased due to the overload problem, the researcher needed to hit the power switch on the control box (Fig. 3.3) to resume the sonication application. During the ultrasound power supply, the temperature of the molten salt were measured with the thermocouple and thermometer. Temperature data were collected at both the sonication on and off, and electrolysis on and off.

The molten lithium salt was very corrosive and would damage the sonication probe. So, the sonication probe was disassembled, washed with water and acetone and dried outside the glovebox each time after the experiment. The weight of the probes were recorded and the performance during the electrolysis was also documented. So, in preparation for the coupled reduction, the sonication probe with good performance record and less weight loss was picked in priority.



### 3.3 Experimental Setup

In this session, it includes details and challenges in carrying out the electroreduction studies. Problems and solutions to the design of experimental setup are in deep discussion.

#### 3.3.1 A Three-electrode Electrolytic Cell

##### 3.3.1.1 Metal Oxide Precursors

Multiple metal oxides have been tested in the electroreduction studies.  $\text{TiO}_2$  is a widely studied metal oxide in electrochemical reductions, and the reduction process is complicated due to its high oxidized status (+4) and involvement of complicated titanates [5,60]. Furthermore, the commercialization of Ti generation through the electroreduction of  $\text{TiO}_2$  in molten salt is still restricted by the low current efficiency. More attention are to be paid in promoting the process which lowers the cost and reduces hazards emission. On the other hand,  $\text{TiO}_2$  is also treated as a proper surrogate for the  $\text{UO}_2$  studies.[73] The first reason is that Ti in  $\text{TiO}_2$  and U in  $\text{UO}_2$  share the same valence at +4. Second,  $\text{TiO}_2$  has similar electrokinetic properties with  $\text{UO}_2$ , such as the isoelectric point. Therefore, any improvement takes place in the  $\text{TiO}_2$  reduction may be also available in the reduction of  $\text{UO}_2$ , and it will give rise to a closing the nuclear fuel cycle. So, in order to make the work more significant and beneficial in a wider area,  $\text{TiO}_2$  was selected as one of the reduction feeds and the particles were designed to be 0.25~0.85 mm, the similar size with depleted  $\text{UO}_2$  from the spent nuclear fuels.  $\text{TiO}_2$  particles at proper sizes (99.995% metal basis, Alfa Aesar) were readily available from commercial supplies.

Before carrying out the electroreduction of  $\text{TiO}_2$ , reduction tests on a simpler feed is performed to verify the feasibility of the electrolytic cell and methods. Reduction of NiO generates Ni metal through a simple one-step mechanism and the current efficiency can reach 87.2% in molten sodium salts. So, it can be concluded that the electroreduction of NiO is an ideal starting point for the experiment. Therefore, the NiO particles were prepared in a size range of 0.25~0.85 mm, and reduced under the same conditions as that in the  $\text{TiO}_2$  reductions.

NiO particles were pelletized from NiO powder (99.95% metal basis, Alfa Aesar) using a mechanical press, a pellet mold (DI=10 mm), a set of sieves (20 and 60 mesh), and mortar and pestle. The particles were made from the following steps. Fig. 3.4 shows the NiO powder (a) and pellet (b). The color of the NiO particles was greyish yellow.

- 1) A small amount of NiO powder was added to the center of the mold.

- 2) The mold was placed in the chamber of the press. A 5-ton force was loaded on the mold, and held for 3 min.
- 3) The 10 mm-pellet was removed from the mold and broken into smaller particles with the mortar and pestle.
- 4) The next step was to sieve all the particles in the sieves. The larger pieces (in the upper sieve of 20 mesh) were knocked in the mortar and sieved again. The smaller pieces (in the bottom collecting pan) were grinded in the mortar and added to the mold for the next press procedure.
- 5) The last step was to collect the particles left in the bottom sieve (60 mesh) which were the products with targeted sizes of 0.25~0.85 mm.

The bulk densities of the oxide particles were roughly determined by weighing the mass of particles collected with a 10 ml volumetric cylinder. It shows that the bulk densities of  $\text{TiO}_2$  and  $\text{NiO}$  particles were at 1.82 and 1.87  $\text{g cm}^{-3}$ , respectively. With the bulk densities known, the size of the particle holders can be estimated based on the weight of the loads. In order to focus on the kinetics and mechanism of the reduction, the amount of metal oxides was in a small scale that 2 g of particles were loaded for each reduction experiment.



(a)

(b)

Figure 3.4 (a) NiO powder, and (b) NiO particles sizing between 0.25~0.85 mm

### 3.3.1.2 Anode / Crucible

In the electrochemical experiments, a crucible was needed to contain the salts during the process. The liner of the furnace in this study was a graphite drum with 65 mm inner diameter and 140 mm height. However, the graphite liner was coarse and easy to fall powder, so it could not be used as the crucible directly. Restricted by the space in the furnace heating zone, the size of the crucible should

be taller than 140 mm and not exceed 65 mm in diameter. Moreover, the salt used in the studies were to be solidified and collected after each experiment. The solidified salt should be removed easily, and the chosen container should be reusable and wiped clean easily.

In order to fulfil the requirements discussed above, a glassy carbon crucible was selected. The commercially available glassy carbon crucible (HTW Hochtemperatur- Werkstoffe GmbH, Germany. GAZ30) was 150 mm in height, 60 mm outer diameter and the thickness was 3 mm. The inner space of the crucible was only 54 mm diameter, so the electrodes and the sonicator probe needed to be closely packed. This crucible had an extremely smooth surface, so the salt would not attach to the wall while cooling down to room temperature. The glassy carbon was also a dense material which would not drop powder in to the salt.

Another advantage of the glassy carbon crucible was its electronic conductivity and therefore it could be used as the anode in the study. By employing the crucible as the anode, the surface area of the anode was guaranteed to be much larger than that of the cathode. The crucible was also heated during the measurement so it would damage the plastic cover of the cord connecting to the potentiostat. So, a conductive extension clamp was used. It clamped the rim of the glassy carbon crucible and left the other end around 15~20 cm away from the heating zone. Though the free end was not as cool as the room temperature, the heat would not cause damage to the connection cords.

Based on the literature, when the carbon material was used as the anode, carbon could release from the bulk, and the crucible wall became thinner.[23] In this case, after using the crucible in several electrochemical experiments, the inner diameter at the lower crucible gradually became bigger than that at the upper session. This change in the structure would not make big change to the electrochemical result, but might affect the post-treatment of solid salts after reductions. Fig. 3.5 shows the drawings of section views of a new crucible and an old one used for a long time. The grey color was the inner surface, the black is the crucible wall, and the dashed area represents the solidified salts. The salt showed a concave shape and shrank a little bit after it cooled down, so it was easy to pull the salt chunk out from the almost new crucibles. When used for many times, the crucible wall was eroded and became thinner. Though the salt would shrink during the solidification, the size of the salt trunk would be bigger than the original inner size of the crucible. At this point, the salt could not be removed from the crucible at room temperature. So, the crucible needed to be changed every once in a while.

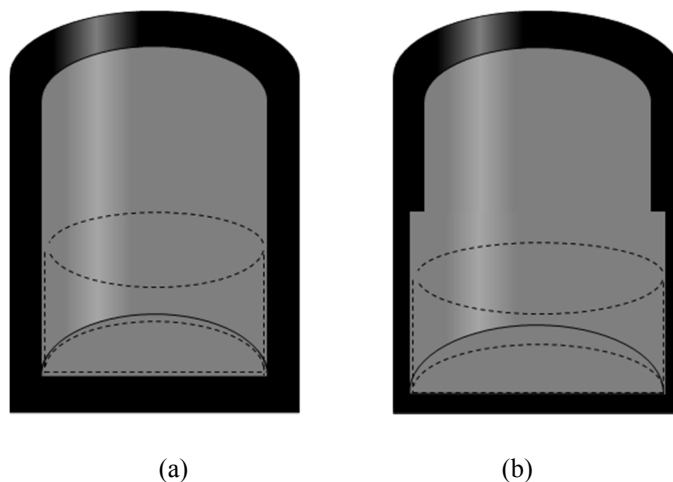


Figure 3.5 Sectional views of a glassy carbon crucible (a) at a new condition, and (b) after used for several times. The dashed lines represent the solidified salt bulk.

### 3.3.1.3 Cathodes and Oxide Baskets

As the electron carrier in the electroreductions, a stainless steel rod was always employed to couple together with a basket. The stainless steel rod was inserted in the oxides bed without touching the bottom of the basket to avoid forming a Faraday cage. A change in dimension of the stainless steel cathode was reported in  $\text{TiO}_2$  reduction in  $\text{Li}_2\text{O}/\text{LiCl}$ . [60] The stainless steel cathode was 3 mm in diameter, and it was enlarged to a 6 mm diameter for the part in the basket. By doing this, the cathode surface had a large contact area with the oxides. Therefore, a large working electrode surface in electroreductions could be achieved by using a stainless steel rod cathode with the diameter of 0.0625" (1.6 mm) which was big enough for the oxide contact but could still fit in the size of the oxide basket.

CV was also measured during the electrochemical study. It was performed to determine the properties of the salt. So during the CV measurement, the electrolysis should not make significant change to the bulk salt. For this purpose, the size of cathode should be relative small compared with that of the anode. The empirical experience in this case was that the surface area for the cathode should not be larger than 1/5 of that for the anode. So, in the CV measurements, the cathode was a stainless steel wire with a diameter of 0.25" (0.6 mm).

In literatures, there are many methods to hold the metal oxides. Researchers wounded the oxide pellet with metal cathode wire [21] or load the oxides at the bottom of the cell or on a spoon [7]. In the pyroprocessing for the LWR spent fuel, it was suggested that the mash basket worked well with molten salt system, for the advantages of high  $\text{Li}_2\text{O}$  mass transfer through hole on the basket wall. [49] So, in

this study, a basket made with economically affordable stainless steel mesh was used as the metal oxides holder. In order to contain 2 g of metal oxides whose bulk densities were  $1.8\sim 1.9\text{ g cm}^{-3}$ , the minimum volume for the basket was  $1.1\text{ cm}^3$ .

The basket was carefully designed taking account the limited space in the glassy carbon crucible, and the volume required for the metal oxide particles and the thick working electrode. A cylindrical shape basket was used in pyroprocessing, so it was also selected as the general shape of the basket in this study. The dimension of the basket was determined as 10 mm in diameter and 25.4 mm height. The inner volume of the basket was around  $1.25\text{ cm}^3$ , covering the space for the oxide particles and the electrode, and around 10% free space. In order to firmly hold the particles while allow mass transfer through the basket wall, two layers of stainless steel cloth at 100 mesh were employed as the basket wall. For the basket bottom, a single layer of 200 mesh stainless steel cloth in a star shape was clipped by the double layer mesh wall. Then the whole basket was wrapped with the 0.032" (0.8 mm) stainless steel wire to maintain the shape and attach to the cathode. To avoid any damage to the 200 mesh bottom while weaving the net around the basket, a 10 mm circle 100 mesh stainless steel cloth was inserted between the 200 mesh cloth and the weaved bottom. A wrap with thin stainless steel wire surrounding the outer 100 mesh would help to maintain the shape of the basket wall while weaving the net around the mesh layers. The center cathode wire was wrapped with an  $\text{Al}_2\text{O}_3$  tube to prevent any electronic contact with the basket or other conductive solids in the cell. The configuration of the cathode was displayed in Fig. 3.6 (a), and a picture of the basket was presented in Fig. 3.6 (b).

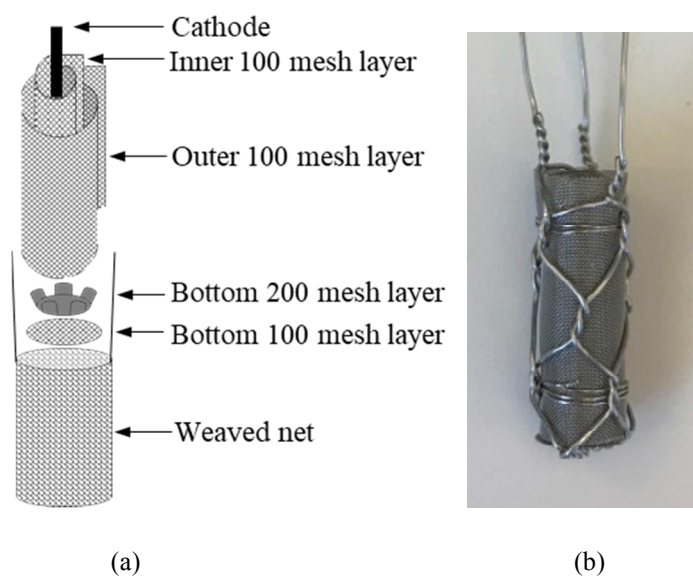


Figure 3.6 (a) configuration, and (b) a picture of the cathode oxide basket

#### 3.3.1.4 Reference Electrode

The reference electrode (RE) is an essential component in the electrochemical studies, especially for the studies focusing on the working electrode. A three-electrode electrolysis cell was built in this study to realize the accurately cathodic potential control. In this project, two types of reference electrodes were tested, the pseudo-reference electrode (such as glassy carbon, tungsten and molybdenum) and unsealed true reference electrode (Ni/NiO reference electrode). The pseudo-reference electrode included the glassy carbon, molybdenum, and tungsten, and the unsealed true reference electrode was the Ni/NiO electrode.

The configuration of the electrodes were shown in Fig. 3.7. The pseudo-reference electrodes were made by inserting each bare rod or wire in an  $\text{Al}_2\text{O}_3$  tube covering the middle part of the tube, to avoid contact with other solid elements in the cell. The  $\text{Al}_2\text{O}_3$  tube was above the liquid salt level. The NiO/NiO electrode was fabricated with a Ni wire, NiO powder and a porous-end MgO tube through several steps.

- 1) Mark a line at 1 inch above the tip at the outside of the MgO tube. The electrode would be immersed in the liquid salt for 1 inch depth, so the NiO was filled to be at the same level of the liquid salt.
- 2) Insert the Ni wire into the tube. The NiO wire touched the inner bottom of the tube and a length of 2~3 inches was left outside the MgO sheath for the potentiostat connection.
- 3) Use a flashlight to see the inside of the tube. The dense MgO wall was partially transparent under the strong light from the flashlight. By looking through the tube, it was easy to find the position of the porous plug.
- 4) Add NiO powder into the tube with a funnel. Add a little amount of NiO powder each time, and check the level of the powder filled with the flashlight. If the loose powder was stuck, gently knock the tube or stir with the NiO wire.
- 5) Gently pat the bottom of the tube. Use the flashlight to make sure the NiO reach to the 1 inch line. Wipe off the marked line.
- 6) Bake the prepared Ni/NiO electrode on a heating plate at 120 °C for 6 h.
- 7) Transfer the electrode to the glovebox. Slowly increase and decrease the pressure in the transfer chamber. Let the electrode stay overnight in the chamber to guarantee the removal of air.

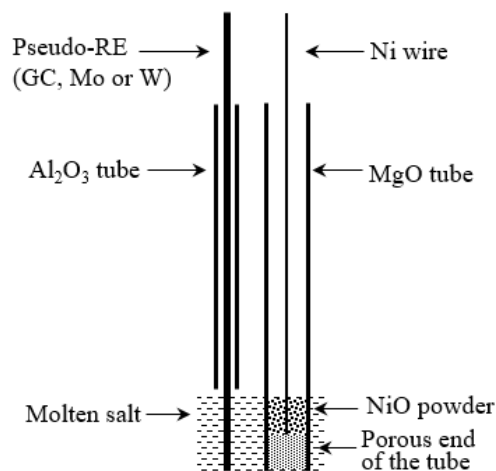


Figure 3.7 Sketch of the assembly of the reference electrodes.

In the electrochemical studies, the pseudo reference electrodes and the Ni/NiO electrode were kept in molten salts for 1~1.5 h before any measurement to reach a thermal stability. Meanwhile, for the Ni/NiO electrode, it also required that period of time to establish an equilibrium among Ni between NiO in the salt.

### 3.3.1.5 Electrolyte Selection

CaO/CaCl<sub>2</sub> and Li<sub>2</sub>O/LiCl were the mostly used electrolyte systems in metal oxide reductions. The operation temperature for the calcium salts was around 850~950 °C, which is much higher than that for the lithium molten salt at 650 °C. On the other hand, the Li<sub>2</sub>O/LiCl was the liquid mediate in the pyroprocessing, and it was one of the goal of this project to promote the spent fuel cycle by doing research on the surrogate TiO<sub>2</sub>. So, the electrolyte for the NiO and TiO<sub>2</sub> reduction in this project was 1 w.t.% Li<sub>2</sub>O/LiCl.

Around 150 g of LiCl was used in each batch of experiment, taking into the account of sizes of sonication probe and electrodes, and the room in the crucible. The density of LiCl was reported at certain temperatures. The densities are 1.4898 and 1.4821 g cm<sup>-3</sup> at 638.6 °C and 655.9 °C, respectively.[74] The density of LiCl melt at 650 °C is not in the literature but it can be determined through the following equation (Eq. 3.1)[75].

$$\rho_T = \rho_m - k(T - T_m) \text{ (Eq. 3.1)}$$

where  $\rho_T$  is the density at temperature  $T$ ,  $\rho_m$  is the density at the melting point  $T_m$ , and  $k$  is a temperature difference related coefficient which is 0.000432 K<sup>-1</sup> for LiCl. The melting point of LiCl is

610 °C and the density at the melting temperature is 1.502 g cm<sup>-3</sup>. This equation is valid at the temperature below 781 °C. After the calculation, the density of LiCl is 1.4847 g cm<sup>-3</sup> at 650 °C, which falls between 1.4898 and 1.4821 g cm<sup>-3</sup> at a temperature range of 638.6 °C and 655.9 °C. So, in this study, 150 g of LiCl was used as the main component of the salt melt, and the volume was around 101.03 ml. Therefore, 30% of the crucible was filled with LiCl, and the liquid salt level in crucible was 44.11 mm height.

Fundamental studies about the salts were also carried out in LiCl salt and Li<sub>2</sub>O/LiCl mixtures. In the electroreductions, oxygen ions were extracted and transferred to the environment. So, the effect of oxygen concentration on the properties of salt mixtures was interested. To get a better understanding of the system, Li<sub>2</sub>O was added to the LiCl to prepare salt mixtures with Li<sub>2</sub>O concentration at 0.25, 0.5, 0.75, 1, 2, and 4 w.t.%. Table 3.1 listed the amount of LiCl and Li<sub>2</sub>O used under each condition regarding the Li<sub>2</sub>O concentration.

Table 3.1 Table of Li<sub>2</sub>O/LiCl salt compositions

Composition (w.t.% of Li <sub>2</sub> O in LiCl)	0.00	0.25	0.5	0.75	1.00	2.00	4.00
Weight of LiCl (g)	150	150	150	150	150	150	150
Weight of Li <sub>2</sub> O (g)	0.00	0.38	0.75	1.13	1.52	3.06	6.25

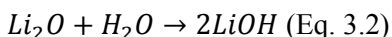
The operation temperature for the experiments was at 650 °C which was the temperature at the molten salt. Heat provided by the furnace could not be 100% efficiently transferred to the salt. So, a calibration step was necessary to find the proper working temperature for the furnace to maintain the temperature of the salt at 650 °C. A thermocouple (Omega, TJ36-CAXL-116G-18) and a thermometer (Fluke 177 True RMS Digital Multimeter) were coupled to measure the salt temperature to find the correct setting point of the furnace. The thermocouple was hung above the crucible and the measuring tip was suspended in the salt without touching the crucible wall. It was found that when the setting temperature of the furnace was at 684 °C, the salt could be stabilized at 650 °C.

### 3.3.1.6 Reduction Atmosphere Control

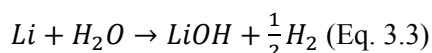
The electroreduction experiment is very sensitive to the environment including the moisture level and the oxygen concentration.



LiCl salt strongly adsorbs moisture. Furthermore, Li<sub>2</sub>O, as the key component in the LiCl solvent, is easy to react with water in the environment (Eq. 3.2). Li<sub>2</sub>O concentration in the melt was proved to have impact on the reduction performance, so it was added at 1 w.t.% initially. However, when water is in the surrounding, it combines with partial of Li<sub>2</sub>O to form LiOH. So, the Li<sub>2</sub>O concentration in the LiCl is out of control, and it makes the experiment less repeatable and reliable.



Moreover, in the overpotential reductions, Li metal will be generated and consumed as the reductive agent. However, at the contact of Li metal and water, typical reaction between alkalis and water takes place (Eq. 3.3). Generation of H<sub>2</sub> makes the mechanism more complicated and almost out of experimental control. It is because the amount of H<sub>2</sub> generated is hard to estimate and its effect on the metal oxide reduction cannot be determined.



In the case of water, LiOH will be produced and distributed in the electrolyte. Both Li<sup>+</sup> and OH<sup>-</sup> have potentials to be reduced at the cathode, but the preference of possible cathode half-reaction depends on the reaction potential. Table 3.2 listed the relative reaction potentials (standard potentials at 25 °C in aqueous solutions), including metal ion reductions, impurity reactions and water electrolysis. Potentials in the table are not under the condition of the molten salt reactions, but they provide clues in basic analysis and comparison. The reduction of Li<sup>+</sup> ion and Ca<sup>2+</sup> ion requires much higher potentials compared with that of water electrolysis. So, in the electrochemical aspect, moisture at the cathode will be reduced first when increasing the reduction potential. When water is decomposed, it also generate OH<sup>-</sup>. On the anode, OH<sup>-</sup>, from chemical reaction and water electrolysis, is oxidized to water and O<sub>2</sub>. At this point, the system becomes more complicated and more uncontrollable parameter involved.

Table 3.2 Standard electrode potentials in aqueous solution at 25 °C

Cathode Half-reaction	Standard potential E <sup>0</sup> (V) vs. NHE
$Li^+ + e^- \rightarrow Li$	-3.04
$Ca^{2+} + 2e^- \rightarrow Ca$	-2.76
$2H_2O + 2e^- \rightarrow H_2 + 2OH^-$	-0.83
$4OH^- \rightarrow 2H_2O + O_2 + 4e^-$	0.40

When O<sub>2</sub> is in the gas above the liquid salt, due to the equilibrium of the O<sub>2</sub> concentration between in the liquid and in the gas phase, it prohibits the O<sub>2</sub> in the molten salt to vaporize and evolve

from the liquid. On the other hand,  $O_2$  can dissolve in the salt melt and slow down or stop the oxygen extraction from the metal oxides or intermediates. Furthermore, the dissolved  $O_2$  around the cathode has potential to re-oxidize the active metal back to the oxidation status.

In conclusion, the moisture can introduce side reactions and by-product, which consumes necessary compound for the reduction and lowers down the efficiency. Also, the oxygen in the atmosphere prohibits the release of oxygen from the salt, and may re-oxidize the metal product when it dissolves in the electrolyte.

The concerns of the moisture and oxygen level were also taken in literatures. In the pyroprocessing, the reductions were carried out in an argon room. Non-radioactive metal oxide reductions were usually performed in a smaller scale. The electroreduction of  $TiO_2$  in molten  $CaCl_2$  was conducted in a sealed cylinder with Ar flowing during the experiment. But it is not applicable to seal the sonication probe inside a chamber leaving the converter at the outside. In this study, an argon glove box (MBraun Labmaster 200G) is used to provide inert atmosphere. The oxygen and moisture level are monitored and controlled at below 5 ppm.

### 3.3.2 Sonication Apparatus

This work marks the first use of sonication in the capacity of electrolytic reduction in high temperature molten salts. The sonication setup will be tested in the fume hood first and then transferred into the glovebox. The configuration of the cell is designed and shown in Fig. 3.8.

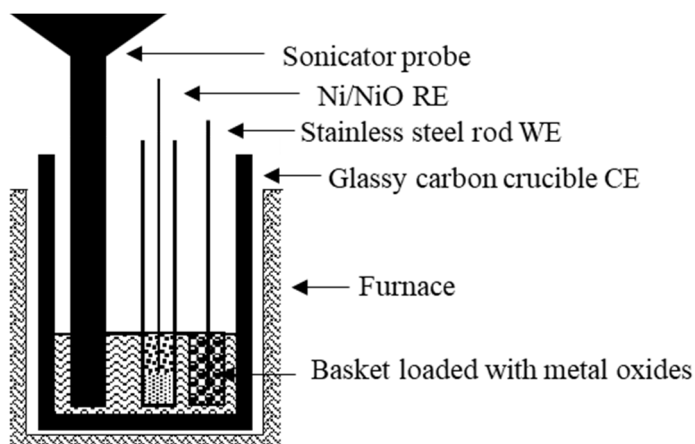


Figure 3.8 Sketch of the cell including the electrolytic reduction and sonication

There are challenges in coupling the ultrasound with the electrolytic reduction. One of the challenges is the high temperature working environment. The molten salt will be heated and kept at

650°C, which is much higher than the general operation range of the ultrasound equipment. The common sonicator probe is designed for sonication in water mediate at ordinary temperatures, so special probes are customized. The second challenge is about the heat tolerance of sonication converter. Other than the probe, the general sonication converter is also design for room temperature use, but the heat from molten salt will be eventually transferred to the convertor which will cause the sonicator stop working due to the overload problem. Therefore, a coolant system will be a solution in cooling down the converter. Third, the whole sonicator setup includes a control box and a sonicator probe. The control box is located outside of the glovebox while the convertor and probe are in the glovebox. The cable needs to be installed to connect the part inside and outside the glovebox. The only way is to build the cable in a feedthrough located at the back ports of the glovebox. The forth change is the movement of the sonication probe. During the reductions, the sonication probe needs to accurately merge in the molten salt, stay at the position and lift up after the experiment. The sonication apparatus is heavy and the surface becomes very hot after held in the salt for several hours. So, a tool or an equipment is required to hold the sonication convertor and control its movement.

Solutions are found and tested to solve the problem discussed above. Customized sonication probes are made for use in the high temperature and high corrosion environment. The probe is made of titanium alloy which is corrosion resistant in extreme environment. Two sizes of probes will be tested, 0.5" (1.27 cm) and 0.75" (1.91 cm) in diameters. Probe larger than 0.75" will be hard to fit in the crucible with electrodes. A modified KF40 feedthrough was fabricated by drilling a hole at the center of the part, letting the cable pass through, and finally sealing gap with a special material from the manufacture. To solve the problem of the high temperature at the sonication converter, an air-cool system was built. The coolant gas lines connected the air cylinder (Airgas, UHP-Air) to the gas ports at the back of the glovebox. Inside the glovebox, two gas pipes are under control by individual valves. Clear hoses connect the inlet gas valve to one of the sonication converter gas port, and the outlet gas from the sonication converter is lead to the outlet gas valve which is connected with ventilation system of the lab. So, there is a light vacuum inside the gas line, and in consequence, coolant air will not escape from the pipe and mix with argon in the glove. The pressure of the dry air was around 15~20 psig and the flow rate was controlled at 100 ml/min. An actuator with a heavy base is employed to hold and control the movement of the sonication converter. By pressing buttons on a remote controller, the elongation and contraction of the vertical actuator arm can lift the sonication probe up and down.

### 3.4 Characterization of Reduced Products and Used Salts

After reductions, products and salts are cooled down to room temperature inside the argon glovebox. Reduced samples are merged in frozen salt as a bulk in the fuel basket. So reduced products need to be separated from the salt and post-treated for further analysis such as X-ray Diffraction (XRD) and Thermogravimetric Analysis (TGA). Used salt samples will be knocked off from the bulk and analyzed with Inductively Coupled Plasma Mass Spectrometry (ICP-MS) to study the changes caused by reductions.

#### 3.4.1 Reduced Sample Treatment and Used Salt Sampling

The product was immersed with the solid lithium salt when it was cooled to room temperature. To minimize the operation process, the oxide basket was cut off from the electrode bundle and the stainless steel rod working electrode was also cut into two pieces. After the basket was transferred out from the glovebox, it was treated through the following steps to be prepared for the X-ray Diffraction and Thermogravimetric Analysis. Samples were dried at room temperature, in order not to re-oxidize the reduced products through heating methods.

- 1) Soak the product basket in the nano-pore water in a 100 ml beaker for 30 min.
- 2) Pour the loose particles on a piece of filter paper in the liquid-solid separation system consisting of the Buchner funnel and filter flask. Connect the side opening to the vacuum.
- 3) Rinse the particles with wash bottles filled with nano-pore water and acetone.
- 4) Turn off the vacuum, and transfer the particles and filter paper to a flat aluminum plate.
- 5) Put the aluminum plate in a vacuum drying chamber.
- 6) Gently turn on the vacuum valve. When the chamber became vacuum, close the ports of the chamber and turn off the vacuum.
- 7) After overnight of vacuum drying, gently open the pressure valve and take the aluminum plate out.
- 8) Ground the dried products in the mortar and pestle to fine powders.
- 9) Storage the fine powders in sealed bags. Keep the bags in the glovebox.

The salt samples were taken after the salt was solidified at room temperature in the argon glove box. The solid salt could be easily slide out from the crucible. Both the top and the bottom of the salt bulk were knocked with a clean metal file, and the dropped materials were collected and storage in sealed bags. All the operations were conducted in the argon glovebox, and the sample bags were kept in the glovebox before transferred out for the ICP-MS analysis.

### 3.4.2 XRD Analysis of Reduced Products

Products after NiO and TiO<sub>2</sub> electroreductions were post-treated into fine powders for the XRD analysis for the phase identification and composition analysis.

The equipment used in this study was the Rigaku SmartLab X-ray Diffractometer. Copper was employed as the anode and the filter was the  $\beta$  filter. So, the incident beam was the Cu K $\alpha$  radiation, owning a wavelength of 1.54 Å. Table 3.3 listed the XRD parameters used in the sample phase identification.

Table 3.3 XRD setting parameters

Parameters	Settings
Detector	Bragg-Brentano (BB)
LL	15 mm
IS	2/3 Degree
RS1	2/3 mm
RS2	20 mm
Range	10~80 degree
Step	0.04 degree
Speed	4 degree min <sup>-1</sup>
Voltage	40 kV
Current	30 mA

Samples without washing were also tried to analyze with XRD. However, it was found that the mixed salt strongly adsorbed the moisture in the air and the sample became a solution on the glass sample plate. At the meanwhile, in the XRD results, the salt, as the major component, showed wide peaks with high intensities, which covered smaller peaks from the reaction products (not shown in this dissertation). So, the XRD results presented were all from washed samples. Though the washed products were free from lithium salts, the fine powder still potentially adsorbed moisture. Therefore, the operations during the XRD analysis were conducted as quickly as possible, including transferring the samples and preparing the glass sample plates. The samples after the XRD analysis could be either discarded, or recycled in separated containers.

### 3.4.3 TGA Analysis of Reduced Products

The products of NiO electroreductions were analyzed with the TGA for the reduced product oxygen level measurement. A TGA/DSC3+ model from the Mettler Toledo was used for the analysis. The balance in the TGA had a high resolution of 0.1/1  $\mu\text{g}$ .

The theory of the TGA analysis was that, by oxidizing the reduced sample, the metal component was oxidized to the oxide and the weight gain during the process was due to the combined oxygen. Then by comparing the weight gain and the original mass the sample, the composition of the metal component could be calculated and the oxygen level of the loaded sample was determined. In the operation, a small amount of reduced sample was loaded in the alumina crucible without a cover. The sample was then oxidized in the oxygen atmosphere at a high temperature until the weigh was no longer changed.

In this study, 10.454 mg of reduced Ni product in fine powder was loaded in an alumina crucible without a lid. An empty crucible was also placed on the weighing bar as the reference of the heat flux. The process of taking and loading sample before heating should also be done quickly. Because the fine powder adsorbed moisture and any weight fluctuation would heavily influenced the accuracy of the measurements. Dry air flew through the pipeline to the TGA furnace to create an oxidative environment, and the air flow rate was at 20 ml  $\text{min}^{-1}$  in the entire measurement. Temperature of the furnace was programmed in three stages as shown in Fig. 3.9. Starting from the room temperature (25  $^{\circ}\text{C}$ ), the temperature was first slowly ramped to 500  $^{\circ}\text{C}$  at 10  $^{\circ}\text{C min}^{-1}$ . On the second heating stage, the temperature was quickly increased to 1150  $^{\circ}\text{C}$  at a heating rate of 50  $^{\circ}\text{C min}^{-1}$ . The temperature was held at 1150  $^{\circ}\text{C}$  for the rest of the experiment.

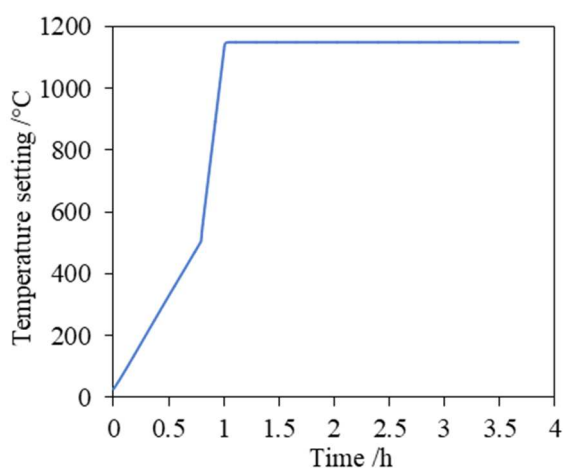


Figure 3.9 Temperature setting for the TGA analysis

#### 3.4.4 ICP-MS Analysis of Used Salts

The ICP-MS was conducted with the Agilent 7900 Inductively Coupled Plasma – Mass Spectrometer. It was used to define and measure the metal composition of the salts after the electro-reductions. The salt samples were sealed in sample bags to avoid the contact with moisture before analysis. In the ICP-MS sample preparation, materials were dissolved in acidic solution in the testing tubes. The samples were prepared through the following steps.

- 1) Measure the weight of empty testing tube.
- 2) Weigh around 0.1 g sample in the testing tube. As mentioned before, the salt easily adsorbed the moisture in the air. So in order to get the accurate weight of salt sample, this step was finished as quickly as possible.
- 3) Add 3 ml concentrated  $\text{HNO}_3$  (5%) to the testing tube. Wait 30 min.
- 4) Add 3 ml concentrated  $\text{HCl}$  (5%) to the tube. Wait overnight for a thorough dissolution.
- 5) Add nano-pore water to the tube to a 50 ml of total volume.
- 6) Transfer 10 ml of acidic solution to the sample tube for the equipment analysis.

In the analysis of the acid-digested samples, Li, Ni and Ti were the targeted elements. Calibration lines for each element were generated by measuring the standard solutions. The calibration lines covered a certain range of element concentrations. During the sample analysis, if the measured concentration was higher than the maximum concentration of the calibration lines, the sample needed to be diluted to fit in the calibration concentration range. The data collected from the measurement were in the unit of  $\mu\text{g/L}$ . When utilizing these data, the calculation should consider the dilution procedure during the measurements.

## Chapter 4: Investigation on Reference Electrodes in Molten Li<sub>2</sub>O/LiCl

### 4.1 Abstract

Glassy carbon (GC), tungsten (W), molybdenum (Mo) and Ni/NiO reference electrodes were explored for cyclic voltammetry measurements in molten lithium salts at 650 °C. CVs were performed at 20 mV s<sup>-1</sup> in LiCl with Li<sub>2</sub>O concentrations at 0, 0.25, 0.5, 0.75, 1, 2 and 4 w.t.%. The Ni/NiO reference electrode showed a consistent Li deposition potential at different Li<sub>2</sub>O concentrations. However, by using GC, W, and Mo reference electrodes, decreases in lithium deposition potential in Li<sub>2</sub>O/LiCl molten salt with increasing Li<sub>2</sub>O concentrations were observed. Correlations of electrode potentials of all the electrode potentials were defined in both pure LiCl and 1 w.t.% Li<sub>2</sub>O/LiCl.

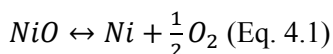
### 4.2 Introduction

High temperature molten salts electrochemistry has been extensively investigated for pyroprocessing for spent nuclear fuel treatments [46,49,76], and Fray-Farthing-Chen (FFC) and Ono-Suzuki (OS) processes for metal productions [25,59,65,71,72,77–79]. Among the elements in an electrolytic cell, the reference electrode (RE) is essential for monitoring and controlling the performances of the systems while remains stable under the high temperature corrosive molten salt environment.[80]

Various reference electrodes have been used in electrochemical measurements in molten lithium salts, including pseudo-reference electrodes such as molybdenum [69], platinum [81], tungsten [82], and carbon [39,83,84], and the unsealed true reference electrode [85] Li-Pb alloy [54,60,86], Li-Bi alloy [70], and Ni/NiO [46,49,62,87]. Molybdenum wire was used as a pseudo-RE to determine Li/Li<sup>+</sup> redox potential using CV in Li<sub>2</sub>O/LiCl molten salt systems at 650 °C.[69] The Li/Li<sup>+</sup> redox potential changed with Li<sub>2</sub>O concentration, decreasing from -1.9 V in pure LiCl to -1.2 V vs. Mo in 1 w.t.% Li<sub>2</sub>O/LiCl. At 665 °C, Li/Li<sup>+</sup> potential was at -1.24 V vs. Mo in 2 w.t.% Li<sub>2</sub>O/LiCl. In the same system of 2 w.t.% Li<sub>2</sub>O/LiCl, OH<sup>-</sup> decomposition potential was determined at -0.6 V vs Mo. When the platinum wire was used as RE, Li/Li<sup>+</sup> redox potential was -1.82 V, and the reduction potentials of U<sup>5.33+</sup> was -1.40 V vs. Pt in 3 w.t.% Li<sub>2</sub>O/LiCl at 650 °C.[81] The tungsten reference electrode was used in CV measurements in 1 w.t.% EuF<sub>3</sub>/LiF-NaF-KF molten salt on a gold working electrode.[82] It showed that potassium was deposited at -1.3 V, Au<sub>2</sub>Na alloy appeared at -0.8 V, and Eu<sup>3+</sup> was reduced to Eu<sup>2+</sup> at -0.3 V vs. W. The deposition of lithium was not observed even when the cathodic potential reached -1.4 V vs. W. Glassy carbon was employed as the reference electrode in 1.2 mol% Ni<sub>2</sub>F/FLiBe melts,



and the open circuit potential (OCP) were measured at 340 mV, 322 mV and 307 mV vs. GC at 500 °C, 525 °C and 550 °C, respectively.[83] In ferrocene (0.05 M) / Et<sub>4</sub>NBF<sub>4</sub> (1 M) / AN, CV measurements were taken with an active carbon (AC) reference electrode at 50 mV/s at room temperature, and the E<sub>1/2</sub> of Fc/Fc<sup>+</sup> was determined at 0.2 V vs. AC.[84] A graphite reference electrode was used in the electroreduction of chromium oxides in molten 2 mol% CaO/CaCl<sub>2</sub>. [39] The Ca/Ca<sup>2+</sup> potential was determined at around -1.35 V vs. graphite, and the electrochemical reduction of Cr<sub>2</sub>O<sub>3</sub> to Cr metal could be achieved by applying -1.0 V vs. graphite. Complex metal alloy REs were used in the electrolytic reductions of metal oxides, such as titanium oxides and uranium oxides in Li<sub>2</sub>O/LiCl salts.[54,60,70,86] The Li/Li<sup>+</sup> redox potential was -0.63 V vs. Li-Pb (32 mol% of Li) for both pure LiCl and 1 w.t.% Li<sub>2</sub>O/LiCl at 650 °C.[86] TiO<sub>2</sub> was reduced to lithium titanates at +0.3 V vs. Li-Pb and lithium titanates were reduced to titanium metal at -0.2 V vs. Li-Pb.[60] UO<sub>2</sub> was reduced at -0.6 V vs. Li-Pb in 1 w.t.% Li<sub>2</sub>O/LiCl at 650 °C.[86] With a Li-Bi RE, the Li<sup>+</sup> reduction potential was -0.76 V and potentials for the formation of Li<sub>2</sub>PtO<sub>3</sub>, O<sub>2</sub> evolution, Pt dissolution and Cl<sub>2</sub> emission were 1.84 V, 2.04 V, 2.44 V and 2.74 V vs. Li-Bi, respectively, in 0.13 mol% Li<sub>2</sub>O/LiCl at 650 °C.[70] The reduction potential of UO<sub>2</sub> was -0.9 V vs. Li-Bi in 1 w.t.% Li<sub>2</sub>O/LiCl at 650 °C.[70] Ni/NiO RE has been extensively used in electrolytic reductions of metal oxides. Different from pseudo REs, a redox equilibrium (Eq. 4.1) is established within the Ni/NiO electrode and enhances its stability in the molten salts especially for systems containing O<sup>2-</sup> ions. The redox potentials for Li/Li<sup>+</sup> were determined as -1.95 V, -1.90 V, -1.85 V, -1.78 V and -1.75 V vs. Ni/NiO in LiCl with Li<sub>2</sub>O concentrations at 0, 0.25, 0.5, 0.75 and 1 w.t.% at 650 °C, respectively.[46,49] Similar values for E<sub>Li/Li<sup>+</sup></sub> were reported in 1 w.t.% Li<sub>2</sub>O/LiCl by other researchers.[62,87] U<sub>3</sub>O<sub>8</sub> was reduced to UO<sub>2</sub> at -1.45 V and then reduced to U metal at -1.62 V vs. Ni/NiO.[49] On the Pt anode, O<sub>2</sub> evolution potential was at 0.75 V vs. Ni/NiO in 0.75 w.t.% and 1 w.t.% Li<sub>2</sub>O/LiCl.[46] And the Pt anode dissolved at 1.4 V and 1.65 V vs. Ni/NiO in 0.25 w.t.% and 0.5 w.t.% Li<sub>2</sub>O/LiCl, respectively.[49]



In literatures, key results such as the Li deposition potentials obtained using different REs varied significantly and made it challenging to compare and understand similar measurements in different studies (Table 4.1). Therefore, this study will investigate the inherent consistency of electrochemical measurements by having our own sets of CV data measured at 650 °C in Li<sub>2</sub>O/LiCl molten salts. Subsequently, these experimentally determined data can be used to unify and compare potentials measured at various conditions using different REs. In this study, a glassy carbon rod, a tungsten wire, a molybdenum wire, and two Ni/NiO electrodes will be used as REs for CVs

measurements. Li deposition potentials and anodic reaction potentials will be determined and reported using these REs in LiCl with Li<sub>2</sub>O concentrations from 0 to 4 w.t.% at 650 °C.

Table 4.1 Summary of  $E_{Li/Li^+}$  using various reference electrodes in molten Li<sub>2</sub>O/LiCl salts

Reference electrode	Electrolyte	Temperature	$E_{Li/Li^+}$	Reference
Mo	LiCl	650 °C	-1.9 V	[69]
	1 w.t.% Li <sub>2</sub> O/LiCl	650 °C	-1.2 V	[69]
	2 w.t.% Li <sub>2</sub> O/LiCl	665 °C	-1.24 V	[69]
Pt	3 w.t.% Li <sub>2</sub> O/LiCl	650 °C	-1.82 V	[81]
Li-Pb	LiCl	650 °C	-0.63 V	[86]
	1 w.t.% Li <sub>2</sub> O/LiCl	650 °C	-0.63 V	[60,86]
Li-Bi	0.13 mol% Li <sub>2</sub> O/LiCl	650 °C	-0.76 V	[70]
Ni/NiO	LiCl	650 °C	-1.95 V	[46,49]
	LiCl	900 °C	-1.90 V	[62]
	0.25 w.t.% Li <sub>2</sub> O/LiCl	650 °C	-1.90 V	[46,49]
	0.50 w.t.% Li <sub>2</sub> O/LiCl	650 °C	-1.85 V	[46,49]
	0.75 w.t.% Li <sub>2</sub> O/LiCl	650 °C	-1.78 V	[46,49]
	1 w.t.% Li <sub>2</sub> O/LiCl	650 °C	-1.75 V	[46,49,87]

### 4.3 Experimental

High purity lithium chloride (LiCl, 99.995% metals basis, ultra-dry, Alfa Aesar) and lithium oxide (Li<sub>2</sub>O, 99.5%, Alfa Aesar) were used to prepare the molten salts. The chemicals were used as received. A glassy carbon rod (3.2 mm diameter), a tungsten wire (0.8 mm diameter), a molybdenum wire (0.8 mm diameter), a stainless steel wire (0.64 mm diameter), a platinum rod (1.0 mm diameter), a nickel wire (0.4 mm diameter) and NiO (99.95% metals basis, Alfa Aesar) were employed to fabricate the electrodes. Al<sub>2</sub>O<sub>3</sub> tubes (McMaster-Carr) were taken as insulator covers, and MgO tubes with one porous end (Ozark Technical Ceramics, Inc., 3.2 mm ID) were involved in preparing the Ni/NiO reference electrodes. A glassy carbon crucible (HTW, GAZ30; height = 150 mm, outer diameter = 60 mm, and thickness = 3 mm) was the container for the salts.

The electrochemical measurements were carried out with a three-electrode electrochemical cell. A nickel wire spiral worked as the counter electrode. The working electrode was a stainless steel wire and a platinum wire for cathodic and anodic studies, respectively. The reference electrodes included a glassy carbon rod, a tungsten wire, a molybdenum wire, and two Ni/NiO electrodes. The Ni/NiO reference electrodes were fabricated by adding NiO powder to the MgO tube, and then a nickel

wire was inserted in the NiO bed. For the Ni/NiO (1) electrode, NiO powder was added to the MgO tube and the height of NiO inside the tube was 1 inch above the bottom of the MgO tube. And for the Ni/NiO (2) electrode, NiO powder was added to the MgO tube and the height of NiO inside the tube was 2 inch above the MgO tube bottom. The NiO powder was dropped into the tube but not tightly packed. Al<sub>2</sub>O<sub>3</sub> tubes were used to cover each bare wire or rod, and the tubes were more than 1 inch above the electrode tips. All the electrodes were bound together with the bottom ends aligned. (Fig. 4.1) Heat was provided with a Kerrlab electric furnace (Auto Electro Melt Maxi) to maintain the salt temperature at 650 °C during the experiments. A VersaSTAT 4 potentiostat (Princeton Applied Research) coupled with the VersaStudio software was used to control the measurements and collect data.

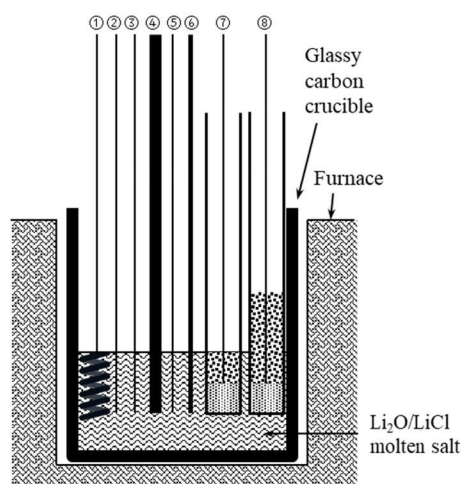


Figure 4.1 Experimental setup for CV measurements. 1: Ni spiral counter electrode. 2: S.S. working electrode for cathodic CVs. 3: Pt wire working electrode for anodic CVs. 4: GC rod reference electrode. 5: W wire reference electrode. 6: Mo wire reference electrode. 7: Ni/NiO (1) reference electrode. 8: Ni/NiO (2) reference electrode

Cyclic voltammograms were measured in LiCl and varying concentrations of Li<sub>2</sub>O in LiCl at 650 °C. Before CV measurements, the electrode bundle was immersed in the melt at 1 inch depth and hold at 650 °C for 2 hours to reach stability. CV measurements were taken in 150 g pure LiCl first. Then, Li<sub>2</sub>O was gradually added in the crucible after the salt from the previous measurement was solidified at the room temperature. CV measurements were taken using the same electrode bundle with Li<sub>2</sub>O concentrations at 0.25, 0.50, 0.75, 1.00, 2.00, and 4.00 w.t.%. CVs were performed at a scan rate of 20 mV/s starting from the open circuit potential. Ni/NiO reference electrodes were employed in both cathodic and anodic scans, and other reference electrodes were used in cathodic scans only. Each CV curve was measured at least twice to guarantee the reproductibility, and data curve that could not be

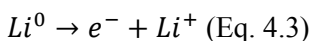
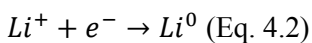
repeated was not presented. All the heating and electrolysis were carried out in a glovebox with argon atmosphere ( $\text{H}_2\text{O}$  and  $\text{O}_2 < 1$  ppm).

## 4.4 Results and Discussion

### 4.4.1 Correlation among Different Reference Electrodes

The correlation among reference electrodes was based on the Li deposition potentials in  $\text{Li}_2\text{O}/\text{LiCl}$  achieved in CV measurements.

Cathodic cyclic voltammograms measurements with the Ni/NiO were displayed in Fig. 4.2. The reduction and oxidation CV peaks were assigned for Li deposition (Eq. 4.2) and stripping (Eq. 4.3), respectively. Since there was no concentration limitation of  $\text{Li}^+$  in electrolyte, the  $\text{Li}^+$  reduction peaks were very sharp. However, in the backward scans, there was a mass limit of metallic Li on the cathode, so the  $\text{Li}^0$  re-oxidation peaks were wide. Cathodic CV measurements with the Ni/NiO (1) reference electrode in pure LiCl, and 0.25 w.t.% to 4.00 w.t.%  $\text{Li}_2\text{O}/\text{LiCl}$  showed the same deposition potential at -1.75 V. Compared with the literatures, Herrmann and colleagues found that with a Ni/NiO reference electrode, the lithium deposition potentials decreased with increasing  $\text{Li}_2\text{O}$  concentration, and the Li/Li<sup>+</sup> potential was -1.75 V only in 1 w.t.%  $\text{Li}_2\text{O}/\text{LiCl}$ . [46,49]



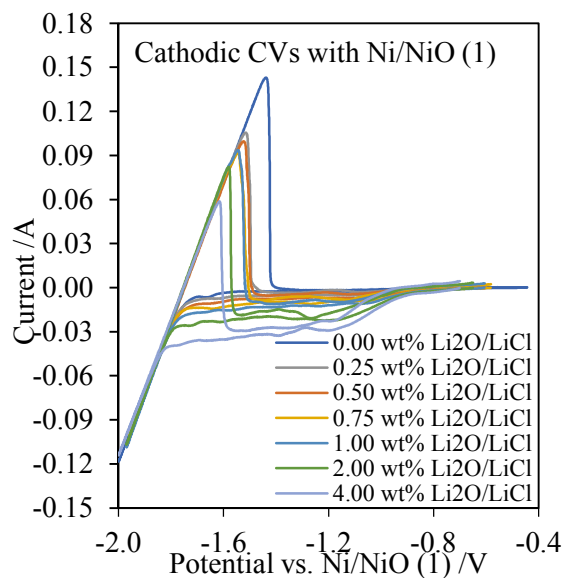


Figure 4.2 Cathodic CVs with Ni/NiO (1) reference electrode in  $\text{Li}_2\text{O}/\text{LiCl}$  at  $650\text{ }^\circ\text{C}$ . W.E.: Stainless steel. C.E.: Nickle spiral. Scan rate =  $20\text{ mV s}^{-1}$ .

Cathodic CVs were also measured with pseudo reference electrodes, including the glassy carbon, tungsten and molybdenum reference electrodes.

Cathodic CVs in  $\text{Li}_2\text{O}/\text{LiCl}$  with the glassy carbon reference electrode were obtained and presented in Fig. 4.3. When  $\text{Li}_2\text{O}$  was initially added to a 0.25 w.t.% concentration, the  $\text{Li}^+$  reduction onset potential decreased dramatically from  $-1.426\text{ V}$  in pure  $\text{LiCl}$  to  $-1.341\text{ V}$ . Then, the change was less significant when the  $\text{Li}_2\text{O}$  concentration was increased in a 0.25 w.t.% interval. The  $\text{Li}$  deposition potential decreased from  $-1.314\text{ V}$  to  $-1.298\text{ V}$ ,  $-1.285\text{ V}$ ,  $-1.264\text{ V}$  and  $-1.236\text{ V}$  when the  $\text{Li}_2\text{O}$  concentration increased from 0.50 to 0.75, 1.00, 2.00 and 4.00 w.t.%, respectively. The positive shift of  $\text{Li}$  deposition potential was in a trend, which was the result of elevating  $\text{Li}_2\text{O}$  concentration.

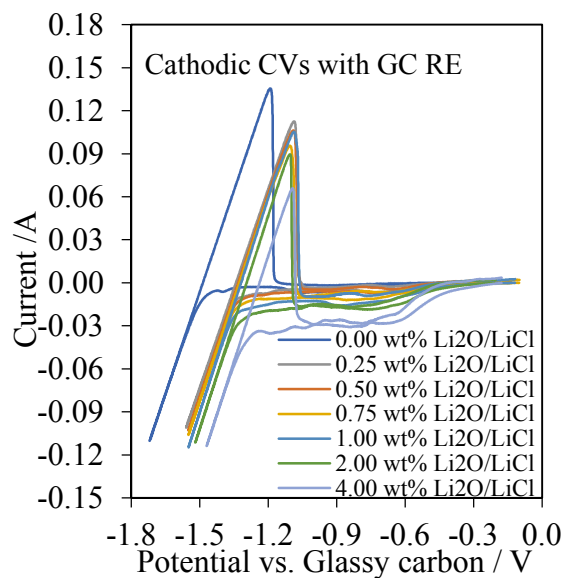


Figure 4.3 Cathodic CVs with glassy carbon reference electrode in Li<sub>2</sub>O/LiCl at 650 °C. W.E.: Stainless steel. C.E.: Nickle spiral. Scan rate = 20 mV s<sup>-1</sup>.

When a tungsten wire was used as the reference electrode in cathodic CV measurements (Fig. 4.4), the Li deposition potential decreased from -1.435 V in pure LiCl to -1.165 V in 0.25 w.t.% Li<sub>2</sub>O/LiCl. With more Li<sub>2</sub>O in LiCl, the Li<sup>+</sup> reduction potential kept decreasing, and the change was not significant. The Li/Li<sup>+</sup> potentials in 0.50, 0.75, 1.00, 2.00 and 4.00 w.t.% Li<sub>2</sub>O/LiCl were -1.148 V, -1.135 V, -1.125 V, -1.116 V and -1.095 V, respectively. Therefore, with a tungsten reference electrode, the potential for Li/Li<sup>+</sup> decreased with higher Li<sub>2</sub>O concentrations, a similar trend observed in CV measurement with the glassy carbon reference electrode.

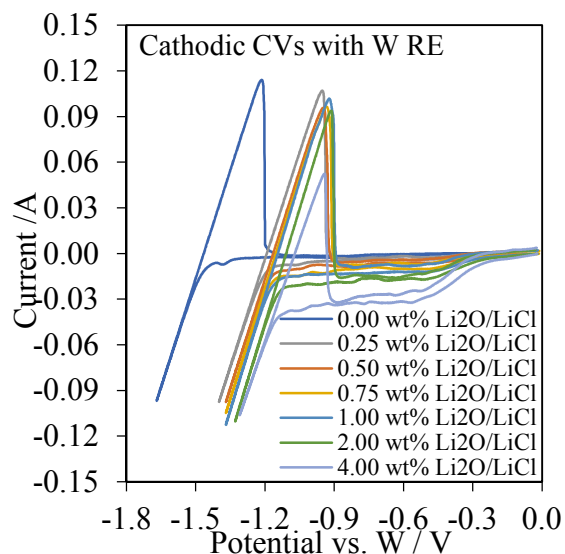


Figure 4.4 Cathodic CVs with tungsten reference electrode in  $\text{Li}_2\text{O}/\text{LiCl}$  at  $650\text{ }^\circ\text{C}$ . W.E.: Stainless steel. C.E.: Nickle spiral. Scan rate =  $20\text{ mV s}^{-1}$ .

A molybdenum wire was also tested as the reference electrode at different  $\text{Li}_2\text{O}$  concentrations and Fig. 4.5 shows the cathodic CV curves. There were more data curve measured with the Mo reference electrode. However, some of the results were obviously off the trend, due to the inconsistency of the Mo wire in corrosive molten salt. So these results were treated as error and not shown in the figure. A significant decrease in  $\text{Li}^+$  reduction potential from  $-1.522\text{ V}$  to  $-1.241\text{ V}$  was observed when  $\text{Li}_2\text{O}$  was initially added to  $0.25\text{ w.t.}\%$ . And then, with more  $\text{Li}_2\text{O}$  added to the system, the Li deposition potential decreased to  $-1.210\text{ V}$ ,  $-1.202\text{ V}$  and  $-1.185\text{ V}$  in  $1.00$ ,  $2.00$  and  $4.00\text{ w.t.}\%$   $\text{Li}_2\text{O}/\text{LiCl}$ . In literature, a molybdenum rod ( $0.5\text{ mm}$  diameter) was also used as a reference electrode in measuring cathodic CVs in molten  $\text{LiCl}$  with  $\text{Li}_2\text{O}$  concentration at  $0$  and  $1\text{ w.t.}\%$  at  $25\text{ mV s}^{-1}$ . [69] The researchers observed a positive shift of cathodic edge when  $\text{Li}_2\text{O}$  concentration was increased, and the Li deposition potential was at  $-1.91\text{ V}$  in pure  $\text{LiCl}$  and at  $-1.21\text{ V}$  in  $1\text{ w.t.}\%$   $\text{Li}_2\text{O}/\text{LiCl}$ . So, the difference between  $\text{Li}/\text{Li}^+$  potentials in pure  $\text{LiCl}$  and  $1\text{ w.t.}\%$   $\text{Li}_2\text{O}/\text{LiCl}$  was  $0.7\text{ V}$  in literature, compared with  $0.312\text{ V}$  in the present study. Though the decomposition potentials are not the same in literature and the current study, both results show the same trend of lower Li deposition potentials at higher  $\text{Li}_2\text{O}$  concentrations.

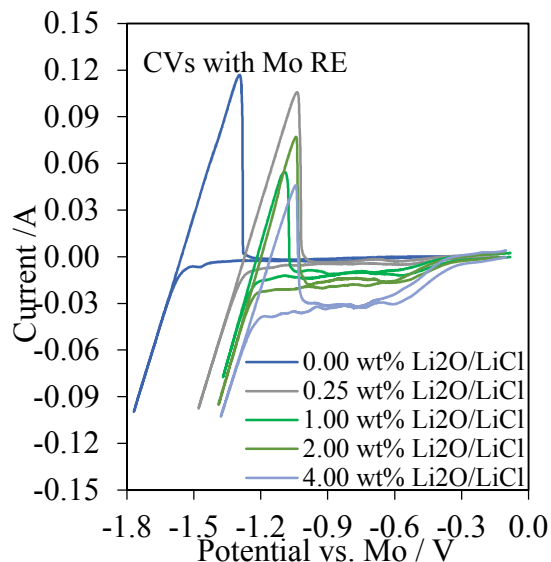


Figure 4.5 Cathodic CVs with molybdenum reference electrode in  $\text{Li}_2\text{O}/\text{LiCl}$  at  $650\text{ }^\circ\text{C}$ . W.E.: Stainless steel. C.E.: Nickel spiral. Scan rate =  $20\text{ mV s}^{-1}$ .

Fig. 4.6 sequences the tested reference electrodes taking Ni/NiO electrode potential as the positive limit. The electrode potential of each reference electrode is determined by taking the measured Li deposit potential as the reference. Since the Li deposition potential measured with Ni/NiO remains constant at various  $\text{Li}_2\text{O}$  concentrations, the Ni/NiO electrode potential is normalized as zero. Fig. 3a shows the Li deposition potentials in molten  $\text{LiCl}$  at  $650\text{ }^\circ\text{C}$ . The electrode potentials of molybdenum, tungsten and glassy carbon reference electrodes were  $0.23\text{ V}$ ,  $0.32\text{ V}$  and  $0.33\text{ V}$  more negative than that of Ni/NiO, respectively. Since  $1\text{ w.t.}\%$   $\text{Li}_2\text{O}/\text{LiCl}$  molten salt is widely used in metal oxides electroreduction studies [46,49,60,61,86], it is worthy studying the correlation among reference electrodes in this electrolyte. Fig. 3b describes the relationship among electrode potentials in  $1\text{ w.t.}\%$   $\text{Li}_2\text{O}/\text{LiCl}$ , showing the electrode potentials of glassy carbon, molybdenum and tungsten reference electrode were  $0.47\text{ V}$ ,  $0.54\text{ V}$  and  $0.63\text{ V}$  more negative compared with Ni/NiO, respectively. The results can be used to estimate the reaction potentials with one reference electrode when the information was known with another reference electrode.



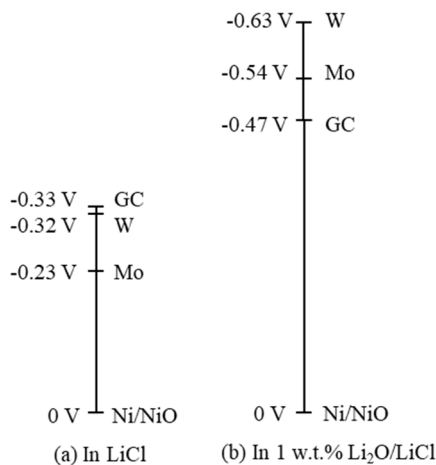


Figure 4.6 Comparisons among reference electrodes at 650 °C in (a) LiCl and (b) 1 w.t.% Li<sub>2</sub>O/LiCl

#### 4.4.2 Effects of O<sup>2-</sup> Concentrations on Electrode Performances

The Nernst equation for lithium redox process (Eq. 4) gives the lithium ions reduction potentials. The activities of solid (Li<sup>0</sup>) and solvent (Li<sup>+</sup>) are ideally taken as unity.[53,88] So, based on Eq. 4.4, the Li<sup>+</sup> reduction potential equals to the standard potential regardless of the Li<sub>2</sub>O concentrations in this study. In other words, an ideal system should not show a Li<sup>+</sup> reduction potential shift even if the concentration of Li<sub>2</sub>O varies.

$$E_{Li/Li^+} = E_{Li/Li^+}^0 + \frac{RT}{F} \ln \frac{a_{Li^+}}{a_{Li^0}} \quad (\text{Eq. 4.4})$$

where  $E^0$  is the standard potential for the reaction,  $R$  is the universal gas constant,  $T$  is the temperature and  $F$  is Faraday's constant.

The Ni/NiO reference electrode undergoes a Ni-NiO equilibrium reaction (Eq. 4.1) inside the reference electrode which counteracts the variations of the surrounding O<sup>2-</sup> concentrations. An equilibrium constant  $K_{Ni/NiO} = [Ni]P_{O_2}^{1/2}/[NiO]$  is established regarding the concentrations of the species. (The brackets represent the concentrations of the species, and partial pressure of O<sub>2</sub> is 1 atm in the glove box.) In high temperature molten LiCl mixturesalts at 650~700 °C, slight Ni metal dissolubtion was observed in the studie of corrosion.[68] NiO was also found to be soluble in molten LiCl mixture salts at 450~500 °C.[89,90] So, in this study, both Ni wire and NiO powder are soluble to some degree, and there are corresponding concentrations of these two species in the liquid phase.

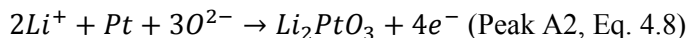
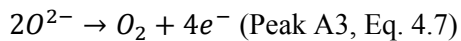
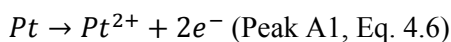
Therefore, based on the Nernst equation for Ni/NiO electrode potential (Eq. 4.5), the electrode potential remains unchanged regardless of O<sup>2-</sup> concentration in electrolyte. Therefore, combing the

Nernst equation studies for Li/Li<sup>+</sup> (Eq. 4.4) and the Ni/NiO equilibrium couples, the Li deposition potential should remain a constant value at different Li<sub>2</sub>O concentrations. The CV results in this study proves this theory.

$$E_{Ni/NiO} = E_{Ni/NiO}^0 + \frac{RT}{2F} \ln \frac{[NiO]}{[Ni]P_{O_2}^{1/2}} = E^0 + \frac{RT}{2F} \ln \left( \frac{1}{K_{Ni/NiO}} \right) \quad (\text{Eq. 4.5})$$

In anodic CVs measured with Ni/NiO (1) reference electrode at various Li<sub>2</sub>O concentrations, anodic peaks shifted left with higher Li<sub>2</sub>O concentrations (Fig. 4.7). For anodic CV in pure LiCl electrolyte, an oxidation peak onset at +1.335 V indicated the dissolution of the Pt electrode (Peak A1, Eq. 4.6). The reduction peak C1 was the reduction of residual Pt<sup>2+</sup> around the Pt electrode, the reverse reaction of Eq. 4.6. When Li<sub>2</sub>O was added, new oxidation peaks A2 and A3 appeared before the Pt dissolution potential. The reaction at anodic peak A3 was the oxidization of O<sup>2-</sup> (Eq. 4.7). The oxidation peak A2 was the formation of a semiconductor Li<sub>2</sub>PtO<sub>3</sub> (Eq. 4.8) on the Pt electrode [54,70,91,92], and the onset potentials were at 0.746 V, 0.680 V, 0.645 V, 0.618 V, 0.544 V and 0.455 V in LiCl with 0.25, 0.50, 0.75, 1.00, 2.00 and 4.00 w.t.% Li<sub>2</sub>O, respectively. For CVs in lithium salt with higher Li<sub>2</sub>O concentrations, peak shapes were similar, while both the Li<sub>2</sub>PtO<sub>3</sub> formation peak and the O<sup>2-</sup> oxidation peak shifted left. Backwards scans in anodic CVs in Li<sub>2</sub>O/LiCl showed two reduction peaks C2 and C3 which did not exist in CV in pure LiCl. C2 was composed of two small separated peaks and they started to merge into one big peak when the intensities became larger. C2 and C3 were also observed by Choi [93] and Sakamura [70]. Choi explained these two peaks as a two-step reduction of Li<sub>2</sub>PtO<sub>3</sub>. [93] Sakamura considered the two reduction peaks as the paired reduction peaks with anodic peaks, meaning that C2 coupled with A2 was the reduction of Li<sub>2</sub>PtO<sub>3</sub>; and C3 corresponded with A3, making it the O<sub>2</sub> reduction peak. [70] Based on CV measurement in this study, A3 remained at the similar current intensity by controlling the applied potential while A2 became larger with increasing Li<sub>2</sub>O concentration, and in response, C2 became bigger while C3 did not change much in intensity with higher Li<sub>2</sub>O concentrations. So, in this study, peak C3 was the reduction of O<sub>2</sub> generated at A3, and peak C2 was the two-step reduction of Li<sub>2</sub>PtO<sub>3</sub> formed at A2. The Nernst equation for the formation of Li<sub>2</sub>PtO<sub>3</sub> is expressed in Eq. 4.9. By taken the activity of solid and solvent as unity, the equation is simplified. A linear line is achieved by plotting the Li<sub>2</sub>PtO<sub>3</sub> formation potential and  $\ln\left(\frac{1}{[O^{2-}]}\right)$  (Fig. 4.8), and the slope is 0.103. The O<sup>2-</sup> activity coefficient is derived from the slope of the line. With the assumption that the activity coefficient is related with the concentration, the apparent activity coefficient is expressed as  $\gamma_{O^{2-}}^{app} = A_{Pt} \times [O^{2-}]^{B_{Pt}}$  ( $A_{Pt}$  and B are constants). Substituting  $\gamma_{O^{2-}}^{app}$  in eq. 4.9 gives  $E = E^0 + \frac{3RT}{4F} \ln \left( \frac{1}{A_{Pt}} \right) + \frac{3(b+1)RT}{4F} \ln \left( \frac{1}{[O^{2-}]} \right)$ .  $\frac{3(b+1)RT}{4F}$  is the slope in th fitting, and the value

of  $B_{Pt}$  is determined as 0.7. Therefore, the apparent activity coefficient of  $O^{2-}$  in  $Li_2O/LiCl$  defined with  $Li_2PtO_3$  formation is  $\gamma_{O^{2-}}^{app} = A_{Pt} \times [O^{2-}]^{0.7}$ .



$$E_{Pt/Li_2PtO_3} = E_{Pt/Li_2PtO_3}^0 + \frac{RT}{4F} \ln \left( \frac{a_{Li_2PtO_3}}{a_{Li^+}^2 a_{Pt} a_{O^{2-}}^3} \right) = E^0 + \frac{3RT}{4F} \ln \left( \frac{1}{\gamma_{O^{2-}} [O^{2-}]} \right) \text{ (Eq. 4.9)}$$

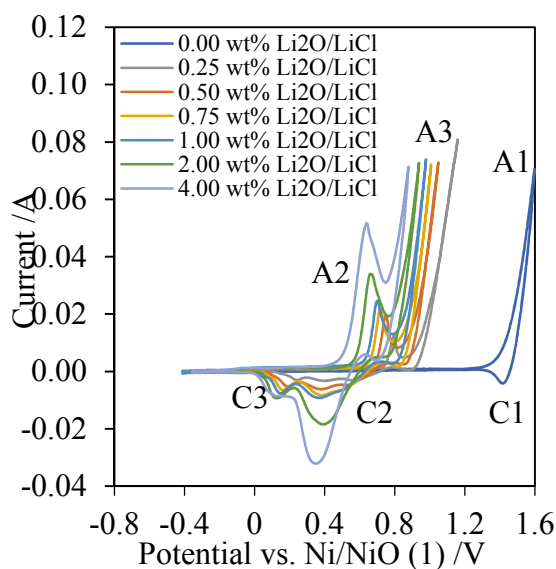


Figure 4.7 Anodic CVs in  $Li_2O/LiCl$  with Ni/NiO (1) reference electrode at 650 °C. Scan rate = 20  $mV s^{-1}$ .

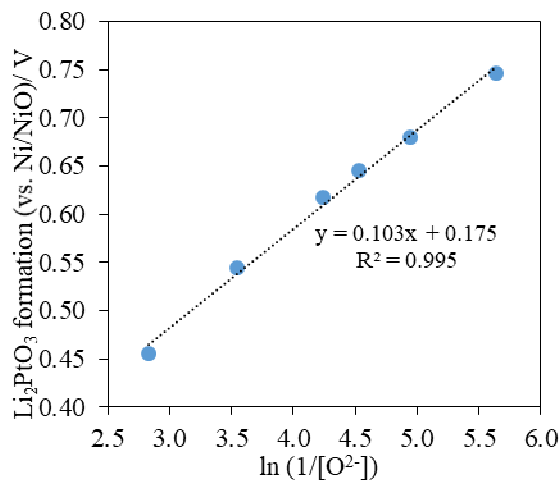


Figure 4.8 Plots of  $Li_2PtO_3$  formation potential with Ni/NiO (1) RE as a function of  $\ln(1/[O^{2-}])$ . The oxygen ion concentrations were in mol%.

The Li deposition potential shift measured with the pseudo-reference electrode is due to the reactions on the reference electrode surface. In cathodic CV measurements, balanced with negative charges on the working electrode, positive current would flow through the reference electrode and oxidation reactions take place.

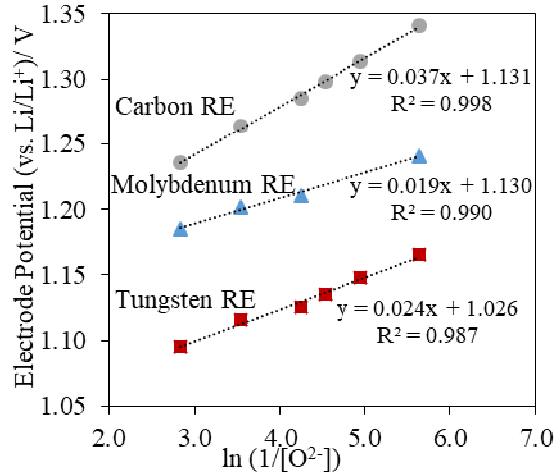
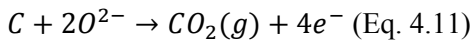
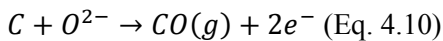


Figure 4.9 Plots of surface reaction potential of glassy carbon electrode, molybdenum electrode, tungsten electrode as a function of  $\ln(1/[O^{2-}])$ . The oxygen ion concentrations were in mol%.

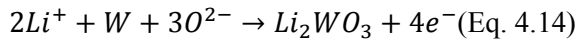
With positive current on the glassy carbon electrode, CO and CO<sub>2</sub> are generated (Eq. 4.10 and Eq. 4.11).[39,94] The Nernst equation for CO and CO<sub>2</sub> emission on the glassy carbon electrode are written in Eq. 7c and Eq. 7d, respectively. The pressure in the glovebox is 1 atm (~1 bar) which is the pressure for CO and CO<sub>2</sub>. So, as the O<sup>2-</sup> concentrations increased, the glassy carbon reference electrode potential decreases. A linear relationship is achieved by plotting the electrode reaction potentials (vs. Li/Li<sup>+</sup>) with  $\ln(\frac{1}{[O^{2-}]})$ , as shown in Fig. 4.9. The apparent activity coefficient of O<sup>2-</sup> in Li<sub>2</sub>O/LiCl is assumed as  $\gamma_{O^{2-}}^{app} = a_c \times [O^{2-}]^{Bc}$ . Based on the plotted slope 0.037, B<sub>c</sub> value is zero. So, the apparent activity coefficient of O<sup>2-</sup> is a constant independent on the O<sup>2-</sup> concentration.



$$E_{C/CO} = E_{C/CO}^0 + \frac{RT}{2F} \ln\left(\frac{a_{CO}}{a_c \times a_{O^{2-}}}\right) = E^0 + \frac{RT}{2F} \ln\left(\frac{p_{CO}}{a_{O^{2-}}}\right) = E^0 + \frac{RT}{2F} \ln\left(\frac{1}{\gamma_{[O^{2-}]}}\right) \text{ (Eq. 4.12)}$$

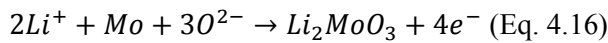
$$E_{C/CO_2} = E_{C/CO_2}^0 + \frac{RT}{4F} \ln\left(\frac{a_{CO_2}}{a_c \times a_{O^{2-}}^2}\right) = E^0 + \frac{RT}{4F} \ln\left(\frac{p_{CO_2}}{a_{O^{2-}}^2}\right) = E^0 + \frac{RT}{2F} \ln\left(\frac{1}{\gamma_{[O^{2-}]}}\right) \text{ (Eq. 4.13)}$$

A linear relationship is also achieved by plotting the surface reaction potentials (vs. Li/Li<sup>+</sup>) as a function of  $\ln(\frac{1}{[O^{2-}]})$  in Fig. 4.9. The surface reaction on the tungsten electrode (Eq. 4.14) is predicted as the formation of Li<sub>2</sub>WO<sub>3</sub>, based on the well-defined reaction of Li<sub>2</sub>PtO<sub>3</sub> generation on the Pt electrode (Eq. 4.8). The surface reaction is expressed in eq. 8a and the corresponding Nernst equation is written in Eq. 4.15. By assuming the apparent activity coefficient of O<sup>2-</sup> to be  $\gamma_{O^{2-}}^{app} = A_W \times [O^{2-}]^{B_W}$ , the B<sub>W</sub> value calculated from the slope of 0.0195 is -0.6. So, the apparent activity coefficient of O<sup>2-</sup> in Li<sub>2</sub>O/LiCl defined with Li<sub>2</sub>WO<sub>3</sub> formation is  $\gamma_{O^{2-}}^{app} = A_W \times [O^{2-}]^{-0.6}$ , indicating that the apparent activity coefficient of O<sup>2-</sup> is dependent on O<sup>2-</sup> concentration.



$$E_{W/Li_2WO_3} = E_{W/Li_2WO_3}^0 + \frac{RT}{4F} \ln \left( \frac{a_{Li_2WO_3}}{a_{Li^+}^2 a_W \times a_{O^{2-}}^3} \right) = E^0 + \frac{3RT}{4F} \ln \left( \frac{1}{\gamma_{[O^{2-}]}} \right) \text{ (Eq. 4.15)}$$

The surface reaction on the molybdenum electrode was also studied based on the relationship between the reaction potential (vs. Li/Li<sup>+</sup>) and the oxygen ion concentration. A linear line is achieved with a slope of 0.0244 by plotting the surface reaction potential vs.  $\ln(\frac{1}{[O^{2-}]})$  (Fig. 4.9). Following the same reaction pattern on the Pt electrode, the reaction on the molybdenum electrode is proposed as the Li<sub>2</sub>MoO<sub>3</sub> generation (Eq. 4.16). With the assumption that the apparent O<sup>2-</sup> activity coefficient is  $\gamma_{O^{2-}}^{app} = A_{Mo} \times [O^{2-}]^{B_{Mo}}$ , combined with the Nernst equation in Eq. 4.17, the value of B<sub>Mo</sub> is -0.7. Therefore, the O<sup>2-</sup> apparent activity coefficient determined with the Mo electrode has a relationship with the O<sup>2-</sup> concentration as  $\gamma_{O^{2-}}^{app} = A_{Mo} \times [O^{2-}]^{-0.7}$ .



$$E_{Mo/Li_2MoO_3} = E_{Mo/Li_2MoO_3}^0 + \frac{RT}{4F} \ln \left( \frac{a_{Li_2MoO_3}}{a_{Li^+}^2 a_{Mo} \times a_{O^{2-}}^3} \right) = E^0 + \frac{3RT}{4F} \ln \left( \frac{1}{\gamma_{[O^{2-}]}} \right) \text{ (Eq. 4.17)}$$

In the measurements of Li deposition potentials in Li<sub>2</sub>O/LiCl melts with all the reference electrodes, results with Ni/NiO reference electrode show a consistent potential at around -1.75 V, while potential drifts are found with GC, W and Mo reference electrodes due to the instability of the electrode materials. The theoretical analysis predicted a constant Li deposition potential in LiCl with different Li<sub>2</sub>O concentrations. Therefore, in order to overcome the influence under the oxygen ions, a reference electrode assisted with an equilibrium (such as Ni/NiO) is expected to have a better performance in a system with varying concentrations of O<sup>2-</sup>.

#### 4.4.3 Effects of Ni/NiO Fabrication Methods

To study the effect of the amount of NiO powder on the reference electrode performance, a Ni/NiO (2) reference electrode was also used in cathodic and anodic CV measurements (Fig. 4.10a and 4.10b). The Li deposition potentials in pure LiCl and 0.25 wt.% Li<sub>2</sub>O/LiCl were the same at -2.07 V. However, a potential gap was observed when more measurements were taken. Li deposition potential in 0.50 wt.% Li<sub>2</sub>O/LiCl dropped to -1.90 V and the Li deposition potentials in higher Li<sub>2</sub>O concentration mixtures were around this value. The anodic CV scans also showed a sharp peak of Pt dissolution in pure LiCl salt at 1.035 V (A1), and peaks for Li<sub>2</sub>PtO<sub>3</sub> formation (A2) and O<sup>2-</sup> oxidation (A3) in Li<sub>2</sub>O/LiCl mixture salts. CVs for 0.25 wt.% Li<sub>2</sub>O/LiCl showed a Li<sub>2</sub>PtO<sub>3</sub> formation peak onset at 0.414 V and an O<sup>2-</sup> oxidation peak onset at 0.542 V. When the Li<sub>2</sub>O concentrations were at 0.5 wt.%, a peak shift of +0.121 V happened on the anodic side, which was the compensation effects of electrode potential shift observed on the cathodic side and the oxidation potential shift due to the Li<sub>2</sub>O concentration change. In CVs for 0.75 wt.% to higher Li<sub>2</sub>O concentrations, the peaks for Li<sub>2</sub>PtO<sub>3</sub> formation and O<sup>2-</sup> oxidation shifted in the cathodic direction. The onset potentials for Li<sub>2</sub>PtO<sub>3</sub> formation were 0.414 V, 0.535 V, 0.505 V, 0.472 V, 0.416 V and 0.317 V in LiCl with 0.25, 0.50, 0.75, 1.00, 2.00, and 4.00 wt.% Li<sub>2</sub>O, respectively.

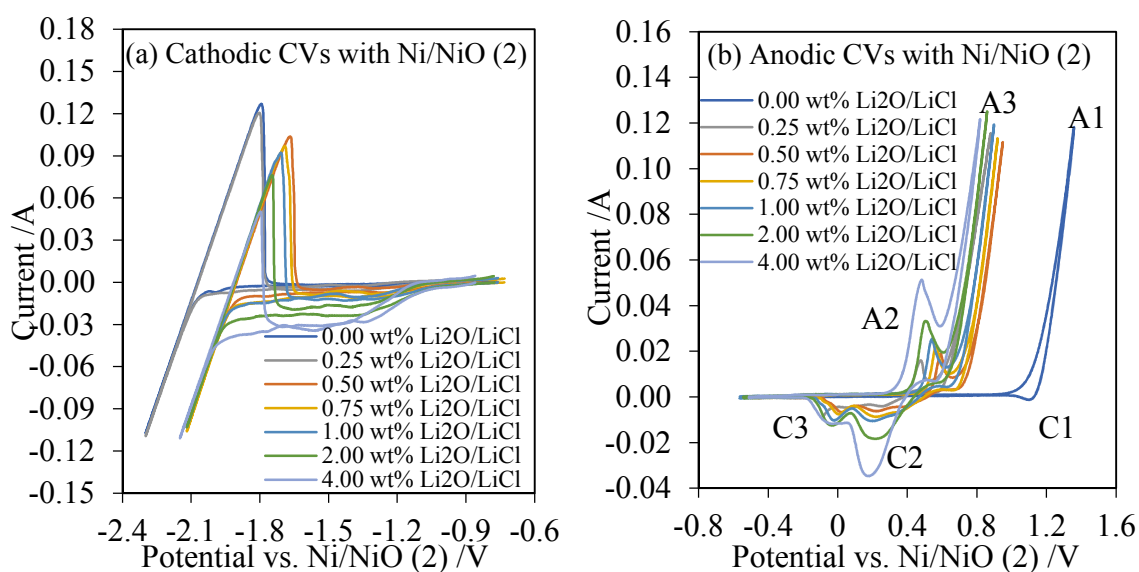


Figure 4.10 Cathodic CVs (a) and anodic CVs (b) in Li<sub>2</sub>O/LiCl with Ni/NiO (2) reference electrode at 650 °C.

Scan rate = 20 mV s<sup>-1</sup>.

The irregular shift in CV measurements with Ni/NiO (2) may come from the structure change inside the MgO tube (Fig. 4.11). When the Ni/NiO (2) reference electrode was initially assembled (a), the NiO powder in the tube was one inch above the molten salt surface level (b). When the tube was

placed in the liquid salt, NiO powder adsorbed salt melt and partial of the upper powder sank in the molten salt, leaving the top part suspending in the tube (c). The powder left in the upper tube were loose and easy to be knocked down during preparation or conduction of the experiments. Then the loose powder adsorbed molten salt when the electrode was in the salt (d). In this study, the Ni/NiO (2) reference electrode was at status (c) for CV measurements in pure LiCl and 0.25 w.t.% Li<sub>2</sub>O/LiCl, at status (d) for the rest of the measurements.

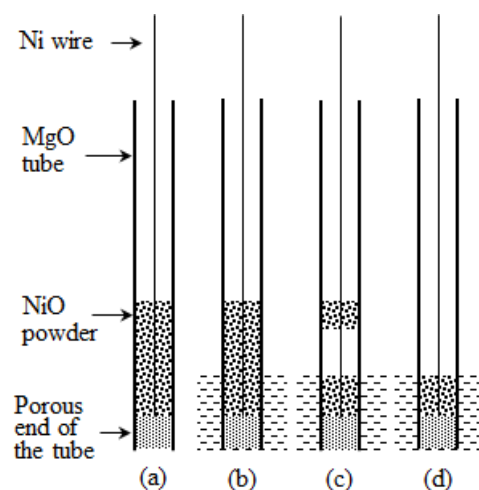


Figure 4.11 Structural changes in Ni/NiO (2) reference electrode during CV measurements

A study on the effect of the length of MgO porous end was carried out by Burak using Ni/NiO as the working electrode in 1 w.t.% Li<sub>2</sub>O/LiCl at 670-680 °C.[95] Similar as the method of electrode fabrication in the current study, a Ni wire was inserted to the NiO bed in the MgO tube, but the NiO powder used in the literature was high above the molten salt level. The Ni/NiO electrodes were pre-soaked in the molten salt for at least 24 hours prior to the measurements, to eliminate the transient characteristic of the reference potential. The MgO tubes were cut to equalize the length at the porous ends. Open circuit potential of the molten salt was measured with untrimmed Ni/NiO working electrode vs. Pb-Li and trimmed Ni/NiO working electrode vs. S.S. By taking the measurement with multiple untrimmed and trimmed Ni/NiO electrodes, the OCP measured with untrimmed Ni/NiO was averaged at -1.6 V vs. Pb-Li with 5.3% relative standard deviation, and the OCP with trimmed Ni/NiO was averaged at -0.52 V vs. S.S. with 1.3% relative standard deviation. So, the trimming procedure for the Ni/NiO electrode was essential in standardized experiment operations and repeatable experiment results.

Therefore, a trimmed Ni/NiO with a proper amount of NiO powder is the key characteristics of the Ni/NiO electrode for reliable and repeatable performances.

#### 4.5 Conclusion

In CV measurements, the Ni/NiO reference electrode shows a consistent Li deposition potential at -1.75 V in cathodic CV measurements in LiCl with different Li<sub>2</sub>O concentrations. So, in a system with a varying O<sup>2-</sup> concentration, reliable and repeatable electrolytic measurements rely on a trimmed Ni/NiO reference electrode with a proper internal structure in the MgO tube.

The lithium deposition achieved with the glassy carbon, tungsten and molybdenum reference electrodes showed positive shifts with increasing Li<sub>2</sub>O concentrations, due to the corrosion on the reference electrode surface in molten salts. The Li<sub>2</sub>PtO<sub>3</sub> formation potentials measured with Ni/NiO reference electrode also varied with Li<sub>2</sub>O composition, less positive potentials at higher Li<sub>2</sub>O concentrations. Linear relationship was found between signature potentials (Li deposition potential and Li<sub>2</sub>PtO<sub>3</sub> formation potential) and  $\ln\left(\frac{1}{[O^{2-}]}\right)$ , and the apparent O<sup>2-</sup> activity coefficients with each reference electrode were proposed based on the relationship. Furthermore, correlations of reference electrode potentials in pure LiCl and 1 w.t.% Li<sub>2</sub>O/LiCl were defined, including Ni/NiO, glassy carbon, tungsten and molybdenum reference electrodes. In both electrolytes, Ni/NiO showed the most positive electrode potentials.



## Chapter 5: High Current Efficiency of NiO Electro-Reduction in Molten Salt

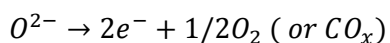
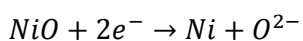
### 5.1 Abstract

Electrolytic reduction of NiO particles were carried out in 1 w.t. % Li<sub>2</sub>O/LiCl molten salt at 650 °C. The reduction potential was controlled at -0.3 V vs. Li/Li<sup>+</sup>, at which Li metal was reduced at the cathode. The NiO was reduced by both the electrons and the *in situ* generated Li metal. The reductions followed a simply one-step reduction mechanism under each reduction mechanism. The electroreduction was fast and reached a high current efficiency at 96.1%, characterized with both XRD and TGA. The high current efficiency suggested that the parameter control and customized electrochemical cell used in this study could be introduced in other studies with similar research targets.

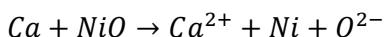
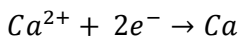
### 5.2 Introduction

Ni metal is an important material for its high melting point and corrosion resistance. These chemical and physical properties made the nickel metal widely used as a structural and magnetic material. The nickel metal is maturely produced in two ways, the hydrometallurgy and pyrogenic process. The hydrometallurgy process, such as electroplating with Watts bath, generally produces nickel metal in a high purity. The other method, the pyrogenic process is involved in the current industry, producing around 90% of the Ni generation in the world. However, the pyrogenic process takes the charcoal as the energy provider, so it suffers from slow process rate and low energy efficiency. [96]

The electrolytic reduction of metal oxides in high temperature molten salt provides a promising method in generating metals, such as niobium, chromium, titanium and nickel.[7,30–32,64,96] Among these metals, the production process of nickel showed the most direct reduction process, without the involvement of intermediates. So, it results in a high reduction efficiency at a low cost. [30,31,97] Two reaction pathways have been proposed for electrolytic reduction of NiO in CaO/CaCl<sub>2</sub> molten salts, including the Fray-Farthing-Chen (FFC) Cambridge process and the Ono-Suzuki (OS) process. In the FFC reduction process, it utilized the electron as the reductive agent to directly reduce the NiO on the cathode, and O<sub>2</sub> or carbon oxides gases were released from the metal or carbon anode. [97]



For the OS reduction mechanism, the reduction potential was higher than that of the FFC process, and the applied potential was high enough to reduce the  $\text{Ca}^{2+}$  to calcium metal. The *in situ* generated Ca chemically reduced the metal oxides into metal. Reactions on the anode were the same process as occurred on the anode in the FFC process.[30]



Various molten salt systems have been employed in the NiO reductions. The calciothermic reduction of NiO in CaO/CaCl<sub>2</sub> at 900 °C produced Ni metal, but the current efficiency was low at about 30%.[30] Current efficiency for NiO reduction in Na<sub>2</sub>O/NaOH at 550 °C reached 87%.[32] Nickel powder was also prepared in a electrolytic cell in molten Na<sub>2</sub>CO<sub>3</sub>/K<sub>2</sub>CO<sub>3</sub> at 750 °C, and it gave a current efficiency at 95.4%.[31] Though the Ni metal can be generated at a relative high current efficiency in some processes, there were still limitations in the high operation temperatures at 900 °C, and long operation hours for 11 hours in reducing only 0.4 g NiO [31].

In this work, the electroreduction of NiO was investigated under the lithiothermic conditions at 650 °C in 1 w.t. % Li<sub>2</sub>O/LiCl molten salt using a three-terminal electrolytic cell. NiO particles were loaded in a metal basket on the cathode. The cathodic reduction potentials were accurately controlled by using a Ni/NiO pseudo reference electrode. Constant potential chronoamperometies with intervals were carried out for the reductions. Reduced products were analyzed with XRD and TGA.

## 5.3 Experimental

### 5.3.1 Chemicals and Materials

Commercially available high purity lithium chloride (LiCl, 99.995% metals basis, ultra-dry, Alfa Aesar) and lithium oxide (Li<sub>2</sub>O, 99.5%, Alfa Aesar) were used as the electrolyte without further treatments. Nickel oxide powders (NiO, 99.95% metals basis, Alfa Aesar) were pelletized and prepared within the size range between 0.25 mm and 0.85 mm for the electrolytic reductions. Stainless mesh clothes (mesh size 100 and 200) and stainless wire were used for weaving the fuel baskets.

### 5.3.2 Experimental Setup

A three-electrode electrochemical cell (Fig. 5.1a) was used for the electrolytic studies including the cyclic voltammetry measurements and metal oxide reductions. The reactor cell was installed inside an argon atmosphere glovebox (MBraun, Labmaster 200G) with moisture and oxygen level lower than 10 ppm. Three electrodes were a working electrode, a Ni/NiO reference electrode and a glassy carbon crucible (HTW Germany) counter electrode. Thus, the glassy carbon crucible worked as both a

container for molten salts and a counter electrode with a large surface area. The pseudo Ni/NiO reference electrode was assembled with Ni wire and Ni powder encapsulated into a dense MgO sheath with a porous MgO plug at one end. For CV measurements, a 0.025" (0.635 mm) diameter stainless steel wire was used as working electrode. For NiO reductions, the working electrode assembly consisted of a stainless steel rod as an electron collector and a stainless steel basket loaded with NiO particles. The cathode basket was made of stainless steel mesh clothes and wires which can hold particles as small as 0.075 mm. The bundled electrode assembly (Fig. 5.1b) consisted of a working electrode assembly for reductions, a working electrode of a stainless steel wire for CV measurements and a Ni/NiO reference electrode. A Kerr lab electric furnace (Auto Electro Melt Maxi) was used for heat supplyment, and keeping the high temperature molten salt at 650 °C. The VersaSTAT 4 (Princeton Applied Research) potentiostat with VersaStudio was used to control the cathodic potentials for CV measurements and NiO reductions, and to collect experimental data.

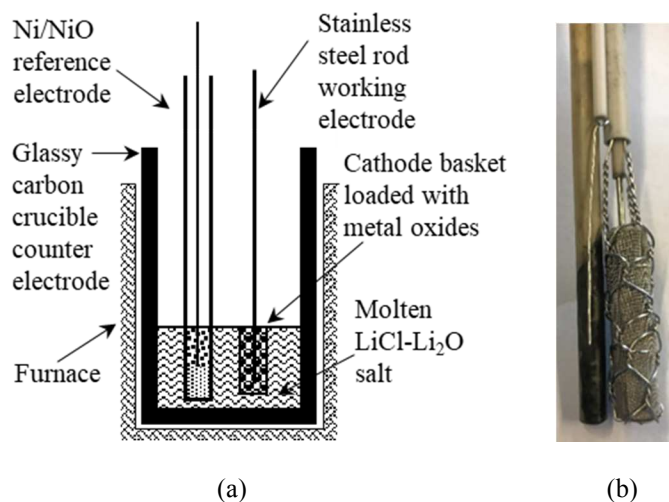


Figure 5.1 (a) Electrochemical Cell setup for NiO reduction, and (b) the fuel basket electrode assembly

### 5.3.3 Methodology

#### 5.3.3.1 CV Measurements

150 g LiCl with 1 w.t.% of Li<sub>2</sub>O was weighed and added into the glassy carbon crucible at room temperature in the argon atmosphere glovebox, and then the crucible was lowered into the electric furnace. It took less than one hour for the furnace to increase to 650 °C, and around 1.5~2 h for the salt to completely melt and homogenize.

CVs were measured in fresh 1 w.t.% Li<sub>2</sub>O/LiCl molten salt, to determine the Li deposit potential vs. Ni/NiO at the cathodic end of the salt decomposition curve. The CV data were collected

in the range of -2.25 V to 0.4 V at a scan rate of 20 mV s<sup>-1</sup>. The working electrode used in CV performance was the 0.025” stainless steel wire. CV curves were also recorded in the used salts after NiO reductions using the same methods and conditions.

#### 5.3.3.2 Electrolytic Reduction of NiO Particles

2 g NiO particles were loaded in the fuel basket (Fig. 5.1b). Then the electrode assembly was lowered down into 150 g 1 w.t.% Li<sub>2</sub>O/LiCl melt at 650 °C with the oxide basket edge submerged right under the salts surface. The reduction process was started after soaking the NiO in the molten salts for 1.5 hours. The cathodic reduction potential at -0.3 V vs. Li/Li<sup>+</sup> was applied continuously for the first 20 minutes and then in a pulsed mode. For the pulsed mode, the power supply was turned on for 8 min and off for 2 min repeatedly until 100% of theoretical charge was applied. The cell was at the open circuit potential (OCP) when the potentiostat was off. The accurate applied charge was calculated by the integration of the current with elapsed time through the VersaStudio software. After reduction was completed, the electrode bundle was lifted up from the salts and cooled down to room temperature inside the glovebox.

#### 5.3.3.3 Post-reduction Analyses

After reductions, the CVs were measured in the used salt at 650 °C. Reduced samples were transferred out from the glovebox. The produces were rinsed with nanopore water first and then acetone, and then dried overnight in vacuum at room temperature. The dried reduced samples were grounded into fine powders. The powders were analyzed with the X – ray diffraction (XRD, Rigaku SmartLab) with Cu K $\alpha$  radiation at 40 kV and 30 mA, from 10° to 80° at 4 ° min<sup>-1</sup>. The dried reduced products were also analyzed for the oxygen level with the Thermogravimetric Analysis (TGA/DSC3+, Mettler Toledo). The fine Ni powder of 10.454 mg was weighted and used for the TGA analysis. The weight of the TGA sample was monitored at 1150 °C with air flow at 20 ml min<sup>-1</sup> until the weight of sample did not change any more. The balance resolution was 0.1/1  $\mu$ g.

#### 5.3.3.4 Theory and Calculations

100% of the theoretical charge (Eq. 5.1) is defined as the charge needed theoretically for a complete reduction of NiO to Ni metal based on the Faraday law, which is in the unit of coulomb.

$$100\% \text{ of the theoretical charge} = 2F \frac{m_{\text{NiO}}}{M_{\text{NiO}}} \text{ (Eq. 5.1)}$$

where  $m_{\text{NiO}}$  is the mass of NiO particles loaded for reductions,  $M_{\text{NiO}}$  is the molecular weight of NiO,  $F$  is Faraday constant  $96485 \text{ C mol}^{-1}$ . The total charge is estimated by the integration of current with elapsed time through the VersaStudio software. The targeted charges for NiO reduction are 100% of the theoretical charge.

TGA result analysis is based on the sample weight gain after oxidation. The reduction extent determined from TGA results is presented in Eq. 5.2.

$$\text{Reduction extent}_{\text{TGA}} = \frac{\frac{(m_{\text{T}} - m_{\text{I}}) * M_{\text{NiO}}}{M_{\text{O}}}}{m_{\text{T}}} \quad (\text{Eq. 5.2})$$

where  $M_{\text{O}}$  is the molar weight of oxygen. The  $m_{\text{I}}$  and  $m_{\text{T}}$  are the weights of TGA samples before and after oxidation, respectively.

The current efficiency is estimated as the percentage of the total charge in the effective Ni metal production (Eq. 5.3).

$$\text{Current efficiency} = \frac{2n_{\text{Ni}}F}{\text{Total Charge}} \quad (\text{Eq. 5.3})$$

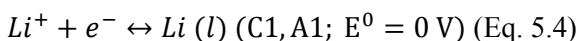
where  $n_{\text{Ni}}$  is the mole of Ni metal;  $F$  is the Faraday constant,  $96485 \text{ C mol}^{-1}$ . The total charge is the integration of current with elapsed time.

## 5.4 Results and Discussion

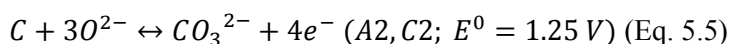
### 5.4.1 CVs in 1 w.t.% $\text{Li}_2\text{O}/\text{LiCl}$ Salts

CVs were measured using a 0.025" stainless steel wire as the cathode and the glassy carbon as the anode. CV peaks indicate reactions occur at certain potentials (Fig. 5.2). It can be seen that all the three CV curves in both fresh and used salts share the same cathodic edge. This phenomenon indicates that lithium species in the molten salt are the same after two reductions.

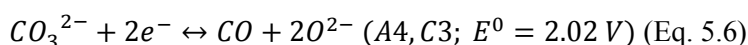
The CV in fresh 1 w.t.%  $\text{Li}_2\text{O} / \text{LiCl}$  salt is shown in Fig. 5.2 blue line. The curve features a sharp edge at C1 which corresponds to the reduction of the lithium ions (Eq. 5.4), and the big oxidation peak A1 represents the re-oxidation of Li metal to ions.[49] The Li deposition potential in 1 w.t. %  $\text{Li}_2\text{O}/\text{LiCl}$  was determined as -1.75 V (vs. Ni/NiO), determined from the onset potential of the reduction peak.



The oxidation peak A2 onset at -0.45 V is the formation peak of  $\text{CO}_3^{2-}$  from oxidation of carbon associated with  $\text{O}^{2-}$  (Eq. 5.5).[8,66,67,98] The generated  $\text{CO}_2$  on the anode dissolves in the salt and associates with  $\text{O}^{2-}$  ion to form  $\text{CO}_3^{2-}$  ( $\text{CO}_2 + \text{O}^{2-} \rightarrow \text{CO}_3^{2-}$ ).[99] Free carbon and  $\text{CO}_3^{2-}$ , though at low concentrations, were generated in the electrolyte during CV cycles. The reaction at cathodic peak C2 on set at -0.37 V is the reverse reaction of A2.  $E_{C/\text{CO}_3^{2-}}^0$  is 1.25 V taking A1 and C1 as reference potential point. Figure 5.3 shows the calculation process for values of  $E^0$ .



The CVs in used salts (Fig. 5.2 green and red curves) show a symmetric reduction peak C3 onset at 0.18 V, accompanied with the increasing oxidation peak A4 onset at 0.24 V. The C3/A4 coupled peaks are the reversible conversion between  $\text{CO}_3^{2-}$  and CO (Eq. 5.6).[67]



The reaction at the oxidation peak A3 onset at -0.12 V is the oxidation of free carbon to form CO (Eq. 5.7), which enhances the reversibility of CO/ $\text{CO}_3^{2-}$  redox reactions (A4, C3).[67]

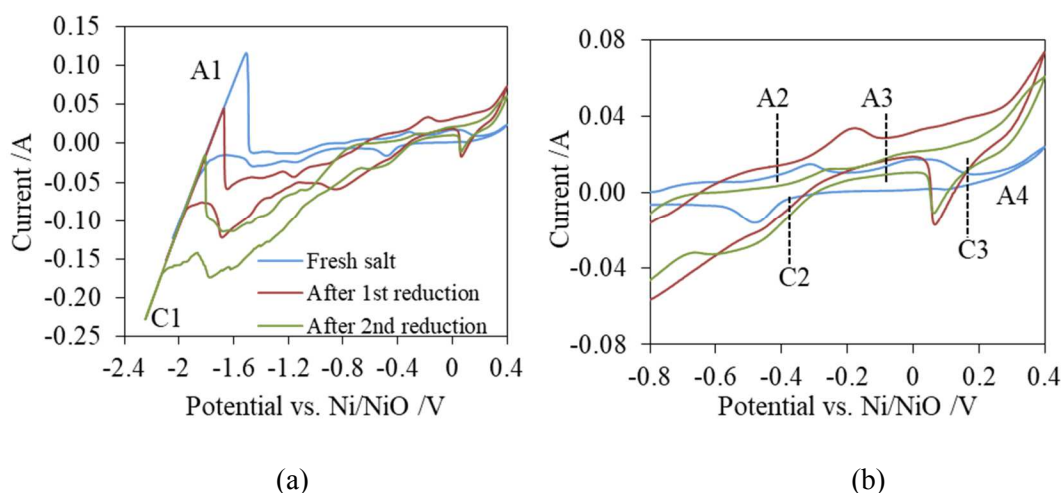
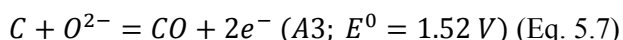


Figure 5.2 (a) CVs in 1.0 w.t. %  $\text{Li}_2\text{O}/\text{LiCl}$  at  $20 \text{ mV s}^{-1}$  using 0.025'' stainless steel working electrode before and after NiO reductions, and (b) enlargement of the anodic branches of the CVs in (a).

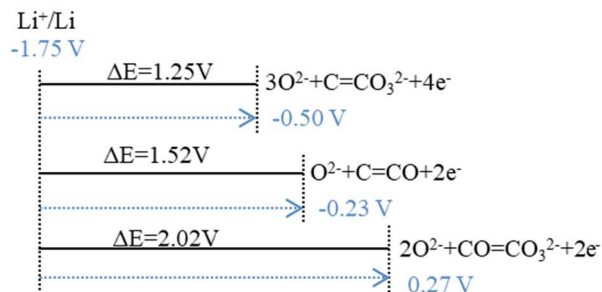


Figure 5.3 Procedures in identification of half-cell potentials (vs. Ni/NiO).

#### 5.4.2 NiO Electroreduction

The NiO reductions were carried out at cathodic potential  $-2.05\text{ V}$  (vs. Ni/NiO) with intervals (Fig. 5.4 green line). The cathodic potential was  $0.3\text{ V}$  more negative than Li deposition potential using a Ni/NiO reference electrode. Under this condition, NiO could be reduced through a lithiothermic reduction. The reductions of NiO were carried out with 100% of the theoretical charge in fresh 1.0 w.t. %  $\text{Li}_2\text{O}/\text{LiCl}$  molten salt and then repeated in the same batch of salt.

During the reduction processes, the current ranged between  $-1.0 \sim -1.2\text{ A}$  and 100% of the theoretical charge was achieved in 1.76 h for reduction in fresh salt (Fig. 5.4 red line) and 1.6 h in used salt (Fig. 5.4 blue line). The currents initially reached to a maximum intensity at  $-1.2\text{ A}$  and stayed for 15 minutes. Then the current decreased to  $-1.0\text{ A}$  and stayed at a plateau for almost one hour. Finally at the end of the reductions, the current dropped dramatically, which suggested the completeness of reduction[17]. NiO reduction in the used salt resulted in higher current responds and shorter reduction duration time. Fig. 5.4b explained the changes in materials at different current stages in terms of the formation and movement of the three-phase interlines. When the potential was applied, the NiO at the surface of the pellet was reduced to Ni metal. At this point, the three-phase interlines Ni|NiO|electrolyte was formed, and the current increased. Then as the interline move to the inside of the pellet, the diffusion path becomes longer, and that caused the current decrease. As the electrolysis continues, an equilibrium was established between the metal generation and long diffusion distance, and current stayed at a plateau. The final current drop indicated the completion of the reduction to a uniform Ni particle.

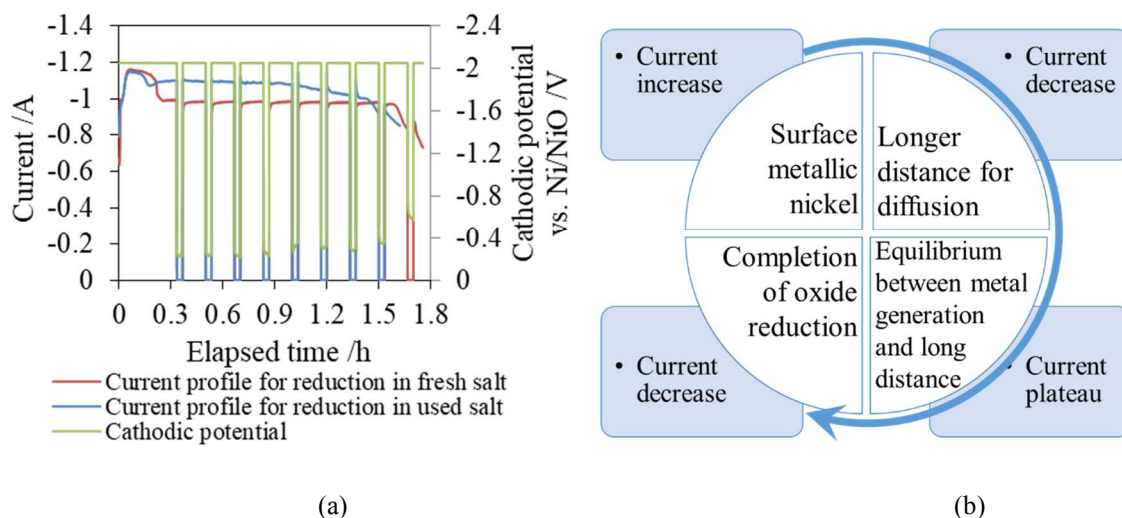


Figure 5.4 (a) Current-time profiles for NiO reductions in fresh (red) and used (blue) 1.0 w.t. %  $\text{Li}_2\text{O}/\text{LiCl}$  salt at  $-0.3\text{ V vs. Li/Li}^+$  using 100% of the theoretical charge, and cathodic potential-time profile (green) for reductions. (b)

The fresh NiO pellets are yellowish green (Fig. 5.5a). The retrieved reduced samples are black powders after washed, dried and grinded (Fig. 5.5b). When the black powders are compressed into a round disc under 6 metric tons, it shows metallic shining appearance (Fig. 5.5c). The color change from black to metallic gold is an optical effect. The black powder status indicates the Ni metal particles are really fine, possibly in the range of nanometers.[100,101] When the fine powders are compressed into disc, the Ni particle size increases and forms a smooth surface with a metallic luster.

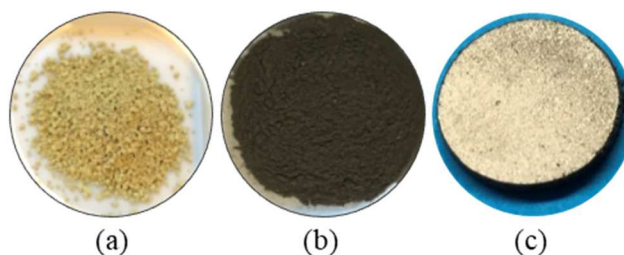


Figure 5.5 (a) NiO pellet samples before reduction; (b) NiO powder samples after reduction; (c) Ni metal disc in  $1/16''$  thickness (compressed powders from Fig 5.4b)

### 5.4.3 Post-reduction XRD and TGA Analysis

The XRD analyses (Fig. 5.6) of the two reduced NiO samples show only metallic Ni peaks without the NiO phase, suggesting a 100% reduction extent of NiO with 100% of the theoretical charge. Thus, the current efficiency for NiO electrolytic reduction is estimated as 100%, which is high



compared with the results from NiO electroreduction in literatures.[32] Moreover, the XRD results confirmed that the dramatic current decrease in current-time profile (Fig. 5.4 red and blue) is a sign for approaching the complete reductions. The particle size for Ni product is estimated through the Scherrer equation:  $d = \frac{K\lambda}{\beta \cos\theta}$ . K is 0.9 as the shape factor;  $\lambda$  is the X-ray wavelength, 1.5406 Å;  $\theta$  is the Bragg angle in rad.  $\beta$  is the line broadening at half the maximum intensity, 0.00365 rad. The particle size is calculated as 41 nm, which confirms that the black production powder is Ni nanopowder.

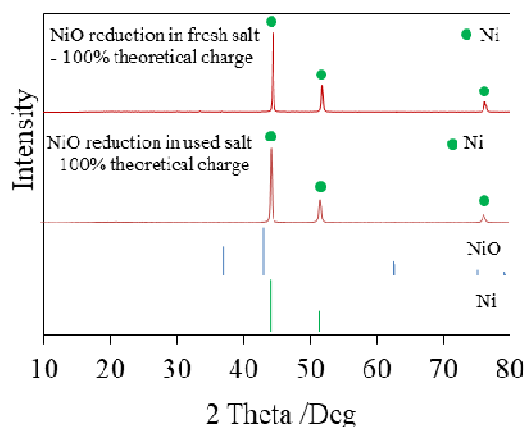


Figure 5.6 XRD profiles for reduced NiO samples in fresh and used salt 1 w.t.% Li<sub>2</sub>O/LiCl at 650 °C.

For more accurate estimations on reduction extent, the reduced sample was also analyzed with TGA in an oxidative environment (Fig. 5.7). In the first half hour, the sample showed a weight loss due to moisture release and free carbon combustion.[102] Then the weight started to increase and reached constant within 2 hours. The net weight gain was 2.673 mg (from 10.314 mg to 12.987 mg), which was due to the oxidation of nickel metal particles ( $\text{Ni} + 1/2 \text{O}_2 \rightarrow \text{NiO}$ ). Consequently, based on TGA analysis, the reduction extent is 96.1% and the current efficiency is 96.1%.

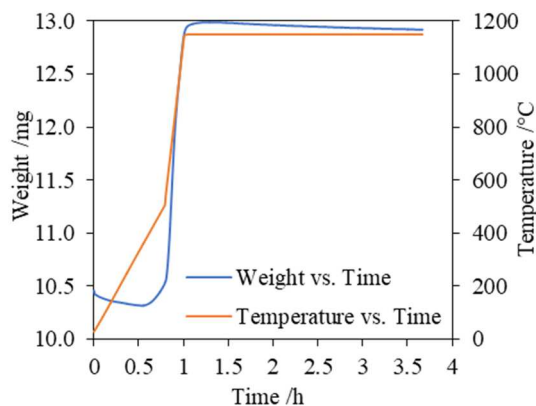
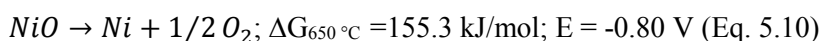
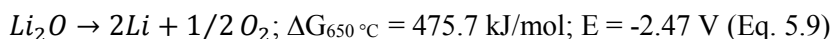
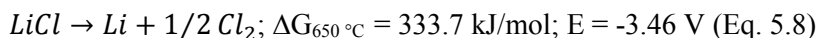


Figure 5.7 TGA analysis profile for the reduced Ni sample (10.314 mg) at a temperature programming with dry air flow rate at  $20 \text{ ml min}^{-1}$ .

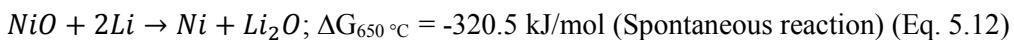
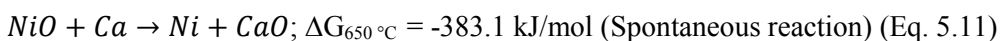
#### 5.4.4 NiO Reduction Mechanism

In this study, NiO was reduced in 1.0 w.t. %  $\text{Li}_2\text{O}/\text{LiCl}$  salt at  $-0.3 \text{ V}$  vs.  $\text{Li}/\text{Li}^+$  at  $650 \text{ }^\circ\text{C}$  with an unprecedented high current efficiency 96.1%. The Gibbs free energy change of NiO, LiCl,  $\text{Li}_2\text{O}$  decomposition reactions at  $650 \text{ }^\circ\text{C}$  were calculated using HSC chemistry (Eq. 5.8~5.10). The corresponding decomposition potentials were obtained based on the thermodynamics calculation ( $E = -\frac{\Delta G}{zF}$ ). Theoretically, the decomposition potential of NiO is more positive than that of  $\text{Li}_2\text{O}$  and LiCl (Eq. 5.8 vs. Eq. 5.10), which means NiO can be reduced before the salt decomposition as the potential becomes more negative.



A similar high NiO reduction current was observed using a metallic cavity electrode in  $\text{CaO}/\text{CaCl}_2$ . [97] No calcium-containing oxide phases were observed in NiO reduction. When the reduction potentials were at a more negative value than that of NiO decomposition, and even more negative than that of salt decomposition potential, two different notable mechanisms were proposed by the OS process and FFC-Cambridge process. In the OS process, the *in situ* generated alkaline metal reacts with metal oxides for reduction. The *in situ* generated Ca in molten  $\text{CaCl}_2$  has been involved in

reducing the NiO to Ni metal.[30] Thermodynamically, both the reactions with Ca and Li for NiO reduction are spontaneous according to Eq. 5.11 and 5.12.



The NiO reduction follows a shrinking core model (Fig. 5.8). Reduction starts on exterior of the grain, and the surface of the pellets is reduced to the metal shell. As the reduction proceeds inwards, the metal shell becomes thicker towards the core and finally converts to uniform metal grains. A newly formed Ni metal layer is inserted between NiO and alkaline metal. Thus, the reduction also follows a secondary mechanism. The Li metal plays a role as an electron donor similar as a current collector in molten LiCl.[104] Therefore, the high current efficiency in NiO reduction is possibly due to a combined mechanism with both the OS and FFC processes. In addition, the generated Li is an electron carrier in transferring electrons to the NiO center core through the Ni shell, which is also an excellent conductor with low resistance. The reduction process is fast, compared with around 11 h in literature.[31] The reduction mechanism for the NiO reduction is proposed as follows.

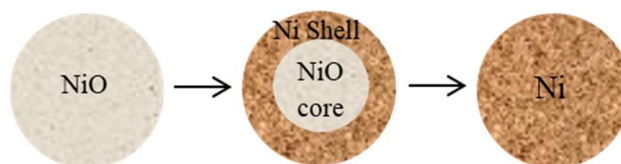
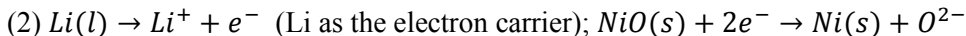
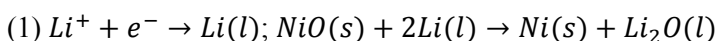


Figure 5.8 Schematic diagram of a shrinking core model for NiO electroreduction.[14]

## 5.5 Conclusion

Lithiothermic NiO reductions were investigated in 1 w.t. % Li<sub>2</sub>O/LiCl molten salt at 650 °C. The reduction was a fast process that 2 g NiO particles could be fully reduced in two hours at -2.05 V (vs. Ni/NiO, -0.3 V vs. Li/Li<sup>+</sup>). The current efficiency for NiO electrolytic reduction is 96.1% with 100% of the theoretical charge. The unprecedented high current efficiency and fast reduction process are due to a combined reduction mechanism. The NiO reduction at overpotentials involve both a lithiothermic reduction and an electrolytic reduction. In addition, the salt after reduction can be reused for more electrolytic studies.

Furthermore, the successful and repeatable NiO reductions with a high current efficiency proves the reduction method is well designed and suitable in reductions of other metal oxides.

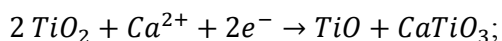
## Chapter 6: Electroreduction of Titanium Dioxide in Molten Li<sub>2</sub>O/LiCl

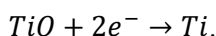
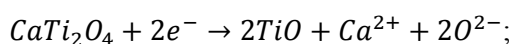
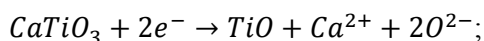
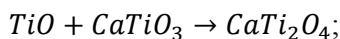
### 6.1 Abstract

The electrolytic reductions of TiO<sub>2</sub> were investigated in 1 w.t.% Li<sub>2</sub>O/ LiCl at 650 °C by directly controlling the cathodic reduction potentials. A multistep reduction mechanism was proposed, accompanied with a shrinking-core model and three phase interlines process. The reduction mechanism included the chemical insertion reaction and partial reduction to generate LiTiO<sub>2</sub>. Lithium titanates products, Li<sub>2</sub>TiO<sub>3</sub> and LiTiO<sub>2</sub>, were identified and quantified through the X-ray diffraction analysis. Reduction of LiTiO<sub>2</sub> was the key rate-determining step in electrolytic reduction of TiO<sub>2</sub> in molten lithium salt. The process was controlled by the accumulation of Li<sub>2</sub>O and the slow diffusion of the Li<sub>2</sub>O within the solid particles. The highest reduction extent obtained in this study is 25%, with the current efficiency at 16.7%.

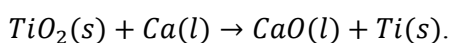
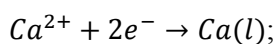
### 6.2 Introduction

Titanium metal is an excellent structural metal due to its low density, high strength, and resistance to corrosion. However, it is very expensive because the extraction of titanium from titanium dioxide is very costly. The industrial approach to reduce TiO<sub>2</sub> is through the traditional Kroll process, which releases hazardous Cl<sub>2</sub> gas and is operated at a temperatures as high as 1100 °C.[4] Electrochemical methods have been established in the recent decades. TiO<sub>2</sub> electrolytic reduction in molten CaCl<sub>2</sub> is a promising technology for low-cost Ti extraction at temperatures between 850 °C and 950 °C.[7,9,13,20,12,18] The Fray – Farthing – Chen (FFC) Cambridge process reduces TiO<sub>2</sub> directly by electrons through titanate intermediates CaTiO<sub>3</sub> and CaTi<sub>2</sub>O<sub>4</sub>, and titanium suboxides such as Ti<sub>2</sub>O<sub>3</sub> and TiO [12,14,18,20], following a shrinking core model.[14] Reduction kinetics pathways and mechanisms were examined using the scanning electron microscope (SEM), X-ray diffraction (XRD), *in situ* synchrotron X-ray, etc.[10,12,13] The electroreduction of solid oxides went through the propagation of the metal|oxide|electrolyte three-phase interlines (3PIs).[15,16] The current efficiency of titanium metal depended the pellet properties. Various precursors were studied to alter the reduction pathway or phase transformation, including perovskite CaTiO<sub>3</sub> [9], highly porous TiO<sub>2</sub> [19,20], dense TiO<sub>2</sub> precursor [18], and different oxide particle sizes [22]. However, there was no significant improvement on current efficiency achieved. A low current efficiency (10%~40%) and long operational hours were the limiting factors of the FFC process.[12,18,20]

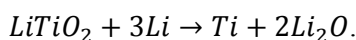
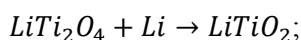
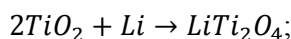
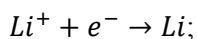




Different from the FFC process, the Ono – Suzuki (OS) process presumes that TiO<sub>2</sub> is reduced by *in situ* generated calcium metal.[23–26,29] Calcium metal is generated at the cathode and reduce the TiO<sub>2</sub> to Ti metal. The current efficiency of the OS process was 12.9%, producing a highly purity metal with very low residual oxygen.[24]



Molten lithium chloride salts were also employed in electroreduction at 650 °C, which is much lower than the temperature required in molten calcium salts. The pure LiCl melt was tested in the electrolytic reduction of TiO<sub>2</sub>. However, this system was limited to the formation of lithium titanate compounds (LiTi<sub>2</sub>O<sub>4</sub> and LiTiO<sub>2</sub>), but not metallic titanium. It was because the LiTiO<sub>2</sub> is thermodynamically more stable than LiCl.[19,59] To increase the oxygen ion activity, Li<sub>2</sub>O was added to the original LiCl. Lithiothermic TiO<sub>2</sub> reductions were carried out in 1 w.t.% Li<sub>2</sub>O/LiCl, and an interrupted controlled potential was applied.[61] The electrochemical reduction of TiO<sub>2</sub> reached almost 100% reduction extent to Ti metal, and achieved a current efficiency as high as 72%.[61,105] Therefore, the Li<sub>2</sub>O/LiCl molten salt mixture was an alternative electrolyte to replace molten calcium salts for TiO<sub>2</sub> reductions at a high current efficiency and lower operation temperatures. The reduction mechanism for TiO<sub>2</sub> reduction in lithium salts was proposed as follows.[61]



In this study, TiO<sub>2</sub> electrolytic reductions in 1 w.t.% Li<sub>2</sub>O/LiCl at 650 °C were investigated systematically by accurately controlling cathodic potentials and charges to gain better understanding of the TiO<sub>2</sub> reduction mechanism. The reduced products were analyzed with X-ray diffraction (XRD). The complementary analysis on fresh salts (lithium salts free from any TiO<sub>2</sub> reduction) and used salts

(lithium salts after  $\text{TiO}_2$  reductions) were performed using cyclic voltammetry measurements. Inductively Couple Plasma – Mass Spectrometry analysis (ICP-MS) was involved to identify and quantify the changes in the lithium salts due to the  $\text{TiO}_2$  reductions. The reduction mechanism was derived based on the experimental results.

### 6.3 Experimental

1 w.t.% of  $\text{Li}_2\text{O}/\text{LiCl}$  was used as the electrolyte for  $\text{TiO}_2$  electrolytic reduction at  $650\text{ }^\circ\text{C}$ . High purity lithium chloride ( $\text{LiCl}$ , 99.995% metals basis, ultra-dry, Alfa Aesar) and lithium oxide ( $\text{Li}_2\text{O}$ , 99.5%, Alfa Aesar) were used as received. Titanium dioxide powders ( $\text{TiO}_2$ , 99.995% metals basis, Alfa Aesar) were pelletized, and sieved between mesh 60 and 20 (particles size  $0.25\text{ mm} \sim 0.85\text{ mm}$ ). For each  $\text{TiO}_2$  reduction run, 2 g  $\text{TiO}_2$  particles were loaded in a stainless steel basket and reduced in a 150 g salt bath.

A three-electrode electrochemical cell within an argon glovebox (MBraun, Labmaster 200G) was used for CV measurements and  $\text{TiO}_2$  electrolytic reductions. The moisture and oxygen level in the glovebox were controlled below 1 ppm. The electrochemical cell consisted of a working electrode, a Ni/NiO reference electrode and a glassy carbon crucible as the counter electrode (HTW GAZ30; height=150 mm, outer diameter=60 mm, and thickness=3 mm). A Kerrlab electric furnace (Auto Electro Melt Maxi) was used to heat the molten salts to  $650\text{ }^\circ\text{C}$ . VersaSTAT 4 Potentiostat (Princeton Applied Research) interfaced with experiments in the gloveboxes was used for electrochemistry measurement up to 2 Amps with VersaStudio for data acquisition. This three-electrode electrochemical cell has shown high current efficiency and reliability in previous study on NiO reduction.[87]

Cyclic voltammetry measurements were performed in molten 1 w.t.%  $\text{Li}_2\text{O}/\text{LiCl}$  at  $650\text{ }^\circ\text{C}$  at a scan rate of  $20\text{ mV s}^{-1}$  using a stainless steel wire ( $\text{DI}=0.64\text{ mm}$ ) working electrode. After a  $\text{TiO}_2$  reduction was conducted with 80% of the theoretical charge, a CV cycle was measured with the basket submerged in the salt. Single CVs were performed in fresh salt and in the used salts after reductions with 150% of the theoretical charge. The first single CV measurement was taken in the fresh 1 w.t.%  $\text{Li}_2\text{O}/\text{LiCl}$ . After a  $\text{TiO}_2$  reduction with 150% of the theoretical charge was conducted in the salt, the basket was removed from the salt, and the salt was cooled down to room temperature. The second CV was measured after this salt was reheated and stabilized at  $650\text{ }^\circ\text{C}$ . Then, another  $\text{TiO}_2$  reduction with 150% of the theoretical charge was carried out in the used salt and the basket was removed from the salt after. The third CV was performed in the same batch of used salt after the salt was solidified after the reduction and reheated to  $650\text{ }^\circ\text{C}$ .

The TiO<sub>2</sub> electrolytic reductions were carried out in molten 1 w.t.% Li<sub>2</sub>O/LiCl at 650 °C using the cathode basket bundle as the working electrode which is described in Session 5.3.2.[87] The cathode basket bundle consisted of a stainless steel rod (DI=1.59 mm) as an electron collector at the center of a stainless steel cathode basket (height=2.5 cm, DI=1 cm) with 2 g TiO<sub>2</sub> particles packed around the stainless steel rod. The electrode bundle was soaked in molten salt for 1~1.5 hours before the electrolytic reduction. To determine the optimal potential for TiO<sub>2</sub> reduction, various cathodic potentials including -0.2 V, -0.3 V and -0.4 V vs. Li/Li<sup>+</sup> were studied, respectively, with 80% of the theoretical charge. The constant reduction potential was applied with an interval mode (electrolysis 8 minutes on and 2 minutes off) to minimize the excessive lithium metal generated on the working electrode. To increase the reduction extent, charges higher than 100% of the theoretical charge, including 130% and 150% were applied at the optimal TiO<sub>2</sub> reduction potential, which was -0.3 V vs. Li/Li<sup>+</sup> in this study. After reductions, the electrode bundles were lifted out of the molten salt, and the whole cell cooled down to room temperature for further product analysis. To determine the starting sample composition for the electrolytic reduction, a soaking test on TiO<sub>2</sub> was performed by immersing TiO<sub>2</sub> particles in the 1 w.t.% Li<sub>2</sub>O/LiCl salt at 650 °C for 5 hours, without electrolysis.

After the soaking tests and reductions, the cooled cathode basket assemblies were transferred out of the glovebox and rinsed with nanopore water to remove the residual Li<sub>2</sub>O/LiCl solid salts. Then, the samples were retrieved and rinsed in acetone for quick dry. The washed sample was then dried overnight in vacuum at room temperature. The completely dried samples were grinded into fine powders using a pestle and mortar. The powder samples were analyzed using the X – ray Diffraction (Rigaku SmartLab XRD) with Cu K- $\alpha$  radiation at 40 kV and 30 mA. The scan range (2 theta) was from 10° to 80° at 4 deg min<sup>-1</sup>. The XRD data were analyzed with the Rietveld refinement using the WPPF (Whole Powder Pattern Fitting) within PDXL 2 from Rigaku, based on which TiO<sub>2</sub>, Li<sub>2</sub>TiO<sub>3</sub> and LiTiO<sub>2</sub>, were identified and quantified. In this study, the reduction extent and current efficiency were estimated by Eq. 6.1 and Eq. 6.2, respectively.

$$\text{Reduction extent} = 100\% - \frac{4 \times \text{TiO}_2 \text{ mol\%} + 4 \times \text{Li}_2\text{TiO}_3 \text{ mol\%} + 3 \times \text{LiTiO}_2 \text{ mol\%}}{4} \quad (\text{Eq. 6.1})$$

$$\text{Current efficiency} = \frac{z n_{\text{LiTiO}_2} F}{\text{Total applied charge}} \quad (\text{Eq. 6.2})$$

where z is the electron transferred for reduction of TiO<sub>2</sub> to the reduction products. In this study, z was 1, because only partial reduction to LiTiO<sub>2</sub> was obtained.  $n_{\text{LiTiO}_2}$  is the molar mass of LiTiO<sub>2</sub>. F is the Faraday constant, 96485 C mol<sup>-1</sup>. Total applied charge is generally represented in terms of the theoretical charge (Eq. 6.3) for the TiO<sub>2</sub> complete reduction to Ti metal.



100% of the Theoretical charge =  $4n_{\text{TiO}_2}F$  (Eq. 6.3)

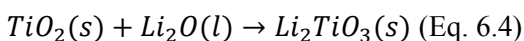
The used salt after two consecutive  $\text{TiO}_2$  reductions at -0.3 V vs.  $\text{Li/Li}^+$  with 150% of the theoretical charge was sampled for the elemental analysis. ICP-MS (Agilent 7900 series) was used for the quantitative analysis of Ti composition in the used salts.

Density Function Theory (DFT) modelling provides theoretical understanding to determine the  $\text{TiO}_2$  reduction pathway and mechanism. Vienna Ab Initio Simulation Package (VASP) was used for the DFT calculation.[106] Gibbs free energy of formation for titanate intermediates including  $\text{Li}_2\text{TiO}_3$  and  $\text{LiTiO}_2$  were calculated. The calculations of total energies and structural relaxations were carried out using the projector augmented wave (PAW) method to treat core electrons.[107] The Helmholtz free energy,  $F(V,T)$ , a function of both crystal volume (V) and temperature (T), can be expressed by  $F(T, V) = E(V) + F_{\text{vib}}(V, T) + F_{\text{el}}(V, T)$ , where  $E(V)$  is the total energy.  $F_{\text{vib}}(V, T)$  and  $F_{\text{el}}(V, T)$  represent the vibrational and thermal electronic contributions to the free energy, respectively.  $E(V)$  of a given crystal can be described by the equation of state (EOS), and its values at different volumes were obtained directly from periodic DFT calculations. Here, the 4<sup>th</sup>-order Birch-Murnaghan (BM4) EOS ( $E(V) = a + bV^{-2/3} + cV^{-4/3} + dV^{-2}$ ) was used.

## 6.4 Results and Discussion

### 6.4.1 Soaking Test of $\text{TiO}_2$

Soaking is a general step for electrolytic measurement with small particle samples.[95] It is proceeded to guarantee the electrolytic stability of the system.[108] The soaked  $\text{TiO}_2$  sample in 1 w.t.%  $\text{Li}_2\text{O/LiCl}$  at 650 °C consists of three phases including 60.8 w.t.% of  $\text{TiO}_2$ , 38 w.t.% of  $\text{Li}_2\text{TiO}_3$ , and 1.2 w.t.% of  $\text{Li}_{0.54}\text{Ti}_{2.86}\text{O}_6$  based on the XRD analysis (Fig. 6.1) and the Rietveld Refinement (Table 6.1). This was the first time  $\text{Li}_2\text{TiO}_3$  phase was identified structurally for  $\text{TiO}_2$  electrolytic reduction in  $\text{LiCl}$  salts. The  $\text{Li}_2\text{TiO}_3$  was formed chemically by intercalation of  $\text{Li}_2\text{O}$  into  $\text{TiO}_2$  on the surface of  $\text{TiO}_2$  particles through Eq. 6.4. Production of  $\text{Li}_2\text{TiO}_3$  was analogous to the formation of perovskite  $\text{CaTiO}_3$  during the  $\text{TiO}_2$  reduction in calcium salts melt systems.[12,13,18,20]



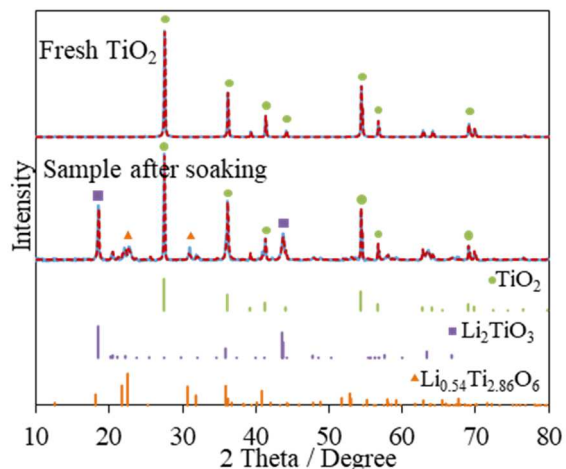


Figure 6.1 XRD results (blue solid lines) and Rietveld refinement fittings (red dash lines, with  $\text{TiO}_2$ ,  $\text{Li}_2\text{TiO}_3$  and  $\text{Li}_{0.54}\text{Ti}_{2.86}\text{O}_6$ ) of fresh  $\text{TiO}_2$  and product soaked in molten 1 w.t.%  $\text{Li}_2\text{O}/\text{LiCl}$  for 5 hours at  $650\text{ }^\circ\text{C}$

Table 6.1 Rietveld refinement results for the soaked products

Products composition (w.t. %)	$\text{TiO}_2$	60.8
	$\text{Li}_2\text{TiO}_3$	38.0
	$\text{Li}_{0.54}\text{Ti}_{2.86}\text{O}_6$	1.2
R factors	$R_{wp}$ (%)	15.98
	$R_p$ (%)	11.23
	$R_e$ (%)	5.57
	S	2.8653
	$\chi^2$	8.2101
	Maximum shift e.s.d.	0.339
Phases	Structure Parameters	
$\text{TiO}_2$ Rutile, syn (01-084-1284) Space group: 136 : P42/mnm	a (Å)	4.544644
	b (Å)	4.544644
	c (Å)	2.927009
	$\alpha$ (Degree)	90
	$\beta$ (Degree)	90
	$\gamma$ (Degree)	90
	V (Å <sup>3</sup> )	60.452834
	Scale factor	68(2)
		U

	Gaussian peak width parameters ( $^{\circ 2}$ )	V	-0.149(4)
		W	0.001(4)
Li <sub>2</sub> TiO <sub>3</sub> Dilithium titanate (IV) (01-080-7163) Space group: 15 : C12/c1,unique-b,cell-1	a (Å)	5.017(3)	
	b (Å)	8.717(5)	
	c (Å)	9.608(6)	
	$\alpha$ (Degree)	90	
	$\beta$ (Degree)	99.74(5)	
	$\gamma$ (Degree)	90	
	V (Å <sup>3</sup> )	414.1(4)	
	Scale factor	40.3 (19)	
	Gaussian peak width parameters ( $^{\circ 2}$ )	U	0.00(14)
		V	0.24(4)
W		0.00(3)	
Li <sub>0.54</sub> Ti <sub>2.86</sub> O <sub>6</sub> Lithium titanium oxide	a (Å)	N/A	
	b (Å)	N/A	
	c (Å)	N/A	
	$\alpha$ (Degree)	N/A	
	$\beta$ (Degree)	N/A	
	$\gamma$ (Degree)	N/A	
	V (Å <sup>3</sup> )	N/A	
	Scale factor	0.99(8)	
	Gaussian peak width parameters ( $^{\circ 2}$ )	U	1.6(13)
		V	-1(4)
W		0.82(16)	

The formation of Li<sub>2</sub>TiO<sub>3</sub> is spontaneous in 1 w.t.% Li<sub>2</sub>O/LiCl at 650 °C. However, 60.8 w.t.% of 2 g TiO<sub>2</sub> persisted after soaking for 5 hours, suggesting the diffusion of Li<sub>2</sub>O through Li<sub>2</sub>TiO<sub>3</sub> layer was very slow. The minor Li<sub>0.54</sub>Ti<sub>2.86</sub>O<sub>6</sub> phase also indicates Li<sub>2</sub>O reacted with bulk TiO<sub>2</sub> phase nonstoichiometrically because the surface Li<sub>2</sub>TiO<sub>3</sub> shell slows down the diffusion of Li<sub>2</sub>O to reach the fresh TiO<sub>2</sub> core.

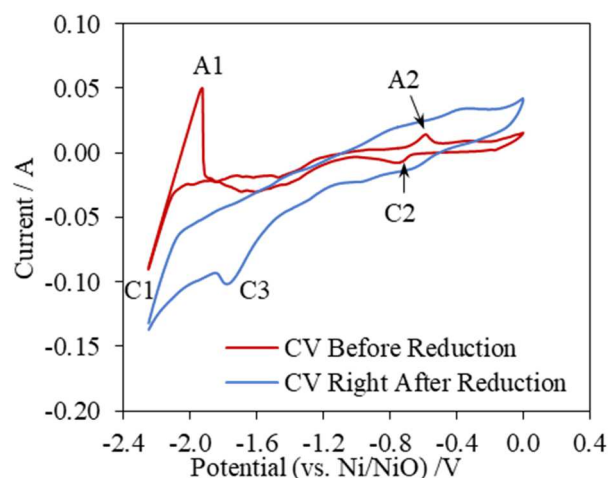
6.4.2 Effect of Reduction Potential on TiO<sub>2</sub> Electrolytic Reductions

Figure 6.2 CVs in fresh 1 w.t.% Li<sub>2</sub>O/LiCl and the used salt right after TiO<sub>2</sub> reduction at -0.3 V vs. Li/Li<sup>+</sup> with 80% of the theoretical charge at 650 °C (Scan rate = 20 mV s<sup>-1</sup>).

The CV in fresh 1 w.t.% Li<sub>2</sub>O/LiCl at 650 °C shows several anodic and cathodic peaks, which were also identified in our previous work (Fig. 6.2, Red curve).[87] The redox potential lithium ions ( $Li^+ + e^- \leftrightarrow Li$  (C1, A1)) corresponds to the peak at -1.93 V vs. Ni/NiO.[108] Peak A2 and C2 are attributed to the reversible oxidation of carbon  $C + 3O^{2-} \leftrightarrow CO_3^{2-} + 4e^-$  (A2, C2).[109] Compared with the CV in fresh salt, post reduction CV in the salt used in TiO<sub>2</sub> reduction at -0.3 V vs. Li/Li<sup>+</sup> with 80% of the theoretical charge shows a new cathodic peak (C3) at -1.76 V while the Li metal re-oxidation peak (A1) is missing (Fig. 6.2, Blue curve). The C3 peak corresponds to the electrolytic reduction of dissolved titanate species.[105] The missing re-oxidation peak of Li metal also means that the *in situ* generated Li metal chemically consumed by dissolved titanium species in the used salt.[105]

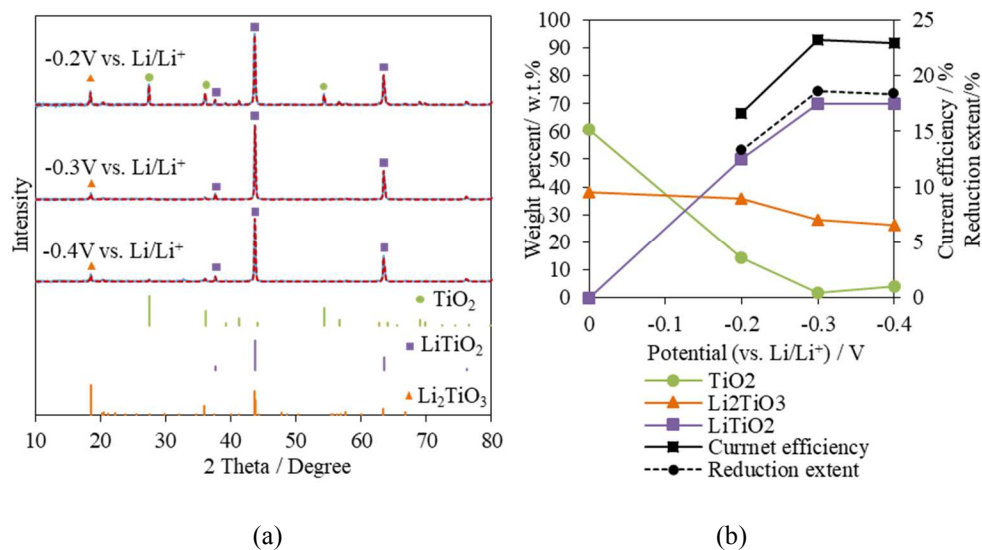


Figure 6.3 XRD results (blue solid lines) and Rietveld refinement analysis (red dash lines) of reduced TiO<sub>2</sub> samples at -0.2 V, -0.3 V and -0.4 V vs. Li/Li<sup>+</sup> with 80% of the theoretical charge; b) Reduced sample compositions, current efficiencies, and reduction extents for TiO<sub>2</sub> reduction at -0.2 V, -0.3 V and -0.4 V vs. Li/Li<sup>+</sup>.

The XRD analysis results for products in TiO<sub>2</sub> electrolytic reduction at cathodic potentials -0.2 V, -0.3 V and -0.4 V vs. Li/Li<sup>+</sup> in 1 w.t.% Li<sub>2</sub>O/LiCl at 650 °C with 80% of the theoretical charge are presented in Fig. 6.3a. For all of the three reduced samples, three titanium-containing phases are identified including unreacted TiO<sub>2</sub>, Li<sub>2</sub>TiO<sub>3</sub> and LiTiO<sub>2</sub> comparing with the standard XRDs. There is no other reduced product or metallic Ti detected. The quantitative compositional changes (Table 6.2) for the three samples reduced at different cathodic potential are shown together with the soaked TiO<sub>2</sub> sample based on Rietveld refinement analysis (Fig. 6.3b). Compared with soaked TiO<sub>2</sub> sample, the unreacted TiO<sub>2</sub> content for the sample reduced at -0.2 V is decreased from 60.8 w.t.% to 14.5 w.t.%, while Li<sub>2</sub>TiO<sub>3</sub> is 35.7 w.t.% remaining the similar level. The partial reduction product LiTiO<sub>2</sub> takes 49.8 w.t.%. These results indicate that TiO<sub>2</sub> was reduced to LiTiO<sub>2</sub> directly by the *in situ* generated Li metal at -0.2 V vs. Li/Li<sup>+</sup> (Eq. 6.5).

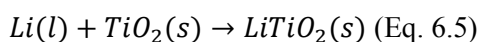


Table 6.2 Rietveld refinement results for the reduced products using 80% of the theoretical charge

Reduction potential (vs. Li/Li <sup>+</sup> )		-0.2 V	-0.3 V	-0.4 V	
Products composition w.t. %	TiO <sub>2</sub>	14.54	1.69	4.05	
	Li <sub>2</sub> TiO <sub>3</sub>	35.66	28.27	26.22	
	LiTiO <sub>2</sub>	49.80	70.04	69.73	
R factors	R <sub>wp</sub> (%)	6.93	6.06	6.99	
	R <sub>p</sub> (%)	4.67	4.16	4.77	
	R <sub>e</sub> (%)	5.73	5.51	5.51	
	S	1.2054	1.0955	1.2644	
	$\chi^2$	1.453	1.2002	1.5986	
	Maximum shift e.s.d.	0.682	0.359	0.075	
Phases	Structural Parameters				
TiO <sub>2</sub> Rutile, syn (01-084-1284) Space group: 136 : P42/mnm	a (Å)	4.58666	4.58666	4.58666	
	b (Å)	4.58666	4.58666	4.58666	
	c (Å)	2.95407	2.95407	2.95407	
	$\alpha$ (Degree)	90	90	90	
	$\beta$ (Degree)	90	90	90	
	$\gamma$ (Degree)	90	90	90	
	V (Å <sup>3</sup> )	62.146099	62.146099	62.146099	
	Scale factor	16.3(9)	3.2(14)	5.7(15)	
	Gaussian peak width parameters ( $\sigma^2$ )	U	0.16(2)	0.19(5)	0.09(4)
		V	-0.16(3)	-0.26(8)	-0.157(11)
W		0.011(7)	0.06(2)	0.051(4)	
LiTiO <sub>2</sub> Lithium titanium(III) oxide (01-074-2257) Space group: 225 : Fm-3m	a (Å)	4.1372(4)	4.1457(5)	4.1355(2)	
	b (Å)	4.1372(4)	4.1457(5)	4.1355(2)	
	c (Å)	4.1372(4)	4.1457(5)	4.1355(2)	
	$\alpha$ (Degree)	90	90	90	
	$\beta$ (Degree)	90	90	90	
	$\gamma$ (Degree)	90	90	90	
	V (Å <sup>3</sup> )	70.813(11)	71.254(15)	70.729(7)	
	Scale factor	32.8(15)	62.6(17)	54.8(17)	
	Gaussian peak width parameters ( $\sigma^2$ )	U	0.27(3)	0.24(6)	0.204(10)
		V	-0.16(3)	-0.26(8)	-0.157(11)
W		0.011(7)	0.06(2)	0.051(4)	
Li <sub>2</sub> TiO <sub>3</sub> Dilithium titanate (IV)	a (Å)	5.0604(16)	5.053(3)	5.0588(8)	
	b (Å)	8.777(5)	8.782(6)	8.7354(13)	

(01-080-7163) Space group: 15 : C12/c1,unique-b,cell-1	c (Å)		9.760(4)	9.714(6)	9.7254(17)
	$\alpha$ (Degree)		90	90	90
	$\beta$ (Degree)		100.12(3)	99.45(7)	99.824(14)
	$\gamma$ (Degree)		90	90	90
	V (Å <sup>3</sup> )		426.7(3)	425.2(5)	423.22(12)
	Scale factor		9.0(7)	12.4(8)	9.2(9)
	Gaussian peak width parameters (° <sup>2</sup> )	U	0.17(3)	0.6(2)	0.092(11)
	V	-0.16(3)	-0.26(8)	-0.157(11)	
	W	0.011(7)	0.06(2)	0.051(11)	

TiO<sub>2</sub> content in the TiO<sub>2</sub> sample reduced at -0.3 V further decreased to 1.69 w.t.% which is close to the XRD detection limit (around 2%). The amount of intermediate Li<sub>2</sub>TiO<sub>3</sub> decreased significantly from 35.7 w.t.% to 28.3 w.t.% while the reduction product LiTiO<sub>2</sub> increased from 49.8 w.t.% to 70.4 w.t.%. It suggests that both Li<sub>2</sub>TiO<sub>3</sub> and TiO<sub>2</sub> were transformed into LiTiO<sub>2</sub> at a higher reduction potential and TiO<sub>2</sub> tended to be more reducible than Li<sub>2</sub>TiO<sub>3</sub>. As the reduction potential further increased to -0.4 V vs. Li/Li<sup>+</sup>, both TiO<sub>2</sub> and Li<sub>2</sub>TiO<sub>3</sub> varied slightly within the range of XRD limit while the concentration of LiTiO<sub>2</sub> stayed almost the same.

The increasing reduction potential promotes TiO<sub>2</sub> electrolytic reductions to a certain extent and then reached the limit. The optimal reduction potential for TiO<sub>2</sub> reduction in the 1w.t.% Li<sub>2</sub>O/LiCl salt is determined as -0.3 V vs. Li/Li<sup>+</sup>. The highest reduction extent at 18.6% was obtained in reduction at -0.3 V vs. Li/Li<sup>+</sup> with 80% of the theoretical charge (Fig 6.3b). A similar trend was also observed in the TiO<sub>2</sub> electrolytic reduction in CaO/CaCl<sub>2</sub>. [20] The extra amount of Li metal generated *in situ* does not always help the reduction of TiO<sub>2</sub>. [110] Reduction at -0.4 V vs. Li/Li<sup>+</sup> results in a reduction extent at 18.4%, slightly lower than that in reduction at -0.3 V. It is found in a previous study that the ratio of Ti<sup>4+</sup>/Ti<sup>3+</sup> increased with Li concentration in the molten salt. [110] So, in this study, less amount of Li<sub>2</sub>TiO<sub>3</sub> was reduced to LiTiO<sub>2</sub> in the presence of more excess Li metal generated in the reduction at -0.4 V. The corresponding highest current efficiency achieved is 23% for TiO<sub>2</sub> reduction at -0.3 V (vs. Li/Li<sup>+</sup>) using 80% of the theoretical charge. The current efficiency at 23% in this study is comparable with the current efficiency reported for the FFC process for TiO<sub>2</sub> in CaO/CaCl<sub>2</sub> at 10~40% [18,20], and higher than that in the calciothermic TiO<sub>2</sub> reduction in CaO/CaCl<sub>2</sub> at 12.9% [24].

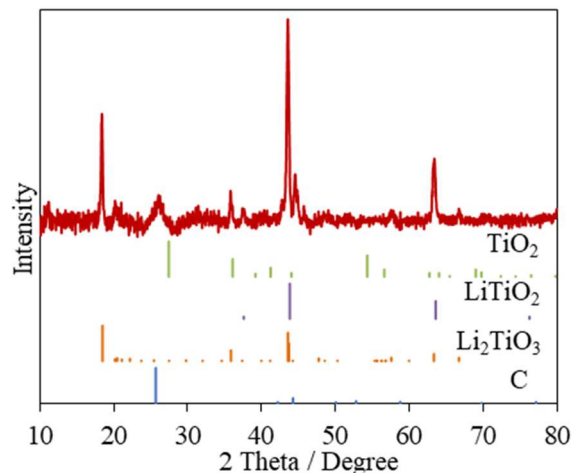


Figure 6.4 XRD for salt sample on the external surface of the cathode basket used for  $\text{TiO}_2$  reduction at  $-0.3 \text{ V}$  vs.  $\text{Li}/\text{Li}^+$  using 80% of the theoretical charge.

Lithium titanates  $\text{Li}_2\text{TiO}_3$  and  $\text{LiTiO}_2$ , as well as carbon, are identified in the materials on the external surface of the cathode basket used for  $\text{TiO}_2$  reduction at  $-0.3 \text{ V}$  vs.  $\text{Li}/\text{Li}^+$  using 80% of the theoretical charge based on XRD analysis (Fig. 6.4). This result suggests some of the  $\text{Li}_2\text{TiO}_3$  and  $\text{LiTiO}_2$  were dissolved into the 1 w.t.%  $\text{Li}_2\text{O}/\text{LiCl}$  salt during  $\text{TiO}_2$  electrolytic reduction at  $650 \text{ }^\circ\text{C}$ . Dissolution of  $\text{Li}_2\text{TiO}_3$  was also observed in studies on  $\text{TiO}_2$  interaction with  $\text{Li}_2\text{O}/\text{LiCl}$  salts.[110] It was found in literature that  $\text{TiO}_2$  was soluble in  $\text{Li}_2\text{O}/\text{LiCl}$  but not in an environment containing Li metal.[110] It explains the absence of  $\text{TiO}_2$  in the materials on the outside of the basket during the lithiothermic reduction. The titanates deposit on the wall of the basket and migrate gradually to the outside of the basket. So, after the reductions, the cathode baskets are wrapped with a black layer containing  $\text{Li}_2\text{TiO}_3$ ,  $\text{LiTiO}_2$  and carbon. The dissolved  $\text{Li}_2\text{TiO}_3$  and  $\text{LiTiO}_2$  will chemically react reversibly with the *in situ* generated Li metal as termite reactions,[111] which explains the missing Li re-oxidation peak in the CV for used 1 w.t.%  $\text{Li}_2\text{O}/\text{LiCl}$  salt (Fig. 6.2 Blue line) and the possible reason for low current efficiency.



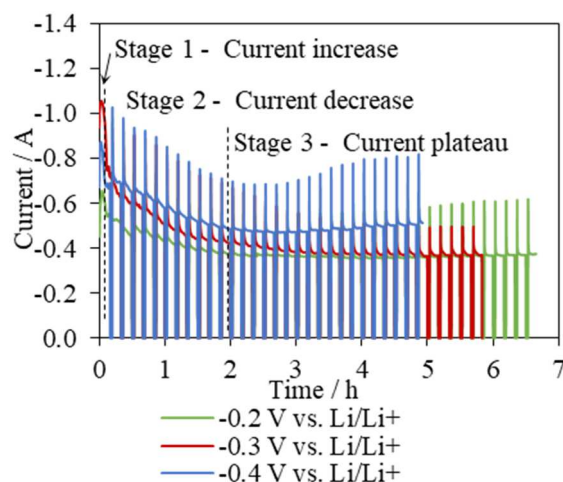


Figure 6.5 Current-time profiles for 2 g  $\text{TiO}_2$  reductions at cathodic reduction potentials at -0.2 V, -0.3 V and -0.4 V (vs.  $\text{Li/Li}^+$ ) with intervals using 80% of the theoretical charge.

I-t curves for  $\text{TiO}_2$  reductions at all three potentials show a three-stage pattern including a sharp current peak (<20 min) and a decrease, and then current plateaus between 0.4 A and 0.6 A (Fig. 6.5).  $\text{TiO}_2$  reduction through the FFC process was also observed with a current decrease and a plateau in the I-t profile.[10,12] The overall current magnitude increases with reduction potential from -0.2 V to -0.4 V (vs.  $\text{Li/Li}^+$ ), which leads to shorter reduction time for completing 80% of the theoretical charge for 2 g  $\text{TiO}_2$  from 6.5 h to 5 h. In  $\text{TiO}_2$  reduction at a cell potential of 3 V in 1 w.t.%  $\text{Li}_2\text{O/LiCl}$ , the I-t curve consisted of a current increase, decrease and a plateau.[60] As the  $\text{TiO}_2$  was converted to  $\text{LiTiO}_2$ , the current increased to 4.3 A. In the stages of current decrease and a plateau at 2.5 A,  $\text{LiTiO}_2$  was progressively reduced to  $\text{TiO}$ ,  $\text{Ti}_2\text{O}$  and finally  $\text{Ti}$  metal. In the  $\text{TiO}_2$  reduction through the FFC process at 2.5 V cell potential, it observed a current decrease and a plateau in the profile.[10,12]  $\text{CaTiO}_3$  was partially reduced to  $\text{Ti}_2\text{O}_3$  as the current decreased from 3 A to a plateau of 0.3 A. During the reduction at the current plateau,  $\text{Ti}$  metal was generated through a series of titanium species, including  $\text{TiO}$  and  $\text{CaTi}_2\text{O}_4$ . It took 120 h to produce  $\text{Ti}$  metal from 8 g  $\text{TiO}_2$ , which is much longer than the duration time in the present study.

The first stage of current increase is attributed to the transformation of insulator  $\text{TiO}_2$  to lithium titanate  $\text{LiTiO}_2$  which has significant conductivity,  $0.5 \text{ S cm}^{-1}$ .[112] According to the three-phase interlines (3PIs) reaction mechanism extensively applicable in previous work on electrolysis of metal oxides, the conductive  $\text{LiTiO}_2$ , insulator  $\text{TiO}_2$  and electrolyte  $\text{LiCl}$  can form 3PIs.[113–115] As 3PI expanded from contacting points to a large area, the charge transfer reactions occurring at 3PIs led to increasing current flow.[115] With more  $\text{LiTiO}_2$  generated, the interline moves inwards to the inside of the  $\text{TiO}_2$  core. The longer diffusion distance for the 3PIs resulted in the sharp current decrease on the

second stage.[17,59] When the current continued to decrease at a smaller slope,  $\text{Li}_2\text{TiO}_3$  shell started being reduced to the more conductive  $\text{LiTiO}_2$  and a new 3PI of  $\text{LiTiO}_2|\text{Li}_2\text{TiO}_3|\text{electrolyte}$  was formed. The continuous propagation of the newly formed 3PI increases the material transfer distance leading to the continuously decreasing current. The following current plateau 0.4 A indicated either the reaction at 3PIs were limited by slow diffusion of reactive species or reached equilibrium. For  $\text{TiO}_2$  electrolytic reduction at -0.2 V vs.  $\text{Li}/\text{Li}^+$ , the final product still contains  $\text{TiO}_2$  while  $\text{Li}_2\text{TiO}_3$  stays almost same suggesting the final charge transfer is more relevant with reactions at the 3PIs of  $\text{LiTiO}_2|\text{TiO}_2|\text{electrolyte}$ . At -0.3 V and -0.4 vs  $\text{Li}^+/\text{Li}$ , the final stage reaction for  $\text{TiO}_2$  reduction halted at conversion of  $\text{Li}_2\text{TiO}_3$  at the 3PIs of  $\text{LiTiO}_2|\text{Li}_2\text{TiO}_3|\text{electrolyte}$ , which is limited by  $\text{O}^{2-}$  diffusion.

#### 6.4.3 The Effect of Applied Charges on $\text{TiO}_2$ Reductions at -0.3 V vs. $\text{Li}/\text{Li}^+$

The further investigation was carried out for  $\text{TiO}_2$  electrolytic reductions by applying more charges (130% and 150% of the theoretical charge) at the optimal cathodic potential -0.3 V vs.  $\text{Li}/\text{Li}^+$ .

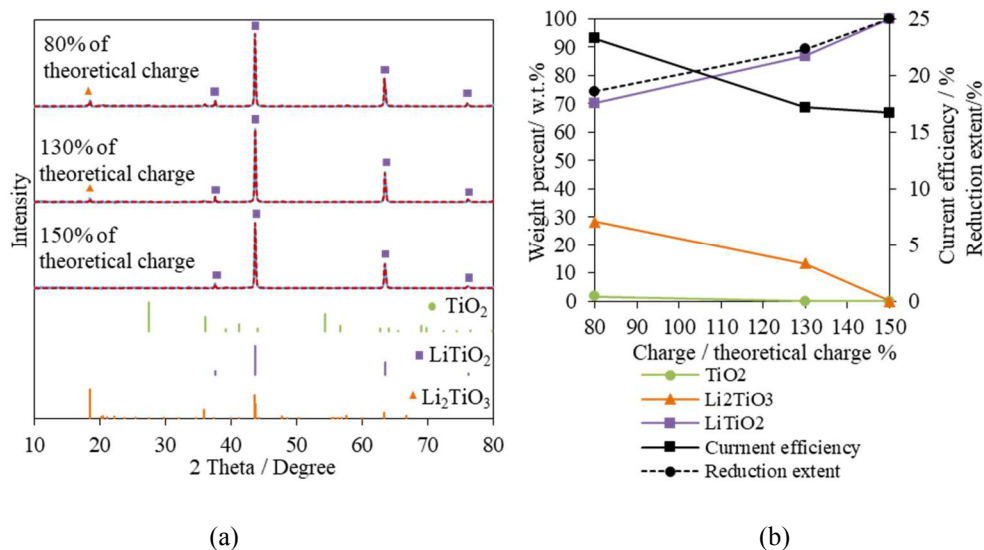


Figure 6.6 a) XRD results (blue solid lines) and Rietveld refinement fittings (red dash lines, with  $\text{TiO}_2$ ,  $\text{Li}_2\text{TiO}_3$  and  $\text{LiTiO}_2$ ) of  $\text{TiO}_2$  reduction products at -0.3 V (vs.  $\text{Li}/\text{Li}^+$ ) using 80%, 130% and 150% of the theoretical charge; b) Product distribution, current efficiencies and reduction extents for  $\text{TiO}_2$  reductions at -0.3 V vs.

$\text{Li}/\text{Li}^+$  using 80%, 130% and 150% of the theoretical charge.

The XRD analyses show that the reduced  $\text{TiO}_2$  samples with increasing charges only consist of  $\text{Li}_2\text{TiO}_3$  and  $\text{LiTiO}_2$  (Fig. 6.6a).  $\text{TiO}_2$  was completely converted in reductions at -0.3 V vs.  $\text{Li}/\text{Li}^+$ . When the applied charge was increased from 80% to 150% of the theoretical charge, the  $\text{Li}_2\text{TiO}_3$  content was decreased from 28.3 w.t.% to 0 w.t.% (Table 6.3), while the  $\text{LiTiO}_2$  increased from 70.0

w.t.% to 100 w.t.%. This indicates that  $\text{Li}_2\text{TiO}_3$  was only fully reduced to the partial reduction intermediate  $\text{LiTiO}_2$  through Eq. 6.6. No metal Ti was generated even using 150% of the theoretical charges within 9 hours. The electrolytic reduction of  $\text{TiO}_2$  is very refractory in 1 w.t.%  $\text{Li}_2\text{O}/\text{LiCl}$  at 650 °C. The previous FFC studies also show that it took 120 h to completely reduce 8 g  $\text{TiO}_2$  to Ti in  $\text{CaO}/\text{CaCl}_2$  at 900 °C.[12] The formation of  $\text{Li}_2\text{TiO}_3$  as a passivation layer during the soaking stage may slow down the reduction process in a couple of ways. Firstly,  $\text{Li}_2\text{TiO}_3$  retards Li metal diffusion in and  $\text{O}^{2-}$  diffusion out. Second, the reduction of  $\text{Li}_2\text{TiO}_3$  is a slow and reversible process.[116] Previous study on  $\text{TiO}_2$  reduction in LiCl salts only obtained partial reduction products including  $\text{LiTiO}_2$  and  $\text{Li}_2\text{TiO}_4$ . [59]



Table 6.3 Rietveld refinement results for reduced products at -0.3 V vs.  $\text{Li}/\text{Li}^+$

Applied charge / % of the theoretical charge		80%	130%	150%	
Products composition /w.t.%	$\text{TiO}_2$	1.69	0.00	0.00	
	$\text{Li}_2\text{TiO}_3$	28.27	13.36	0.00	
	$\text{LiTiO}_2$	70.04	86.64	100.00	
R factors	$R_{\text{wp}}$ (%)	6.06	6.33	6.42	
	$R_{\text{p}}$ (%)	4.16	4.56	4.52	
	$R_{\text{e}}$ (%)	5.51	5.58	5.47	
	S	1.0955	1.1328	1.1721	
	$\chi^2$	1.2002	1.2832	1.3737	
	Maximum shift e.s.d.	0.359	0.366	0.002	
Phases	Structural Parameters				
$\text{TiO}_2$ Rutile, syn (01-084-1284) Space group: 136 : P42/mnm	a (Å)	4.58666	---	---	
	b (Å)	4.58666	---	---	
	c (Å)	2.95407	---	---	
	$\alpha$ (Degree)	90	---	---	
	$\beta$ (Degree)	90	---	---	
	$\gamma$ (Degree)	90	---	---	
	V (Å <sup>3</sup> )	62.146099	---	---	
	Scale factor	3.2(14)	---	---	
	Gaussian peak width parameters (° <sup>2</sup> )	U	0.19(5)	---	---
		V	-0.26(8)	---	---
W		0.06(2)	---	---	
$\text{LiTiO}_2$	a (Å)	4.1457(5)	4.1400(5)	4.14000	

Lithium titanium(III) oxide (01-074-2257) Space group: 225 : Fm-3m	b (Å)	4.1457(5)	4.1400(5)	4.14000
	c (Å)	4.1457(5)	4.1400(5)	4.14000
	$\alpha$ (Degree)	90	90	90
	$\beta$ (Degree)	90	90	90
	$\gamma$ (Degree)	90	90	90
	V (Å <sup>3</sup> )	71.254(15)	70.957(16)	70.957937
	Scale factor	62.6(17)	66.9(19)	62.7(17)
	Gaussian peak width parameters (° <sup>2</sup> )	U	0.24(6)	0.20(4)
V		-0.26(8)	-0.17(4)	-1.00(15)
W		0.06(2)	0.053(11)	0.248(2)
Li <sub>2</sub> TiO <sub>3</sub> Dilithium titanate (IV) (01-080-7163) Space group: 15 : C12/c1,unique-b,cell-1	a (Å)	5.053(3)	5.035(6)	---
	b (Å)	8.782(6)	8.790(2)	---
	c (Å)	9.714(6)	9.767(4)	---
	$\alpha$ (Degree)	90	90	---
	$\beta$ (Degree)	99.45(7)	100.22(2)	---
	$\gamma$ (Degree)	90	90	---
	V (Å <sup>3</sup> )	425.2(5)	427.8(2)	---
	Scale factor	12.4(8)	7.0(6)	---
Gaussian peak width parameters (° <sup>2</sup> )	U	0.6(2)	0.6(2)	---
	V	-0.26(8)	-0.6(2)	---
	W	0.06(2)	0.08(3)	---

22.3% reduction extent was obtained for TiO<sub>2</sub> electrolytic reduction using 130% of the theoretical charge while 25% reduction extent was reached with 150% of the theoretical charge. The current efficiencies for TiO<sub>2</sub> reductions are 17% and 16% for the reductions using 130% and 150% of the theoretical charge, respectively. Various ways have been used for calculation of TiO<sub>2</sub> reduction current efficiency including subtraction of background current consumption from the total charges, which lead to different level of current efficiencies.[59] The total applied charge used for the current efficiency calculation in this study is the integrated area under the I-t curve without background subtraction.

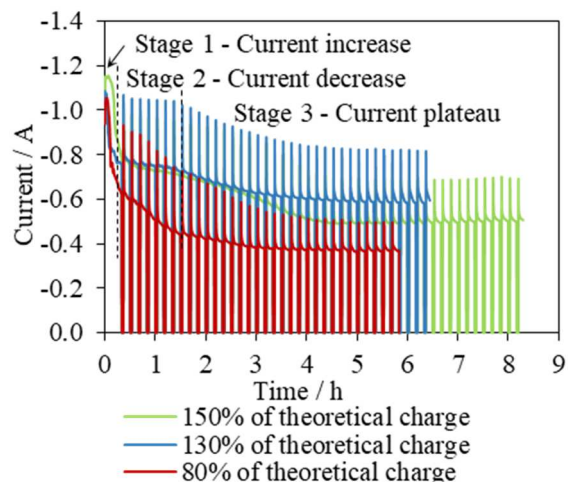


Figure 6.7 Current-time profiles for TiO<sub>2</sub> reductions at -0.3 V (vs. Li/Li<sup>+</sup>) using 80%, 130% and 150% of the theoretical charge for 2 g TiO<sub>2</sub>.

Similar I-t profiles with a 3-stage pattern as discussed in the previous section are observed in TiO<sub>2</sub> reductions at -0.3 V (vs. Li/Li<sup>+</sup>) but with extended time using 130% and 150% of the theoretical charges (Fig. 6.7). It took 8.2 h to apply 150% of the theoretical charges, and it took the longest experiment among all the TiO<sub>2</sub> electrolytic tests in this study, with the highest reduction extent of 25% of 2 g TiO<sub>2</sub>. Comparably, the FCC process showed that the products were a mixture of TiO, CaTiO<sub>3</sub> and CaTi<sub>2</sub>O<sub>4</sub> after 8 h of electrolytic TiO<sub>2</sub> reduction in molten CaCl<sub>2</sub> at around 900 °C.[12] The electrolytic reduction of TiO<sub>2</sub> is challenging even at higher reduction temperatures and more kinetically favorable conditions.

The current plateau reached for TiO<sub>2</sub> reductions at -0.3 V (vs. Li/Li<sup>+</sup>) using 130% and 150% of the theoretical charges reflects the final charge transfer for the conversion of Li<sub>2</sub>TiO<sub>3</sub> at the 3PIs of LiTiO<sub>2</sub>|Li<sub>2</sub>TiO<sub>3</sub>|electrolyte, which is limited by O<sup>2-</sup> diffusion [62].

#### 6.4.4 Reusability of Lithium Salts for TiO<sub>2</sub> Electroreductions

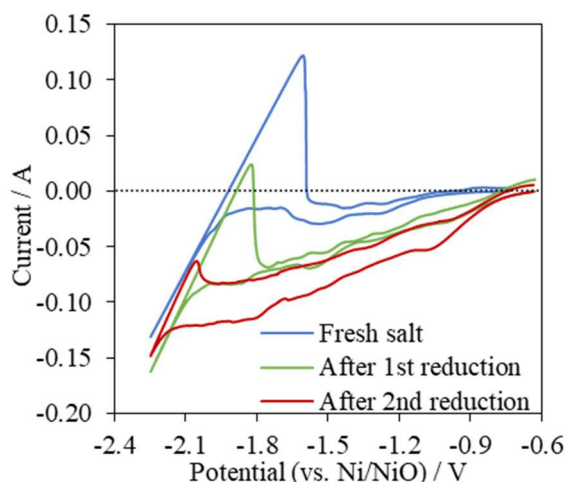
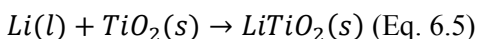
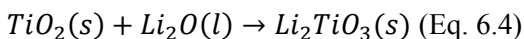


Figure 6.8 CVs for lithium salt before and after TiO<sub>2</sub> reductions at -0.3 V vs. Li/Li<sup>+</sup> with 150% of the theoretical charge (Scan rate = 20 mV s<sup>-1</sup>)

Cathodic CVs are compared for fresh 1 w.t.% Li<sub>2</sub>O/LiCl and for used salts after two consecutive TiO<sub>2</sub> reductions using 150% of the theoretical charge from OCP to -2.25 V vs. Ni/NiO (Fig. 8). The CVs in used salts show a huge slope off the baseline right after the OCP, which indicates the increasing background current due to the increasing impurities, such as CO<sub>3</sub><sup>2-</sup> and titanate species, generated during the TiO<sub>2</sub> reduction (Fig. 6.8 Green).[20] The re-oxidation peak of the Li metal became smaller for the used salts, suggesting that the *in situ* generated Li metal in the forward scan is partially consumed by the soluble titanate species. The Li<sub>2</sub>O/LiCl salt after two repeated TiO<sub>2</sub> reductions turns into a dark grey color, due to the carbon dust from the redox reaction of the glassy carbon anode.[38] The ICP-MS analysis of the used salt dough shows that the accumulated titanium element concentration is 4112 ppm (2 w.t.% metal basis, balanced with Li) in the Li<sub>2</sub>O/LiCl salt after two reductions, which verifies the slight solubility of titanate species in the salts. Insoluble black carbon particles due to the reactions at glassy carbon anode were also observed during the salt sample preparation for ICP-MS analysis.

#### 6.4.5 DFT for TiO<sub>2</sub> Reduction Mechanism

Based on the discussion in the above sections, reduction reactions (Eq. 6.4, 6.5, 6.6) have been proposed and discussed for TiO<sub>2</sub> electrolytic reduction process.





DFT simulation provide a theoretical understanding on the reaction mechanism for  $\text{TiO}_2$  electrolytic reduction in 1 w.t.%  $\text{Li}_2\text{O}/\text{LiCl}$  at 650 °C. DFT calculations for the crystalline bulks were performed using the Vienna Ab Initio Simulation Package (VASP).[106] The total energies and structural relaxations were carried out using the projector augmented wave (PAW) method to treat core electrons.[107] The energy cutoff up to 520 eV was used for the plane wave basis set. The Perdew-Burke-Ernzerhof (PBE) functional was employed to account for the electron exchange-correlation effects.[117] Spin polarizations were considered in all calculations. A Monkhorst–Pack scheme was used to generate the k-point mesh for the Brillouin zone sampling. The most stable phase for each involved bulk crystal (i.e.,  $\text{TiO}$ ,  $\text{TiO}_2$ ,  $\text{Ti}$ ,  $\text{Li}_2\text{TiO}_3$ ,  $\text{Li}_2\text{O}$ , and  $\text{LiTiO}_2$ ) were used. The unit cell structures are illustrated in Fig. 6.9. PBE + U calculations were performed on all oxide and perovskite crystals containing the Ti species, and U-J is set to be 2.0 eV, which has been shown to produce more accurate reaction energies for the PBE+U methods.[118] The optimized bulk lattice structures based on periodic DFT calculations using the described modeling method were tabulated in Table 6-4.

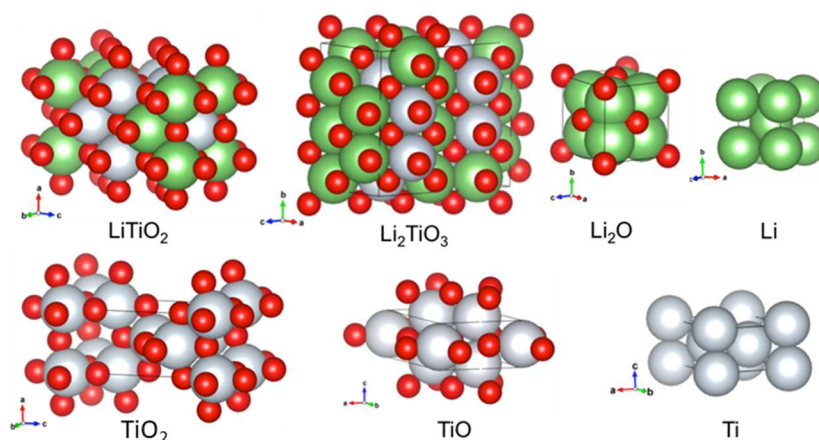


Figure 6.9 Optimized bulk crystal structures for the Li system,  $\text{TiO}_2$ ,  $\text{TiO}$ , and  $\text{Ti}$ .  $\text{Ti}$ ,  $\text{Li}$ , and  $\text{O}$  are in grey, green, and red, respectively. Black lines indicate the boundaries of the unit cell. Axis labels along the a, b, c directions are also shown

Table 6.4 Optimized bulk lattice parameters.

Crystals	Crystal lattice	
	Space group	Lattice parameters
LiTiO <sub>2</sub>	4/ <i>m</i> <i>m</i> <i>m</i>	a = b = 4.08 Å, c = 8.56 Å; α = β = γ = 90°
Li <sub>2</sub> TiO <sub>3</sub>	2/ <i>m</i>	a = 5.11 Å, b = 8.88 Å, c = 9.83 Å; α = 90°, β = 100.24°, γ = 90°
TiO	$\bar{6}m2$	a = b = 5.06 Å, c = 2.92 Å; α = β = 90°, γ = 120°
TiO <sub>2</sub>	4/ <i>m</i> <i>m</i> <i>m</i>	a = b = 3.84 Å, c = 9.74 Å; α = β = γ = 90°
Li <sub>2</sub> O	<i>m</i> $\bar{3}m$	a = b = c = 4.63 Å; α = β = γ = 90°
Ti	6/ <i>m</i> <i>m</i> <i>m</i>	a = b = 4.58 Å, c = 2.83 Å; α = β = 90°, γ = 120°
Li	<i>m</i> $\bar{3}m$	a = b = c = 3.43 Å; α = β = γ = 90°

A quasiharmonic approach would be adopted to estimate the thermodynamics of solids at high temperatures. The Helmholtz free energy,  $F(V, T)$ , a function of both crystal volume ( $V$ ) and temperature ( $T$ ), could be expressed by Eq. 6.7.

$$F(T, V) = E(V) + F_{vib}(V, T) + F_{el}(V, T) \text{ (Eq. 6.7)}$$

where  $E(V)$  is the total energy.  $F_{vib}(V, T)$  and  $F_{el}(V, T)$  represent the vibrational and thermal electronic contributions to the free energy, respectively.

$E(V)$  of a given crystal can be described by the equation of state (EOS), and its values at different volumes were obtained directly from periodic DFT calculations. Here, the 4<sup>th</sup>-order Birch-Murnaghan (BM4) EOS was used. Specifically,  $E(V)$  is expressed as Eq. 6.8.

$$E(V) = a + bV^{-2/3} + cV^{-4/3} + dV^{-2} \text{ (Eq. 6.8)}$$

The EOS expressions for all materials considered for free energy calculations are listed in Table 6.5. Then, the bulk modulus ( $B(V)$ ) and pressure ( $P$ ), both in GPa, can be represented by Eqs. 6.9 and 6.10, respectively.

$$B(V) = V \frac{\partial^2 E}{\partial V^2} \text{ (Eq. 6.9)}$$

$$P = -\frac{\partial E}{\partial V} \text{ (Eq. 6.10)}$$

Values of  $B(V)$  at the equilibrium volume ( $V_0$ ) determined from respective BM4 EOS are also listed in Table 6.5. The vibrational free energy contribution,  $F_{vib}(T)$ , can be rigorously obtained from explicit phonon calculations. In this study, the calculation of  $F_{vib}(T)$  at the equilibrium volume ( $V_0$ ) follows the formulation of a simplified Debye model, as expressed in Eq. 6.11.



$$F_{vib}(T) = \frac{9}{8}k_B\Theta_D + k_B T \left\{ 3 \ln \left[ 1 - \exp\left(-\frac{\Theta_D}{T}\right) \right] - D\left(\frac{\Theta_D}{T}\right) \right\} \text{ (Eq. 6.11)}$$

where  $\Theta_D$  is the Debye temperature;  $D(\Theta_D/T)$  is the Debye function, expressed by Eq. 6.12.

$$D(x) = \frac{3}{x^3} \int_0^x \frac{t^3}{\exp(t)-1} dt \text{ (Eq. 6.12)}$$

The Debye temperature was approximated by the Debye-Wang model [119], as in Eq. 6.13.

$$\Theta_D = sAV^{1/6} \left\{ \frac{1}{M} \left[ B(V) - \frac{2(\lambda+1)}{3} P \right] \right\}^{1/2} \text{ (Eq. 6.13)}$$

where  $s = 0.617$ ,  $A = 231.04$ , and  $\lambda = -0.5$ .  $M$  is the molecular weight in gram/mole. In this work, we assume that the effect related to crystal thermal expansion can be neglected. The values for  $B$  and  $P$  were taken at  $V_0$ , resulting in  $P(V_0) = 0$ . Then, the Debye temperature can be expressed as  $\Theta_D = sAV_0^{1/6} (B(V_0)/M)^{1/2}$ .

The electronic free energy contribution  $F_{el}(T)$  at  $V_0$  is represented by Eq. 6.14.

$$F_{el}(T) = E_{el}(T) + TS_{el}(T) \text{ (Eq. 6.14)}$$

where  $E_{el}(T)$  and  $S_{el}(T)$  are the internal energy and entropy due to electronic excitation, and are given by Eqs. 6.15 and 6.16:

$$E_{el}(T) = \int n(\varepsilon) f \varepsilon d\varepsilon - \int^{\varepsilon_f} n(\varepsilon) \varepsilon d\varepsilon \text{ (Eq. 6.15)}$$

$$S_{el}(T) = -k_B \int n(\varepsilon) [f \ln f + (1-f) \ln(1-f)] d\varepsilon \text{ (Eq. 6.16)}$$

where  $n(\varepsilon)$  represents the electronic density of states (DOS), and can be obtained from DFT calculations,  $f(\varepsilon, T)$  is the Fermi distribution function, as shown in Eq. 6.17.

$$f(\varepsilon, T) = \frac{1}{\exp\left(\frac{\varepsilon-\mu}{k_B T}\right)+1} \text{ (Eq. 6.17)}$$

where  $k_B$  is the Boltzmann's constant,  $\varepsilon_f$  is the Fermi energy, and  $\mu$  is the electronic chemical potential, which ensures that the Fermi function produces the total number of electrons at  $T$ . Values of  $\mu$  corresponding to each material can be found in Table 6.5.

Table 6.5 Equation of state, equilibrium volumes ( $V_0$ ) determined from corresponding BM4 EOS, bulk moduli, and electronic potentials for the materials modeled from DFT.

Crystal	BM4 EOS				$V_0$ ( $\text{\AA}^3$ )	$B(V_0)$ (GPa)	$\mu$ (eV)
	$a$	$b$	$c$	$d$			
LiTiO <sub>2</sub>	-571.9	41551.2	$-1.25 \times 10^6$	$1.24 \times 10^7$	143.8	139.7	7.07
Li <sub>2</sub> TiO <sub>3</sub>	-79.3	-23671	249893	$1.68 \times 10^7$	440.9	107.8	2.55
TiO	177.5	-9384.75	126016	-540527	65	215.3	8.35
TiO <sub>2</sub>	35.8	-6282	35014.2	935552	143.7	180.6	1.88
Li <sub>2</sub> O	-1.42	-2395.5	25495.8	929.43	99.4	80.5	1.386
Ti	26.4	-1503.21	12977.2	-23850.9	51.4	113	5.9
Li	1.65	-147.2	1191	-2524.4	40.7	13.8	0.56

Gibbs free energy changes for the reactions possibly involved in TiO<sub>2</sub> reduction are calculated based on the optimized bulk structures of the relevant compounds including Li and Ti (Table 6.6). The negative Gibbs free energy of  $\Delta G_{650^\circ\text{C}}$ ,  $-125 \text{ kJ mol}^{-1}$  for the insertion of Li<sub>2</sub>O to TiO<sub>2</sub> (Eq. 6.4) confirms that the formation of Li<sub>2</sub>TiO<sub>3</sub> is spontaneous at 650 °C. This theoretical result is consistent with the TiO<sub>2</sub> soaking test with the formation of Li<sub>2</sub>TiO<sub>3</sub> shell.  $\Delta G_r$  for TiO<sub>2</sub> reduction with Li metal is more negative than that for the reduction of Li<sub>2</sub>TiO<sub>3</sub> with Li metal which suggests the reduction of TiO<sub>2</sub> with Li is more favorable than Li<sub>2</sub>TiO<sub>3</sub> (Eq. 6.5 vs. Eq. 6.6). The remaining core of TiO<sub>2</sub> particles is most likely reduced to LiTiO<sub>2</sub> before Li<sub>2</sub>TiO<sub>3</sub> shell reduction, and this process may be slowed down by the Li<sub>2</sub>TiO<sub>3</sub> passivation layer. The unit cell volume of Li<sub>2</sub>TiO<sub>3</sub> is three times as much as the one for TiO<sub>2</sub>, which will elongate diffusion pathway (Fig. 6.10).[9,104] Reduction of Li<sub>2</sub>TiO<sub>3</sub> by Li metal generates Li<sub>2</sub>O (Eq. 6.6) which need to diffuse through the new LiTiO<sub>2</sub> layer to the bulk molten salts and promote further reaction. The slow diffusion of O<sup>2-</sup> slows down the reduction of Li<sub>2</sub>TiO<sub>3</sub> which may reach equilibrium due to the accumulation of Li<sub>2</sub>O trapped in the solid particle. The further reduction of LiTiO<sub>2</sub> by Li metal is an irreversible reaction and generates Li<sub>2</sub>O ( $\Delta G_r=0.8 \text{ kJ mol}^{-1}$ ). Both reduction of LiTiO<sub>2</sub> pathway are most likely halted due to the high local Li<sub>2</sub>O concentration (Eq. 6.18 and 6.22), which becomes the key limiting step for further reduction and takes elongate time. The DFT analysis supports the experimental TiO<sub>2</sub> electrolytic reduction results obtained in this study that the LiTiO<sub>2</sub> is the most reduced product ever achieved even using 150% of the theoretical charge. The thermostability of LiTiO<sub>2</sub> was also reported on previous electrolytic reduction of TiO<sub>2</sub> in LiCl molten salts.[59,104]

Table 6.6 Gibbs free energy change and reaction potentials for reactions at 650 °C by DFT calculations.

Reaction		$\Delta G_r$ (at 650 °C) / kJ mol <sup>-1</sup>	$\Delta E$ /V
$TiO_2 + Li_2O \rightarrow Li_2TiO_3$	(Eq. 6.4)	-125.0	Chemical reaction
$Li + TiO_2 \rightarrow LiTiO_2$	(Eq. 6.5)	-113.0	1.17
$Li_2TiO_3 + Li \rightarrow LiTiO_2 + Li_2O$	(Eq. 6.6)	-11.0	0.11
$LiTiO_2 + Li \rightarrow TiO + Li_2O$	(Eq. 6.18)	0.8	-0.01
$TiO + 2Li \rightarrow Ti + Li_2O$	(Eq. 6.19)	-22.3	0.12
$TiO \rightarrow Ti + 1/2O_2$	(Eq. 6.20)	227.0	-1.18
$Li_2TiO_3 \rightarrow LiTiO_2 + 1/2 Li_2O + 1/4 O_2$	(Eq. 6.21)	222.0	-2.30
$LiTiO_2 \rightarrow TiO + 1/2 Li_2O + 1/4 O_2$	(Eq. 6.22)	212.0	-2.20

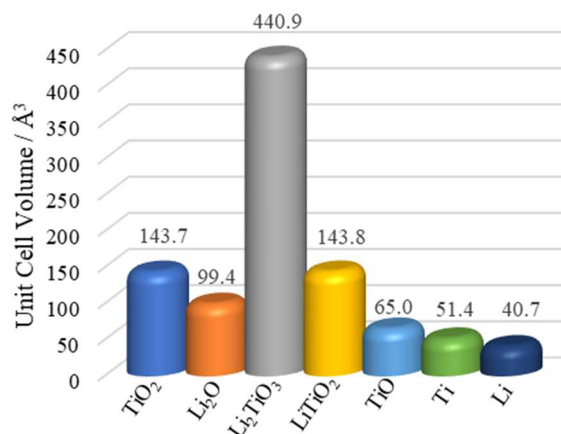


Figure 6.10 Unit cell volumes for the related chemicals during the TiO<sub>2</sub> electrolytic reduction in molten 1 w.t.% Li<sub>2</sub>O/LiCl at 650 °C.

Direct electrolytic reductions of Li<sub>2</sub>TiO<sub>3</sub> and LiTiO<sub>2</sub> are alternative pathways in the titanium dioxides reduction (Eq. 6.21 and Eq. 6.22). At the cathodic potential -0.3 V vs. Li/Li<sup>+</sup>, theoretically electrochemical decomposition of Li<sub>2</sub>TiO<sub>3</sub> and LiTiO<sub>2</sub> is feasible. However, the most reduced product obtained in this study is LiTiO<sub>2</sub> with 150 % of the theoretical charge. Furthermore, previous TiO<sub>2</sub> pellets electrolytic reduction at cell potential 1.8 V and 3.2 V only obtained LiTi<sub>2</sub>O<sub>4</sub> and LiTiO<sub>2</sub>, respectively.[59] The direct electrolytic reduction of Li<sub>2</sub>TiO<sub>3</sub> and LiTiO<sub>2</sub> could not be achieved due to Li<sub>2</sub>O accumulation, which also alternate the conductivity of the mixtures.

By combining the experimental and DFT results, a multi-step reaction mechanism for TiO<sub>2</sub> electrolytic reduction at overpotentials in the 1 w.t.% Li<sub>2</sub>O/LiCl salt at 650 °C is proposed in this study.

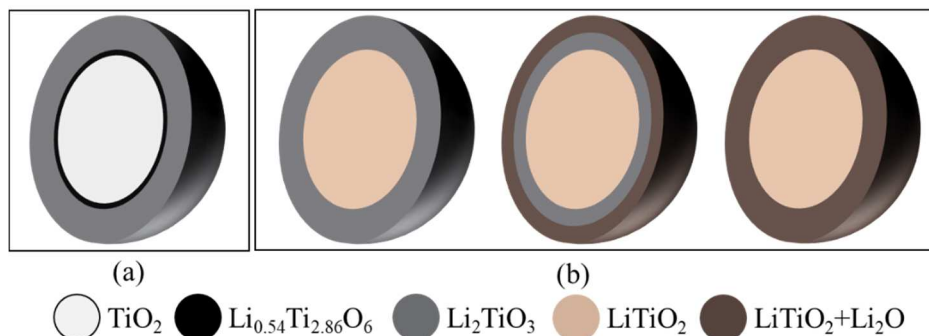
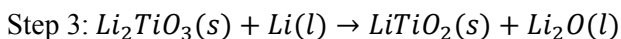
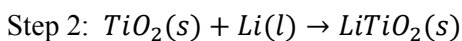
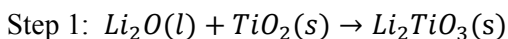


Figure 6.11 Shrinking core model for (a) the  $\text{TiO}_2$  soaking process, and (b) for the electrolytic reduction of  $\text{TiO}_2$  process with passivation layers

As illustrated in Fig. 6.11, the soaking process follows shrinking core mechanism where the insertion of  $\text{Li}_2\text{O}$  and  $\text{TiO}_2$  forms a stoichiometric  $\text{Li}_2\text{TiO}_3$  layer on the external surface of the  $\text{TiO}_2$  particles.[14] The  $\text{Li}_2\text{TiO}_3$  layer becomes thicker and slows  $\text{Li}_2\text{O}$  diffusion leading to a nonstoichiometric  $\text{Li}_{0.54}\text{Ti}_{2.86}\text{O}_6$  formation with unreacted  $\text{TiO}_2$  core. The  $\text{Li}_2\text{TiO}_3|\text{TiO}_2|\text{electrolyte}$  interline initially forms on the surface of the oxide particle, and gradually moves to the interior of the particle.

At second step, the Li metal diffuses through the  $\text{Li}_2\text{TiO}_3$  and reduces the  $\text{TiO}_2$  core directly into  $\text{LiTiO}_2$ . The 3PIs of  $\text{LiTiO}_2|\text{TiO}_2|\text{electrolyte}$  is formed. It continuously moves to the center of the  $\text{TiO}_2$  core until the core is fully converted to  $\text{LiTiO}_2$ . This step is controlled by the Li diffusion through the  $\text{Li}_2\text{TiO}_3$  and newly formed  $\text{LiTiO}_2$  layer. The second reaction also follows a shrinking-core model.

When  $\text{TiO}_2$  is completely reduced to  $\text{LiTiO}_2$ , the  $\text{Li}_2\text{TiO}_3$  shell starts to be reduced to a mixture of  $\text{LiTiO}_2$  and  $\text{Li}_2\text{O}$ , which is different from the inner  $\text{LiTiO}_2$  core. The reaction occurs at the external layer of  $\text{Li}_2\text{TiO}_3$  and forms a new 3PI of  $\text{Li}_2\text{O}+\text{LiTiO}_2|\text{Li}_2\text{TiO}_3|\text{electrolyte}$ . It stops when the interline approaches the  $\text{LiTiO}_2$  core.

$\text{LiTiO}_2$  was so far the most reduced product at even 150% of the theoretical charge. The  $\text{LiTiO}_2$  component was detected in the product with 80% of the theoretical charge, and it accumulated in the cathode basket till 150% of the theoretical charge was applied. This indicated that the under no circumstance would the  $\text{LiTiO}_2$  be reduced. Based on the literature reviews in Session 2.1.2.2, the

reduction of  $\text{LiTiO}_2$  with Li metal produced TiO and more  $\text{Li}_2\text{O}$ . [60] It indicates that  $\text{LiTiO}_2$  is relatively stable and the reduction of  $\text{LiTiO}_2$  is refractory.

The key to improve the  $\text{TiO}_2$  reduction in  $\text{Li}_2\text{O}/\text{LiCl}$  molten salts is to promote the diffusion of  $\text{O}^{2-}$  out of solid phase and reduce the  $\text{Li}_2\text{O}$  local concentration. Strategies include lowering  $\text{Li}_2\text{O}$  concentration in the molten salts and applying sonication or mechanical stirring to accelerate  $\text{O}^{2-}$  diffusion. [120]

### 6.5 Conclusion

$\text{TiO}_2$  electrolytic reduction in  $\text{Li}_2\text{O}/\text{LiCl}$  salts at 650 °C were examined for soaking only test, effect of reduction potential, and effect of applied charges. Lithium titanates  $\text{Li}_2\text{TiO}_3$  and  $\text{LiTiO}_2$  were identified during the reduction processes. The chemical formation of  $\text{Li}_2\text{TiO}_3$  is achieved spontaneously by soaking  $\text{TiO}_2$  in molten  $\text{Li}_2\text{O}/\text{LiCl}$  salt without electrolysis.  $\text{LiTiO}_2$  is the final product with 150% of the theoretical charge, indicating a maximum of 25% reduction extent and 16.7% current efficiency achieved in current work.

Based on the experimental study as well as the DFT calculations, the electrolytic reduction of  $\text{TiO}_2$  in molten  $\text{Li}_2\text{O}/\text{LiCl}$  is proposed to follow a stage-wise reaction mechanism consisting of chemical and electrolytic reactions. Reduction of the oxide particle fits the shrinking core model. The reduction process could be explained as the formation and movement of three-phases interlines. The external surface of  $\text{TiO}_2$  particles is first chemically combined with  $\text{Li}_2\text{O}$  in the electrolyte to form  $\text{Li}_2\text{TiO}_3$ . Then in the second step, as the electrolysis started, Li metal was generated, diffused through the  $\text{Li}_2\text{TiO}_3$  shell and reduced the  $\text{TiO}_2$  core to  $\text{LiTiO}_2$ . Then as the center core was fully converted to  $\text{LiTiO}_2$ , the  $\text{Li}_2\text{TiO}_3$  shell was reduced with Li metal and turned to a layer of  $\text{LiTiO}_2$  mixture with high local  $\text{Li}_2\text{O}$  concentration. The formation and reduction of lithium titanates are also evidenced by current intensity changes in the current-time profile during electrolysis.

$\text{O}^{2-}$  diffusion in the solid layers is the rate-determining factor in  $\text{TiO}_2$  electrolytic reduction in molten  $\text{Li}_2\text{O}/\text{LiCl}$ . The possible strategy to realize the reduction of the  $\text{LiTiO}_2$  to Ti metal is to decrease the  $\text{Li}_2\text{O}$  concentration within the solid particles. It can be achieved by promoting the  $\text{Li}_2\text{O}$  diffusion within the solid particles.

## Chapter 7: Sonication Assisted Electroreduction of TiO<sub>2</sub> in Li<sub>2</sub>O/LiCl

### 7.1 Abstract

The sonication was coupled with the TiO<sub>2</sub> electroreduction in molten 1 w.t. Li<sub>2</sub>O/LiCl in both overpotential and underpotential processes. The application of sonication increased the current efficiency in both types of reductions. The improvement by 21.2% in underpotential reduction was more significant than that in overpotential reduction. The highest current efficiency reached 44.5% in underpotential reduction with sonication. The increase in current efficiency is the results of improvement of O<sup>2-</sup> diffusion, possibly due to sonication fragmentation and the sono-capillary effect. High ultrasound power can break large particles into small ones, and it can generate high pressure in the mediate which press liquid mediate deep inside the particles at a fast speed. The temperature of the system was not highly affected by the pulsed ultrasound power, and the pulsed mode (20 s or 40 s interval) didn't impact on the reduction performance. Due to the characteristics of the sonication, the probe should be used in an inert atmosphere and the power setting should be in a moderate range such as 30% of the maximum power supply (1500 W).

### 7.2 Introduction

The ultrasound has been applied extensively in food processing, material chemistry and industrial manufacturing processes as it is a great way to promote chemical and physical processing at high efficiencies, fast procedures and low energy consumptions.[120–123] The sonication was applied to the systems of interest mostly as a method of agitation for promoting the mass transfer.

Mechanisms of the ultrasonic were studied to understand the fundamentals and broaden the applications of the technology. Ultrasound power can cause dramatic reductions in particle sizes or fragmentation of the raw materials by inter-particle collisions due to the cavitation bubbles in the liquid.[124] For example, in the extraction of chlorophyll from spinach leaves, sonication pretreatment of the leaves resulted in an averaged particle size of 200 μm compared with 300 μm using the traditional maceration method.[125] The particles size was so much reduced that the surface area was much higher which increased the mass transfer, extraction rate and yield. The ultrasound also have localized effect on the feeds, such as the erosion, local shear stress, and detexturation. In the extraction of boldine from boldo leaves, the implosion cavitation bubbles generated on the leaves surface damaged the structures of trichomes.[126] It lead to an erosion on the material, enhancing the release in the extraction medium. In mixtures of solids and liquids, cavitation bubbles created shear forces in the liquid and at vicinity of

the solids. During the extractions of basil essential oil, cavitation bubbles collapsed at the oil glands, and the generated shear forces broke the oil glands at the leaves surface.[127] Sonoporation, another proposed sonication mechanism, was the results of cavitation on the wall or membrane structure and the change could be either reversible or irreversible. At high ultrasound frequencies (0.5 to 5 MHz) [128] or sometimes at generally used 20 kHz [129], pores grew on the cell wall, and the cell membranes became permeable for mass transfer in and out, known as the sonoporation.[130] The sonoporation was generated by cavitation [131] and shear stress [132]. In the studies of human prostate cancer cell, sonoporation at 21 kHz was exposed to the cells.[133] With the treatment of ultrasound, pores were observed with SEM on a part of the membrane, indicating a reversible sonoporation process. The reversible sonoporation was also used in medical treatments in organs. By applying local sonoporation to the kidney, the oligonucleotides could pass through the glomerular filtration barrier at a high efficiency.[134] Ultrasound waves also have impact on the materials without damages in the structures, such as sonocapillary. The sonocapillary effect is the result of liquid pressurization in capillary structures due to the acoustic vibrations.[135] It increased the depth and velocity of liquid penetration into canals and pores in the materials.[136] An increase of water absorption was observed with the ultrasound processing, about 70% higher than that of the general maceration in dealing with the apple pomace.[137] The results showed that the extraction kinetics was improved under the ultrasound and the sonocapillary effect directly promoted the mass transfer.

Parameters were studied to find the correlation with the products, including the sonicator type, ultrasound power, sonication time, mediates, transducer position, etc. By introducing a sonicator (500 W, 20 kHz) as both a heating source and mixing method, researchers studied the catalytic 5-hydroxymethylfurfural (HMF) generation from glucose in the mediate of 1-butyl-3-methylimidizonium chloride.[138] It was found that the probe-type sonicator had a better synthesis results than a bath-type, due to its high localized intensity. Several key operation parameters were under studied. The HMF yield and glucose conversion were improved with increasing power load until 60% of the ultrasonic power was applied, and then further increment of the power would not improve the process. At 60% of the power load (to avoid damage of the probe at higher power), the yield of HMF increased from 1% to a maximum 43% within first 3 minutes, slightly changed in the following 20 minutes, and then started to decrease due to the degradation of the HMF under the harsh conditions. It was also observed that, since the intense sonication zone was directly beneath the probe, it made no difference in the reactions if the probe was located at an upper position in the mediate with a proper amount. In chemical reactions, the sonication will not only increase the yield, but also generate products in a nanoscale. During the synthesis of tin nanorods in a  $\text{SnCl}_2$ / ethylene glycol degassed mixture, sonication played roles as both an agitation method and a necessary reaction condition.[139] In the reaction steps, ethylene glycol

dehydrated to acetaldehyde, and  $\text{SnCl}_2$  was hydrolyzed into  $\text{Sn}(\text{OH})_2$ . For further reaction between acetaldehyde and  $\text{Sn}(\text{OH})_2$ , it required the application of sonication. The Sn generation under the current condition was not thermodynamically favorable. However, the cavitation bubbles released heat that was high enough to drive the reaction. In order to form the bubbles easily, less viscous polyol was preferred, such as the ethylene glycol whose chain was the shortest. The tin nanorod products were 50-100 nm in diameters. For metal electrodepositions in ionic liquids, the sonication was also added for the purpose of mixing. In  $\text{AlCl}_3/[\text{BMIm}]\text{Cl}$  (1.5:1 molar ratio), aluminum metal was deposited on the brass substrate.[140] The electrolytic studies concluded that the sonication did not change the nucleation and growth mechanisms, but the morphology studies showed an increase in the deposit surface roughness by forming larger crystals.

The sonication technology has been studied in low temperature molten salts of  $\text{CuCl}_2/\text{ChCl}/\text{EG}$  and  $\text{CuCl}/\text{ChCl}/\text{EG}$ .[120] Mass transfer coefficient  $k_D$  was derived by linear voltammetry measurements. Comparisons were made by using different agitation method, a rotating disc electrode (RDE) and the sonication. The mass transfer coefficients were listed in Table 7.1. At 25 °C, in both electrolytes, the mass transfer coefficients with sonication were 2~3 times higher than that with the RDE. And at 50 °C, the temperature was higher and the viscosity of the liquid was lower than that at 25 °C. The results showed that the improvement by using sonication at 50 °C was more than that at 25 °C. The experiments proved that the sonication could effectively improve the mass transfer and it was more efficient at in liquid with a low viscosity.

Table 7.1 Mass transfer coefficients with RDE and sonication at 25 °C and 50 °C

Operation conditions	Temperature /°C	$k_D \text{ Cu}^{2+} / \text{cm s}^{-1}$	$k_D \text{ Cu}^+ / \text{cm s}^{-1}$
RDE at 5000 rpm	25	$5.7 \times 10^{-4}$	$6.9 \times 10^{-4}$
RDE at 5000 rpm	50	$11.1 \times 10^{-4}$	$10.7 \times 10^{-4}$
Ultrasound at 20 kHz	25	$15.5 \times 10^{-4}$	$13.2 \times 10^{-4}$
Ultrasound at 20 kHz	50	$36 \times 10^{-4}$	$67 \times 10^{-4}$

Electrolytic reduction of metal oxides becomes a promising method of traditional approaches for metal production due to the advantages of lower operation temperature, less hazards emission, and higher metal purity.[4,7,23] However, the commercialization of the electroreduction method is impeded because of the low current efficiency,[13,24] which was limited by the diffusion of  $\text{O}^{2-}$  anions through the solid oxide.[62] According to the three-phase interlines mechanism,  $\text{O}^{2-}$  should be released from



the  $\text{LiTiO}_2/\text{Li}_2\text{O}|\text{Li}_2\text{TiO}_3|\text{Electrolyte}$  interlines to the electrolyte when  $\text{Li}_2\text{TiO}_3$  is reduced to  $\text{LiTiO}_2$ . However, as the  $\text{O}^{2-}$  ions accumulate in the solid phase, the local high  $\text{Li}_2\text{O}$  concentration slows down the reaction, kinetically and thermodynamically.

Attempts are made to increase the  $\text{O}^{2-}$  diffusion in the oxides and improve the current efficiency. Electrolyte oxides were added to the chlorides salts to initiate the oxide flow.  $\text{CaO}$  was added to the  $\text{CaCl}_2$  in both FFC and OS process.[18,20,24,29] For the FFC process, reduction in a 2 mol%  $\text{CaO}/\text{CaCl}_2$  electrolyte resulted in a current efficiency of 40%, about three times higher than that of the reduction in  $\text{CaCl}_2$ . In the calciothermic reduction, Ti metal was produced only after 0.5~1 mol% of  $\text{CaO}$  was added to  $\text{CaCl}_2$  and the current efficiency was 12.9%.[24] The low current efficiency in the OS process was due to the generation of extra amount of Ca metal, and the Ca metal participated in side reactions, covered the oxide surface, or converted to a high local  $\text{CaO}$  concentration which hinder the  $\text{O}^{2-}$  transfer. To solve the problem of excess liquid metal generated at overpotentials, a rotating oxide basket was used for a uniform distribution of Ca metal over the feed.[24,25] However, the rotating basket resulted in a lower efficiency, owing to less contact time of Ca metal with the oxides. Addition of  $\text{Li}_2\text{O}$  to  $\text{LiCl}$  molten salt also helped the metal generation. In pure  $\text{LiCl}$ , the reduction product was either  $\text{LiTi}_2\text{O}_4$  or  $\text{LiTiO}_2$ , based on the applied reduction potential.[59] There was no Ti metal product from the reaction. In comparison, in molten 1 w.t.%  $\text{Li}_2\text{O}/\text{LiCl}$ , Ti metal was produce in 100% reduction extent at a current efficiency at 71.2%.[60] Changes were also made to the reduction feeds. In the FFC process, it was found that the generation of  $\text{CaTiO}_3$  was inevitable and took long time, so the perovskite was synthesized *ex situ* through a chemical process and reduced following the FFC process.[9] The results proved that by directly reduce the perovskite, the current efficiency was improved to 28% with less than half of time to reduce  $\text{TiO}_2$  at a current efficiency of 15%.  $\text{TiO}_2$  particles with low and high porosity were also tested and compared.[18,20] Dense  $\text{TiO}_2$  (15%~16% porosity) followed a different reduction mechanism with porous  $\text{TiO}_2$  (25%~30% porosity). Though both reduction of both  $\text{TiO}_2$  precursors could generate Ti metal, reduction of porous  $\text{TiO}_2$  reduction had a higher current efficiency (40% vs. 32%) and the product contained less oxygen (2000 ppm vs. 12000), compared with those in dense  $\text{TiO}_2$  reductions. Different  $\text{TiO}_2$  particle sizes were also reduced through the OS process, to define it effect on the reduction results. Three different sizes were tested under the same conditions, including micro- ( $D=2.0 \mu\text{m}$ ), submicro- ( $D=90 \text{ nm}$ ) and nano- ( $D=13 \text{ nm}$ ) particles.[26] In the reduction of nano-particles, Ti metal was produced, while the reduction of submicro  $\text{TiO}_2$  produced a mixture of Ti and  $\text{Ti}_2\text{O}$ . Electroreduction of micro  $\text{TiO}_2$  particles produced a more complicated and less reduced products, including Ti metal, perovskite  $\text{CaTiO}_3$  and  $\text{Ti}_2\text{O}$ . Amount the products,  $\text{Ti}_2\text{O}$  was an intermediate product which could be further reduced to Ti metal. The formation of  $\text{CaTiO}_3$  was due to the slow diffusion of  $\text{CaO}$  away from the particle. The research efforts in accelerating the  $\text{O}^{2-}$  diffusion in the

solid and increasing the current efficiency were successful for the purpose. However, the improvement in current efficiency still could not satisfy the requirement of commercial production.

Agitation is a favorable method in improving mass transfer in a system. Among the agitation methods, the sonication has been introduced in low temperature molten salt electrolysis for the purpose of increasing the diffusion of targeted species.[120,140] However, the sonication has not been adopted in applications in high temperature molten salts. In this study, the electroreduction of  $\text{TiO}_2$  was carried out at both overpotential and underpotential in 1 w.t.%  $\text{Li}_2\text{O}/\text{LiCl}$  with and without sonication. Reductions in the silent mode was employed as the baseline for the sonication assisted reductions. The sonication was applied under various parameters, including the relative depth to the oxide basket, the sonication pulsed mode and the power load. Reduced products were analyzed with XRD. Reduction extent, current efficiency and particle sizes were calculated based on XRD results.

### 7.3 Experimental

High purity lithium chloride ( $\text{LiCl}$ , 99.995% metals basis, ultra-dry, Alfa Aesar) and lithium oxide ( $\text{Li}_2\text{O}$ , 99.5%, Alfa Aesar) were used for the electrochemical measurements without further treatment. The electrolyte used in this study was the mixture of 1 w.t.% of  $\text{Li}_2\text{O}/\text{LiCl}$ . Titanium dioxide powders ( $\text{TiO}_2$ , 99.995% and 99.5% metals basis, Alfa Aesar) were pelletized, grounded, and sieved between mesh 60 and 20 (particles size 0.25 mm ~ 0.85 mm). In each  $\text{TiO}_2$  reduction run, 2.0 g  $\text{TiO}_2$  particles were loaded within a 150 g salt mixture bath. The VersaSTAT 4 (Princeton Applied Research) potentiostat with VersaStudio was used to control the electrolysis of CV measurements and  $\text{TiO}_2$  reductions and for the data acquisition. The ultrasound was controlled with Sonics VCF1500. All the electrolysis operations were carried out in an argon atmosphere glovebox (moisture and  $\text{O}_2$  level < 5 ppm).

To define the cathodic decomposition potential of the electrolyte, cyclic voltammetry was measured in a potential range of -2.00 V to OCP vs. Ni/NiO at 20  $\text{mV s}^{-1}$  before reductions. A stainless steel wire (0.025") was used as the cathode and a glassy carbon crucible (HTW GAZ30; Inner height=147 mm, inner diameter=54 mm) was employed as both the anode and the salt container. The reference electrode was a Ni/NiO electrode. CVs were also measured after the reductions in the same potential range to estimate the change in the salt due to the reductions.

2 g  $\text{TiO}_2$  was loaded in the cathode basket inside the glovebox. The electrode bundle and sonication probe (a 0.5" Ti alloy rod) were lowered down into a glassy carbon crucible anode containing the salt before reduction. Reduction were conducted at -0.3 V and +0.05 V vs.  $\text{Li}/\text{Li}^+$  and stopped when

it reached a desired amount of charge. Sonication was operated along with the electrolysis at a 30% output amplitude in a pulsed mode (20 s or 40 s interval). Temperature was also measured during the progress. The coolant air (Airgas, UHP-Air, 100 ml min<sup>-1</sup>) was opened before the sonication probe was lowered down to the salt melt, and closed after the probe was lifted out.

After reductions, the electrode bundle and the sonication probe were lifted out from the salt and the whole set up was cooled to room temperature. The reduction products were transferred out of the glovebox, washed with nano-pore water and acetone, dried under vacuum overnight, and then grinded into fine powder. Powder samples were analyzed using XRD (Rigaku SmartLab) with Cu K-alpha radiation at 40 kV and 30 mA. The scan range was from 10 to 80 degree at 4 deg min<sup>-1</sup>. The particle sizes were derived through the Scherrer equation  $d = \frac{K\lambda}{\beta \cos\theta}$ . K is 0.9 as the shape factor;  $\lambda$  is the X-ray wavelength, 1.5406 Å;  $\theta$  is the Bragg angle in rad.  $\beta$  is the line broadening at half the maximum intensity.

## 7.4 Results and Discussion

### 7.4.1 Sonication Parameters Optimization

#### 7.4.1.1 Effect of the Basket Depth

To study the effect of the relative position of the probe and the oxide basket, three different basket positions were tested in the sonication-assisted TiO<sub>2</sub> reductions at a constant potential of +0.05 V vs. Li/Li<sup>+</sup>. In this study, the reduction potential was in a continuous mode without interruption. There was no lithium metal generation during the underpotential reductions, so it was not necessary to apply reduction potentials in a pulsed mode. Sonication was applied at 30% of 1500 W power in a pulsed mode with 20 s intervals. Three positions were presented in Fig. 7.1 inset. The bottom of the basket was placed at 1/3", 2/3" and 1" below the probe tip.

In I-t curves achieved in reduction at different basket depths (Fig. 7.1), the curves showed the similar starting current at -1 A, and an immediate current drop to a plateau at -0.3 A. The current in reduction with basket at 2/3 beneath position was a little lagged drop, compared with the current curves in other two conditions.

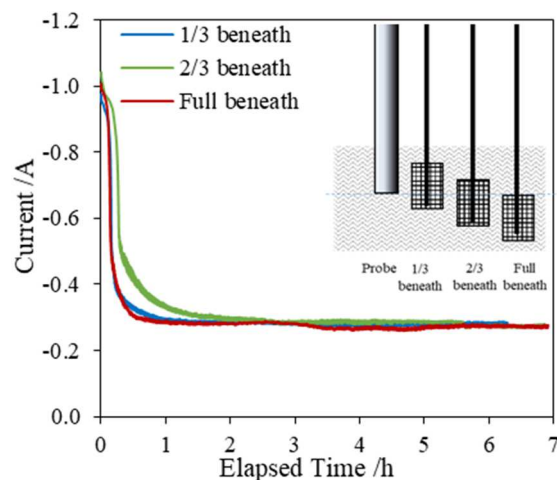


Figure 7.1 I-t curves of  $\text{TiO}_2$  reductions at  $+0.05 \text{ V vs. Li/Li}^+$  with sonication at three different depths. Inset: the geometries of the relative positions of the sonication probe and cathode baskets. Inset: sketch of the probe and cathode basket.

Effect of the position of the probe was studied in literatures. Fig. 7.2 shows the convective flow distribution around the horn, which is dominated by the acoustic streaming. The nonlinear effect also creates a strong and rapid flow below the sonic horn ( $10\text{-}100 \text{ cm s}^{-1}$ ). [138] It was found that in the bulk generation of HMF from glucose, as long as the probe was 1/3 of the total height of the solution, the reaction kinetics were not changed and the results were consistent.[138] However, in the electrochemistry with a face-on geometry of the electrode and sonication horn [141], researchers investigated the relationship between the horn-to-electrode distance and the limiting current in an aqueous solution of  $0.8 \text{ mM}$  sodium iodide.[142] Results showed that with a longer distance, the limiting current became lower. The previous studies also proved that the diffusion coefficient was increased by applying sonication [120] and the improvement was more significant with a smaller horn-to-electrode distance.[142] It was explained that the acoustic streaming resulted in an turbulent flow pattern and the flow near the sonication probe is more intensive.

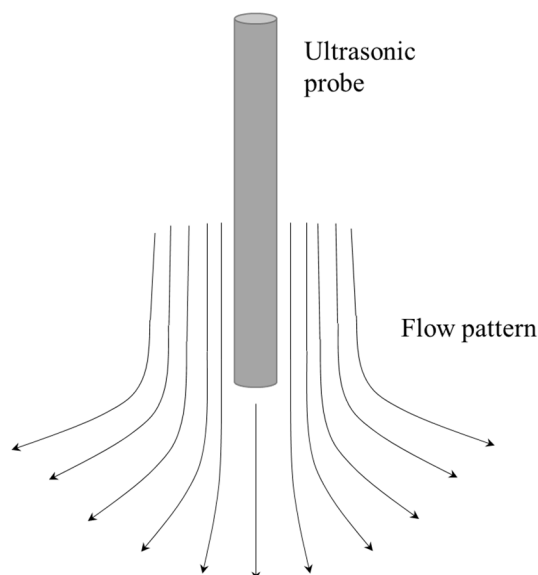


Figure 7.2 Schematic drawing of a typical flow pattern around a sonication probe[142]

In the present study, the sonication probe tip was 1" in the molten salt, and the cathode basket (1" height) was located on the side of the sonication probe. Three basket immersion depth were tested with the top edge of the basket 1/3", 2/3" and 1" below the molten salt surface level.  $\text{TiO}_2$  reductions were carried out at +0.05 V vs.  $\text{Li/Li}^+$  with sonication controlled in a 20 s interval pulsed mode with 30% of 1500 W.

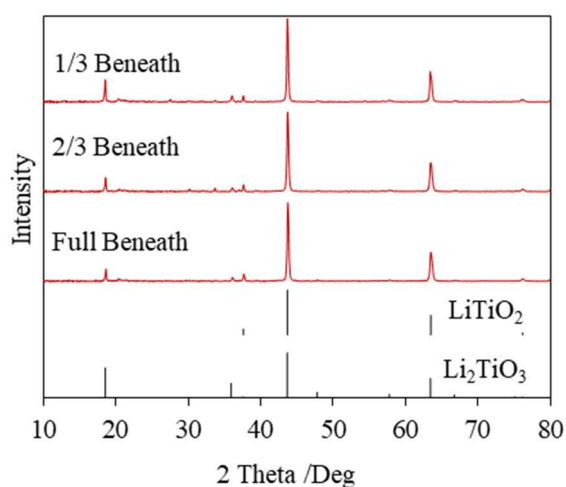


Figure 7.3 XRD analysis of samples in reduction processes with different basket positions

The XRD analysis was shown in Fig. 7.3. Compositions of the reduction products were estimated from the XRD results through the Rietveld refinement (Table 7.2). The compositions were  $\text{Li}_2\text{TiO}_3$  and mainly  $\text{LiTiO}_2$ . There was neither  $\text{TiO}_2$  nor Ti metal identified in the products. The summary of the reduction products were listed in Table 7.3. The reduction extent was increased when

more charge was applied. The reduction extent was 18.9% with 61% of the theoretical charge at the 1/3 beneath position, and it was increased to 21.5% when the applied charges was 76% of the theoretical at the full beneath position. Current efficiency at the basket location close to the surface was the highest, followed by the lowest position, and the reduction with basket at the middle level resulted in the smallest current efficiency. With the basket level closest to the molten salt surface, the status of the liquid was affected by not only the direct ultrasound but also the surface vertical wave generated from the vibration of the sonicator probe (Fig. 7.4). At the current stage, this explanation is a deduction from the observation, and more work needs to be done to make it clear. So, the effect of sonication on the reduction with basket at 1/3 beneath position was enhanced, and in result, it showed the highest reduction extent. With the basket level moved away from the molten salt surface to the probe tip, the external impact would come from the sonication only. Particle sizes, determined with the Scherrer equation using the XRD intensity peak at 43~44 °, decreased with longer sonication time and lower basket positions. The TiO<sub>2</sub> particle before reduction sizes 56.40 nm, derived from Fig. 6.1. The particle size in the basket at 1/3 beneath position was the largest at 38.04 nm and that in the basket at the full beneath position was the smallest at 32.06 nm. Since the effect of sonication was the most intense near the tip of the horn, it would have a significant impact on the basket at the full beneath position. So, in this case, the fragmentation was the dominated the result from the ultrasound.

Table 7.2 Rietveld refinement results for the products reduced at +0.05 V vs. Li/Li<sup>+</sup> with different basket depth. Sonication interval: 20 s, ultrasound power: 30% of 1500 W.

Basket Depth (inch below the sonication probe tip)		1/3	2/3	1
Products composition w.t. %	TiO <sub>2</sub>	0	0	0
	Li <sub>2</sub> TiO <sub>3</sub>	29.0	16.7	17.0
	LiTiO <sub>2</sub>	71.0	83.3	83.0
R factors	R <sub>wp</sub> (%)	6.92	7.49	6.83
	R <sub>p</sub> (%)	4.96	5.16	4.91
	R <sub>e</sub> (%)	5.72	5.76	5.89
	S	1.2069	1.2984	1.1576
	χ <sup>2</sup>	1.4565	1.6859	1.34
	Maximum shift e.s.d.	0.944	0.096	1.755
Phases	Structural Parameters			
LiTiO <sub>2</sub> Lithium titanium(III) oxide (01-074-2257) Space group: 225 : Fm-3m	a (Å)	4.1423(4)	4.1638(4)	4.1556(9)
	b (Å)	4.1423(4)	4.1638(4)	4.1556(9)
	c (Å)	4.1423(4)	4.1638(4)	4.1556(9)
	α (Degree)	90	90	90
	β (Degree)	90	90	90

	$\gamma$ (Degree)		90	90	90
	V ( $\text{\AA}^3$ )		71.075(12)	72.187(13)	71.77(3)
	Scale factor		60(2)	2.09(9)	62(3)
	Gaussian peak width parameters ( $^{\circ 2}$ )	U	0.33(16)	0.22(16)	0.27(18)
		V	-0.23(16)	-0.14(16)	-0.13(19)
		W	0.06(4)	0.06(4)	0.05(5)
Li <sub>2</sub> TiO <sub>3</sub> Dilithium titanate (IV) (01-080-7163) Space group: 15 : C12/c1,unique-b,cell-1	a ( $\text{\AA}$ )		5.060(2)	5.120(2)	5.0741(12)
	b ( $\text{\AA}$ )		8.760(3)	8.8238(6)	8.818(5)
	c ( $\text{\AA}$ )		9.753(5)	9.802(3)	9.758(3)
	$\alpha$ (Degree)		90	90	90
	$\beta$ (Degree)		99.77(5)	99.38(3)	100.17(3)
	$\gamma$ (Degree)		90	90	90
	V ( $\text{\AA}^3$ )		426.1(3)	437.0(2)	429.8(3)
	Scale factor		9.6(7)	4.2(6)	6.9(5)
	Gaussian peak width parameters ( $^{\circ 2}$ )	U		0.34(19)	1.489(18)
V			-0.12(10)	-1.0(3)	-0.38(10)
W			0.042(12)	0.100(5)	0.036(11)

Table 7.3 Summary of products in reductions at +0.05 V vs. Li/Li<sup>+</sup> at different basket positions

Basket Depth	Charge of theoretical	Sonication duration /h	Particle size /nm	Composition (w.t.%)			Reduction extent	Current efficiency
				TiO <sub>2</sub>	Li <sub>2</sub> TiO <sub>3</sub>	LiTiO <sub>2</sub>		
1/3 beneath	61%	6.29	38.04	0	29.0	71.0	18.9%	30.9%
2/3 beneath	83%	6.86	32.67	0	16.7	83.3	21.6%	26%
Full beneath	76%	6.91	32.06	0	17.0	83.0	21.5%	28.3%

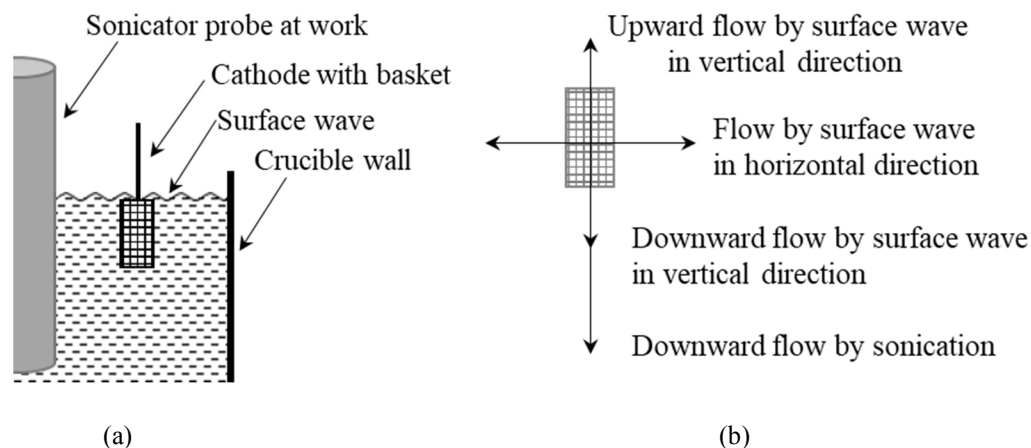


Figure 7.4 (a) Schematic drawing of setup when the sonication is on. (b) Flow analysis at the basket when the basket is close to the molten salt surface.

In summary, the basket at different depth was impacted differently by the effect of sonication. As the basket closer to the sonication tip, the effect of ultrasound wave is stronger and the current efficiency is higher. At the meantime, when the bakset was closer to the molten salt surface, it received agitation from both the sonication and the liquid surface wave, and the combined effected resulted in a current efficiency higher than that resulted from the ultrasound power only. So, a basket at the liquid surface level is recommend.

#### 7.4.1.2 Effect of the Sonication Pulse Modes

The effect of sonication pulse mode was studied at 20 s interval and 40 s interval pulse modes during  $\text{TiO}_2$  reduction at  $-0.3\text{V vs. Li/Li}^+$  for 4 h. The basket was merged in the molten salt with the upper edge of basket at the molten salt surface level, meaning 'zero' inch below the sonication probe. 80% of the theoretical charge was applied for reduction under sonication at 20 s interval, and 58% of the theoretical charge was applied for reduction under sonication at 40 s interval. The ultrasound power was at 30% of 1500 W. The corresponding I-t curves were presented in Fig. 7.5a, and the XRD analyses of the products were shown in Fig. 7.5b.



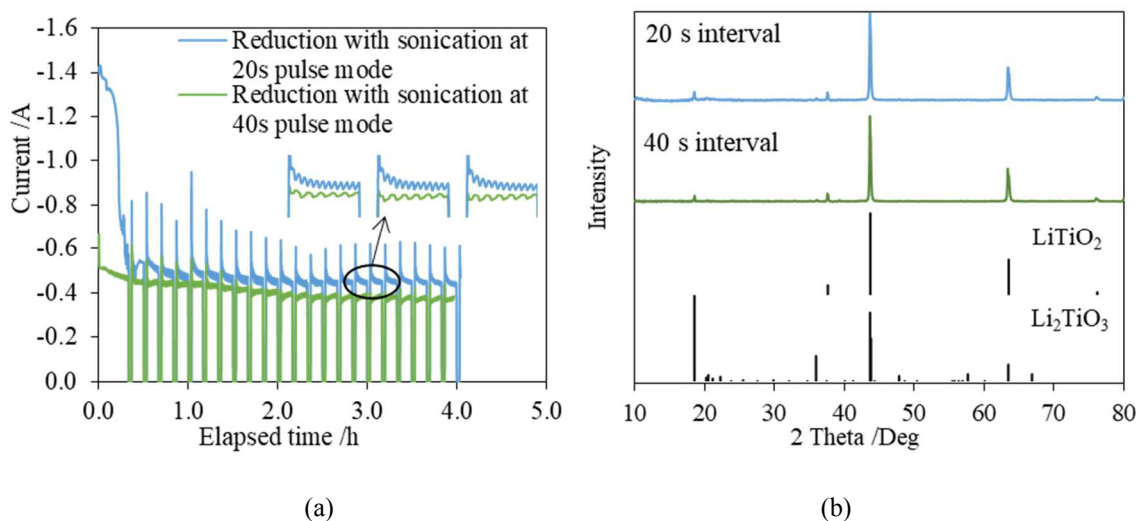


Figure 7.5 (a) Current-time profiles and (b) XRD results for  $\text{TiO}_2$  reductions at  $-0.3\text{V}$  vs.  $\text{Li}/\text{Li}^+$  with sonication in 20 s and 40 s interval pulse modes

In the current-time profiles, a current peak was observed in blue line while it is not shown in the green line. The difference was due to different  $\text{TiO}_2$  soaking time before electrolysis, as discussed in Session 6.4.1.  $\text{TiO}_2$  particles were soaked in the molten salt for 1.5 h before reduction with 20 s interval of sonication, and the soaking time for reduction with 40 s interval sonication was 4 h. After 4 h of soaking,  $\text{Li}_2\text{TiO}_3$  shell is thicker, and the diffusion distance for the  $\text{LiTiO}_2|\text{TiO}_2|\text{Electrolyte}$  is much longer, so the current decreases earlier than that in reduction with shorter soaking time. Also, for the  $\text{LiTiO}_2/\text{Li}_2\text{O}|\text{Li}_2\text{TiO}_3|\text{Electrolyte}$  interlines, the thick  $\text{Li}_2\text{TiO}_3$  shell takes longer time to reduce, and with higher concentration of  $\text{Li}_2\text{O}$  generated, it slows down the  $\text{Li}_2\text{TiO}_3$  reduction. So, the current plateau in longer soaking time reduction is lower than that in shorter soaking time reductions. Therefore, a shorter soaking time is recommended.

Current oscillations show differences at 20s and 40s pulse (Fig. 7.5a inset). A wider current oscillation is observed in the 40s pulse curve, compared with that of 20s pulse mode. XRD results of products reduced in 20s and 40s sonication pulse modes consisted of similar concentrations of  $\text{LiTiO}_2$  and  $\text{Li}_2\text{TiO}_3$ .  $\text{TiO}_2$  was fully converted in both conditions. In conclusion, different sonication pulse modes results in different current oscillation widths, but it didn't improve reduction extent significantly. So, based on this study, either interval mode works.

### 7.4.1.3 Effect of the Sonication Power with 20 s Pulsed Mode

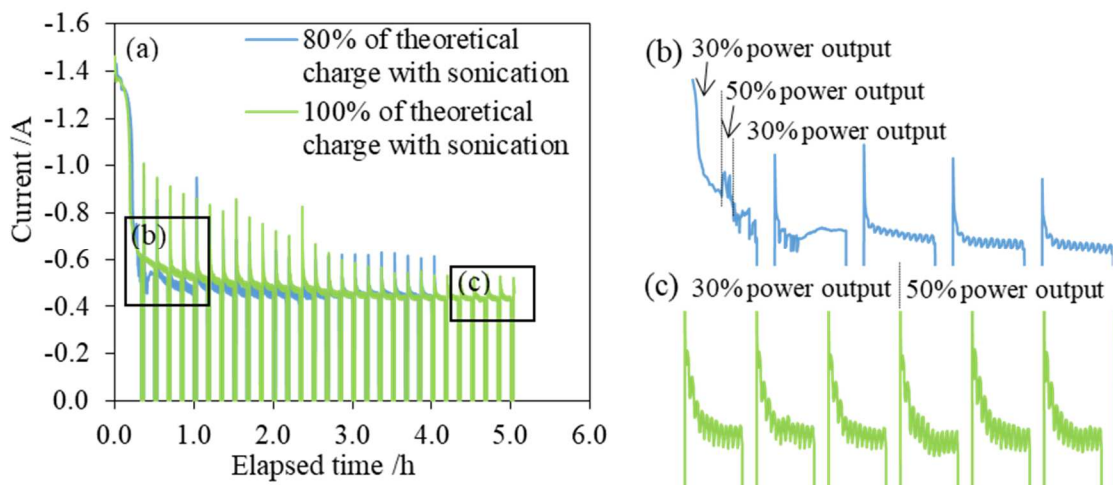


Figure 7.6 Current-time profiles in  $\text{TiO}_2$  reductions at  $-0.3$  V vs.  $\text{Li/Li}^+$  with 30% and 50% of maximum power output 1500 W at (a) whole range, (b) current decrease section and (c) current plateau section

In the reductions of  $\text{TiO}_2$  at  $-0.3$  V vs.  $\text{Li/Li}^+$ , the top of the basket was at the molten salt level. The power supply was switched between 30% and 50% of 1500 W (the maximum power of the supply) to study the effect of sonication power on the reduction current (Fig. 7.6a). In Fig. 7.6b, when power was switched during current decrease in the I-t curve, a small current increment was observed when the power supply was switched from 30% to 50% of 1500 W. But due to power overload after 40s, the sonication was stopped and the current dropped back to the level without sonication. When the sonication was resumed immediately after power overload, it still ran into the problem of power load even at 30% of 1500 W. While after around 8 min of rest time, the sonication started to work normally at 30% of 1500 W. Fig. 7.6c shows the current response when power was increased in current plateau section. There was no significant change in current when power was increased to 50% of 1500 W, and the sonication kept working at the higher power for 30 min. In conclusion, in the current decreasing section, the current shows a jump when sonication power was increased; but in the current plateau, the increase in sonication power does not show significant change in current response. In terms of applying a higher power supply, the problem of power overload may happen which forces the sonication to stop.

## 7.4.2 Effects of Sonication on Temperatures

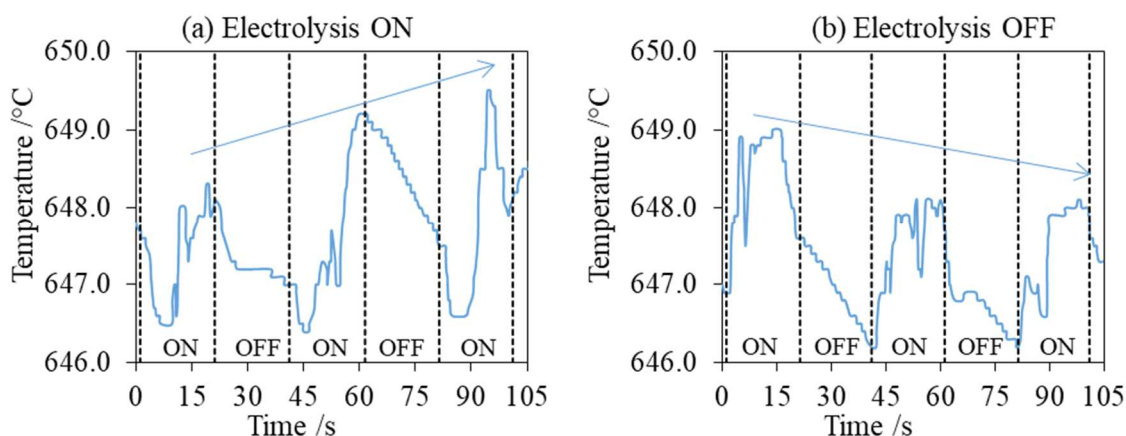


Figure 7.7 A portion of temperature profile with pulsed sonication (20 s interval) when (a) electrolysis is ON and (b) electrolysis is OFF

Figure 7.7 shows the effect of pulsed sonication on temperatures. The trend of temperature changes were different when the potential was applied (Fig. 7.7a) and when the system stayed at the OCP (Fig. 7.7b). There was a 4 s delay in the temperature response. The temperature increased from 646.5 °C to 649.5 °C as the ultrasound power was applied. It was because the cavitation of the high pressure gas bubble (CO or CO<sub>2</sub>) generated by the ultrasound power. When sonication was off, the temperature dropped to the original temperature before the sonication was applied. During the electrolysis, the temperature gradually increased in each sonication cycle when electrolysis was on and decreased when electrolysis was at rest. The increase of temperature during electrolysis may be the results of several reasons. By applying reduction potentials to the cell, the temperature would be slightly increased due to the power input. Also, the temperature increase due to just the sonication would decrease the solubility of gas generated during reduction, so the generated CO or CO<sub>2</sub> bubbles on the anode underwent the cavitation. It promoted the formation and release of CO/CO<sub>2</sub> and would improve the reduction.

It can be observed from the plots that the temperature oscillated during the procedure kept within a certain range of 3°C. Therefore, temperature is not a big concern when sonication is applied in a pulse mode.

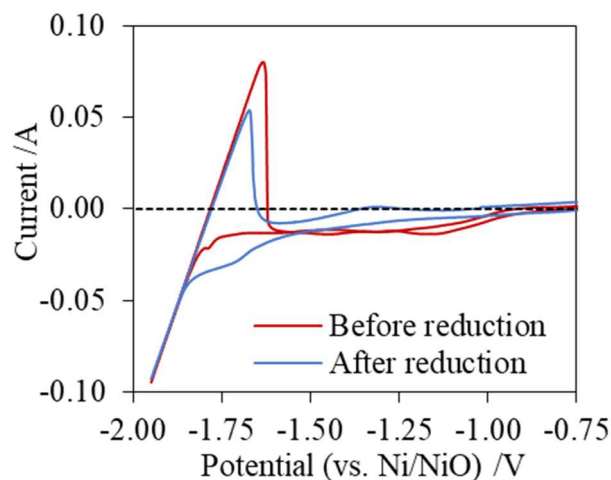
7.4.3 Effects of Sonication on TiO<sub>2</sub> Reductions

Figure 7.8 CVs in molten 1 w.t. % Li<sub>2</sub>O/LiCl at 20 mV s<sup>-1</sup> before and after TiO<sub>2</sub> reductions at -0.3 V vs. Ni/NiO. W.E.: Stainless steel wire. C.E.: glassy carbon.

CVs in the salts were measured before and after reduction, as shown in Fig. 7.8. The cathodic decomposition potentials were almost the same for the two CV measurements, at -1.83 V vs. Ni/NiO. Lithium reduction peaks were at the same current while the re-oxidation peak for used salt is smaller than that of fresh salt. The difference in re-oxidation current may be that the generated lithium metal was consumed elsewhere in used salt, such as reactions with intermediates dissolved in salt during TiO<sub>2</sub> reduction run. The CV curve for used salt in this experiment has a larger Li Re-oxidation peak, more similar cathodic edge as that for fresh salt, and a smaller current slope than the CVs for used salt after reduction without sonication (Fig. 6.8) The improvement may be the quick release of gaseous carbon oxides, and less generation of carbonates. It indicates that the properties of salt after reduction are not changed so much if the reduction undergoes sonication.

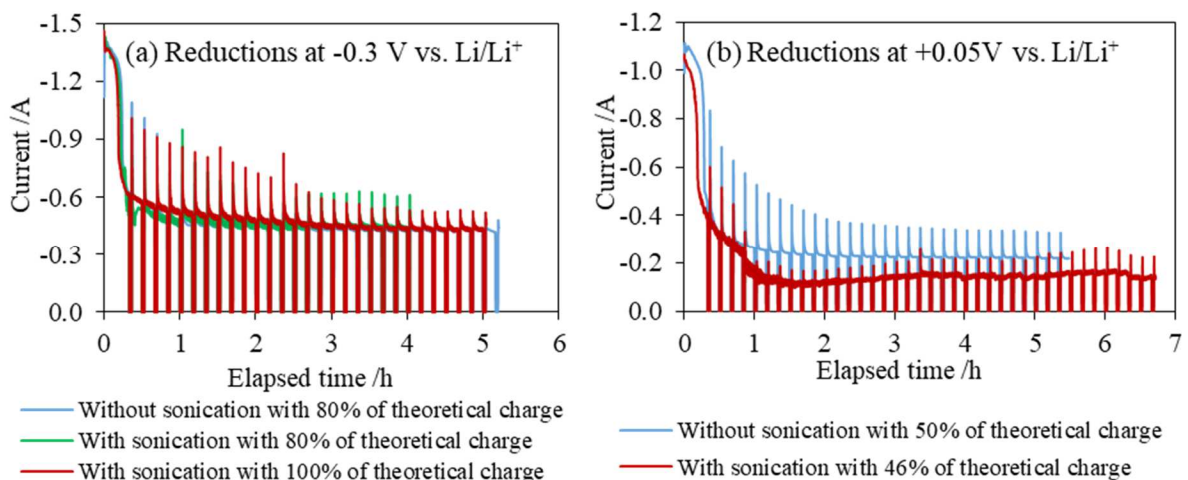


Figure 7.9 I-t curves of sonication-assisted  $\text{TiO}_2$  reductions at (a) overpotential at  $-0.3 \text{ V vs. Li/Li}^+$  and (b) underpotential at  $+0.05 \text{ V vs. Li/Li}^+$

Fig. 7.9a shows the current-time profiles of  $\text{TiO}_2$  reduction at  $-0.3 \text{ V vs. Li}^+/\text{Li}$ . All three experiments show a similar current pattern which contains a current peak at  $-1.4 \text{ A}$  and then decrease to a plateau at around  $-0.44 \text{ A}$ . Reduction with sonication shows a little higher current response, which decrease reaction time. The silent reduction showed a current peak at the beginning; however, in the sonication-assisted reductions, the current dropped directly as the sonication and electrolysis started. Reductions with sonication were more time-efficient than the silent reduction. To apply 80% of the theoretical charge, the silent reduction took 5.2 h, which was longer than the 4 h reduction with sonication. Reduction with 100% of the theoretical charge with sonication took 5 h, which was still shorter than silent reduction to reach 80% of the theoretical charge. In the reductions with ultrasound, current spikes in the I-t curve were associated with cavitation bubbles collapsing on the electrode surface.[120] In the reduction at  $+0.05 \text{ V vs. Li/Li}^+$ , the current pattern (Fig. 7.9b) was the same as reduction at  $-0.3 \text{ V}$ , but both the initial current response and the current plateaus were lower than that in reductions at  $-0.3 \text{ V}$ . The current drop in reduction with sonication was earlier than in the silent reduction. Both sonication-assisted reduction and silent reduction showed the similar maximum current at  $-1.1 \text{ A}$ . The current in sonication-assisted reduction dropped fast, reached the lowest at  $-0.1 \text{ A}$ , and then slightly increased to  $-0.15 \text{ A}$ . The current plateau in silent reduction was  $-0.22 \text{ A}$ , higher than that in reduction with sonication.

The reduction products were analyzed with XRD (Fig. 7.10). The XRD results were further studied for the composition with the Rietveld refinement (Table 7.4 and 7.5), and the summary was listed in Table 7.6. In the overpotential reduction products,  $\text{TiO}_2$  was fully converted, and  $\text{LiTiO}_2$  was the major component, balanced with  $\text{Li}_2\text{TiO}_3$  (Fig. 7.10a, Table 7.4). In the reductions with 80% of

charges, the application of sonication improved both reduction extent and current efficiency by around 2%. In sonication-assisted reductions, by applying more charge to 100% of the theoretical charge, the reduction extent was increased from 21.9% to 22.6%, around 3% higher. However, the current efficiency was decreased dramatically from 27.4% to 22.6%, about 17.5% lower. The decrease in the current efficiency may be the generation of excess Li at overpotential electrolysis. Product particle sizes derived from the Scherer equation was decreased in the sonication-assisted reductions, and the size was increased with more charges. The decrease in particle size may due to the fragmentation caused by ultrasound power.[124] And the increase in particle size with longer sonication time may be the expansion of the particle through the sono-capillary effect.[136] The XRD analyses of the underpotential products (Fig. 7.10b, Table 7.5) were similar as overpotential reduction products. There was no  $\text{TiO}_2$  left;  $\text{LiTiO}_2$  was the major component, and  $\text{Li}_2\text{TiO}_3$  was the minor component. In underpotential reductions, the current efficiencies were higher than that in overpotential reductions. In the reduction at underpotential, the current efficiency was 36.7%. When the reduction was assisted with sonication, the current efficiency was 44.5%, 21.25% improved compared with reduction without sonication. The product particle size in sonication-assisted reductions was bigger than that in the silent reduction, which might be the compensation effect of fragmentation and sono-capillary effect.

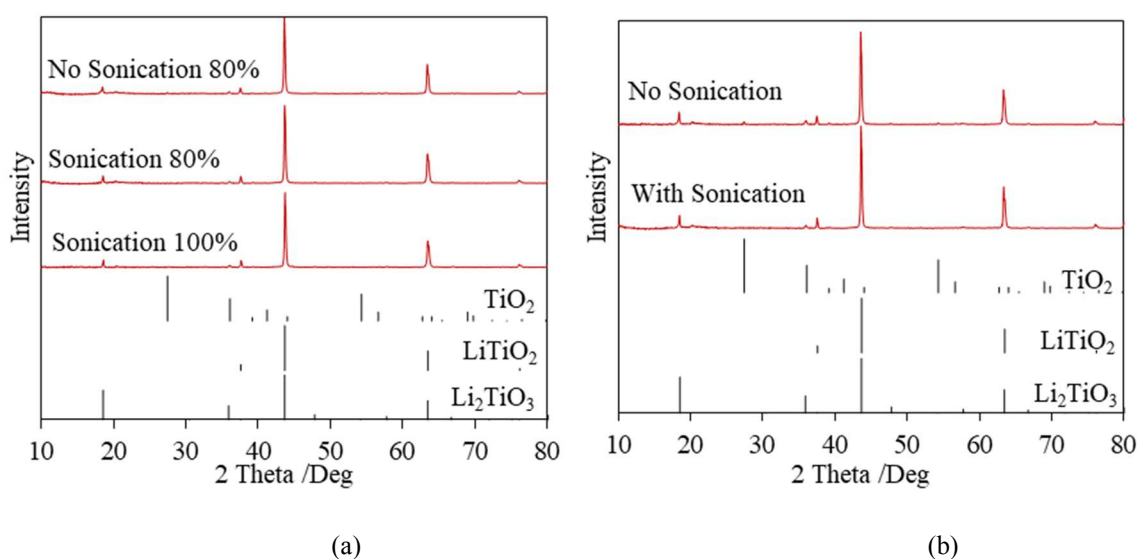


Figure 7.10 XRD analysis of reduction products at (a)  $-0.3$  V and (b)  $+0.05$  V vs.  $\text{Li/Li}^+$ .

Table 7.4 Rietveld refinement results for the products reduced at -0.3 V vs. Li/Li<sup>+</sup> with and without sonication. Sonication interval: 20 s, ultrasound power: 30% of 1500 W.

Reduction		No sonication	Sonication	Sonication	
Applied charge of the theoretical		80%	80%	100%	
Products composition w.t. %	TiO <sub>2</sub>	0	0	0	
	Li <sub>2</sub> TiO <sub>3</sub>	17	15	12	
	LiTiO <sub>2</sub>	83	85	88	
R factors	R <sub>wp</sub> (%)	6.98	6.55	7	
	R <sub>p</sub> (%)	4.9	4.61	4.94	
	R <sub>e</sub> (%)	5.79	5.62	5.78	
	S	1.2042	1.1637	1.21014	
	$\chi^2$	1.4502	1.3542	1.465	
	Maximum shift e.s.d.	0.478	0.06	0.119	
Phases	Structural Parameters				
LiTiO <sub>2</sub> Lithium titanium(III) oxide (01-074-2257) Space group: 225 : Fm-3m	a (Å)		4.0722(14)	4.1476(15)	4.14007(12)
	b (Å)		4.0722(14)	4.1476(15)	4.14007(12)
	c (Å)		4.0722(14)	4.1476(15)	4.14007(12)
	$\alpha$ (Degree)		90	90	90
	$\beta$ (Degree)		90	90	90
	$\gamma$ (Degree)		90	90	90
	V (Å <sup>3</sup> )		67.53(4)	71.35(5)	70.962(4)
	Scale factor		68(2)	61(2)	65.0(18)
	Gaussian peak width parameters ( <sup>o</sup> 2)	U	0.15(6)	0.30(9)	0.32(8)
		V	-0.12(7)	-0.26(9)	-0.29(8)
W		0.042(16)	0.08(2)	0.09(2)	
Li <sub>2</sub> TiO <sub>3</sub> Dilithium titanate (IV) (01-080-7163) Space group: 15 : C12/c1,unique-b,cell-1	a (Å)		5.014(2)	5.092(4)	5.177(8)
	b (Å)		8.611(6)	8.806(8)	8.592(13)
	c (Å)		9.5885(5)	9.732(9)	10.194(12)
	$\alpha$ (Degree)		90	90	90
	$\beta$ (Degree)		99.80(4)	99.35(11)	108.91(19)
	$\gamma$ (Degree)		90	90	90
	V (Å <sup>3</sup> )		406.6(4)	430.6(6)	429.0(10)
	Scale factor		7.1(12)	10.0(16)	9.9(17)
	Gaussian peak width parameters ( <sup>o</sup> 2)	U	0.2(3)	1.6(5)	4.5(2)
		V	-0.2(3)	-0.23(8)	-0.7(4)
W		0.07(6)	0.00(8)	0.0(3)	

Table 7.5 Rietveld refinement results for the products reduced at +0.05 V vs. Li/Li<sup>+</sup> with and without sonication. Sonication interval: 20 s, ultrasound power: 30% of 1500 W.

Reduction		Without sonication	With sonication	
Applied charge of the theoretical		50%	46.3%	
Products composition w.t. %	TiO <sub>2</sub>	0	0	
	Li <sub>2</sub> TiO <sub>3</sub>	31%	21%	
	LiTiO <sub>2</sub>	69%	79%	
R factors	R <sub>wp</sub> (%)	6.98	6.49	
	R <sub>p</sub> (%)	4.54	4.38	
	R <sub>e</sub> (%)	5.54	5.59	
	S	1.2574	1.1589	
	χ <sup>2</sup>	1.581	1.343	
	Maximum shift e.s.d.	0.088	0.199	
Phases	Structural Parameters			
LiTiO <sub>2</sub> Lithium titanium(III) oxide (01-074-2257) Space group: 225 : Fm-3m	a (Å)	4.1356(2)	4.18165(18)	
	b (Å)	4.1356(2)	4.18165(18)	
	c (Å)	4.1356(2)	4.18165(18)	
	α (Degree)	90	90	
	β (Degree)	90	90	
	γ (Degree)	90	90	
	V (Å <sup>3</sup> )	70.732(7)	73.121(5)	
	Scale factor	61(2)	72(2)	
	Gaussian peak width parameters ( <sup>o</sup> 2)	U	0.17(8)	0.04(5)
		V	-0.13(8)	-0.02(5)
W		0.0444(19)	0.019(12)	
Li <sub>2</sub> TiO <sub>3</sub> Dilithium titanate (IV) (01-080-7163) Space group: 15 : C12/c1,unique-b,cell-1	a (Å)	5.0572(12)	5.1099(5)	
	b (Å)	8.7433(15)	8.8665(9)	
	c (Å)	9.691(3)	9.8309(14)	
	α (Degree)	90	90	
	β (Degree)	99.705(19)	100.321(13)	
	γ (Degree)	90	90	
	V (Å <sup>3</sup> )	422.37(19)	438.21(9)	
	Scale factor	9.9(10)	4.9(3)	
	Gaussian peak width parameters ( <sup>o</sup> 2)	U	0.01(12)	0.30(5)
		V	-0.09(2)	-0.18(3)
W		0.036(10)	0.024(3)	



Table 7.6 Summary of products in reductions at -0.3 V and +0.05 V vs. Li/Li<sup>+</sup> with and without sonication

Reduction potential /V vs. Li/Li <sup>+</sup>	Charge / % of theoretical	Sonication /h	Particle size /nm	Composition /w.t.%			Reduction extent	Current efficiency
				TiO <sub>2</sub>	Li <sub>2</sub> TiO <sub>3</sub>	LiTiO <sub>2</sub>		
-0.3	80%	N/A	38.37	0	17	83	21.5%	26.9%
-0.3	80%	4.05	35.96	0	15	85	21.9%	27.4%
-0.3	100%	5.04	38.04	0	12	88	22.6%	22.6%
+0.05	50%	N/A	38.02	0	31	69	18.3%	36.7%
+0.05	46.3%	6.72	39.07	0	21	79	20.6%	44.5%

In conclusion, sonication can improve the current efficiency in both lithiothermic and direct electron reductions of TiO<sub>2</sub>. In overpotential reductions, liquid Li metal blocks the O<sup>2-</sup> transfer by covering the oxide particles.[33,86] Under the ultrasound pressure, the solid oxide particles are broken into smaller pieces and the Li layer will either become thinner or transfer into the pallet through the newly generated tunnels. In underpotential reductions, after the particle breaks down, fresh salt with rich electrons reaches to unreacted session easily. Then, under both reduction conditions, O<sup>2-</sup> ions generated from the reduction only need to travel a short distance inside the particle to be leased at the solid surface. So, with the sonication, the O<sup>2-</sup> diffusion to the outside of the particle became easier and the current efficiency increased. Another consequence from the ultrasonic vibration was the sono-capillary effect, under both overpotential and underpotential conditions. It pressurized the molten salt into the capillary structure inside the materials, and the depth and velocity of liquid salt penetration into the canals and the pores. Fresh lithium salt is pushed in the porse when the sonication is applied. Then during the sonication is pulsed, oxide reduction occurs inside the particle and O<sub>2</sub> ions are released to the cappilaris pores. And after the sonication is resumed, new lithium salt goes into the cappliary structure and force the O<sub>2</sub>-rich lithium salt out from the solid. So, in general, the liquid lithium salt passed thoroughly inside the particles, taking the released O<sup>2-</sup> to the outside and leaving the particle at a relative low O<sup>2-</sup> concentration. In overpotential reductions, the vibration could also press liquid Li to the inside pores of the particle and accelerate the lithiothermic reduction. Though the time efficiency of sonication assisted underpotential reduction is low, the current effieincy is dramatically high. Meanwhile, the flow of the salt melt through the capillary structure would generate pressure inside the particle and slightly expanded the particle size. The increment in particle size was also observed in long-time sonication-assisted electrolysis (Table 7.6). Improvement in current efficiency was more

sufficient in underpotential reduction, indicating the diffusion of  $O^{2-}$  through the solid particle was the main reason of low reduction current efficiency.

#### 7.4.4 Corrosion of Sonicator Probes under Different Operation Conditions

Effect of operation conditions was studied by testing the sonication in air and argon atmospheres. Pictures of probes (Fig. 7.11) were used to visualize the corrosion results. Probes were titanium alloy (Fig. 7.11a) customized for application in molten salts at 650 °C. When tested in air, overloading problem occurred after 15 minutes, and as the result, the sonication was forced to stop. It was because the extreme oxidative reaction occurred on the probe surface with air. The probe was corroded (Fig. 7.11b), and the condition of the probe was changed. So it could not work as manufacture tuned.

When used in argon, the probe kept working for more than 3 hour with electrolysis before it was turned off. Probe after tested in argon (Fig. 7.11c) showed a metal shinny surface compared with the probe tested in air (Fig. 7.11b). The probe surface after operating at an even longer time in molten salt with electrolysis (Fig. 7.11d) still looked better than that tested in air. The reason that the probe works longer in argon is that the system is free from moisture and oxidative species which are corrosive.

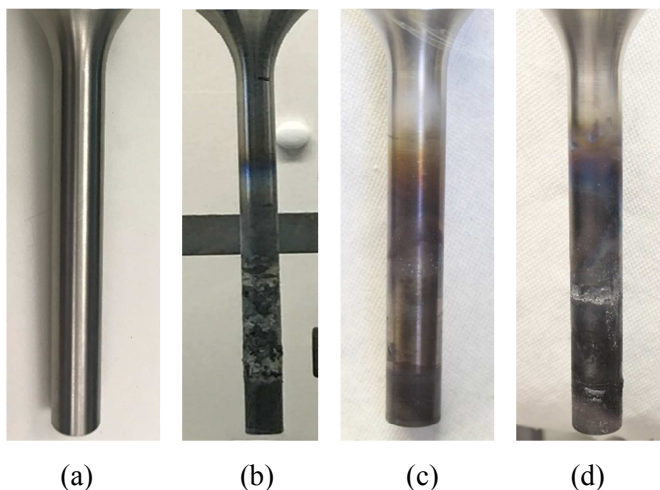


Figure 7.11 Sonicator probes when it is (a) new, (b) tested in air without electrolysis, and (c) tested in argon without electrolysis. (d) is the probe (c) used in argon after reduction.

## 7.5 Conclusion

TiO<sub>2</sub> reductions with various sonication control modes were carried out in this study. Introduction of sonication can increase the current efficiency. At overpotential reductions, application of sonication reduced the operation time, and the current efficiency was slightly improved when sonication was applied, at around 2%. At underpotential electroreduction, current response is lower and time is longer. However, the current efficiency in underpotential reduction is much higher than that can be achieved in overpotential reductions. The highest current efficiency in reduction with sonication was 44.5% which was improved by 21.25% compared with reduction without sonication. The improvement may be due to the fragmentation or sono-capillary effect of the sonication that increased the oxygen ion diffusion in the solid materials. Large particles are broken in to smaller ones, and the liquid mediate is pushed into deep particles to provide fresh reactant and take away products. Location of the cathode basket also has impact on current efficiency. When the basket was in the enhanced sonication area close to the probe tip, the current efficiency was the highest. In the case of a single effect of sonication, the current efficiency was improved when the basket was close to the probe tip. By applying sonication during the reduction, impurity residual in the molten became less. Sonication in high temperature molten salts worked well only in inert environment. The overall temperature of the system was not significantly impacted by the application of sonication in a pulsed mode, so the temperature change in the system is not a big concern in the reduction. Sonication pulse mode of 20 s or 40 s intervals didn't impact the reduction results. High sonication power output increased current responses before current plateau, but the sonication stopped working due to the power overload problem. In conclusion, the application of sonication can improve the O<sup>2-</sup> diffusion and therefore, increase the reduction current efficiency.

## Chapter 8: Conclusion and Future Work

The electrolytic reduction of metal oxides is a promising approach in producing precious metals. The electrochemical methods are low in cost and operation requirements. However, there are obstacles of the commercialization of the method. In recent decades, research efforts have been focused on defining the problem and searching for the solutions. It was found that the  $O^{2-}$  diffusion in the solid particles was the limitation of the process which gave rise to a low current efficiency.

In this study, metal oxides, NiO and TiO<sub>2</sub>, were reduced through electrochemical process in molten 1 w.t.% Li<sub>2</sub>O/LiCl at 650 °C. Both underpotential and overpotential were applied to the oxides for reductions. The operations included the concept and experimental details from the FFC process, the OS process and pyroprocessing. The uniqueness of this project lies in that the reduction was carried out in a small scale of metal oxides by accurately controlling the reduction potential (vs. Ni/NiO RE) and applied charge, as well as the coupling of sonication. High purity electrolytes were used, so that the analysis of the result is free from the interference of impurities. The metal oxides were loaded in the baskets which were designed and fabricated especially for this project. There are mainly two electrolytic measurements involved in the experiments, cyclic voltammetry and chronoamperometry. The properties of the molten salt, such as the decomposition potentials and the electrolytic reaction of salt component at different potentials, were defined with the cyclic voltammetry measurements. Reductions were controlled through the chronoamperometry measurements by applying a constant cathodic potential on the working electrode, and stopped when it reached to a desired amount of charge. The reduced products were analyzed with XRD and TGA for the composition and oxygen level. ICP-MS was introduced in defining the used salt metal composition, including Li, Ni and Ti.

Important contributions and conclusions derived from this work are listed as follows:

1. This study realized successful reductions of metal oxides in a small scale of 150 g molten salts and 2 g metal oxides. The success verified the feasibility of the setup and the practicality of the reduction methods and parameter controls. Therefore, the electrochemical experiment elements in this study can be used in the electroreduction of many other kinds of metal oxide or nonmetal oxides.
2. The performances of several pseudo-reference electrodes (glassy carbon, tungsten, molybdenum and Ni/NiO electrodes) were compared with CV measurements in Li<sub>2</sub>O/LiCl molten salt. In defining the Li deposition potential in LiCl salts with various Li<sub>2</sub>O concentration, the Ni/NiO provided a constant deposition potential. The lithium deposition achieved with the GC, W and Mo reference electrodes showed positive shifts with increasing Li<sub>2</sub>O concentrations. So, the Ni/NiO reference electrode was more favorable in

use in molten LiCl with a varying Li<sub>2</sub>O concentration, and it was employed in this work for other measurements. Furthermore, correlations of reference electrode potentials in pure LiCl and 1 w.t.% Li<sub>2</sub>O/LiCl were defined. Also, the apparent O<sup>2-</sup> activity coefficients were derived in each cell with different reference electrode.

3. Lithiothermic NiO reductions produced Ni metal with 100% of the theoretical charge. The products were analyzed with XRD and TGA. The current efficiency for the process was very high at 96.1%. It took around 2 hour to fully reduce 2 g of NiO pellets. It indicated that the reduction followed one-step mechanism and it possessed a fast reduction kinetics. CV study showed that the used salt didn't contain unacceptable amount of impurities after the NiO reduction, so the salt could be reused in future reductions which reduce the cost of the process.
4. The electrolytic reductions of TiO<sub>2</sub> in molten Li<sub>2</sub>O/LiCl were controlled in multiple ways and the reduction mechanism was proposed. It followed a stage-wise reaction mechanism. The reduction of the oxide particle was considered as the shrinking core model. The reduction process could be explained as the formation and movement of three-phases interlines. The external surface of TiO<sub>2</sub> particles was first chemically combined with Li<sub>2</sub>O in the electrolyte to form Li<sub>2</sub>TiO<sub>3</sub>. As the overpotential was applied, the generated Li metal reduced the TiO<sub>2</sub> core to LiTiO<sub>2</sub>. Finally, the Li<sub>2</sub>TiO<sub>3</sub> shell was reduced by Li metal, leaving a LiTiO<sub>2</sub> shell with high Li<sub>2</sub>O concentration. The highest current efficiency in TiO<sub>2</sub> reduction was 16.7%. The Li<sub>2</sub>O diffusion to the outside of the solid particles was the obstacle of the process.
5. Sonication was coupled with TiO<sub>2</sub> reductions and it improved the current efficiency for reductions at both overpotential and underpotential. The improvement for the underpotential reduction was much more significant than that in overpotential reduction. The current efficiency reached to 44.5% in the sonication-assisted underpotential reduction. So, it was proved that the sonication was effective in accelerating the oxygen ion diffusion in the solids which was the limitation of the metal oxide electrolytic reductions.
6. It was the first time the operation of sonication was utilized in electrolysis in high temperature molten salts. The modified sonication setup in this study could be confidentially introduced in other high temperature molten salt studies. In order to guarantee a stable function of the sonication, it should be used in an inert atmosphere, such as in an argon glovebox. Handling of sonication in a glovebox required several experimental elements, including a dry air coolant system, power cable installed in a

feedthrough, and an actuator for the movement control. The sonication should be operated in a pulsed mode at a low power input.

The success in combining the sonication with metal oxide reductions makes this work have profound implications. This study provides information in aspects of the metal oxide reduction experiments, approaches to derive the mechanism, and the application of sonication. Subsequent work can be done to make the work more complete.

1. The small experimental scale and the control methods will find extended applications in reduction of other oxides and derivation of the reduction mechanisms. Theoretical models, such as the DFT calculation, will support the work and make the results more reliable and comprehensive.
2. Since the sonication has been proved to be effective in improving the current efficiency in metal oxides electroreduction, it promotes the commercialization of the metal generation through electrochemical process. So, the scaling up of the sonication-assisted electroreduction will practically realize the industrial production. Effect of sonication could be enhanced and cover more materials by installing the probe in matrix, which might be one of the possible approaches.
3. In this study, the improvement by the sonication was considered as the acceleration of oxygen ion in the solid phases. It was the conclusion by researchers studying metal oxide reductions in the literatures. However, there is no adequate data provided in this aspect in this study. So, in order to get more solid evidences of the effect of sonication, it is necessary to quantitatively define the  $O^{2-}$  diffusion coefficient in the reduction process under silent and sonication conditions. Also, the determination of flow pattern under a combined effect of sonication and liquid surface wave (Fig. 7.4) is not clear. Calculation or modeling work such as COMSOL will be needed to complete the understanding.
4. This work evidenced the effectiveness of sonication in improving the oxygen ion diffusion through the solid phase in the reduction of  $TiO_2$ . The reaction conditions in this study are quite similar as those in pyroprocessing. So, there is a potential of transferring this work to the pyroprocessing. After overcome the challenges in scaling up the sonication setup to an engineering scale, it is promising to apply the technique to the pyroprocessing in spent oxide fuel treatment. It will speed up treatment of the spent fuel from the light water reactor.

### References

- [1] H. Dircks, Contributions towards a history of Electro-Metallurgy, establishing the origin of the art, E.&F.N. Spon, London, UK, 1863.
- [2] F. Habashi, Handbook of extractive metallurgy, Wiley-Vch, 1997.
- [3] A. Bruneau, Global Trends in Industrial Markets, International Titanium Association, Las Vegas, 2018.
- [4] W. Kroll, The Production of Ductile Titanium, Trans. Electrochem. Soc. 78 (1940) 35–47.  
<https://doi.org/10.1149/1.3071290>.
- [5] D.J. Fray, T.W. Farthing, Z. Chen, Removal of oxygen from metal oxides and solid solutions by electrolysis in a fused salt, WO1999064638A1, 1999.  
<https://patents.google.com/patent/WO1999064638A1/en>.
- [6] A.M. Abdelkader, K.T. Kilby, A. Cox, D.J. Fray, DC Voltammetry of Electro-deoxidation of Solid Oxides, Chem. Rev. 113 (2013) 2863–2886. <https://doi.org/10.1021/cr200305x>.
- [7] G.Z. Chen, D.J. Fray, T.W. Farthing, Direct electrochemical reduction of titanium dioxide to titanium in molten calcium chloride, Nature. 407 (2000) 361–364.  
<https://doi.org/10.1038/35030069>.
- [8] G.Z. Chen, D.J. Fray, T.W. Farthing, Cathodic deoxygenation of the alpha case on titanium and alloys in molten calcium chloride, Metall. Mater. Trans. B. 32 (2001) 1041–1052.  
<https://doi.org/10.1007/s11663-001-0093-8>.
- [9] K. Jiang, X. Hu, M. Ma, D. Wang, G. Qiu, X. Jin, G.Z. Chen, “Perovskitization”-Assisted Electrochemical Reduction of Solid TiO<sub>2</sub> in Molten CaCl<sub>2</sub>, Angew. Chem. Int. Ed. 45 (2006) 428–432. <https://doi.org/10.1002/anie.200502318>.
- [10] D.J. Fray, G.Z. Chen, Reduction of titanium and other metal oxides using electrodeoxidation, Mater. Sci. Technol. 20 (2004) 295–300. <https://doi.org/10.1179/026708304225012242>.
- [11] G. Doughty, D. Fray, The FFC-Cambridge Process for Titanium Metal Winning, Key Eng. Mater. - KEY ENG MAT. 436 (2010) 13–25.  
<https://doi.org/10.4028/www.scientific.net/KEM.436.13>.
- [12] C. Schwandt, D.J. Fray, Determination of the kinetic pathway in the electrochemical reduction of titanium dioxide in molten calcium chloride, Electrochimica Acta. 51 (2005) 66–76.  
<https://doi.org/10.1016/j.electacta.2005.03.048>.
- [13] D.T.L. Alexander, C. Schwandt, D.J. Fray, Microstructural kinetics of phase transformations during electrochemical reduction of titanium dioxide in molten calcium chloride, Acta Mater. 54 (2006) 2933–2944. <https://doi.org/10.1016/j.actamat.2006.02.049>.

- [14] P. Kar, J.W. Evans, A shrinking core model for the electro-deoxidation of metal oxides in molten halide salts, *Electrochimica Acta*. 53 (2008) 5260–5265.  
<https://doi.org/10.1016/j.electacta.2008.02.053>.
- [15] T. Nohira, K. Yasuda, Y. Ito, Pinpoint and bulk electrochemical reduction of insulating silicon dioxide to silicon, *Nat. Mater.* 2 (2003) 397–401. <https://doi.org/10.1038/nmat900>.
- [16] P. Lai, M. Hu, Z. Qu, L. Gao, C. Bai, S. Zhang, Transformation of the Three-Phase Interlines During the Electrochemical Deoxidation of TiO<sub>2</sub>, *Int. J. Electrochem. Sci.* 13 (2018) 4763–4774. <https://doi.org/doi:10.20964/2018.05.23>.
- [17] G.Z. Chen, E. Gordo, D.J. Fray, Direct electrolytic preparation of chromium powder, *Metall. Mater. Trans. B*. 35 (2004) 223–233. <https://doi.org/10.1007/s11663-004-0024-6>.
- [18] D.T.L. Alexander, C. Schwandt, D.J. Fray, The electro-deoxidation of dense titanium dioxide precursors in molten calcium chloride giving a new reaction pathway, *Electrochimica Acta*. 56 (2011) 3286–3295. <https://doi.org/10.1016/j.electacta.2011.01.027>.
- [19] R.L. Centeno-Sánchez, D.J. Fray, G.Z. Chen, Study on the reduction of highly porous TiO<sub>2</sub> precursors and thin TiO<sub>2</sub> layers by the FFC-Cambridge process, *J. Mater. Sci.* 42 (2007) 7494–7501. <https://doi.org/10.1007/s10853-007-1588-8>.
- [20] C. Schwandt, D.T.L. Alexander, D.J. Fray, The electro-deoxidation of porous titanium dioxide precursors in molten calcium chloride under cathodic potential control, *Electrochimica Acta*. 54 (2009) 3819–3829. <https://doi.org/10.1016/j.electacta.2009.02.006>.
- [21] P. Kar, J.W. Evans, A model for the electrochemical reduction of metal oxides in molten salt electrolytes, *Electrochimica Acta*. 54 (2008) 835–843.  
<https://doi.org/10.1016/j.electacta.2008.06.040>.
- [22] M. Ma, D. Wang, W. Wang, X. Hu, X. Jin, G.Z. Chen, Extraction of titanium from different titania precursors by the FFC Cambridge process, *J. Alloys Compd.* 420 (2006) 37–45.  
<https://doi.org/10.1016/j.jallcom.2005.10.048>.
- [23] K. Ono, R.O. Suzuki, A new concept for producing Ti sponge: Calciothermic reduction, *JOM*. 54 (2002) 59–61. <https://doi.org/10.1007/BF02701078>.
- [24] R.O. Suzuki, Calciothermic reduction of TiO<sub>2</sub> and in situ electrolysis of CaO in the molten CaCl<sub>2</sub>, *Proc. 11th Int. Conf. High Temp. Mater. Chem. HTMC-XI*. 66 (2005) 461–465.  
<https://doi.org/10.1016/j.jpccs.2004.06.041>.
- [25] R.O. Suzuki, Direct reduction processes for titanium oxide in molten salt, *JOM*. 59 (2007) 68–71. <https://doi.org/10.1007/s11837-007-0014-7>.



- [26] T. Kikuchi, M. Yoshida, S. Matsuura, S. Natsui, E. Tsuji, H. Habazaki, R.O. Suzuki, Rapid reduction of titanium dioxide nano-particles by reduction with a calcium reductant, *J. Phys. Chem. Solids*. 75 (2014) 1041–1048. <https://doi.org/10.1016/j.jpcs.2014.04.016>.
- [27] R.O. Suzuki, S. Fukui, Reduction of TiO<sub>2</sub> in Molten CaCl<sub>2</sub> by Ca Deposited during CaO Electrolysis, *Mater. Trans.* 45 (2004) 1665–1671. <https://doi.org/10.2320/matertrans.45.1665>.
- [28] K. Ono, T.H. Okabe, R.O. Suzuki, Design, Test and Theoretical Assessments for Reduction of Titanium Oxide to Produce Titanium in Molten Salt, *Mater. Trans.* 58 (2017) 313–318. <https://doi.org/10.2320/matertrans.MK201604>.
- [29] R.O. Suzuki, K. Ono, K. Teranuma, Calciothermic reduction of titanium oxide and in-situ electrolysis in molten CaCl<sub>2</sub>, *Metall. Mater. Trans. B.* 34 (2003) 287–295. <https://doi.org/10.1007/s11663-003-0074-1>.
- [30] R.F. Descallar-Arriescado, N. Kobayashi, T. Kikuchi, R.O. Suzuki, Calciothermic reduction of NiO by molten salt electrolysis of CaO in CaCl<sub>2</sub> melt, *Electrochimica Acta*. 56 (2011) 8422–8429. <https://doi.org/10.1016/j.electacta.2011.07.027>.
- [31] D. Tang, H. Yin, X. Cheng, W. Xiao, D. Wang, Green production of nickel powder by electro-reduction of NiO in molten Na<sub>2</sub>CO<sub>3</sub>–K<sub>2</sub>CO<sub>3</sub>, *Int. J. Hydrog. Energy*. 41 (2016) 18699–18705. <https://doi.org/10.1016/j.ijhydene.2016.06.078>.
- [32] J. Ge, F. Zhang, H. Jiao, S. Jiao, Metallic Nickel Preparation by Electro-Deoxidation in Molten Sodium Hydroxide, *J. Electrochem. Soc.* 162 (2015) E185–E189. <https://doi.org/10.1149/2.0811509jes>.
- [33] D. Wang, G. Qiu, X. Jin, X. Hu, G.Z. Chen, Electrochemical Metallization of Solid Terbium Oxide, *Angew. Chem. Int. Ed.* 45 (2006) 2384–2388. <https://doi.org/10.1002/anie.200503571>.
- [34] M. Erdoğan, İ. Karakaya, Electrochemical Reduction of Tungsten Compounds to Produce Tungsten Powder, *Metall. Mater. Trans. B.* 41 (2010) 798–804. <https://doi.org/10.1007/s11663-010-9374-4>.
- [35] X.Y. Yan, D.J. Fray, Production of niobium powder by direct electrochemical reduction of solid Nb<sub>2</sub>O<sub>5</sub> in a eutectic CaCl<sub>2</sub>-NaCl melt, *Metall. Mater. Trans. B.* 33 (2002) 685–693. <https://doi.org/10.1007/s11663-002-0021-6>.
- [36] Q. Song, Q. Xu, X. Kang, J. Du, Z. Xi, Mechanistic insight of electrochemical reduction of Ta<sub>2</sub>O<sub>5</sub> to tantalum in a eutectic CaCl<sub>2</sub>-NaCl molten salt, *J. Alloys Compd.* 490 (2010) 241–246. <https://doi.org/10.1016/j.jallcom.2009.09.168>.

- [37] E. Gordo, G.Z. Chen, D.J. Fray, Toward optimisation of electrolytic reduction of solid chromium oxide to chromium powder in molten chloride salts, *Electrochimica Acta*. 49 (2004) 2195–2208. <https://doi.org/10.1016/j.electacta.2003.12.045>.
- [38] K.T. Kilby, S. Jiao, D.J. Fray, Current efficiency studies for graphite and SnO<sub>2</sub>-based anodes for the electro-deoxidation of metal oxides, *Electrochimica Acta*. 55 (2010) 7126–7133. <https://doi.org/10.1016/j.electacta.2010.06.049>.
- [39] Schwandt Carsten, Fray Derek J., The Electrochemical Reduction of Chromium Sesquioxide in Molten Calcium Chloride under Cathodic Potential Control, *Z. Für Naturforschung A*. 62 (2007) 655. <https://doi.org/10.1515/zna-2007-10-1115>.
- [40] C.E. Till, Y.I. Chang, W.H. Hannum, The intergral fast reactor-an overview, *Technol. Integral Fast React. Its Assoc. Fuel Cycle*. 31 (1997) 3–11. [https://doi.org/10.1016/0149-1970\(96\)00001-7](https://doi.org/10.1016/0149-1970(96)00001-7).
- [41] U.S. Department of Energy, Record of Decision for the Treatment and Management of Sodium-Bonded Spent Nuclear Fuel, *Fed. Regist.* 65 (2000) 56565–56570.
- [42] C. Solbrig, B. R. Westphal, T. Johnson, S. Li, K. Marsden, K.M. Goff, *Pyroprocessing Progress at Idaho National Laboratory*, in: United States, 2007. <https://www.osti.gov/servlets/purl/927638>.
- [43] A.J. Bard, *Encyclopedia of Electrochemistry of the Elements*, New York; Basel: Marcel Dekker, cop., 1976.
- [44] S.X. Li, Anodic Process of Electrorefining Spent Nuclear Fuel in Molten LiCl-KCl-UCl<sub>3</sub>/Cd System, *ECS Proc. Vol. 2002–19* (2002) 541–552. <https://doi.org/10.1149/200219.0541PV>.
- [45] S.X. Li, M.F. Simpson, Anodic process of electrorefining spent driver fuel in molten LiCl-KCl-UCl<sub>3</sub>/Cd system, *Min. Metall. Explor.* 22 (2005) 192–198. <https://doi.org/10.1007/BF03403322>.
- [46] S.D. Herrmann, S.X. Li, Separation and Recovery of Uranium Metal from Spent Light Water Reactor Fuel Via Electrolytic Reduction and Electrorefining, *Nucl. Technol.* 171 (2010) 247–265. <https://doi.org/10.13182/NT171-247>.
- [47] S. X. Li, T. A. Johnson, B. R. Westphal, K. M. Goff, R. W. Benedict, *Electrorefining Experience For Pyrochemical Reprocessing of Spent EBR-II Driver Fuel*, in: United States, 2005. <https://www.osti.gov/servlets/purl/911150>.
- [48] Michael F. Simpson, *Developments of Spent Nuclear Fuel Pyroprocessing Technology at Idaho National Laboratory*, United States, 2012. <https://doi.org/10.2172/1044209>.

- [49] S. Herrmann, S. Li, M. Simpson, Electrolytic Reduction of Spent Light Water Reactor Fuel Bench-Scale Experiment Results, *J. Nucl. Sci. Technol.* 44 (2007) 361–367.  
<https://doi.org/10.1080/18811248.2007.9711295>.
- [50] S. D. Herrmann, S. X. Li, M. F. Simpson, Electrolytic Reduction of Spent Oxide Fuel - Bench-Scale Test Results, United States, 2005.  
<http://www.inl.gov/technicalpublications/Documents/3398091.pdf>.
- [51] S.D. Herrmann, S.X. Li, M.F. Simpson, S. Phongikaroon, Electrolytic Reduction of Spent Nuclear Oxide Fuel as Part of an Integral Process to Separate and Recover Actinides from Fission Products, *Sep. Sci. Technol.* 41 (2006) 1965–1983.  
<https://doi.org/10.1080/01496390600745602>.
- [52] S. D. Herrmann, Electrolytic Reduction of Spent Nuclear Oxide Fuel -- Effects of Fuel Form and Cathode Containment Materials on Bench-Scale Operations, in: Boise, Idaho, United States, 2007. <https://www.osti.gov/servlets/purl/918184>.
- [53] J.-M. Hur, S.M. Jeong, H. Lee, Underpotential deposition of Li in a molten LiCl–Li<sub>2</sub>O electrolyte for the electrochemical reduction of U from uranium oxides, *Electrochem. Commun.* 12 (2010) 706–709. <https://doi.org/10.1016/j.elecom.2010.03.012>.
- [54] S.M. Jeong, H.-S. Shin, S.-H. Cho, J.-M. Hur, H.S. Lee, Electrochemical behavior of a platinum anode for reduction of uranium oxide in a LiCl molten salt, *Electrochimica Acta.* 54 (2009) 6335–6340. <https://doi.org/10.1016/j.electacta.2009.05.080>.
- [55] E.-Y. Choi, C.Y. Won, D.-S. Kang, S.-W. Kim, J.-S. Cha, S.-J. Lee, W. Park, H.S. Im, J.-M. Hur, Production of uranium metal via electrolytic reduction of uranium oxide in molten LiCl and salt distillation, *J. Radioanal. Nucl. Chem.* 304 (2015) 535–546.  
<https://doi.org/10.1007/s10967-014-3842-2>.
- [56] E.-Y. Choi, I.-K. Choi, J.-M. Hur, D.-S. Kang, H.-S. Shin, S.M. Jeong, In Situ Electrochemical Measurement of O<sub>2</sub>– Concentration in Molten Li<sub>2</sub>O/LiCl during Uranium Oxide Reduction Process, *Electrochem. Solid-State Lett.* 15 (2011) E11–E13.  
<https://doi.org/10.1149/2.016203esl>.
- [57] S. Herrmann, S. Li, B. Serrano-Rodriguez, Observations of Oxygen Ion Behavior in the Lithium-Based Electrolytic Reduction of Uranium Oxide, (2009).  
<https://inldigitalibrary.inl.gov/sites/sti/sti/4363820.pdf>.
- [58] E.-Y. Choi, C. Won, J.-S. Cha, W. Park, H. Im, S.-S. Hong, J.-M. Hur, Electrochemical reduction of UO<sub>2</sub> in LiCl–Li<sub>2</sub>O molten salt using porous and nonporous anode shrouds, *J. Nucl. Mater.* 444 (2014) 261–269. <https://doi.org/10.1016/j.jnucmat.2013.09.061>.

- [59] K. Jiang, Hu, Sun, Wang, Jin, Ren, G.Z. Chen, Electrochemical Synthesis of  $\text{LiTiO}_2$  and  $\text{LiTi}_2\text{O}_4$  in Molten  $\text{LiCl}$ , *Chem. Mater.* 16 (2004) 4324–4329. <https://doi.org/10.1021/cm0494148>.
- [60] H.-S. Shin, J.-M. Hur, S.M. Jeong, K.Y. Jung, Direct electrochemical reduction of titanium dioxide in molten lithium chloride, *J. Ind. Eng. Chem.* 18 (2012) 438–442. <https://doi.org/10.1016/j.jiec.2011.11.111>.
- [61] H. Jin-Mok, L. Su-Chul, J. Sang-Mun, S. Chung-Seok, Electrochemical Reduction of  $\text{TiO}_2$  in Molten  $\text{LiCl-Li}_2\text{O}$ , *Chem. Lett.* 36 (2007) 1028–1029. <https://doi.org/10.1246/cl.2007.1028>.
- [62] K. Dring, Direct Electrochemical Reduction of Titanium Dioxide in Molten Salts, *Key Eng. Mater.* 436 (2010) 27–34. <https://doi.org/10.4028/www.scientific.net/KEM.436.27>.
- [63] S.M. Jeong, J.-Y. Jung, C.-S. Seo, S.-W. Park, Characteristics of an electrochemical reduction of  $\text{Ta}_2\text{O}_5$  for the preparation of metallic tantalum in a  $\text{LiCl-Li}_2\text{O}$  molten salt, *J. Alloys Compd.* 440 (2007) 210–215. <https://doi.org/10.1016/j.jallcom.2006.05.139>.
- [64] S.M. Jeong, H.Y. Yoo, J.-M. Hur, C.-S. Seo, Preparation of metallic niobium from niobium pentoxide by an indirect electrochemical reduction in a  $\text{LiCl-Li}_2\text{O}$  molten salt, *Proc. 12th Int. IUPAC Conf. High Temp. Mater. Chem.-HTMC XII.* 452 (2008) 27–31. <https://doi.org/10.1016/j.jallcom.2007.02.057>.
- [65] G.Z. Chen, D.J. Fray, Voltammetric Studies of the Oxygen-Titanium Binary System in Molten Calcium Chloride, *J. Electrochem. Soc.* 149 (2002) E455–E467.
- [66] J.-M. Hur, J.-S. Cha, E.-Y. Choi, Can Carbon Be an Anode for Electrochemical Reduction in a  $\text{LiCl-Li}_2\text{O}$  Molten Salt?, *ECS Electrochem. Lett.* 3 (2014) E5–E7. <https://doi.org/10.1149/2.0071410eel>.
- [67] H.V. Ijje, R.C. Lawrence, N.J. Siambun, S.M. Jeong, D.A. Jewell, D. Hu, G.Z. Chen, Electrodeposition and re-oxidation of carbon in carbonate-containing molten salts, *Faraday Discuss.* 172 (2014) 105–116. <https://doi.org/10.1039/C4FD00046C>.
- [68] J.C. Gomez-Vidal, R. Tirawat, Corrosion of alloys in a chloride molten salt ( $\text{NaCl-LiCl}$ ) for solar thermal technologies, *Sol. Energy Mater. Sol. Cells.* 157 (2016) 234–244. <https://doi.org/10.1016/j.solmat.2016.05.052>.
- [69] Natalie J. Gese, Batric Pesic, Electrochemistry of  $\text{LiCl-Li}_2\text{O-H}_2\text{O}$  Molten Salt Systems, in: *Research Org.: Idaho National Laboratory (INL)*, 2013. <https://inldigitallibrary.inl.gov/sites/sti/sti/5650454.pdf>.
- [70] Y. Sakamura, M. Kurata, T. Inoue, Electrochemical Reduction of  $\text{UO}_2$  in Molten  $\text{CaCl}_2$  or  $\text{LiCl}$ , *J. Electrochem. Soc.* 153 (2006) D31–D39. <https://doi.org/10.1149/1.2160430>.

- [71] A. Samin, Z. Wang, E. Lahti, M. Simpson, J. Zhang, Estimation of key physical properties for  $\text{LaCl}_3$  in molten eutectic  $\text{LiCl-KCl}$  by fitting cyclic voltammetry data to a BET-based electrode reaction kinetics model, *J. Nucl. Mater.* 475 (2016) 149–155.  
<https://doi.org/10.1016/j.jnucmat.2016.04.002>.
- [72] P. Bagri, M.F. Simpson, Determination of activity coefficient of lanthanum chloride in molten  $\text{LiCl-KCl}$  eutectic salt as a function of cesium chloride and lanthanum chloride concentrations using electromotive force measurements, *J. Nucl. Mater.* 482 (2016) 248–256.  
<https://doi.org/10.1016/j.jnucmat.2016.10.006>.
- [73] F. Lumia, L. Ramond, C. Pagnoux, G. Bernard-Granger, Fabrication of homogenous pellets by freeze granulation of optimized  $\text{TiO}_2\text{-Y}_2\text{O}_3$  suspensions, *J. Eur. Ceram. Soc.* 39 (2019).  
<https://doi.org/10.1016/j.jeurceramsoc.2019.01.036>.
- [74] E.R. Van Artsdalen, I.S. Yaffe, Electrical Conductance and Density of Molten Salt Systems:  $\text{KCl-LiCl}$ ,  $\text{KCl-NaCl}$  and  $\text{KCl-KI}$ , *J. Phys. Chem.* 59 (1955) 118–127.  
<https://doi.org/10.1021/j150524a007>.
- [75] D.R. Lide, *CRC Handbook of Chemistry and Physics: A Ready-reference Book of Chemical and Physical Data*, CRC-Press, 1995. <https://books.google.com/books?id=q2qJId5TKOkC>.
- [76] L.D. Brown, R. Abdulaziz, R. Jervis, V. Bharath, T.J. Mason, R.C. Atwood, C. Reinhard, L.D. Connor, D. Inman, D.J.L. Brett, P.R. Shearing, A novel molten-salt electrochemical cell for investigating the reduction of uranium dioxide to uranium metal by lithium using it in situ synchrotron radiation, *J. Synchrotron Radiat.* 24 (2017) 439–444.  
<https://doi.org/10.1107/S1600577517000625>.
- [77] Y. Sakamura, M. Iizuka, S. Kitawaki, A. Nakayoshi, H. Kofuji, Formation and reduction behaviors of zirconium oxide compounds in  $\text{LiCl-Li}_2\text{O}$  melt at 923 K, *J. Nucl. Mater.* 466 (2015) 269–279. <https://doi.org/10.1016/j.jnucmat.2015.08.011>.
- [78] S.P. Fusselman, J.J. Roy, D.L. Grimmett, L.F. Grantham, C.L. Krueger, C.R. Nabelek, T.S. Storvick, T. Inoue, T. Hijikata, K. Kinoshita, Y. Sakamura, K. Uozumi, T. Kawai, N. Takahashi, Thermodynamic Properties for Rare Earths and Americium in Pyropartitioning Process Solvents, *J. Electrochem. Soc.* 146 (1999) 2573–2580.  
<https://doi.org/10.1149/1.1391974>.
- [79] Q. Wang, Y. Li, S. Jiao, H. Zhu, Producing metallic titanium through electro-refining of titanium nitride anode, *Electrochem. Commun.* 35 (2013) 135–138.  
<https://doi.org/10.1016/j.elecom.2013.07.047>.

- [80] A.J. Bard, L.R. Faulkner, *Electrochemical Methods: Fundamentals and Applications*, 2nd Edition, 2008.
- [81] C.S. SEO, S.B. PARK, B.H. PARK, K.J. JUNG, S.W. PARK, S.H. KIM, Electrochemical Study on the Reduction Mechanism of Uranium Oxide in a LiCl-Li<sub>2</sub>O Molten Salt, *J. Nucl. Sci. Technol.* 43 (2006) 587–595. <https://doi.org/10.1080/18811248.2006.9711137>.
- [82] N.W. Shay, *Electrochemical Sensor Development for Fluoride Molten Salt Redox Control*, The Ohio State University, 2017.  
[https://etd.ohiolink.edu/etd.send\\_file?accession=osu149265579014054&disposition=inline](https://etd.ohiolink.edu/etd.send_file?accession=osu149265579014054&disposition=inline).
- [83] F. Carotti, H. Wu, R.O. Scarlat, Characterization of a Thermodynamic Reference Electrode for Molten LiF-BeF<sub>2</sub> (FLiBe), *J. Electrochem. Soc.* 164 (2017) H854–H861.  
<https://doi.org/10.1149/2.1591712jes>.
- [84] P.W. Ruch, D. Cericola, M. Hahn, R. Kötz, A. Wokaun, On the use of activated carbon as a quasi-reference electrode in non-aqueous electrolyte solutions, *J. Electroanal. Chem.* 636 (2009) 128–131. <https://doi.org/10.1016/j.jelechem.2009.09.007>.
- [85] G.L. Fredrickson, G. Cao, P.K. Tripathy, M.R. Shaltry, S.D. Herrmann, T.-S. Yoo, T.Y. Karlsson, D.C. Horvath, R. Gakhar, A.N. Williams, R.O. Hoover, W.C. Phillips, K.C. Marsden, Review—Electrochemical Measurements in Molten Salt Systems: A Guide and Perspective, *J. Electrochem. Soc.* 166 (2019) D645–D659. <https://doi.org/10.1149/2.0991913jes>.
- [86] S.M. Jeong, H.-S. Shin, S.-S. Hong, J.-M. Hur, J.B. Do, H.S. Lee, Electrochemical reduction behavior of U<sub>3</sub>O<sub>8</sub> powder in a LiCl molten salt, *Electrochimica Acta.* 55 (2010) 1749–1755.  
<https://doi.org/10.1016/j.electacta.2009.10.060>.
- [87] M. Shi, S. Li, H. Zhao, High Current Efficiency of NiO Electro-Reduction in Molten Salt, *J. Electrochem. Soc.* 165 (2018) E768–E772. <https://doi.org/10.1149/2.0781814jes>.
- [88] T.F. Fuller, J.H. Harb, *Electrochemical Engineering*, John Wiley & Sons Inc., 2018.  
<https://www.wiley.com/en-us/Electrochemical+Engineering-p-9781119446590>.
- [89] D. Horvath, M.F. Simpson, Electrochemical Monitoring of Ni Corrosion Induced by Water in Eutectic LiCl-KCl, *J. Electrochem. Soc.* 165 (2018) C226–C233.  
<https://doi.org/10.1149/2.0391805jes>.
- [90] H.A. Laitinen, B.B. Bhatia, Electrochemical Study of Metallic Oxides in Fused Lithium Chloride-Potassium Chloride Eutectic, *J. Electrochem. Soc.* 107 (1960) 705.  
<https://doi.org/10.1149/1.2427812>.
- [91] S.D. Herrmann, P.K. Tripathy, S.M. Frank, J.A. King, Comparative study of monolithic platinum and iridium as oxygen-evolving anodes during the electrolytic reduction of uranium

- oxide in a molten LiCl–Li<sub>2</sub>O electrolyte, *J. Appl. Electrochem.* 49 (2019) 379–388.  
<https://doi.org/10.1007/s10800-019-01287-1>.
- [92] M.J. O'Malley, H. Verweij, P.M. Woodward, Structure and properties of ordered Li<sub>2</sub>IrO<sub>3</sub> and Li<sub>2</sub>PtO<sub>3</sub>, *J. Solid State Chem.* 181 (2008) 1803–1809.  
<https://doi.org/10.1016/j.jssc.2008.04.005>.
- [93] E.-Y. Choi, J.W. Lee, J.J. Park, J.-M. Hur, J.-K. Kim, K.Y. Jung, S.M. Jeong, Electrochemical reduction behavior of a highly porous SIMFUEL particle in a LiCl molten salt, 22nd Int. Symp. Chem. React. Eng. ISCRE 22. 207–208 (2012) 514–520.  
<https://doi.org/10.1016/j.cej.2012.06.161>.
- [94] C.R.V.S. Nagesh, Challenges in the Development of Electrochemical Reduction of TiO<sub>2</sub> to Titanium Metal, *Trans. Indian Inst. Met.* (2020). <https://doi.org/10.1007/s12666-020-01906-y>.
- [95] A.J. Burak, M.F. Simpson, Electrochemical Measurement of Li<sub>2</sub>O in Molten LiCl Salt, *ECS Trans.* 75 (2016) 55–61. <https://doi.org/10.1149/07515.0055ecst>.
- [96] X.Y. Yan, D.J. Fray, Fused salt electrolytic reduction of solid oxides and oxide mixtures for green production of metals and alloys, *Miner. Process. Extr. Metall.* 116 (2007) 17–24.  
<https://doi.org/10.1179/174328507X163742>.
- [97] G. Qiu, M. Ma, D. Wang, X. Jin, X. Hu, G.Z. Chen, Metallic Cavity Electrodes for Investigation of Powders: Electrochemical Reduction of NiO and Cr<sub>2</sub>O<sub>3</sub> Powders in Molten CaCl<sub>2</sub>, *J. Electrochem. Soc.* 152 (2005) E328–E336. <https://doi.org/10.1149/1.2012567>.
- [98] M. Mohamedi, B. Børresen, G.M. Haarberg, R. Tunold, Anodic Behavior of Carbon Electrodes in CaO □ CaCl<sub>2</sub> Melts at 1123 K, *J. Electrochem. Soc.* 146 (1999) 1472–1477.  
<https://doi.org/10.1149/1.1391789>.
- [99] T. Wakamatsu, T. Uchiyama, S. Natsui, T. Kikuchi, R.O. Suzuki, Solubility of gaseous carbon dioxide in molten LiCl–Li<sub>2</sub>O, *Fluid Phase Equilibria.* 385 (2015) 48–53.  
<https://doi.org/10.1016/j.fluid.2014.10.046>.
- [100] A.H. Wang, X.L. Zhang, X.F. Zhang, X.Y. Qiao, H.G. Xu, C.S. Xie, Ni-based alloy/submicron WS<sub>2</sub> self-lubricating composite coating synthesized by Nd:YAG laser cladding, *Int. Symp. Inorg. Interfacial Eng.* 2006. 475 (2008) 312–318. <https://doi.org/10.1016/j.msea.2007.04.087>.
- [101] N. Hanada, E. Hirotohi, T. Ichikawa, E. Akiba, H. Fujii, SEM and TEM characterization of magnesium hydride catalyzed with Ni nano-particle or Nb<sub>2</sub>O<sub>5</sub>, *J. Alloys Compd.* 450 (2008) 395–399. <https://doi.org/10.1016/j.jallcom.2006.10.128>.

- [102] J.H. Lehman, M. Terrones, E. Mansfield, K.E. Hurst, V. Meunier, Evaluating the characteristics of multiwall carbon nanotubes, *Carbon*. 49 (2011) 2581–2602.  
<https://doi.org/10.1016/j.carbon.2011.03.028>.
- [103] L. Wei, J. Xianbo, H. Fulong, C.G. Z, Metal to Oxide Molar Volume Ratio: The Overlooked Barrier to Solid State Electroreduction and a “Green” Bypass through Recyclable  $\text{NH}_4\text{HCO}_3$ , *Angew. Chem. Int. Ed.* 49 (2010) 3203–3206. <https://doi.org/10.1002/anie.200906833>.
- [104] Qiu Guohong, Jiang Kai, Ma Meng, Wang Dihua, Jin Xianbo, Chen George Z., Roles of Cationic and Elemental Calcium in the Electro-Reduction of Solid Metal Oxides in Molten Calcium Chloride, *Z. Für Naturforschung A*. 62 (2014) 292. <https://doi.org/10.1515/zna-2007-5-610>.
- [105] H.-S. Shin, J.-M. Hur, S.M. Jeong, K.Y. Jung, Direct Electrochemical Reduction of Titanium Dioxide in Molten Lithium Chloride, *J. Ind. Eng. Chem.* 18 (2012) 438–442.
- [106] G. Kresse, J. Hafner, Ab initio molecular dynamics for liquid metals, *Phys. Rev. B*. 47 (1993) 558–561. <https://doi.org/10.1103/PhysRevB.47.558>.
- [107] G. Kresse, D. Joubert, From ultrasoft pseudopotentials to the projector augmented-wave method, *Phys. Rev. B*. 59 (1999) 1758–1775. <https://doi.org/10.1103/PhysRevB.59.1758>.
- [108] T.B. Joseph, N. Sanil, K.S. Mohandas, K. Nagarajan, A Study of Graphite as Anode in the Electro-Deoxidation of Solid  $\text{UO}_2$  in  $\text{LiCl-Li}_2\text{O}$  Melt, *J. Electrochem. Soc.* 162 (2015) E51–E58. <https://doi.org/10.1149/2.0521506jes>.
- [109] H.V. Ijije, R.C. Lawrence, G.Z. Chen, Carbon electrodeposition in molten salts: electrode reactions and applications, *RSC Adv.* 4 (2014) 35808–35817.  
<https://doi.org/10.1039/C4RA04629C>.
- [110] A. Merwin, Material Interactions with Molten  $\text{LiCl-Li}_2\text{O-Li}$ , Dissertation, University of Nevada, 2016. <https://scholarworks.unr.edu/handle/11714/2115>.
- [111] J.D. WALTON JR., N.E. POULOS, Cermets From Thermite Reactions, *J. Am. Ceram. Soc.* 42 (1959) 40–49. <https://doi.org/10.1111/j.1151-2916.1959.tb09140.x>.
- [112] M.B. Robin, P. Day, Mixed Valence Chemistry-A Survey and Classification, in: H.J. Emeléus, A.G. Sharpe (Eds.), *Adv. Inorg. Chem. Radiochem.*, Academic Press, 1968: pp. 247–422.  
[https://doi.org/10.1016/S0065-2792\(08\)60179-X](https://doi.org/10.1016/S0065-2792(08)60179-X).
- [113] Y. Deng, Wang, W. Xiao, Jin, Hu, G.Z. Chen, Electrochemistry at Conductor/Insulator/Electrolyte Three-Phase Interlines: A Thin Layer Model, *J. Phys. Chem. B*. 109 (2005) 14043–14051. <https://doi.org/10.1021/jp044604r>.



- [114] T. Wu, Jin, W. Xiao, Hu, Wang, G.Z. Chen, Thin Pellets: Fast Electrochemical Preparation of Capacitor Tantalum Powders, *Chem. Mater.* 19 (2007) 153–160.  
<https://doi.org/10.1021/cm0618648>.
- [115] W. Xiao, X. Jin, Y. Deng, D. Wang, X. Hu, G.Z. Chen, Electrochemically Driven Three-Phase Interlines into Insulator Compounds: Electroreduction of Solid SiO<sub>2</sub> in Molten CaCl<sub>2</sub>, *ChemPhysChem.* 7 (2006) 1750–1758. <https://doi.org/10.1002/cphc.200600149>.
- [116] T. Ohzuku, Zero-Strain Insertion Material of Li[Li<sub>1/3</sub>Ti<sub>5/3</sub>]O<sub>4</sub> for Rechargeable Lithium Cells, *J. Electrochem. Soc.* 142 (1995) 1431.  
<https://doi.org/10.1149/1.2048592>.
- [117] J.P. Perdew, K. Burke, M. Ernzerhof, Generalized Gradient Approximation Made Simple, *Phys. Rev. Lett.* 77 (1996) 3865–3868. <https://doi.org/10.1103/PhysRevLett.77.3865>.
- [118] Z. Hu, H. Metiu, Choice of U for DFT+U Calculations for Titanium Oxides, *J. Phys. Chem. C.* 115 (2011) 5841–5845. <https://doi.org/10.1021/jp111350u>.
- [119] Y. Wang, R. Ahuja, B. Johansson, Mean-field potential approach to the quasiharmonic theory of solids, *Int. J. Quantum Chem.* 96 (2004) 501–506. <https://doi.org/10.1002/qua.10769>.
- [120] A. Mandroyan, M. Mourad-Mahmoud, M.-L. Doche, J.-Y. Hihn, Effects of ultrasound and temperature on copper electro reduction in Deep Eutectic Solvents (DES), *AOSS 2013.* 21 (2014) 2010–2019. <https://doi.org/10.1016/j.ultsonch.2014.02.019>.
- [121] Z. Ma, W. Zhao, J. Yan, D. Li, Interfacial reaction of intermetallic compounds of ultrasonic-assisted brazed joints between dissimilar alloys of Ti6Al4V and Al4Cu1Mg, *Ultrason. Sonochem.* 18 (2011) 1062–1067. <https://doi.org/10.1016/j.ultsonch.2011.03.025>.
- [122] Z. Liu, M. Rakita, W. Xu, X. Wang, Q. Han, Ultrasound assisted salts–metal reaction for synthesizing TiB<sub>2</sub> particles at low temperature, *Chem. Eng. J.* 263 (2015) 317–324.  
<https://doi.org/10.1016/j.cej.2014.11.043>.
- [123] J.H. Bang, K.S. Suslick, Applications of Ultrasound to the Synthesis of Nanostructured Materials, *Adv. Mater.* 22 (2010) 1039–1059. <https://doi.org/10.1002/adma.200904093>.
- [124] K.A. Kusters, S.E. Pratsinis, S.G. Thoma, D.M. Smith, Ultrasonic fragmentation of agglomerate powders, *Chem. Eng. Sci.* 48 (1993) 4119–4127. [https://doi.org/10.1016/0009-2509\(93\)80258-R](https://doi.org/10.1016/0009-2509(93)80258-R).
- [125] F. Chemat, N. Rombaut, A.-G. Sicaire, A. Meullemiestre, A.-S. Fabiano-Tixier, M. Abert-Vian, Ultrasound assisted extraction of food and natural products. Mechanisms, techniques, combinations, protocols and applications. A review, *Ultrason. Sonochem.* 34 (2017) 540–560.  
<https://doi.org/10.1016/j.ultsonch.2016.06.035>.

- [126] L. Petigny, S. Périno-Issartier, J. Wajsman, F. Chemat, Batch and Continuous Ultrasound Assisted Extraction of Boldo Leaves (*Peumus boldus* Mol.), *Int. J. Mol. Sci.* 14 (2013). <https://doi.org/10.3390/ijms14035750>.
- [127] D.R. Gang, J. Wang, N. Dudareva, K.H. Nam, J.E. Simon, E. Lewinsohn, E. Pichersky, An Investigation of the Storage and Biosynthesis of Phenylpropenes in Sweet Basil, *Plant Physiol.* 125 (2001) 539. <https://doi.org/10.1104/pp.125.2.539>.
- [128] R. Karshafian, P.D. Bevan, R. Williams, S. Samac, P.N. Burns, Sonoporation by Ultrasound-Activated Microbubble Contrast Agents: Effect of Acoustic Exposure Parameters on Cell Membrane Permeability and Cell Viability, *Ultrasound Med. Biol.* 35 (2009) 847–860. <https://doi.org/10.1016/j.ultrasmedbio.2008.10.013>.
- [129] D.L. Miller, S.V. Pislaru, J.F. Greenleaf, Sonoporation: Mechanical DNA delivery by ultrasonic cavitation, *Somat. Cell Mol. Genet.* 27 (2002) 115–134. <https://doi.org/10.1023/A:1022983907223>.
- [130] S. Ohta, K. Suzuki, S. Miyagawa, Y. Ogino, M. Villacorte, Y. Wada, G. Yamada, Sonoporation in Developmental Biology, in: H. Nakamura (Ed.), *Electroporation Sonoporation Dev. Biol.*, Springer Japan, Tokyo, 2009: pp. 317–326. [https://doi.org/10.1007/978-4-431-09427-2\\_27](https://doi.org/10.1007/978-4-431-09427-2_27).
- [131] A. Meullemiestre, C. Breil, M. Abert-Vian, F. Chemat, Microwave, ultrasound, thermal treatments, and bead milling as intensification techniques for extraction of lipids from oleaginous *Yarrowia lipolytica* yeast for a biojetfuel application, *Bioresour. Technol.* 211 (2016) 190–199. <https://doi.org/10.1016/j.biortech.2016.03.040>.
- [132] J. Wu, Shear stress in cells generated by ultrasound, *Eff. Ultrasound Infrasound Relev. Hum. Health.* 93 (2007) 363–373. <https://doi.org/10.1016/j.pbiomolbio.2006.07.016>.
- [133] J.-Z. Zhang, J.K. Saggar, Z.-L. Zhou, B. Hu, Different effects of sonoporation on cell morphology and viability, *Bosn. J. Basic Med. Sci.* 12 (2012) 64–68. <https://doi.org/10.17305/bjbms.2012.2497>.
- [134] R. Ishida, D. Kami, T. Kusaba, Y. Kirita, T. Kishida, O. Mazda, T. Adachi, S. Gojo, Kidney-specific Sonoporation-mediated Gene Transfer, *Mol. Ther.* 24 (2016) 125–134. <https://doi.org/10.1038/mt.2015.171>.
- [135] S. Tamura, M. Hatakeyama, The role of acoustic cavitation in liquid pressurization in narrow tubes, *J. Appl. Phys.* 113 (2013) 144905. <https://doi.org/10.1063/1.4801422>.
- [136] N.V. Malykh, V. Petrov, G. Sankin, On the Sonocapillary Effect, *Proc. 5th World Congr. Ultrason. WCU.* (2003) 1343–1346.

- [137] D. Pingret, A.-S. Fabiano-Tixier, C.L. Bourvellec, C.M.G.C. Renard, F. Chemat, Lab and pilot-scale ultrasound-assisted water extraction of polyphenols from apple pomace, *J. Food Eng.* 111 (2012) 73–81. <https://doi.org/10.1016/j.jfoodeng.2012.01.026>.
- [138] A. Sarwono, Z. Man, N. Muhammad, A.S. Khan, W.S.W. Hamzah, A.H.A. Rahim, Z. Ullah, C.D. Wilfred, A new approach of probe sonication assisted ionic liquid conversion of glucose, cellulose and biomass into 5-hydroxymethylfurfural, *Ultrason. Sonochem.* 37 (2017) 310–319. <https://doi.org/10.1016/j.ultsonch.2017.01.028>.
- [139] L. Qiu, V.G. Pol, J. Calderon-Moreno, A. Gedanken, Synthesis of tin nanorods via a sonochemical method combined with a polyol process, *Ultrason. Sonochem.* 12 (2005) 243–247. <https://doi.org/10.1016/j.ultsonch.2004.02.001>.
- [140] E. Berretti, A. Giaccherini, S.M. Martinuzzi, M. Innocenti, T.J.S. Schubert, F.M. Stiemke, S. Caporali, Aluminium Electrodeposition from Ionic Liquid: Effect of Deposition Temperature and Sonication, *Mater. Basel Switz.* 9 (2016) 719. <https://doi.org/10.3390/ma9090719>.
- [141] F. Marken, R.P. Akkermans, R.G. Compton, Voltammetry in the presence of ultrasound: the limit of acoustic streaming induced diffusion layer thinning and the effect of solvent viscosity, *J. Electroanal. Chem.* 415 (1996) 55–63. [https://doi.org/10.1016/S0022-0728\(96\)04641-4](https://doi.org/10.1016/S0022-0728(96)04641-4).
- [142] C.E. Banks, R.G. Compton, A.C. Fisher, I.E. Henley, The transport limited currents at insonated electrodes, *Phys. Chem. Chem. Phys.* 6 (2004) 3147–3152. <https://doi.org/10.1039/B403751K>.